HIGH-SPEED GUIDED-WAVE ELECTRO-OPTIC MODULATORS AND POLARIZATION CONVERTERS IN III-V COMPOUND SEMICONDUCTORS

by

FARNOOSH RAHMATIAN

B. A. Sc. (Honours), The University of British Columbia, 1991
M. A. Sc., The University of British Columbia, 1993

A THESIS SUBMITTED IN PARTIAL FULFILMENT OF

THE REQUIREMENTS FOR THE DEGREE OF

DOCTOR OF PHILOSOPHY

in

THE FACULTY OF GRADUATE STUDIES

(The Department of Electrical and Computer Engineering)

We accept this thesis as conforming
to the required standard

THE UNIVERSITY OF BRITISH COLUMBIA

June 1997

In presenting this thesis in partial fulfilment of the requirements for an advanced degree at the University of British Columbia, I agree that the Library shall make it freely available for reference and study. I further agree that permission for extensive copying of this thesis for scholarly purposes may be granted by the head of my department or by his or her representatives. It is understood that copying or publication of this thesis for financial gain shall not be allowed without my written permission.

Department of _Electrical and Computer Engineering_

The University of British Columbia
Vancouver, Canada

Date _Aug 20, 1997_

DE-6 (2/88)

Abstract

In the last few decades, the need for electronic communication has increased by several orders of magnitude. Due to the rapid growth of the demand for transmission bandwidth, development of very high-speed communication systems is crucial. This thesis describes integrated-optic electro-optic modulators using travelling-wave electrodes in compound semiconductors for ultra-high-speed guided-wave optical communications. Both Mach-Zehnder (MZ) interferometric modulators and polarization converters (PC) have been studied with particular emphasis on the latter ones. Slow-wave travelling-wave electrodes in compound semiconductors have previously been proposed and demonstrated. Here, a study of slow-wave, travelling-wave electrodes on compound semiconductors has been performed in order to significantly improve their use in ultra-wide-band guided-wave electro-optic devices.

The most important factors limiting the high frequency performance of such devices, in general, are the microwave-lightwave velocity mismatch and the microwave loss on the electrodes. Based on the deeper understanding acquired through our study, we have designed, fabricated, and tested low-loss, slow-wave, travelling-wave electrodes on semi-insulating GaAs (SI-GaAs) and AlGaAs/GaAs substrates. Microwave-to-lightwave velocity matching within 1% was achieved using slow-wave coplanar strip electrodes; many of the electrodes had effective microwave indices in the range 3.3 to 3.4 (measured at frequencies up to 40 GHz). For the electrodes fabricated on SI-GaAs substrates, microwave losses of 0.22 Np/cm and 0.34 Np/cm (average values at 40 GHz) were measured for the slow-wave

coplanar strip and the slow-wave coplanar waveguide electrodes, respectively. For the electrodes fabricated on the AlGaAs/GaAs substrates containing the modulators, the corresponding losses were, on average, 0.17 Np/cm higher at 40 GHz.

For the first time, ultra-wide-band polarization converters using slow-wave electrodes have been designed, fabricated, and tested. A detailed analysis of the use of the slow-wave electrodes together with optical ridge waveguides as polarization converters has been provided. The effects of the modal birefringence of the optical waveguides, the microwave loss on the electrodes, and the residual microwave-lightwave velocity mismatch have all been taken into account in our study. Low frequency optical measurements showed very good qualitative agreement between the measured and the predicted results as regards the effect of the modal birefringence; it was also shown that the modal birefringence has to be kept to very small values to keep the efficiency of such modulators high.

High-speed optical measurements were performed at frequencies up to 20 GHz (limited by the equipment bandwidth); the 3-dB optical bandwidths exceeded 20 GHz for both the MZ type and the PC type devices. The MZ modulators, however, had significantly larger half-wave voltages, ~25 V, and their electrodes were significantly "over-slow" (by ~15%). Evidence acquired through this study suggests that reducing the half-wave voltages below 5 volts and keeping the bandwidth in excess of 40 GHz is extremely difficult for these MZ type devices. The PC type devices using slow-wave coplanar strip electrodes, on the other hand, had lower half-wave voltages, as low as 7 V was measured, and had very good microwave-to-lightwave velocity matching, within 1%. From this study we conclude that these devices can be designed to have bandwidths in excess of 100 GHz and half-wave voltages less than 2 V.

Table of Contents

List of Figures

List of Tables

Acknowledgements

My deepest appreciations go to my parents for their love, trust, and support throughout my life including the course of this work. I would also like to thank my fiance, my brothers, and my sister for their encouragement and understanding.

My personal thanks go to Dr. Nicolas A. F. Jaeger for his friendly supervision and support during my research. His dedication and kind guidance have been most invaluable to me and are very much appreciated..

I am most grateful to Dr. Alina Kulpa and Mr. Hiroshi Kato for their valuable discussions and assistance during device fabrication. My thanks extend to our collaborators at the Communications Research Centre (CRC), Ottawa, Ontario, Dr. O. Berolo, Mr. R. James, Mr. H. Khazaei, Ms. L. Skrzek, Dr. W. Wang, Mr. H. Hua, Ms. C. Glaser, Mrs. S. Bernhoff, and Mr. P. Borkowski, for their contributions to this work and their kind assistance during the time I was at the CRC. My gratitude also goes to many individuals in the Department of Electrical and Computer Engineering for their assistance and helpful discussions regarding my work.

Finally, I would like to acknowledge the University of British Columbia and the Natural Sciences and Engineering Research Council of Canada for their generous financial support of this work.

Chapter 1. Introduction

1.1. Introduction

The use of light as the signal carrier can provide an ultra-wide bandwidth for communications. Semiconductor lasers together with optical fibres have provided a significant improvement in the quality and performance of our communications systems. As compared to the systems that use electrical signals travelling on metallic conductors, the systems that use laser light and fibre optics can provide many advantages; e.g., the latter offer much wider transmission bandwidth, immunity to electromagnetic interference, and lower losses [1, p. 1]. Generally, there are two ways of impressing the electrical signal upon the optical carrier: 1) direct modulation of a semiconductor laser diode's current, and 2) external modulation of the laser light [2]. Each method has its own merits; however, for ultra-high-speed modulation, at larger than 30 GHz, the external modulators appear to be the more promising technology [3], [4]. At frequencies larger than 20 GHz, the direct modulation of the laser current, for various types of semiconductor lasers, is restricted by linewidth broadening, frequency chirping, and/or a number of other factors depending on the type of the particular laser used [4]-[14]. The use of external modulators, on the other hand, effectively eliminates a number of the problems encountered in the direct modulation of the laser light and offers a wider bandwidth.

External modulators, typically, exploit either the linear electro-optic effect [2], [15] or electro-absorption [16], [17]. The electro-absorptive modulators can have very small drive powers and devices having bandwidths up to 50 GHz have been demonstrated [18].

Weinmann et al. [17] have shown devices having bandwidths ~40 GHz and drive voltages of 2.5 V for an extinction ratio of ~20 dB. The electro-optic modulators, on the other hand, are the more mature technology, are typically easier to fabricate, have lower insertion losses, and offer wider bandwidths. Devices of this type having bandwidths in excess of 50 GHz have been shown [19]-[22]. The drive voltage for these modulators is, however, larger than the minimum values reported for the electro-absorptive modulators. One of the goals of our research is to show that external electro-optic modulators having bandwidths $\geq$ 100 GHz and low drive voltages, less than 2 V, are possible.

In this thesis both Mach-Zehnder (MZ) type and polarization converter (PC) type electro-optic modulators in compound semiconductors are studied. Velocity-matched coplanar electrodes on AlGaAs/GaAs ridge waveguides are used to fabricate the modulators [23]-[30]. An MZ modulator of this type, having a bandwidth in excess of 40 GHz, has been shown recently [31]. However, this device still suffers from a rather high drive voltage; the half-wave voltage is 14 V at 1.3 μm and 16.8 V at 1.55 μm. A significant reduction in the half-wave voltage for the MZ devices of this type without sacrificing the bandwidth appears to be very difficult. PC type devices, on the other hand, offer lower losses and are easier to design and fabricate. They are studied in detail and are compared with the MZ type devices in terms of both their bandwidths and the required drive powers. The possibility of achieving PC type devices having bandwidths in excess of 100 GHz and drive voltages less than 2 V is investigated.

1.2. Organization of the Thesis

Chapter 2 provides an overview of external electro-optic modulators. The use of slow-wave (SW) travelling-wave (TW) coplanar electrodes on compound semiconductors is reviewed in detail. Then several modulator configurations using slow-wave electrodes are proposed. Finally, an extensive analysis of polarization converters using slow-wave electrodes in III-V compound semiconductors is provided. The analysis is provided in a general form so that it can easily be extended to other polarization converters, such as those fabricated in lithium niobate.

The design and fabrication of the modulators are described in Chapter 3. Several batches of electrodes and modulators were designed and fabricated. The results of the measurements that were used in the design of the latest generations of the modulators are presented and discussed. The design procedure is explained in detail and the fabrication steps are outlined.

Chapter 4 contains the results of the measurements made on the fabricated devices. The microwave performances of the electrodes at frequencies up to 40 GHz are reported. Optical measurements, for both the MZ type devices and the PC type devices, are presented. High-speed optical results at frequencies up to 20 GHz are provided.

A summary and a discussion of the results are provided in Chapter 5. The MZ type and the PC type devices are compared and the conclusions drawn are presented. Finally, some suggestions for future work on these modulators are offered.

Chapter 2. Background and Theory

2.1. Introduction

There are two major groups of materials that have been used for electro-optic modulators: oxygen octahedral ferroelectrics, such as lithium niobate ($LiNbO_3$) and lithium tantalate ($LiTaO_3$), and compound semiconductors (mostly GaAs- or InP-based). Waveguides in lithium niobate are usually fabricated by titanium (Ti) indiffusion [32] or proton-exchange [33], [34]; proton-exchanged waveguides in $LiTaO_3$ have also been demonstrated [35], [36]. The optical waveguides in the semiconductors are usually in the form of rib or ridge waveguides. Lithium niobate generally provides lower optical propagation loss, higher electro-optic coefficients, and lower fibre-to-waveguide insertion loss as compared to the compound semiconductor based devices [37], [38]. Compound semiconductor based modulators, on the other hand, are potentially integrable with opto-electronic circuits, e.g., transistors, lasers, and detectors. Currently, research in external optical modulators includes both oxygen octahedral ferroelectrics and compound semiconductor devices.

In the early stages of the development of the lithium niobate technology, the late 1970's and the early 1980's, researchers introduced several devices which performed various functions, e.g., switches/modulators, mode-converters, filters, and multiplexers [2, pp. 174-206], without much emphasis on their high-speed operation. Similar devices were also proposed and/or fabricated using compound semiconductors [2, pp. 374-382]. A great deal of the later work in the 1980's and early 1990's focussed on the optimization of modulators

to achieve very wide bandwidths. Several electrode designs, such as various types of coplanar electrodes, were modified and used to modulate optical waves at these speeds [15], [20]-[22], [25], [27]-[30], [37], [39]-[54].

There are two kinds of coplanar electrode structure that are usually used with external electro-optic modulators: lumped and travelling-wave (TW) electrodes, see Figure 2.1.1. Here, L represents the electrode length, W represents the electrode width, and G represents the inter-electrode gap. The length of the electrode, for a lumped circuit, has to be small as compared to modulating signal's wavelength. For lumped electrode structures, the modulation bandwidth, Δf, is dependent on the larger of the optical transit time and the time constant of the lumped circuit parameters. The latter is usually more restrictive [2, p. 159]; i.e., the modulation speed is usually limited by the electrode charging time ($\Delta f = 1/\pi RC$).

For TW electrode structures, the electrodes can be considered to be an extension of the transmission line. The modulation bandwidth is restricted by the difference between the speeds of the optical and the modulating electrical waves (and not by the electrode charging time). When conventional coplanar strips or coplanar waveguides are used on lithium niobate (impedance matched at 50Ω), the optical signal travels faster than the microwave modulating signal. For compound semiconductors the reverse situation exists, i.e., the microwave signal travels faster than the optical signal, when using conventional TW electrodes [2], [37]. Researchers have reported on electrode structures for lithium niobate modulators where the microwave signal is speeded up, i.e., "fast-wave electrodes" are used [20], [47], [55]. There are also some "slow-wave electrodes" proposed and demonstrated for compound semiconductor based devices [21]-[31], [37], [53], [56]-[61]. In this thesis, slow-wave TW

5

electrodes for compound semiconductor modulators are studied. A detailed analysis of the use of such electrodes with polarization converters fabricated on AlGaAs/GaAs ridge waveguides is provided. The analysis takes the effects of microwave-lightwave velocity mismatch, microwave loss, and modal birefringence in the optical waveguide, all into account. The effects of these factors on the bandwidth and the drive-power are studied. Modulators and polarization converters in compound semiconductors using low-loss, slow-wave electrodes are proposed and have been designed, fabricated, and tested.
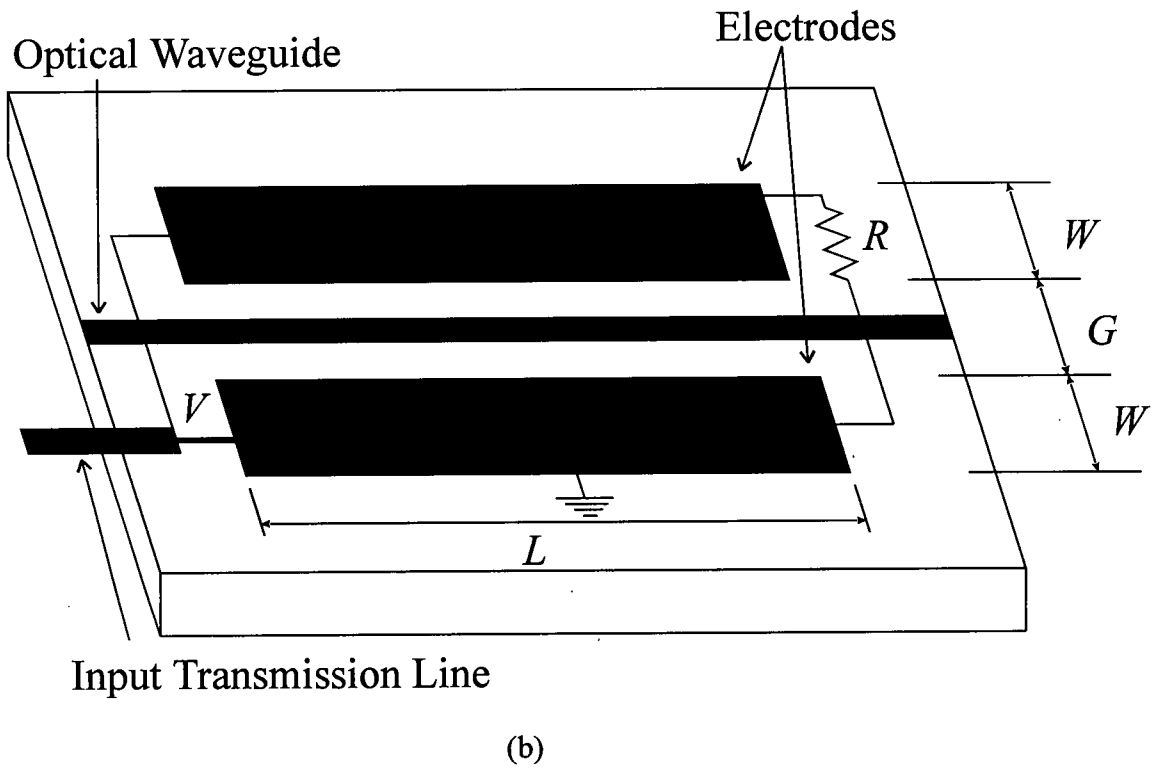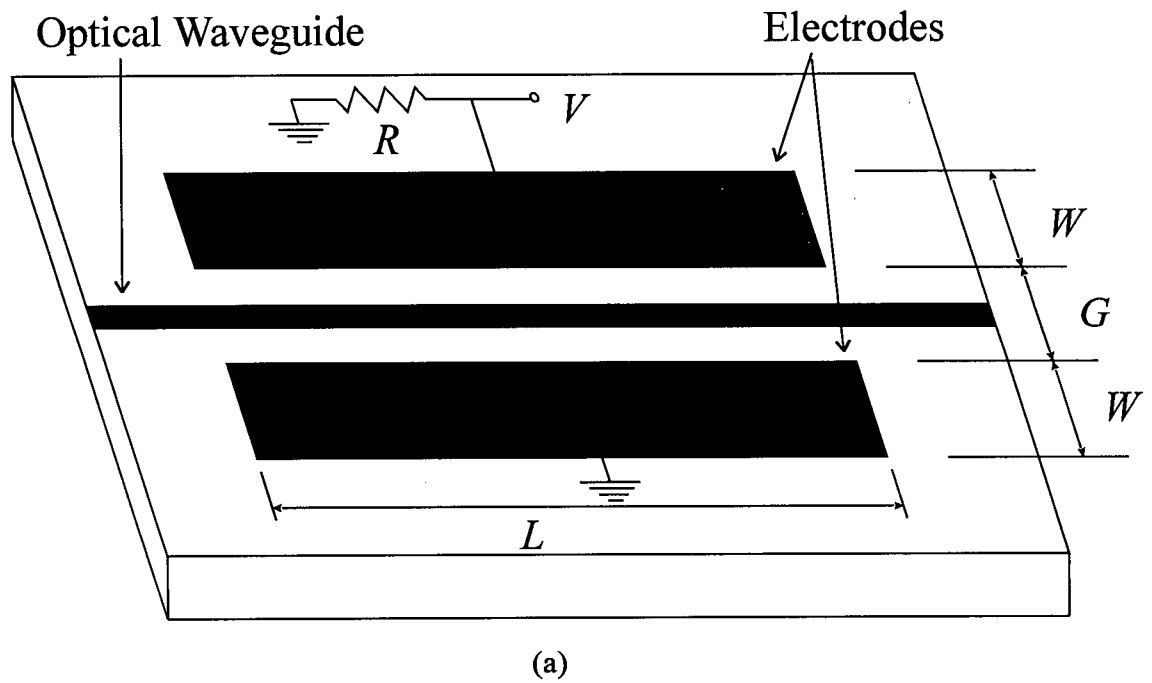
Figure 2.1.1. Lumped, (a), and travelling-wave, (b), coplanar electrodes for guided-wave optical modulators.

2.2. Slow-Wave Electrodes

Typically, for modulators fabricated using compound semiconductors, such as AlGaAs/GaAs and InGaAsP/InP, the modulating microwave, propagating on conventional, surface-deposited, TW electrodes, travels faster than the lightwave does. The effective index, n_{eff}, of an optical mode guided by a typical graded-index $Al_xGa_{1-x}As$ or $In_{1-x}Ga_xAs_yP_{1-y}$, rib waveguide is about 3.2 to 3.4 at $\lambda_o = 1.3$ μm, depending on the values of mole fractions x and y [2, p. 321]. The value of n_{eff} at $\lambda_o = 1.55$ μm is in the same range [2, p. 321]. The microwave index, n_μ, for conventional, thin, surface-deposited, coplanar strips (CPS) or coplanar waveguides (CPW) fabricated on a GaAs or InP substrate can be approximated by [37]

$$n_\mu = \sqrt{\frac{\epsilon_r + 1}{2}} \qquad (2.2.1)$$

where ϵ_r is the dielectric constant of the substrate. The value of n_μ for GaAs is close to that for InP, ~2.6. This difference between n_μ and n_{eff} limits the bandwidth of the modulators that use conventional coplanar electrodes (see [2] p. 161).

2.2.1. Microwave-Lightwave Velocity Matching

Let us study the microwave-lightwave velocity mismatch in more detail. The voltage along the electrode can be written as

$$V(x,t) = V_o e^{-\alpha x} \cos\left(\frac{2\pi n_\mu}{\lambda_\mu} x - 2\pi f t\right) \qquad (2.2.2)$$

8

Where V_o is the amplitude of the applied voltage, f and λ_μ are the microwave frequency and the free-space wavelength, respectively, x denotes the distance along the electrode, t denotes the time, and α is the microwave loss (typically in Np/cm if x is in cm). The voltage "seen" by an optical wave entering the optical waveguide (at the beginning of the electrode) at time t_o can then be written as

$$V = V_o\, e^{-\alpha x} \cos\left(\frac{2\pi f}{c}(n_\mu - n_{eff})x \, - \, 2\pi f t_o \right) . \qquad (2.2.3)$$

Let us ignore the effect of the loss for now, i.e., let $\alpha = 0$, and concentrate on the effect of microwave-lightwave velocity mismatch, i.e., the factor $(n_\mu - n_{eff})$. For a phase modulator, the electro-optically induced phase shift, $\Delta\phi$, for light entering the waveguide at time t_o and travelling the length of the electrode, L, can be written as

$$\Delta\phi = \int_{x=0}^{x=L} K\, V(f,x)\, dx = K\, V_o\, L\, \frac{\sin(\pi f / f_o)}{\pi f / f_o} \cos\left(\pi f / f_o - 2\pi f t_o \right) \qquad (2.2.4)$$

where

$$f_o = \frac{c}{L\,|n_\mu - n_{eff}|}, \qquad (2.2.5)$$

and K depends on the appropriate electro-optic coefficient of the material, r, the free-space optical wavelength, λ_o, the refractive index of the material, n, the gap between the electrodes where the electric field due to the applied voltage is established, G, and the overlap integral, Γ, between the optical field and the applied electric field ($\Gamma = G / V \times \int_{-\infty}^{\infty} \int_{-\infty}^{\infty} E\, E_{op}^2\, dy\, dz$ where

E is the applied electric field and E_{op} is the normalized optical electric field and here the yz plane is the transverse plane, see [2, p. 155]). K can be written as

$$K = \frac{\pi n^3 r \Gamma}{\lambda_o G}.$$

(2.2.6)

Let us define Δf to be the optical 3-dB bandwidth, i.e., Δf is the frequency for which $\Delta\phi$ is reduced to half of its value at low frequency ($f = 0$). Then, from equation (2.2.4), $\Delta f \approx 2f_o/\pi$, or more accurately, $\Delta f \approx 0.603 \times f_o$. For example, for a modulator in GaAs having a 2-cm long, conventional, coplanar electrode, where $n_\mu = 2.6$ and $n_{eff} = 3.4$, $\Delta f \approx 11$ GHz. The closer n_μ is to n_{eff}, the larger f_o, and the larger Δf will be. Therefore, to have a modulator with a wide bandwidth, velocity matching, i.e., $n_\mu \approx n_{eff}$, has to be achieved. Also, when $n_\mu \approx n_{eff}$, the length of the electrode can be large without restricting the bandwidth (see equation (2.2.5) and, again, we are ignoring the effect of microwave loss here); consequently, long devices requiring low drive powers can be obtained.

In this thesis, slow-wave coplanar electrodes are demonstrated that can be designed to have an n_μ such that $n_\mu \approx n_{eff}$ and, therefore, allow for wider bandwidths and smaller drive-powers. The proposed electrodes consist of CPS or CPW electrodes periodically loaded with capacitive elements which consist of fins and pads [23]-[31], [57]-[61]; this is schematically illustrated in Figure 2.2.1. The addition of the capacitive elements to the coplanar electrodes results in an increase in the capacitance per unit length and a decrease in the inductance per unit length of the electrodes. The geometry of the fins and pads can be chosen such that the net ratio of the line capacitance to the line inductance is increased,

resulting in a higher microwave index, n_μ; i.e., one can obtain slow-wave electrodes. More precisely, at high frequencies,

$$n_\mu = c\sqrt{LC} \tag{2.2.7}$$

where c is speed of light in vacuum, and L and C denote line inductance per unit length and line capacitance per unit length of the electrode, respectively. The addition of fins and pads, if they are narrow, increases C significantly whereas the decrease in L is relatively small, hence, the product LC becomes larger for electrodes with fins and pads than it is for conventional electrodes (without fins and pads). The dimensions of the capacitive elements can be chosen to achieve the desired increase in n_μ so that $n_\mu \approx n_{eff}$.

2.2.2. Microwave Loss

Even if the velocity-match condition can be achieved, the frequency-dependent electrical losses may limit the bandwidth of such a modulator [27]. Assuming perfect velocity match, $n_\mu = n_{eff}$, and now concentrating on the effect of microwave loss, equations (2.2.3) and (2.2.4) can be written as

$$V = V_o\, e^{-\alpha x}, \tag{2.2.8}$$

and

$$\Delta\phi = \int_{x=0}^{x=L} K\,V(f,x)\,dx = K V_o \frac{1 - e^{-\alpha L}}{\alpha}. \tag{2.2.9}$$

Microwave loss, α, itself is a function of the frequency and some electrode and substrate

11

material parameters. At high frequencies, where the electrode thickness, τ, is smaller than the skin depth, δ, α can be written as a function of frequency as follows:

$$\alpha(f) = \alpha_o \sqrt{f} + \alpha_{o\epsilon} f \qquad (2.2.10)$$

where α_o depends on the "electrode" dimensions and resistivity (see [62, p. 116]), and $\alpha_{o\epsilon}$ mostly depends on the quality (more specifically, the loss tangent) of the "substrate" material. $\alpha_{o\epsilon}$ may be written as [62, pp. 116-117]

$$\alpha_{o\epsilon} = \frac{\pi\, n_\mu}{c} \left(\frac{1 - 1/n_\mu^2}{1 - 1/\epsilon_r} \right) \tan\delta_\epsilon, \qquad (2.2.11)$$

where, c is the speed of light in vacuum, ϵ_r is the relative permittivity of the substrate ($\epsilon_r = 12.9$ for semi-insulating GaAs (SI-GaAs) [62, p. 25]), and $\tan\delta_\epsilon$ is the loss tangent of the material ($\tan\delta_\epsilon = 0.002$ at 10 GHz for SI-GaAs [62, p. 25]). Typically, in the frequency range of interest ($f < 200$ GHz), for velocity-matched, $n_\mu = 3.4$, coplanar electrodes on high-quality GaAs substrates (i.e., $\tan\delta_\epsilon = 0.002$), the second term on the right-hand-side (RHS) of equation (2.2.10) is significantly smaller ($\alpha_{o\epsilon} \sim 0.0007$ Np/cm/GHz) than the first term on the RHS of equation (2.2.10) ($\alpha_o \geq 0.05$ Np/cm/GHz$^{1/2}$, see [27]); hence, equation (2.2.10) may be fairly accurately approximated by

$$\alpha(f) = \alpha_o \sqrt{f}. \qquad (2.2.12)$$

This is the equation that many researchers often use [2, pp. 162], [20], [63], [64]. Now, assuming $n_\mu = n_{eff}$, the optical 3dB bandwidth of the modulator, Δf, can be estimated as the frequency for which the RHS of equation (2.2.9) becomes equal to ($0.5\, K\, V_o\, L$). Solving for

12

α, one gets

$$\alpha(\Delta f)L = 1.59.\qquad(2.2.13)$$

Using equation (2.2.12), one gets

$$\Delta f = \frac{2.54}{(\alpha_o L)^2}.\qquad(2.2.14)$$

For example, for a 2-cm long, conventional electrode with $\alpha_o \sim 0.15$ Np/cm/GHz$^{1/2}$ (see [15], [54], [65]) $\Delta f \sim 30$ GHz. Even though the electrode loss appears to be less restrictive as compared to the velocity mismatch problem for conventional electrodes, it needs to be addressed in order to achieve ultra-wide-band modulators. Reducing α_o by half will allow for a 2-cm long device to have a bandwidth in excess of 100 GHz if the velocity-match is attained.

The electrode loss is primarily dependent on the size of the electrode; most specifically on the inter-electrode gap and the width of the main electrodes, see [30]. The larger the inter-electrode gap and the wider the main electrodes are, the smaller the loss is. The current along the electrode is concentrated on the inner edges of the main electrodes, and the presence of fins and pads does not significantly alter the current and voltage distribution on the main electrodes. Note that microwave wavelength at frequencies of interest (< 200 GHz) is significantly larger than the dimensions of these fins and pads. Figure 2.2.2 illustrates the distribution of current on slow-wave CPS electrodes. It is calculated using a multilayered EM simulator, Sonnet™ [66], for planar circuits. Current density distribution on the electrode is shown using colours. Red colour indicates the highest current density and dark-blue (violet)

13

indicates the lowest current density. Orange, yellow, green, and light-blue are the intermediate values in the scale from red to dark-blue. As shown in the figure, the current into and out of the fins and pads is extremely small, and, therefore, the presence of the fins and pads is not expected to affect the microwave loss of the electrode significantly.

The effective modulating electric field seen by the light that passes through the optical waveguide is typically given by

$$E = \frac{V \, \Gamma}{G} \qquad (2.2.15)$$

where V is the voltage difference between the ground and the signal electrode, Γ is the overlap integral [2, p. 155], and G is the gap between the electrodes adjacent to the waveguide (also see equation (2.2.4), (2.2.6), and (2.2.9) above). Generally, G has to be small to attain an efficient use of the drive power. In devices that use conventional TW electrodes, without fins and pads, G is the gap between the main electrodes. If G is small, the microwave loss will be large, and if G is large, then E will be small for a given voltage, and a large amount of drive power is needed. Use of slow-wave electrodes having fins and pads can help overcome this problem. If the optical waveguide is located in an appropriate position close to the pads, then G in equation (2.2.15) is the gap between the pads which can be very small without significantly affecting the microwave loss. In fact, the gap between the pads can be quite a bit smaller than the gap between the electrodes, see [27] and [30], resulting in much more efficient modulators. The gap between the main electrodes of the slow-wave structure, on the other hand, can be quite large to result in low-loss electrodes. To summarize, slow-wave electrodes using fins and pads, can provide microwave-to-

lightwave velocity matching and be very low-loss and, at the same time, allow for a very efficient use of drive-power. Equation (2.2.16) shows the collective effect of the microwave-lightwave velocity mismatch and the microwave loss on $\Delta\phi$ [63]

$$\Delta\phi = \frac{\pi n^3 r \Gamma V_o L}{\lambda_o G} \sqrt{\frac{(e^{-\alpha L} - 1)^2 + 4 e^{-\alpha L} \sin^2 u}{(\alpha L)^2 + (2 u)^2}} \sin(\theta - 2\pi f t_o) \qquad (2.2.16)$$

where

$$\theta = \tan^{-1}\left(\frac{e^{-\alpha L} \sin(2u)}{e^{-\alpha L} \cos(2u) - 1}\right) - \tan^{-1}\left(\frac{\alpha L}{2u}\right), \qquad (2.2.17)$$

and

$$u = \frac{\pi f}{f_o} = \frac{\pi f L |n_\mu - n_{eff}|}{c}. \qquad (2.2.18)$$

Note that the smaller α, u, and G are, the larger $\Delta\phi$ will be. Also note that if we set the loss coefficient $\alpha = 0$ in equation (2.2.16), equation (2.2.4) is obtained, and if we set u equal to zero (i.e., if we ignore the velocity mismatch), then equation (2.2.9) is obtained.

15
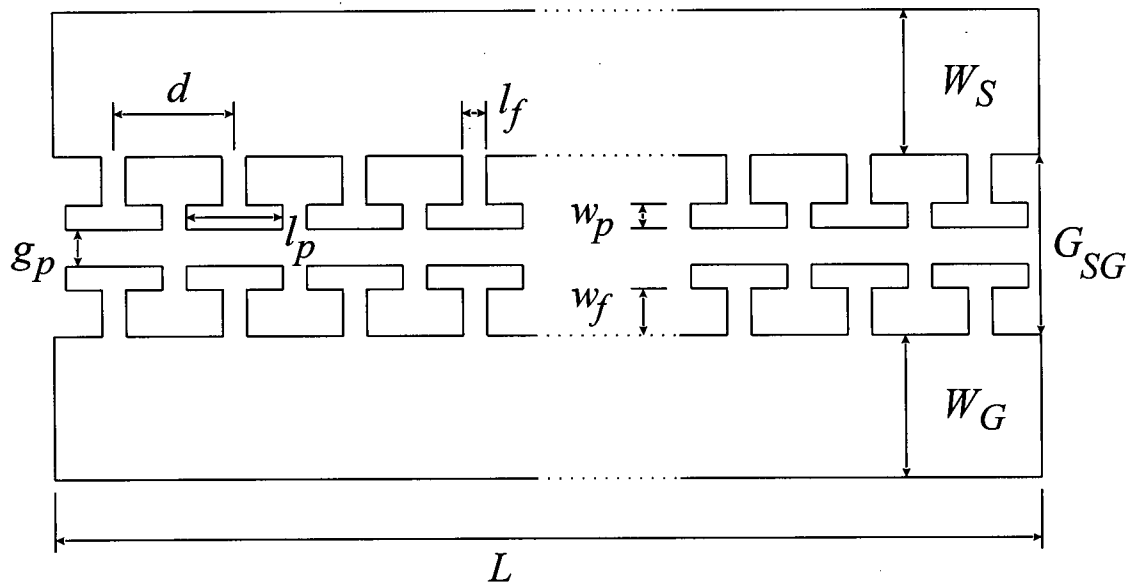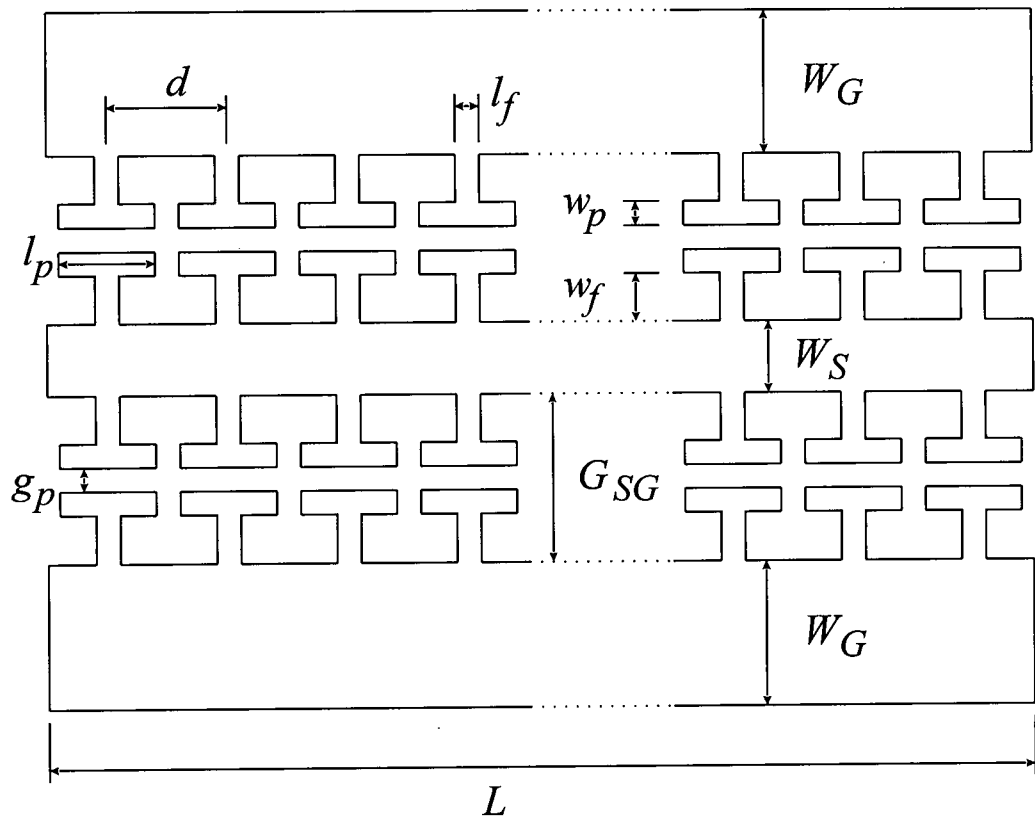
Figure 2.2.1. Slow-wave coplanar strip, (a), and slow-wave coplanar waveguide, (b), travelling-wave electrodes.

16
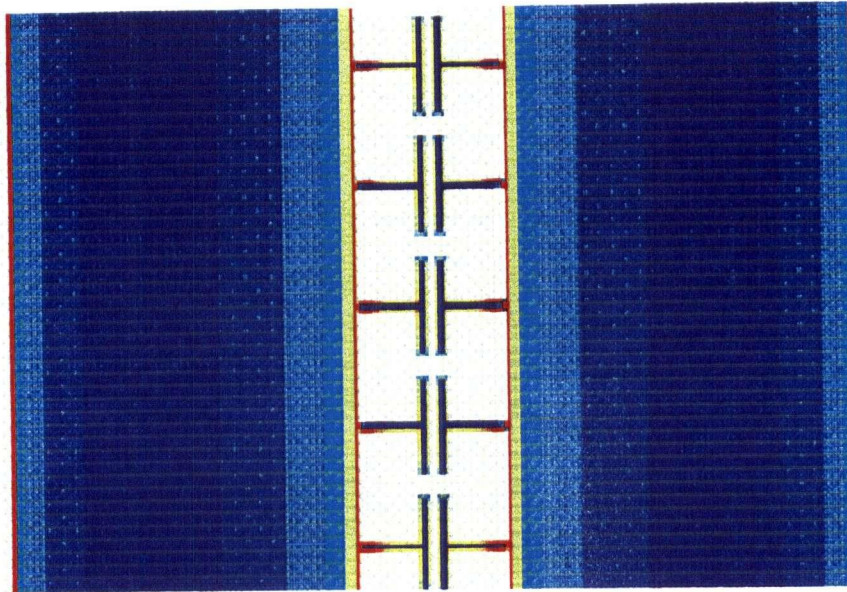
(a)
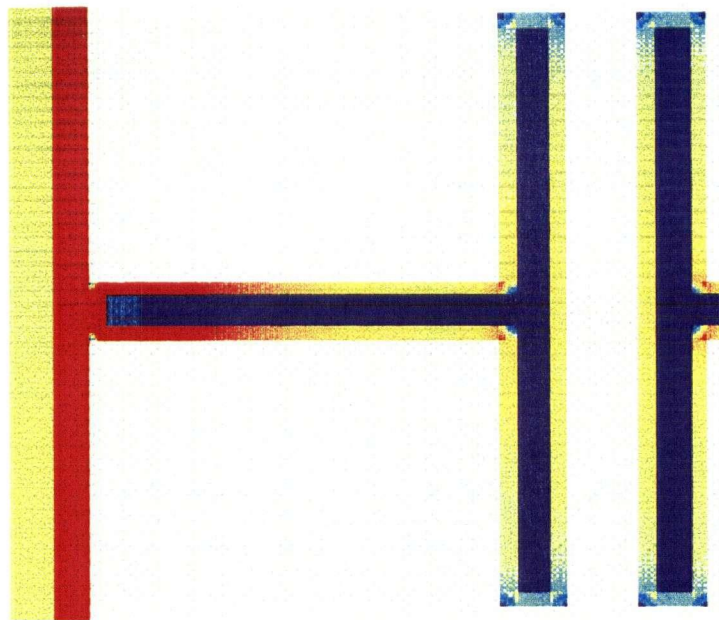
(b)

Figure 2.2.2. a) Current distribution on slow-wave coplanar-strip electrodes. b) A part of (a) expanded for clarity. On a relative scale, red represents the highest and dark blue represents the lowest (close to zero) current density.

2.3. Modulator Configurations

The guided-wave modulators of interest here, the ones that use slow-wave coplanar electrodes on compound semiconductors, can be divided into two major categories: the Mach-Zehnder (MZ) type modulators and the polarization converter (PC) type ones. In this section, a number of different configurations for each of the two types are presented and the advantages and disadvantages of each are explained. Each modulator configuration is given a name to make the reference to the type easier in the rest of this thesis. The differences amongst various configurations in each category come about due to either the type of electrodes used or the positioning of the electrodes relative to the optical waveguides. Generally, the slow-wave CPW electrodes (since they have "two" interelectrode gaps) can give higher microwave slowing (typically more than that required) than slow-wave CPS electrodes, having similar size fins and pads, do. Also, CPW electrodes are more lossy (due to their relatively smaller signal (middle) conductor size). On the other hand, it appears to be easier to couple a microwave signal into the CPW electrodes as compared to CPS ones (see Chapter 4).

2.3.1. Interferometric Mach-Zehnder (MZ) Type Modulators

Here, three types of interferometric Mach-Zehnder (MZ) modulator are given. The first type, MZ-A, which is shown in Figure 2.3.1, consists of slow-wave CPS (or CPW) electrodes with the branches of the MZ optical modulator lying underneath the main electrodes. Since the electric field under the inner edges of the electrode is larger than that underneath the mid-sections of the electrodes, it is preferred to have the optical waveguides

18

under the inner-edges of the electrodes. This configuration is very similar to MZ modulators that use conventional coplanar electrodes (MZ-conventional), except that, in this configuration, fins and pads are added to the electrodes to "slow down" the microwave. The obvious advantages of MZ-A modulators over MZ-conventional ones is that it is not limited by the microwave-lightwave velocity mismatch problem. The general draw-back, similar to MZ-conventional, is that the gap between the electrodes has to be large enough to avoid the coupling of light between the two branches of the MZ and, therefore, the electric field resulting from the voltage applied to the electrodes is not very large (see equation (2.2.15)). This will result in an inefficient use of the drive power (the gap, G_B, typically, has to be larger than ~ 12 µm, see [30] and [67], and G_{SG} has to be ≥ that). This problem can be somewhat overcome if CPW electrodes are used, see Figure 2.3.1.b. In this configuration the gap between the electrodes, G_{SG}, is not limited to G_B. However, G_{SG} is still limited by the space needed for the fins and pads. Moreover, if G_{SG} is very small, electrode loss will be very large and the bandwidth of the modulator will be reduced, see section 2.2.2.

The second type of MZ modulator presented here, type MZ-B-CPW, shown in Figure 2.3.2, has the branches of the optical waveguides underneath the pads. The obvious advantage of this type over MZ-A is that there is no particular restriction on the value of G_{SG} as far as its effect on the efficiency of the modulator is concerned. The value of the gap size to be used in equation (2.2.15) or (2.2.16) is the gap between the pads, g_p, and g_p, typically 4 µm, can be quite a bit smaller than G_{SG}, resulting in an efficient use of the drive power (it may be useful to remember, here, that the microwave wavelength in the frequency range of interest, < 200 GHz, is significantly larger than the sizes of the fins and pads here). G_{SG}, on

19

the other hand, can be quite large, typically ~ 50 μm (see Chapter 3), resulting in a low microwave loss. This will, in turn, allow for an ultra-wide-band modulator, see section 2.2.2. A minor drawback in this configuration is that the pads do not cover the entire length of the optical waveguides in the region between the electrodes, i.e., $(l_p / d) < 1$. However, the advantages mentioned above significantly outweigh this disadvantage.

A third MZ configuration, MZ-C, presented here, shown in Figure 2.3.3. uses interdigitated capacitive elements. The optical waveguides run underneath the inner edges of the electrodes. This structure offers many of the advantages of MZ-B and can be used with both CPS and CPW electrodes. The main difference between MZ-B and MZ-C is that MZ-C can allow for even more extra capacitance per unit length. For our structures and typical dimensions, MZ-C provides either too much slowing of the microwave or (l_p / d) has to be significantly < 1. Also, fabrication of MZ-C electrodes are harder (to insure that pads and adjacent fins do not short). So, generally, type MZ-B has a better performance. MZ-C seems to be useful with CPS electrodes only.

Other configurations using MZ modulators with slow-wave coplanar electrodes are also possible. However, most of them are variations of these three major types provided here. For example, for MZ-B-CPW modulators, the fin size, w_f, for the fins attached to the middle conductor of the CPW and those connected to the ground electrodes can be different. Or the optical waveguides can run between the pads, as opposed to underneath them (in this case, different DC biases for each of the ground electrodes is required to get a well-operating device, see [61]). Nevertheless, in this thesis we will restrict our investigations of the Mach-Zehnder type devices to the three major types described here.

2.3.2. Polarization Converter (PC) Type Modulators

Polarization converters (PC) are another kind of optical guided-wave device that can use slow-wave travelling-wave electrodes. Due to their novel nature, a large portion of this thesis is dedicated to an extensive analysis of their behaviour, which is presented in the following section. These devices can be used as "polarization converters," changing a generally elliptical polarization at the input to some other polarization at the output, "mode converters," a special case of the PC where, for example, TE-polarized light is converted to TM-polarized light, or "modulators," a combination of a PC and an analyzer at the output. PC type modulators presented here all use a single optical channel waveguide. As compared to MZ type which has two branches and Y junctions, the optical power loss is significantly lower for the polarization converters. Also, device fabrication is easier and the over-all modulator length is less because no Y-branches have to be formed. In fact, the over all modulator length does not need to be any longer than the electrode length.

Figure 2.3.4 shows one type of polarization converter, named PC-A-CPS, that has the optical waveguide between the pads of a coplanar CPS electrode. This configuration can also be used with CPW electrodes, named PC-A-CPW, with one or two optical waveguides between the pads. If there are two optical waveguides, either of them can be used for the PC. The optical waveguide can also be underneath the pads, PC-B type, see Figure 2.3.5; however, in that case, the polarization converter is not as efficient because it has only one (as opposed to two) active electro-optic axis for the waveguide, see [15] or section 2.4 for more details.

Figure 2.3.6 shows another type of a PC device, PC-C, that uses interdigitated

21

electrodes. Again, this can use CPS or CPW type electrodes with the optical waveguide(s) in the inter-electrode gaps, underneath the inner edges of the electrodes, or underneath the pads. The advantages and disadvantages of each type of electrode were discussed in the previous section. And, again, it is possible to come up with various other configurations which are not significantly different from the three general types given here. A detailed analysis of these polarization converters is provided in the following sections, and various devices are reported on in the following chapters.
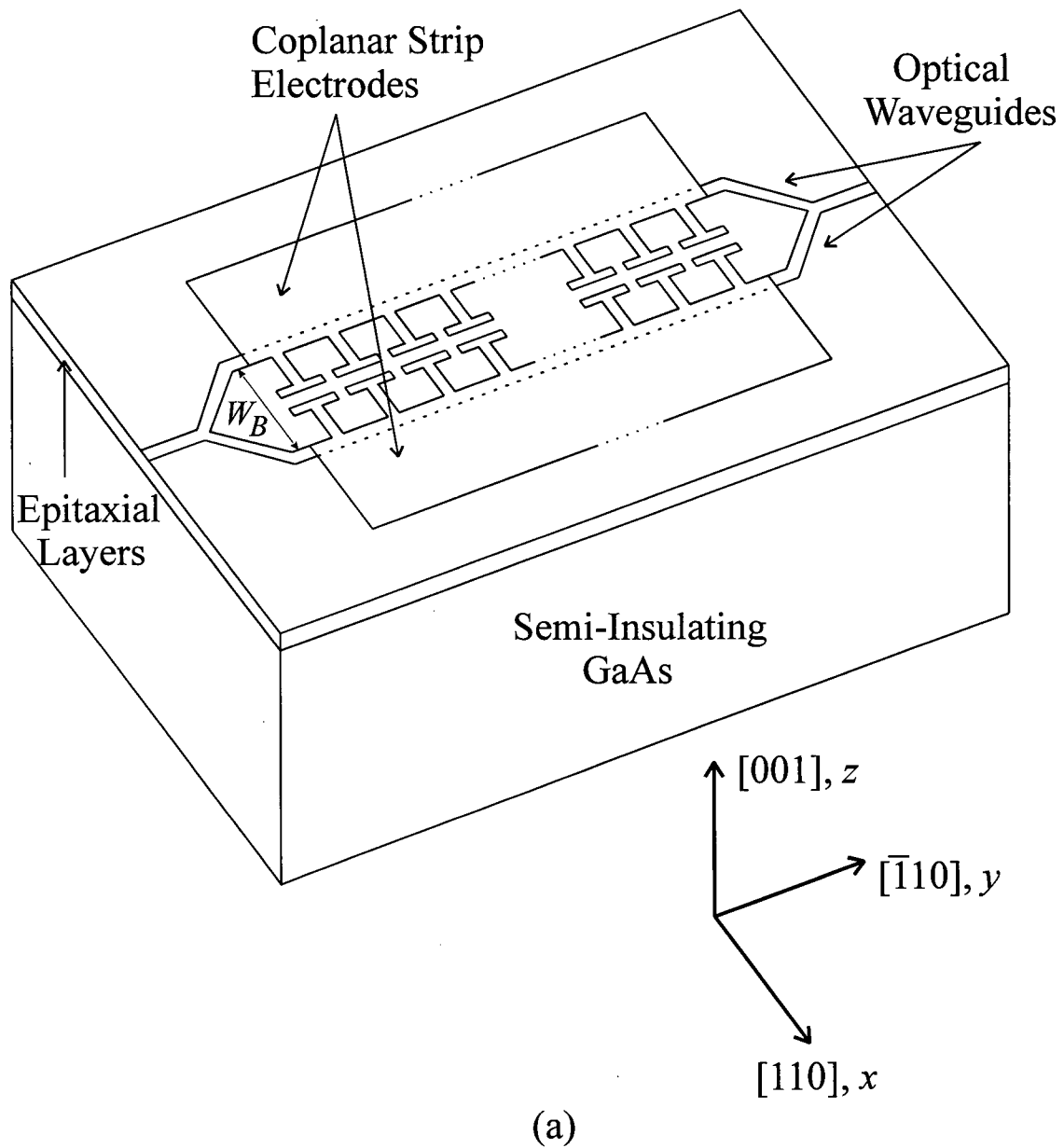
Figure 2.3.1. Schematics of integrated optic Mach-Zehnder modulators of type (a)
MZ-A-CPS and (b) MZ-A-CPW using slow-wave coplanar travelling-wave electrodes.

Coplanar Waveguide Electrodes

Optical Waveguides

Epitaxial Layers

Semi-Insulating GaAs

$[001], z$

$[\bar{1}10], y$

$[110], x$

(b)

Coplanar
Waveguide
Electrodes

Optical
Waveguides

Epitaxial
Layers

Semi-Insulating
GaAs

$[001], z$

$[\bar{1}10], y$

$[110], x$
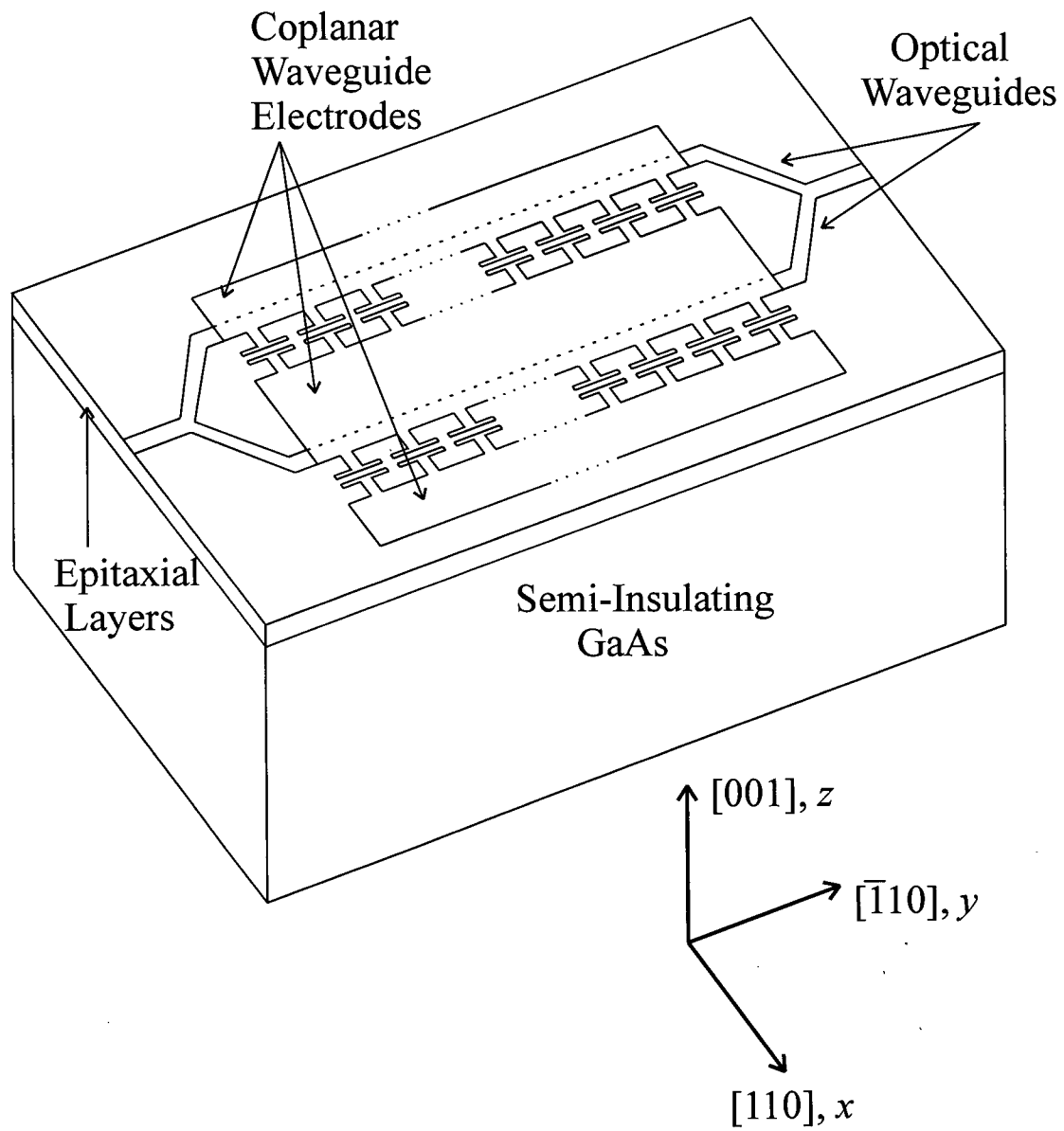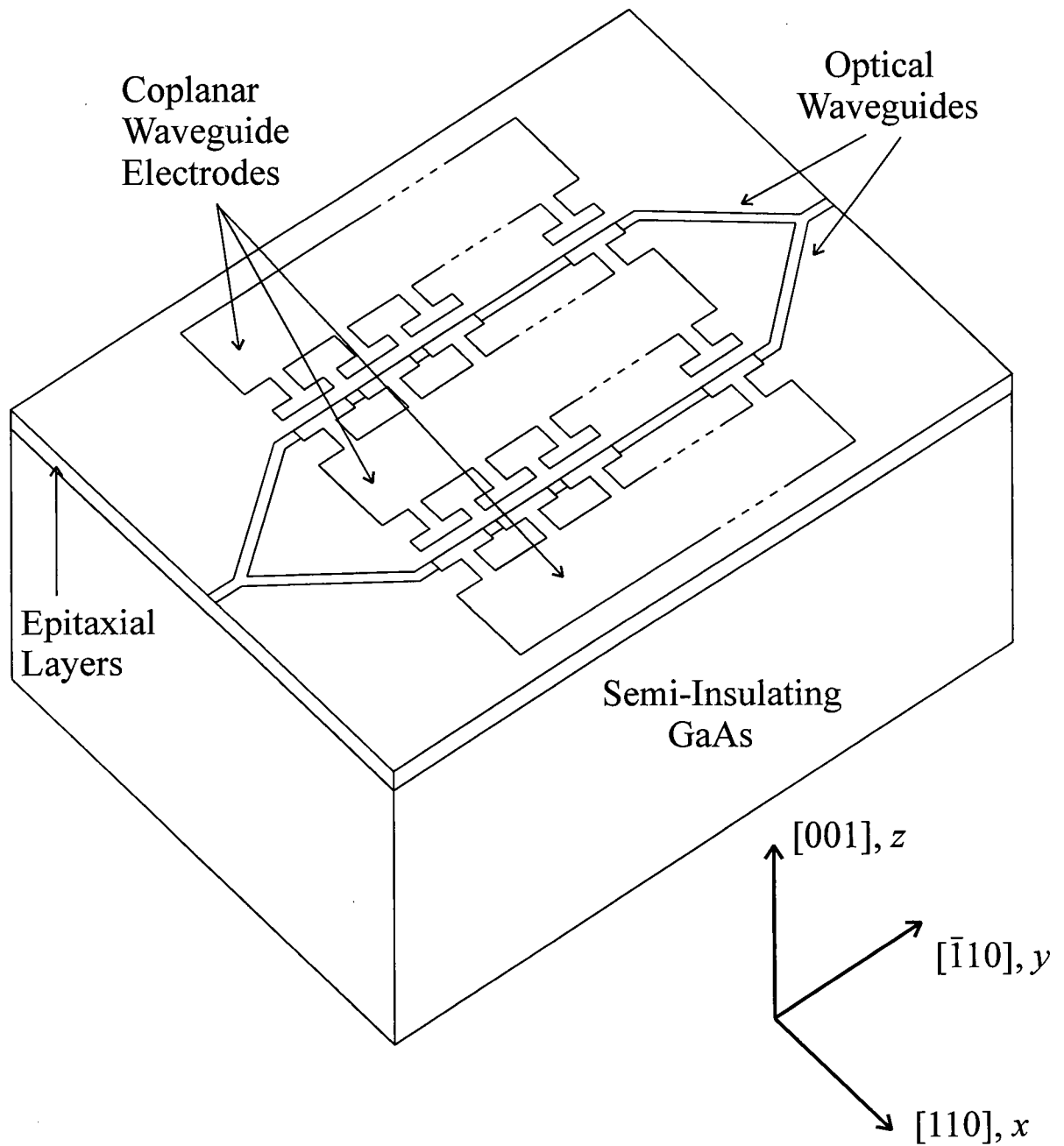
Figure 2.3.2. Schematic of an integrated optic Mach-Zehnder modulator of type
MZ-B-CPW using slow-wave, coplanar waveguide, travelling-wave electrodes.
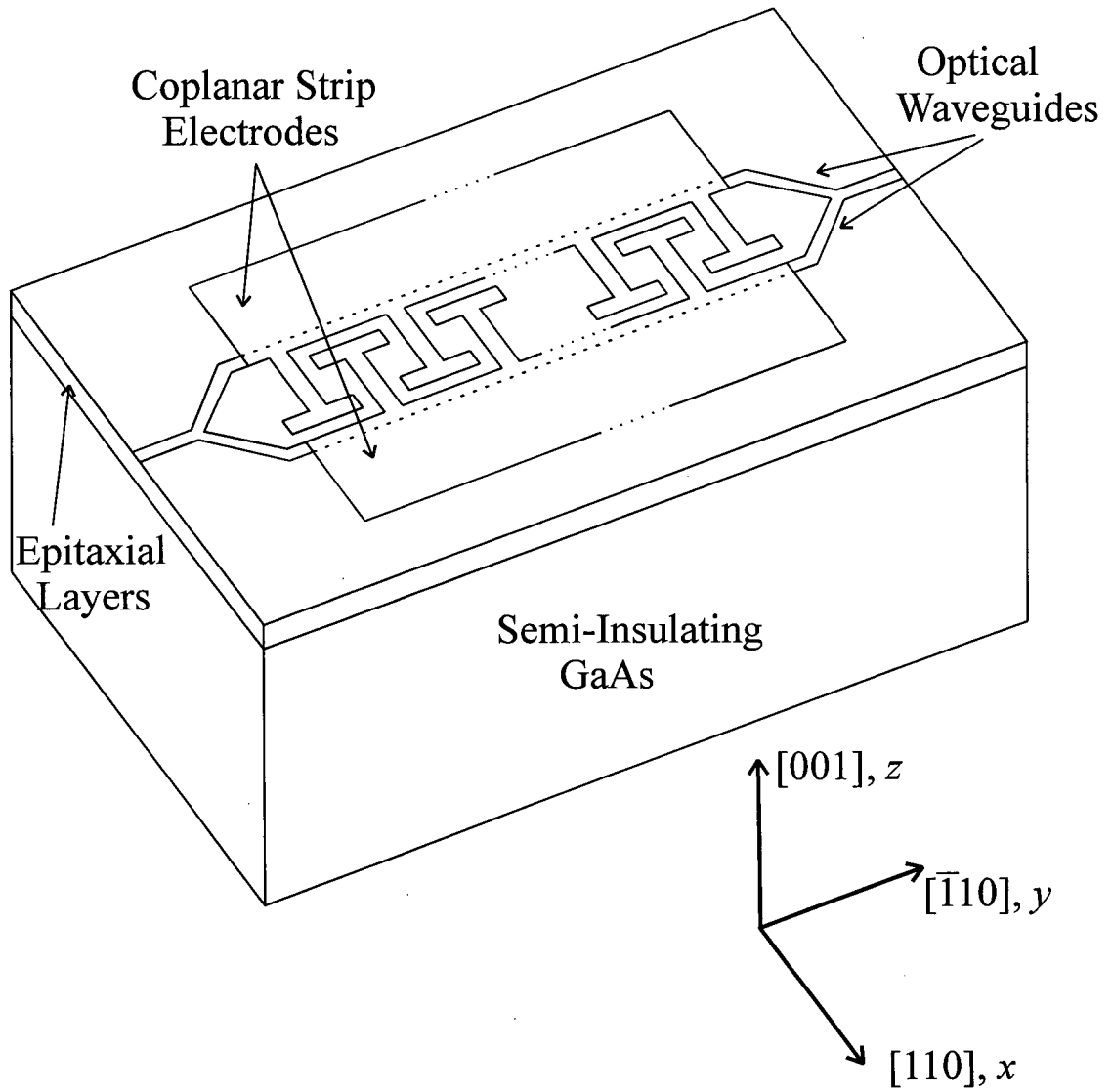
Figure 2.3.3. Schematic of an integrated optic Mach-Zehnder modulator of type MZ-C-CPS using slow-wave, coplanar strip, travelling-wave electrodes.

26
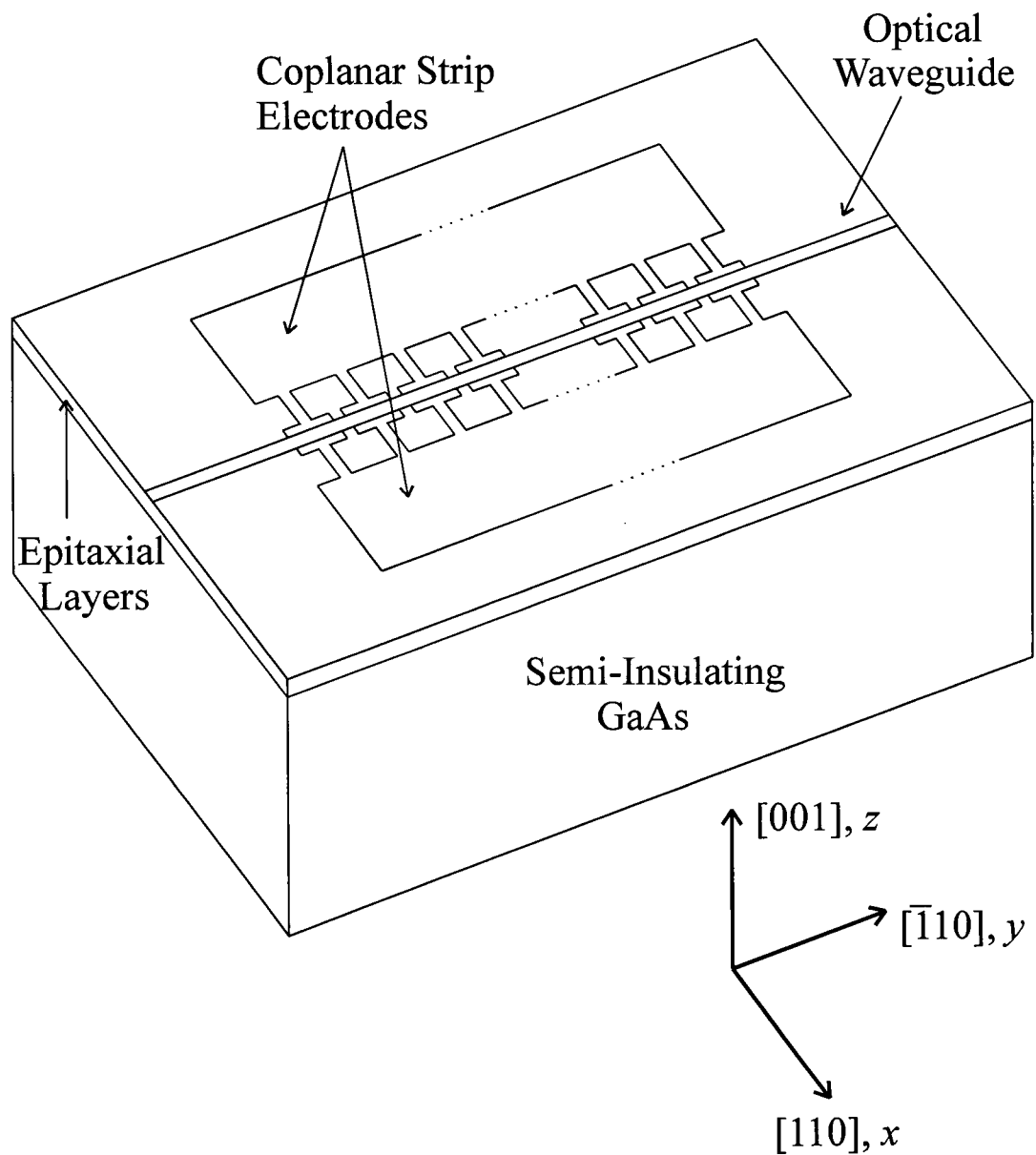
Figure 2.3.4. Schematic of an integrated optic Polarization Converter of type PC-A-CPS using slow-wave, coplanar strip, travelling-wave electrodes.

Coplanar
Waveguide
Electrodes

Optical
Waveguide

Epitaxial
Layers

Semi-Insulating
GaAs

$[001], z$

$[\bar{1}10], y$

$[110], x$
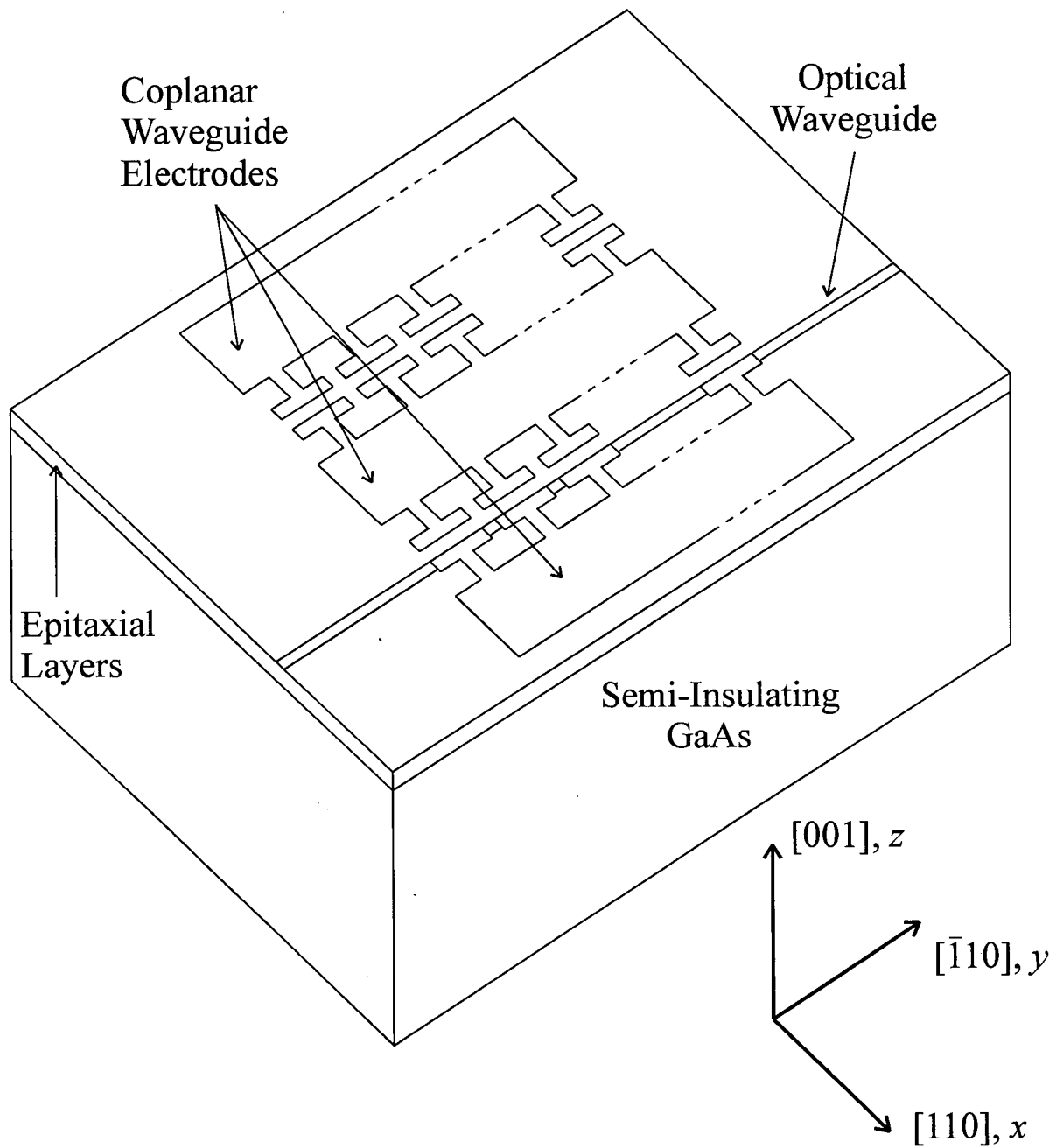
Figure 2.3.5. Schematic of an integrated optic Polarization Converter of type
PC-B-CPW using slow-wave, coplanar waveguide, travelling-wave electrodes.
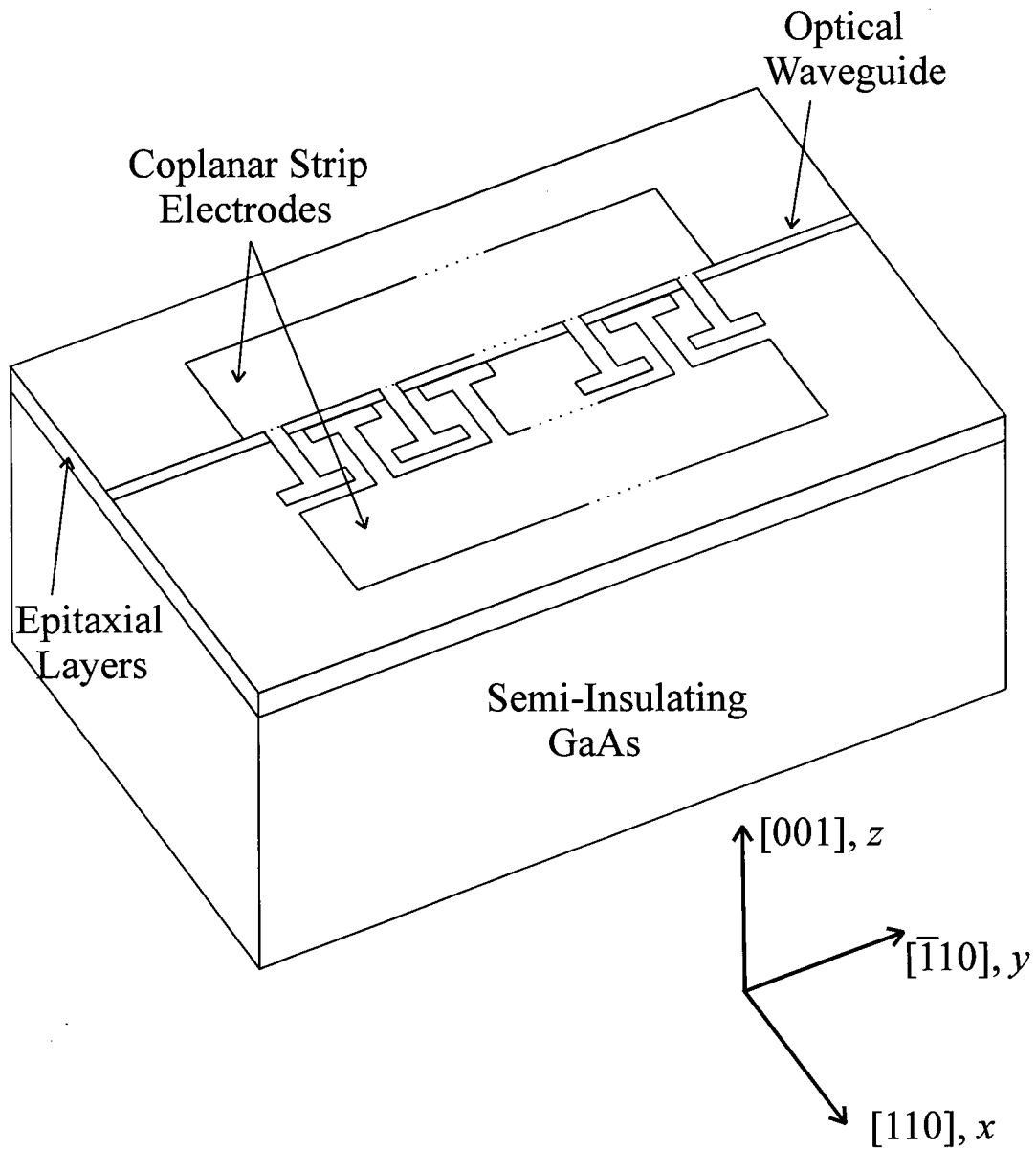
Figure 2.3.6. Schematic of an integrated optic Polarization Converter of type PC-C-CPS using slow-wave, coplanar strip, travelling-wave electrodes.

2.4. Polarization Converters Using Slow-Wave Electrodes

2.4.1. Introduction

In this section electro-optic polarization converters, PC, using slow-wave electrodes are discussed. These devices can be used as polarization/mode converters or modulators. The effects of microwave-lightwave velocity mismatch, microwave loss, and the difference between the propagation constants of the TE-like and the TM-like modes supported by the optical waveguide, are all taken into account in the analysis. The theory presented here specifically addresses the issues relevant to modulators using III-V compound semiconductor, e.g., AlGaAs/GaAs, ridge waveguides together with slow-wave electrodes. Nevertheless, it is easily extendable to many other mode converters, such as the ones that use conventional or fast-wave electrodes and Ti:LiNbO$_3$ waveguides.

2.4.2. Theory

Consider the electro-optic effect in a channel waveguide fabricated in an arbitrary direction on a (001) substrate of AlGaAs/GaAs. For ease of discussion, let us call the [001] direction the z axis, the direction of the waveguide on the substrate the y axis, and the direction perpendicular to y and z axes the x axis, such that x, y, and z make a right-handed orthogonal set of axes. Assume that the direction of the waveguide, y axis, makes an angle ψ with the [010] crystallographic direction. Then the electro-optic coefficient matrix, r, for GaAs (and AlGaAs) with respect to our xyz axes is given by

30

$$r = \begin{bmatrix} 0 & 0 & r_{41}\sin(2\psi) \\ 0 & 0 & -r_{41}\sin(2\psi) \\ 0 & 0 & 0 \\ r_{41}\cos(2\psi) & -r_{41}\sin(2\psi) & 0 \\ r_{41}\sin(2\psi) & r_{41}\cos(2\psi) & 0 \\ 0 & 0 & r_{41}\cos(2\psi) \end{bmatrix}. \qquad (2.4.1)$$

Figures 2.3.4-2.3.6 show possible schematics for the mode converters under consideration. The electrodes are coplanar strips (CPS) or coplanar waveguides (CPW) having capacitively-loading fins and pads in the inter-electrode gap. The optical ridge waveguide, located either between or underneath the pads of the electrodes, is formed along the [$\bar{1}$10] crystallographic direction of the substrate. Optical ridge waveguides in (001) III-V semiconductor substrates are usually made at 45° to [100], or [010], direction because the orientation of the natural cleavage planes is at 45° to these two directions. Using the convention given above for the choice of x, y, and z axes, the [110], [$\bar{1}$10], and [001] directions form the x, y, and z directions, respectively, and $\psi = 45°$.

Application of a voltage to the electrodes results in an electric field, E, having components, E_1, E_2, and E_3, in the x, y, and z directions, respectively, in the substrate. Due to the electro-optic effect in AlGaAs/GaAs waveguide, E, if large enough, can change the polarization of the light at the output of the waveguide.

Here, a simplified model for the analysis of such polarization converters is used; the

input and output sections of the waveguide where no electrode exists, the regions where the optical waveguide is between the pads, and the regions where no pads exist are all treated as separate "wave-plates". By cascading the effects of all these regions along the waveguide, the polarization state of the light at the output of the device can be determined. For each section, wave-plate, the index ellipsoid can be written as

$$B_{11}x^2 + B_{22}y^2 + B_{33}z^2 + 2B_{12}xy + 2B_{13}xz + 2B_{23}yz = 1, \qquad (2.4.2.a)$$

where

$$B_{11} = \frac{1}{n_1^2} + r_{41}E_3 \sin(2\psi), \qquad (2.4.2.b)$$

$$B_{22} = \frac{1}{n_2^2} - r_{41}E_3 \sin(2\psi), \qquad (2.4.2.c)$$

$$B_{33} = \frac{1}{n_3^2}, \qquad (2.4.2.d)$$

$$B_{12} = r_{41}E_3 \cos(2\psi), \qquad (2.4.2.e)$$

$$B_{13} = r_{41}(E_1 \sin(2\psi) + E_2 \cos(2\psi)), \qquad (2.4.2.f)$$

and $$B_{23} = r_{41}(E_1 \cos(2\psi) - E_2 \sin(2\psi)). \qquad (2.4.2.g)$$

Here, n_1, n_2, and n_3, are the refractive indices for the x, y, and z axes, respectively. For light propagating in the y direction, in the waveguide, the cross-section of index ellipsoid is obtained by setting $y = 0$ in equation (2.4.2) above giving

$$B_{11}x^2 + B_{33}z^2 + 2B_{13}xz = 1. \qquad (2.4.3)$$

Now, the major and the minor axes of the ellipse described by equation (2.4.3) are the slow and fast axes of the wave-plate, respectively, and their orientations and magnitudes are functions of the applied electric field E. Let us call the fast and the slow axes u and v. u and v are at an angle θ to x and z, respectively, where θ is given by

$$\tan(2\theta) = \frac{2 B_{13}}{B_{11} - B_{33}} \qquad (2.4.4)$$

if $B_{11} \neq B_{33}$, and $\theta = 45°$ if $B_{11} = B_{33}$. Equation (2.4.3) can be written as

$$\frac{u^2}{n_u^2} + \frac{v^2}{n_v^2} = 1 \qquad (2.4.5)$$

in the uv set of axes, where

$$n_u = \sqrt{B_{11} \cos^2\theta + B_{33} \sin^2\theta + B_{13} \sin(2\theta)}, \qquad (2.4.6.a)$$

and

$$n_v = \sqrt{B_{11} \cos^2\theta + B_{33} \sin^2\theta - B_{13} \sin(2\theta)}. \qquad (2.4.6.b)$$

Now let us take an arbitrary polarization state for the light propagating in the y direction entering the wave-plate:

$$E_{x,z}(y=0) = E_{xo,zo} \cos(\omega t - \delta_{x,z}). \qquad (2.4.7)$$

Here, E_x and E_z represent the magnitudes of the transverse electric-field vectors for the TE-like and the TM-like components of the light, and δ_x and δ_z represent arbitrary phases for the two polarizations. After propagation in the wave-plate for a length l, we have

$$E_{x,z}(y=l) = E_{xl,zl} \cos(\omega t - \gamma_{x,z}) \qquad (2.4.8)$$

where

$$E_{xl,zl} = \sqrt{A_{x,z}^2 + B_{x,z}^2} \,, \qquad (2.4.9)$$

$$\gamma_{x,z} = \tan^{-1}\left(\frac{B_{x,z}}{A_{x,z}}\right), \qquad (2.4.10)$$

$$A_{x,z} = E_{xo,zo} \times \left(\sin^2\theta \cos(\beta_{v,u} l + \delta_{x,z}) + \cos^2\theta \cos(\beta_{u,v} l + \delta_{x,z})\right)$$
$$+ E_{zo,xo} \times \left(\sin\theta \cos\theta \left[\cos(\beta_v l + \delta_{z,x}) - \cos(\beta_u l + \delta_{z,x})\right]\right) \quad , \qquad (2.4.11)$$

$$B_{x,z} = E_{xo,zo} \times \left(\sin^2\theta \sin(\beta_{v,u} l + \delta_{x,z}) + \cos^2\theta \sin(\beta_{u,v} l + \delta_{x,z})\right)$$
$$+ E_{zo,xo} \times \left(\sin\theta \cos\theta \left[\sin(\beta_u l + \delta_{z,x}) - \sin(\beta_v l + \delta_{z,x})\right]\right) \quad , \qquad (2.4.12)$$

and
$$\beta_{v,u} = \frac{2\pi n_{v,u}}{\lambda_o} \,. \qquad (2.4.13)$$

Equation (2.4.8) gives the polarization state of light after travelling through a wave-plate where an arbitrary electric field E is applied. Using equation (2.4.2)-(2.4.13) one can investigate the polarization state of light after it passes through several wave-plates having different lengths, l, and electric fields, E.

The equations above are given for TEM light propagating in the wave-plates. For a weakly guiding ridge, or other kind of channel waveguide, n_1 and n_3 are replaced with n_{TE} and n_{TM}, respectively, where n_{TE} and n_{TM} are the effective refractive indices for light polarized parallel to the x and z axes, respectively, i.e.,

34

$$n_{TE,TM} = \frac{\beta_{TE,TM} \lambda_o}{2\pi} \ . \qquad (2.4.14)$$

β_{TE} and β_{TM} are the propagation constants for the TE-like and the TM-like modes, respectively, and λ_o is the free-space optical wavelength.

To analyze a polarization converter that uses slow-wave electrodes, the PC is divided into several small sections, and each section is treated as a wave-plate. The polarization state at the output of one section is used as the polarization state at the input of the next section. A typical polarization converter of this kind may be divided into several hundreds of wave-plates.

2.4.3. Mode Converters

A mode converter is a particular example of the polarization converter. Here, a PC of type PC-A-CPS (see section 2.3.2) is used as an example to demonstrate the application of the theory in section 2.4.2. The optical waveguide is between the pads, hence, E_2 and E_3 components of the applied electric field can be taken to be zero. $\psi = \pi/4$ and θ can be given by

$$\theta = 0.5 \times \tan^{-1}\left(\frac{2r_{41}E_1}{1/n_{TE}^2 - 1/n_{TM}^2} \right) \ . \qquad (2.4.15)$$

The above equation is valid only when $n_{TE} \neq n_{TM}$, if $n_{TE} = n_{TM}$, then $\theta = \pi/4$. For the sections, wave-plates, where no pads exist, E_1 is relatively small, and is taken to be zero. Therefore, the wave-plate has its fast and slow axes along the x and z axes, i.e., $\theta = 0$. As a

35

result, no coupling of light from the TE-like mode to the TM-like mode, or vice versa, happens in these regions. However, the phase difference between the light components propagating in each mode changes (in the general case where $n_{TE} \neq n_{TM}$).

In the regions where the optical waveguide is passing between the pads, application of a voltage to the electrodes will result in an electric field E_1 which can, if it is large enough, change the orientations of the fast and slow axes of the wave-plate, i.e., $\theta \neq 0$. In this case the polarization state of the light that passes through the wave-plate changes such that some light from the TE-like mode is coupled to the TM-like mode, or vice versa, see equations (2.4.7)-(2.4.13). The total response of the polarization converter can be obtained by cascading the effects of all these wave-plates.

Let us consider a mode converter of type PC-A-CPS having the dimensions given in Table 2.4.1 for its slow-wave CPS electrode. Figure 2.4.1 shows a plot of the optical power converted from the TE-like polarization (parallel to the x axis) into the TM-like polarization (parallel to the z axis) as a function of the applied voltage (low-frequency) for the device of Table 2.4.1; the optical power is normalized with respect to the total optical power out of the waveguide. The data plotted in Figure 2.4.1 are obtained using the equations given in section 2.4.2. In the regions where the waveguide propagates between the pads, the effective electric field E_1 is related to the applied voltage V by $E_1 = V \Gamma / g_p$, see equation (2.2.15). For this plot, $n_{TE} = n_{TM} = 3.3580$ (close to the calculated value for the TE-like mode of our ridge waveguides, see chapter 3), $\Gamma = 1$, and $r_{41} = 1.4 \times 10^{-12}$ m/V for GaAs [68] (and close to that for AlGaAs) at $\lambda_o = 1.3$ μm. Note that for practical devices $\Gamma < 1$, and the applied voltage shown in Figure 2.4.1 should be scaled accordingly, see equation (2.2.15).

36

The transfer function shown in Figure 2.4.1 can be expressed by

$$I_{TM} = \frac{I_{TE}}{2} \left[1 - \cos\left(\pi \, \frac{V}{V_\pi} \right) \right] \qquad (2.4.16)$$

where I_{TM} represents the output optical power (TM-like polarized), I_{TE} represents the input optical power (TE-like polarized), and V_π represents the half-wave voltage given by

$$V_\pi = \frac{\lambda_o \, g_p \, d}{2 \, n^3 \, r_{41} \, L \, \Gamma \, l_p}. \qquad (2.4.17)$$

For the values given here, $V_\pi = 3.92$ V. Equations (2.4.16) and (2.4.17) describe the response of a push-pull interferometric modulator of length $(L \times l_p / d)$, as expected.

For a more typical, realistic, device where the propagation constants for the TE- and TM-like modes are not the same, i.e., $\beta_{TE} \neq \beta_{TM}$, the efficiency of mode conversion depends, amongst many other factors, on the difference between β_{TE} and β_{TM}. Figures 2.4.2-2.4.7 show the response of the same mode converter for $n_{TE} = 3.35805$, 3.35810, 3.35815, 3.35820, 3.35825, and 3.35830, respectively; $n_{TM} = 3.35800$ for all these cases (these values for n_{TE} were chosen because our modelling showed that the difference between effective refractive indices for the TE- and TM-like modes of the optical ridge waveguides of interest is typically < 0.0003, see chapter 3). It can now be appreciated that for $n_{TE} \neq n_{TM}$ the simple equations (2.4.16) and (2.4.17) cannot explain the behaviour of the device, and our elaborate model, given in section 2.4.2 is needed.

For $n_{TE} \neq n_{TM}$, the efficiency, η, of the mode converter, defined as the ratio of the maximum possible optical power out of one mode to the optical power input into the

other mode, is dependent on the applied field (or, equivalently, the applied voltage) and can

be given by

$$\eta = \frac{(r_{41} n^3 E_1 \tau)^2}{(r_{41} n^3 E_1 \tau)^2 + (n_{TE} - n_{TM})^2} , \qquad (2.4.18)$$

where $n \approx n_{TE} \approx n_{TM}$ and the duty cycle $\tau = l_p / d$. η is also plotted in Figures 2.4.2-2.4.7;

note that Figures 2.4.1-2.4.7 all show that the transfer function has an envelope following η.

η is an indication of the limitation of the mode converter due the modal birefringence of its

optical waveguide and the value of the duty cycle. Figures 2.4.2-2.4.7, or equivalently,

equation (2.4.18), imply that to have a highly efficient mode converter the device has to be

biased using a d.c. voltage. Also, the optical waveguide should be designed to have $|n_{TE} - n_{TM}|$

as small as possible to minimize the value of the d.c. bias required.

There are, also, other ways of increasing the efficiency. One way is to apply an

electric field, E_3, in the z, [001], direction. That can be achieved by putting a narrow

electrode on the top of the ridge and applying a d.c. voltage to it. An electric field in the z

direction changes the effective refractive index for the TE-like mode without affecting that

for the TM-like polarization, see equation (2.4.1) and (2.4.2). If E_3 is large enough, and has

the appropriate polarity, it can result in smaller, or even zero, $|n_{TE} - n_{TM}|$. Consequently, the

device can have a high efficiency at low values of the bias voltage applied to the TW

electrodes, see equation (2.4.18).

It should also be noted that the model used in this section includes certain simplifying

assumptions. For example, it assumes sharp transitions between the regions with and the

regions without pads. In reality the electric field changes more smoothly and does not drop to zero in a "zero" distance. Also, here, the relatively small electric field that exists in the regions without the pads is completely ignored. Nevertheless, the model gives a very good qualitative description for the performance of such devices (see chapter 4). Also note that the model given in section 2.4.2 does not have any of these simplifying assumptions in it and can be used for a more extensive and realistic modelling of such devices. However, considering the tolerances and inaccuracies in the fabrication of such devices, a more detailed analysis at this stage is not required.

2.4.4. Analysis of Mode Converters Using Jones Calculus

Jones calculus can also be used in the analysis of polarization converters. This approach has the advantage of being somewhat more intuitive and providing more insight into how such devices work. Again the same concept of wave-plates, as in section 2.4.2, is used, and the device in Table 2.4.1 is chosen for this exercise. The following Jones matrix can be obtained for the kth wave-plate of length l_k using the Mohr circle construction (see, for example, [69, p. 44]):

$$
W = \begin{bmatrix} \cos^2\theta\, e^{\frac{-jk_o l_k}{\sqrt{S_1}}} + \sin^2\theta\, e^{\frac{-jk_o l_k}{\sqrt{S_2}}} & \dfrac{\sin2\theta}{2}\left(e^{\frac{-jk_o l_k}{\sqrt{S_1}}} - e^{\frac{-jk_o l_k}{\sqrt{S_2}}} \right) \\[3em] \dfrac{\sin2\theta}{2}\left(e^{\frac{-jk_o l_k}{\sqrt{S_1}}} - e^{\frac{-jk_o l_k}{\sqrt{S_2}}} \right) & \sin^2\theta\, e^{\frac{-jk_o l_k}{\sqrt{S_1}}} + \cos^2\theta\, e^{\frac{-jk_o l_k}{\sqrt{S_2}}} \end{bmatrix}
\tag{2.4.19}
$$

where θ is given by equation (2.4.15), i.e.,

$$\theta = 0.5 \times \tan^{-1}\left(\frac{2r_{41}E_k}{1/n_{TE}^2 - 1/n_{TM}^2}\right), \qquad (2.4.20)$$

S_1 and S_2 are as follows:

$$S_1 = \frac{1}{2}\left(\frac{1}{n_{TE}^2} + \frac{1}{n_{TM}^2}\right) - \sqrt{\frac{1}{4}\left(\frac{1}{n_{TE}^2} - \frac{1}{n_{TM}^2}\right) + (r_{41}E_k)^2}, \qquad (2.4.21.a)$$

$$S_2 = \frac{1}{2}\left(\frac{1}{n_{TE}^2} + \frac{1}{n_{TM}^2}\right) + \sqrt{\frac{1}{4}\left(\frac{1}{n_{TE}^2} - \frac{1}{n_{TM}^2}\right) + (r_{41}E_k)^2}, \qquad (2.4.21.b)$$

and $k_o = 2\pi/\lambda_o$. E_k is the electric field in the x direction, E_1, in the kth wave-plate. It can be found from the applied voltage using equation (2.2.15).

The Jones matrix for a wave-plate where the applied electric field is small (or zero) reduces to

$$W \approx \begin{bmatrix} e^{\frac{-jk_o l_k}{n_{TE}}} & 0 \\ 0 & e^{\frac{-jk_o l_k}{n_{TM}}} \end{bmatrix}. \qquad (2.4.22)$$

A mode converter having electrodes with the dimensions given in Table 2.4.1 can be divided into several wave-plates as follows: the input section and the output section, where the are no electrodes, having lengths l_{in} and l_{out}, respectively, and the "electroded" section consisting of N "padded" sections, each followed by an "un-padded" section. Again we assume that the electric field in the unpadded section is zero and we refer to these sections

as "unmodulated" sections. The length of a padded section, a "modulated" section, is l_p (see Figure 2.2.1) and the length of an unmodulated section is $l_u = d - l_p$. The transfer matrix for the entire polarization converter becomes

$$T = W_{out} M_N M_{N-1} \cdots M_2 M_1 W_{in} \tag{2.4.23}$$

where W_{in} and W_{out} are given by equation (2.4.22) with $l_k = l_{in}$ and $l_k = l_{out}$, respectively, and M_k is given by

$$M_k \approx \begin{bmatrix} e^{\frac{-jk_o l_u}{n_{TE}}}\left(\cos^2\theta e^{\frac{-jk_o l_p}{\sqrt{S_1}}} + \sin^2\theta e^{\frac{-jk_o l_p}{\sqrt{S_2}}}\right) & \frac{e^{\frac{-jk_o l_u}{n_{TE}}}\sin2\theta}{2}\left(e^{\frac{-jk_o l_p}{\sqrt{S_1}}} - e^{\frac{-jk_o l_p}{\sqrt{S_2}}}\right) \\ \frac{e^{\frac{-jk_o l_u}{n_{TM}}}\sin2\theta}{2}\left(e^{\frac{-jk_o l_p}{\sqrt{S_1}}} - e^{\frac{-jk_o l_p}{\sqrt{S_2}}}\right) & e^{\frac{-jk_o l_u}{n_{TM}}}\left(\sin^2\theta e^{\frac{-jk_o l_p}{\sqrt{S_1}}} + \cos^2\theta e^{\frac{-jk_o l_p}{\sqrt{S_2}}}\right) \end{bmatrix} \tag{2.4.24}$$

Note that, in general, for each section, the value of E_k used to obtain M_k depends on the microwave loss and microwave-lightwave velocity mismatch (see the following section, 2.4.5). For the low-frequency response, we ignore the microwave loss, i.e., $\alpha = 0$, and the microwave-lightwave velocity mismatch, i.e., $|n_{TE} - n_{TM}| = 0$; as a result, equation (2.4.23) reduces to

$$T = W_{out} M^N W_{in} \tag{2.4.25}$$

since all M_k's are the same. For the electrode of Table 2.4.1, $N = 312$. As expected, the transfer function of the modulator obtained using the above equations is identical to those obtained in section 2.4.3, see Figures 2.4.1-2.4.7.

2.4.5. High-Frequency Response

Effects of microwave-lightwave velocity mismatch and microwave loss have to be considered in order to understand the performance of these polarization converters at high frequencies. The model given in sections 2.4.2 and 2.4.4 can still be used for the high-frequency analysis. However, there are some factors to be considered when using the model at high frequencies. For the low-frequency examples given in sections 2.4.3 and 2.4.4, the voltage difference between the ground and signal pads, for all wave-plates that represented the padded regions, was the same. At high frequencies, an optical wave propagating through the optical waveguide "sees" different voltages (more accurately electric fields) in each padded region, because of the microwave loss and the walk-off between the microwave and the optical wave. So the models given in sections 2.4.2 and 2.4.4 are still valid, except that appropriate voltages have to be considered at each wave-plate. Equation (2.2.3) gives the appropriate voltage to be used at each wave-plate that represents a padded region; i.e.,

$$V = V_b + V_o e^{-\alpha y} \cos\left(\frac{2\pi f}{c} (n_\mu - n_{eff}) y - 2\pi f t_o \right) . \qquad (2.4.26)$$

Equation (2.4.26) is essentially the same as equation (2.2.3), with the addition of V_b, a d.c. bias voltage. y denotes the distance of the wave-plate, more precisely, the distance of its centre where the fin is located, from the beginning of the slow-wave electrode. Again, it should be noted that fins and pads should be significantly smaller than the microwave wavelength, so that each fin and pad region can be taken as a virtually equipotential surface. For the frequencies of interest, < 200 GHz, and the pad sizes in our designs, see chapter 3, this condition is well satisfied.

42

2.4.5.1. Large-Signal Response

Let us look at the performance of the device given in section 2.4.3 at high frequencies.

Large-signal performance of the modulator is investigated first. Figures 2.4.8-2.4.10 show

the transfer function of the device at 40 GHz, for $n_{TE} = n_{TM} = 3.35800$. $\alpha = 0$ Np/cm and n_μ

$= 3.300$ for Figure 2.4.8, $\alpha = 0.5$ Np/cm and $n_\mu = 3.358$ for Figure 2.4.9, and $\alpha = 0.5$ Np/cm

and $n_\mu = 3.300$ for Figure 2.4.10. These three situations where chosen so that one can see

the effects of the microwave loss and the velocity-mismatch each individually and collectively.

The numbers chosen for α and n_μ are values that can easily be achieved (see chapter 4). One

can see that when slow-wave electrodes are used, at up to 40 GHz, the most important factor

affecting the bandwidth and the drive-power required is the microwave loss, and not the

microwave-lightwave velocity mismatch. Velocity mismatch starts playing a more significant

role as the frequency increases. Figures 2.4.11-2.4.13 are similar to Figures 2.4.8-2.4.10,

except the frequency is 100 GHz here. Note that the loss is assumed to increase linearly with

the square-root of frequency, see equation (2.2.12). It is clear that as frequency increases,

as expected, the velocity mismatch becomes more important. Nevertheless, with slow-wave

electrodes, very accurate microwave-lightwave velocity matching can be achieved (see

chapter 4). Therefore, the critical issue is the microwave loss.

The devices used for Figures 2.4.14-2.4.16 are similar to those used for Figures 2.4.8-

2.4.10, respectively, with the exception that here $n_{TE} = 3.3583$, and a bias voltage of $V_b = 16$

V, see Figure 2.4.7, is applied. It is again clear that the difference between n_{TE} and n_{TM}

significantly degrades the performance of the device. Also the effects of the microwave loss

and the microwave-lightwave velocity mismatch are more apparent.

2.4.5.2. Small-Signal Response

Figure 2.4.17 shows the estimated small-signal performance of the device analyzed in section 2.4.3 at 40 GHz, having $n_{TE} = n_{TM}$; the electrode dimensions are given in Table 2.4.1. The figure shows plots of the change of output power (normalized with respect to the total possible output power of the waveguide) for the TM-like mode as a function of the applied small-signal voltage to the electrodes for several different devices. Again, the input light is polarized parallel to the x axis (TE-like mode). The device used for plot (a), the ideal case, is the same as the one used for Figure 2.4.1. There is a bias voltage of $V_b = 2V$ applied to it, and $n_\mu = n_{TE} = n_{TM} = 3.35800$. All relevant specifications for plots (a) to (h) of Figure 2.4.17 are given in Table 2.4.2. Plot (a) represents a device with no microwave loss, perfect microwave-to-optical-wave velocity match, and no modal birefringence ($n_{TE} = n_{TM}$). The modulators used for plots (b), (c), and (d), are all similar to the one used for plot (a) with differences in microwave loss and/or velocity matching, see Table 2.4.2. Plot (d) shows a realistic case, provided that a waveguide where $n_{TE} = n_{TM}$ is used. For (d) a microwave loss of 0.5 Np/cm is used. The typical values measured for our fabricated electrodes on our AlGaAs/GaAs substrate was less than 0.5 Np/cm. Also an $n_\mu = 3.300$ is used for case (d). This value is about 2% lower than the target value of 3.358. This amount of accuracy can easily be attained by the fabrication process for the electrodes, see chapter 4.

Plots (e) to (h) represent modulators having the same optical waveguide as the one used for (a) to (d) together with conventional (as opposed to slow-wave) coplanar electrodes.

44

To make the comparison easier, the gap between the coplanar strips for cases (e) to (h) is chosen equal to g_p for cases (a) to (d), i.e., equal to 4 μm. The values of microwave loss used for (f) and (h), 1.0 Np/cm, is an optimistic lower bound for the actual value of the loss for these conventional coplanar electrodes; it is based on the values available in the literature for electrodes of similar dimensions fabricated on similar substrates [15], [54], [65]. Plots (g) and (h) represent a device having the optimum length, i.e, giving the best performance, at 40 GHz considering the effect of microwave-lightwave velocity mismatch (see equations (2.2.3) and (2.2.4)).

A comparison of plots (a) and (b) with plots (c) and (d), respectively, shows that we have practically overcome the problem of microwave-lightwave velocity mismatch. In other words, our accuracy in fabricating slow-wave electrodes (~2% deviation at this point in time) is sufficient to achieve ultra-wide bandwidth, efficient modulators. Also, a comparison of any of the devices (a) to (d) with the devices (e) to (h) shows that velocity matching significantly improves efficiency and bandwidth. For example, the power needed for the same amount of modulation at 40 GHz for case (h) is more than an order of magnitude larger than that needed for case (d) (see Table 2.4.2).

Figure 2.4.18 shows a plot similar to Figure 2.4.17 with the difference being that n_{TE} = 3.35830 (and n_{TM} = 3.35800). This amount of difference between the effective index of the two modes (0.0003) is used to demonstrate an extreme case here. All values calculated for the difference between the effective indices of the two modes for various waveguide structures of interest to us were (for some, significantly) smaller than 0.0003. For low-frequency behaviour of devices (a) to (d) in Figure 2.4.18 refer to Figure 2.4.7. Appropriate

45

specifications for devices of Figure 2.4.18 are given in Table 2.4.3. In general, trends similar to those in Figure 2.4.17 can be observed here. There are, however, two important differences. First, large values of d.c. bias are required for these devices to work efficiently. Using these biases may not be practical and/or convenient for actual devices. Second, the amount of microwave power needed for a constant amount of optical signal modulation in case (a) of Figure 2.4.17 (where $n_{TE} = n_{TM}$) is only 20% of that needed for case (a) of Figure 2.4.18. So it is important to try to get n_{TE} and n_{TM} as close as possible in order to get the best possible efficiency.

2.4.6. Other Polarization Converters

The polarization converters discussed in the previous sections were all TE-to-TM (or TM-to-TE) mode converters. Depending on the polarization of the input light, these devices can show different transfer functions which may be more favourable, or more efficient, for certain applications, specially if $n_{TE} \neq n_{TM}$. For example consider the PC-A-CPS type device used in the previous section; the dimensions for its electrodes are given in Table 2.4.1. Let us assume that $n_{TE} - n_{TM} = 0.0001$. Consider a case where the input light is polarized at 45° to the x axis, the input and the output sections are 1 mm long ($l_{in} = l_{out} = 1$ mm), and the analyzer is oriented with its polarization axis parallel to the z axis, so that the power from the TM-like mode is detected. Figure 2.4.19 shows the transfer function for this device. Figure 2.4.20 shows the transfer function of a similar device with the difference that the input light is polarized at 20° to the x axis. This figure, Figure 2.4.20, shows an intermediate stage between the case for Figure 2.4.3 (the input light being polarized at 0° to the x axis) and the

case for Figure 2.4.19. As can be seen from the above figures, the configuration with the input light polarized at 45° to the x axis is more favourable for small-signal near-linear modulation of light when there is no bias voltage available. On the other hand, the configuration with the input light polarized at 0° to the x axis is more favourable for digital modulation with a very high extinction (on-off) ratios.

Another useful device is a polarization converter of the type PC-B as shown in Figure 2.3.5. The difference between a PC-A type device and a PC-B type one is that for the former the optical waveguide is located between the pads (i.e., E_1 is the significant component of the electric field in the waveguide) whereas for the latter the optical waveguide is located underneath the pads (i.e., E_3 is the significant component of the electric field in the waveguide). Figure 2.4.21 shows the transfer function of a PC-B-CPS type device having the same electrode dimensions as those given in Table 2.4.1. The input and the output sections are again 1 mm long each, the input light is polarized at 45° to the x axis, and the analyzer is oriented with its polarization axis at -45° to the x axis. The transfer function shown in Figure 2.4.21 can also be given by

$$I_{out} = \frac{I_{in}}{2}\left[1 - \cos\left(\pi\,\frac{V}{V_\pi} + \phi_i\right)\right]$$

(2.4.27)

where I_{out} represents the output optical power, I_{in} represents the input optical power, V_π represents the half-wave voltage given by

$$V_\pi = \frac{\lambda_o\, g_p\, d}{n^3\, r_{41}\, L\, \Gamma\, l_p},$$

(2.4.28)

47

and ϕ_i is the intrinsic bias of the device which is a function of the length of the optical waveguide, L_{op}, and its modal birefringence and can is given by

$$\phi_i = \frac{2 \pi L_{op} (n_{TE} - n_{TM})}{\lambda_o}.$$

(2.4.29)

For the example here, $\lambda_o = 1.3$ μm, $n_{TE} - n_{TM} = 0.0001$, and $L_{op} = 17$ mm. Using the dimensions given in Table 2.4.1, $n_{TE} = 3.3580$, $\Gamma = 1$, and $r_{41} = 1.4 \times 10^{-12}$ m/V, $V_\pi = 7.84$ V and $\phi_i = 2.6\pi$ is obtained. Note the value of V_π obtained for this case is exactly twice that for the mode converter of Figure 2.4.1, where no modal birefringence is present (compare equations (2.4.17) and (2.4.28)). The reason for this is that the mode converter configuration whose response is given in Figure 2.4.1 has two active electro-optic axes (at $\pm 45°$ to the x axis) whereas the one used here has only one active electro-optic axis (the x axis). E_3 only affects the refractive index of the TE-like mode of the waveguide and does not affect the TM-like mode (see, equations (2.4.1)-(2.4.2)). This is a direct result of the material symmetry of GaAs. The result is that this device, as a modulator, is half as efficient as the mode-converter of Figure 2.4.1. However, for the cases where modal birefringence exists (most of the practical cases), the configuration presented here, except for its intrinsic phase, is insensitive to the value of $|n_{TE} - n_{TM}|$ and can outperform the mode converters given in section 2.4.3 (see Figure 2.4.2-2.4.7). A very strong advantage of this particular configuration is that for a certain value of the modal birefringence of the waveguide, $|n_{TE} - n_{TM}|$, the length of the waveguide can be chosen, using equation (2.4.29), to bias the modulator in the desired region of the transfer function.

To summarize, many other configurations or modes of operation are possible for these polarization converters and they all can be analyzed using the model developed in section 2.4.2. The choice of the optimum configuration depends on the particular application for which the modulator is to be used.

As a final note, it should be pointed out that the variations and the imperfection in the fabrication process will inevitably result in devices that have slightly different transfer functions as compared to those predicted here. For example, if the optical ridge waveguide is not perfectly centred between the pads, the net amount of the electric field component E_3 in the waveguide will not be zero when a voltage is applied to the electrodes. For example consider the device whose transfer function is given in Figure 2.4.3. Figure 2.4.22 shows the transfer function of the same device for $E_3 = 0.1 \times E_1$. As can be seen from the figure, the transfer function is slightly altered due to the presence of the (albeit small) vertical electric field, E_3. Effects of this kind can actually be exploited to obtain devices needing lower bias voltages or having a more linear response over certain portions of the transfer function.

Table 2.4.1. The dimensions for a slow-wave CPS electrode used in a mode converter formed on an AlGaAs/GaAs substrate. The optical ridge waveguide is 3 μm wide. The input optical waveguide and the output optical waveguide are each 2 mm long.

L (mm)	W_S (μm)	W_G (μm)	G_{SG} (μm)	g_p (μm)	w_f (μm)	w_p (μm)	l_f (μm)	l_p (μm)	d (μm)
15	120	120	60	4	26	2	4	40	48

Table 2.4.2. Specifications of the devices represented in Figure 2.4.17 where $n_{TE} = n_{TM} = 3.35800$. α represents the microwave signal loss at 40 GHz; L is the electrode length; the duty cycle $\tau = l_p/d$ for the slow-wave electrodes; $\tau = 1$ for conventional electrodes; Δf is the 3-dB optical bandwidth, η_{ss} (or small-signal efficiency) is the ratio of the small-signal optical power modulation of each case to that of an ideal device, i.e., case (a), given in percentage; and *Power Ratio* is the ratio of the microwave power needed for a constant (and very small) optical signal modulation in each case to that needed for the ideal case (a). η_{ss} and *Power Ratio* are both calculated at 40 GHz. Frequency = 40 GHz where not otherwise indicated.

Plot	Electrode Type	V_b (V)	α (Np/cm)	n_μ	L (mm)	τ	Δf (GHz)	η_{ss} %	Power Ratio
(a)	slow-wave	2	0	3.358	15	0.833	∞	100	1
(b)	slow-wave	2	0.5	3.358	15	0.833	180	71.1	2.02
(c)	slow-wave	2	0	3.300	15	0.833	202	97.9	1.05
(d)	slow-wave	2	0.5	3.300	15	0.833	105	69.6	2.11
(e)	conventional	1.64	0	2.6	15	1	16	25.7	15.7
(f)	conventional	1.64	1	2.6	15	1	11	15.6	42.9
(g)	conventional	5	0	2.6	4.9	1	48	25.8	15.7
(h)	conventional	5	1	2.6	4.9	1	40	20.5	24.8

Table 2.4.3. Specifications of the devices represented in Figure 2.4.18 where $n_{TE} = 3.35830$, and $n_{TM} = 3.35800$. See the caption of Table 2.4.2 for the explanation of the other terms in the table. Note that the *Power Ratio* of the case (a) of Table 2.4.2 to the case (a) of Table 2.4.3 is 5.03 at 40 GHz, i.e., these devices are significantly less efficient than those given in Table 2.4.2.

Plot	Electrode Type	V_b (V)	α (Np/cm)	n_μ	L (mm)	τ	Δf (GHz)	η_{ss} %	Power Ratio
(a)	slow-wave	31	0	3.358	15	0.833	∞	100	1
(b)	slow-wave	31	0.5	3.358	15	0.833	180	70.6	2.01
(c)	slow-wave	31	0	3.300	15	0.833	202	97.5	1.05
(d)	slow-wave	31	0.5	3.300	15	0.833	105	68.9	2.11
(e)	conventional	26	0	2.6	15	1	16	22.3	20.1
(f)	conventional	26	1	2.6	15	1	11	14	50.5
(g)	conventional	38	0	2.6	4.9	1	48	34.9	8.15
(h)	conventional	38	1	2.6	4.9	1	40	27.9	12.8
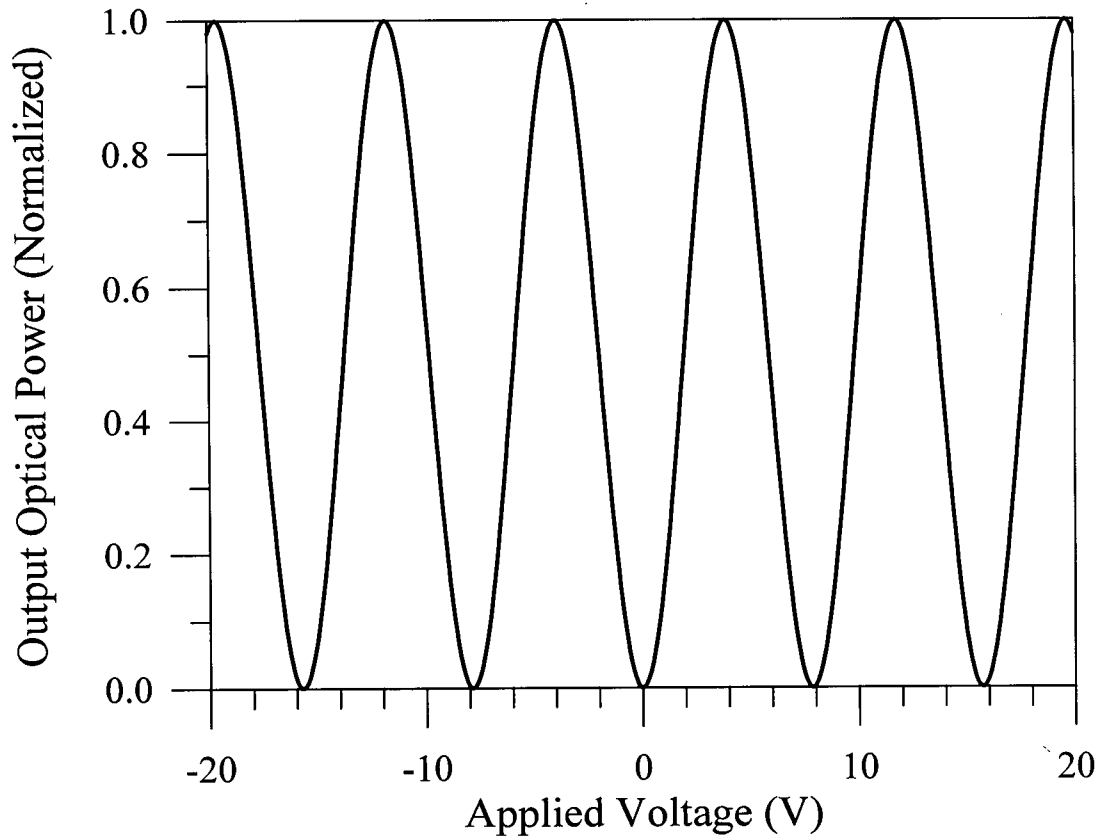
Figure 2.4.1. Normalized optical power converted from the TE-like polarization (parallel to the x axis) into the TM-like polarization (parallel to the z axis) as a function of the applied voltage for the device of Table 2.4.1. $n_{TE} = n_{TM} = 3.35800$.
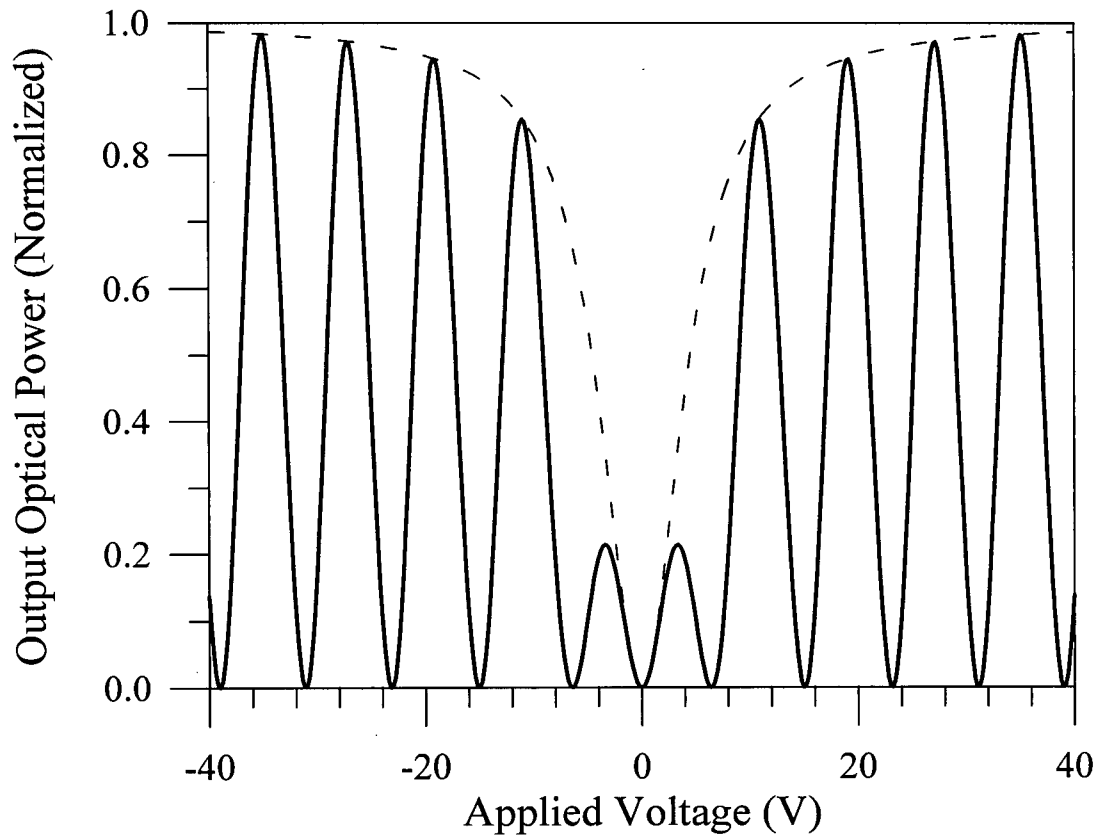
Figure 2.4.2. Normalized optical power converted from the TE-like polarization (parallel to the x axis) into the TM-like polarization (parallel to the z axis) as a function of the applied voltage for the device of Table 2.4.1. $n_{TE} - n_{TM} = 0.00005$. η is shown by the dashed line.
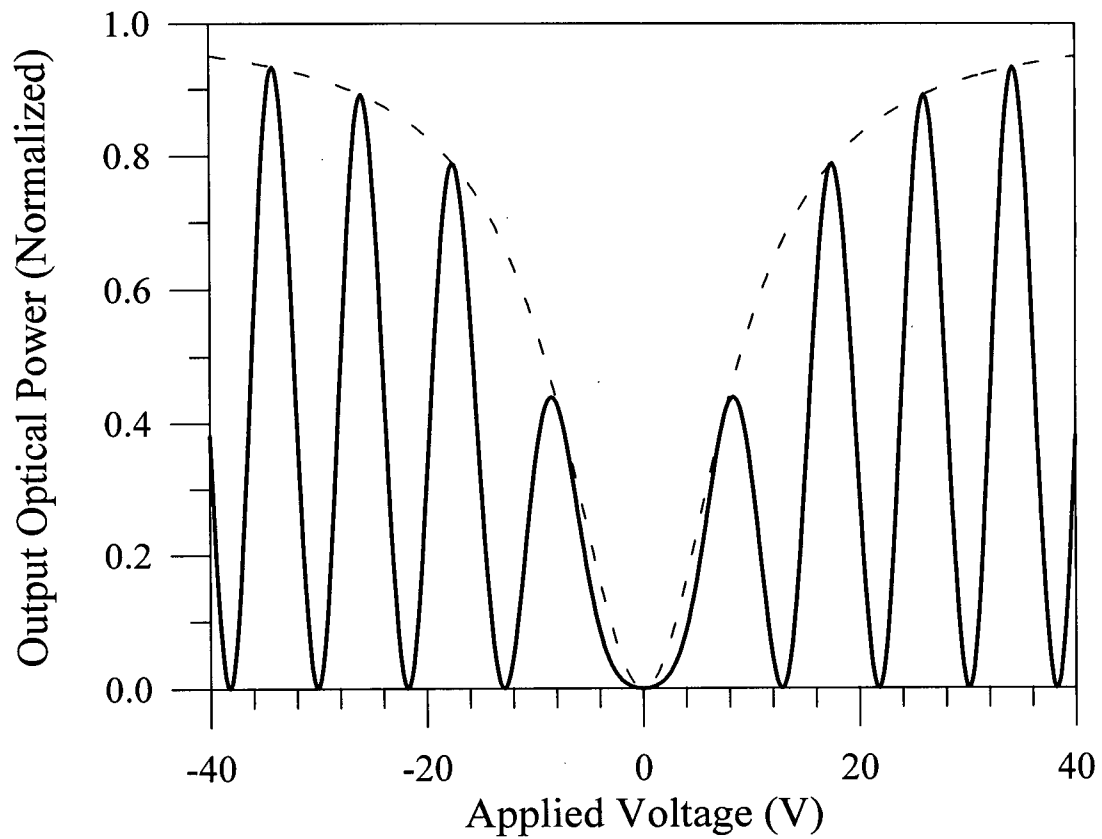
Figure 2.4.3. Normalized optical power converted from the TE-like polarization (parallel to the x axis) into the TM-like polarization (parallel to the z axis) as a function of the applied voltage for the device of Table 2.4.1. $n_{TE} - n_{TM} = 0.00010$. η is shown by the dashed line.
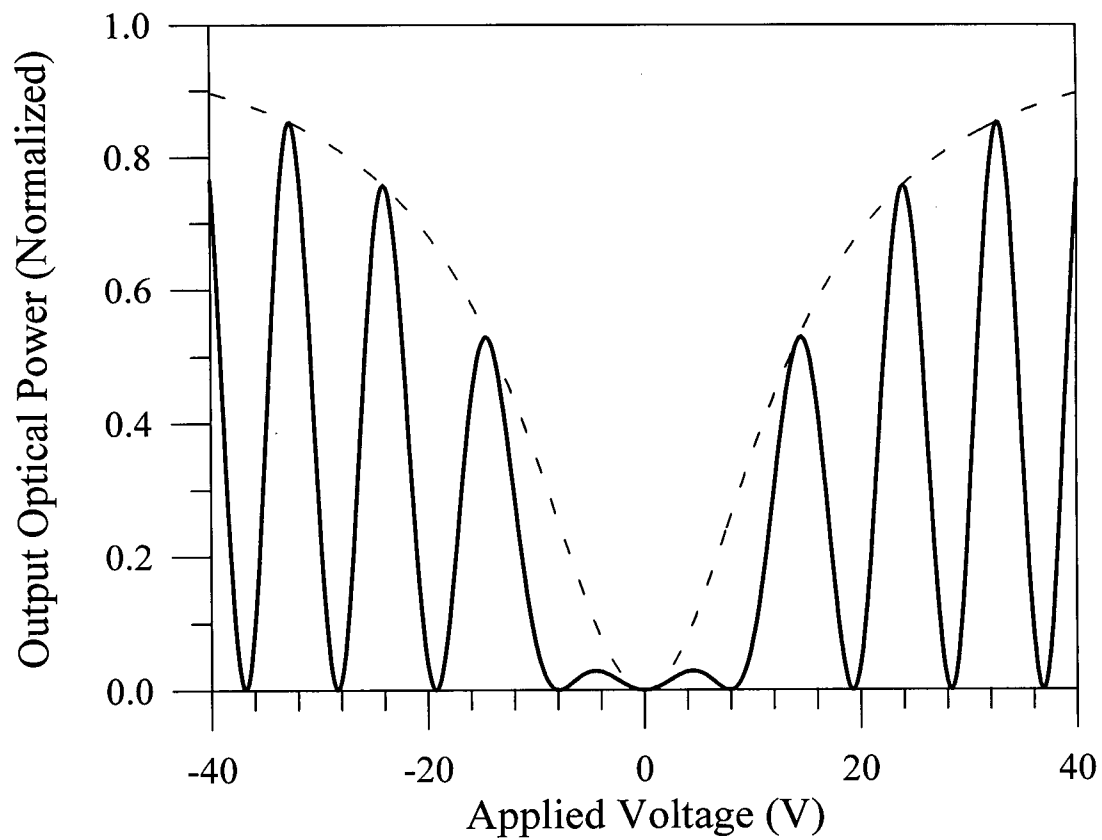
Figure 2.4.4. Normalized optical power converted from the TE-like polarization (parallel to the x axis) into the TM-like polarization (parallel to the z axis) as a function of the applied voltage for the device of Table 2.4.1. $n_{TE} - n_{TM} = 0.00015$. η is shown by the dashed line.
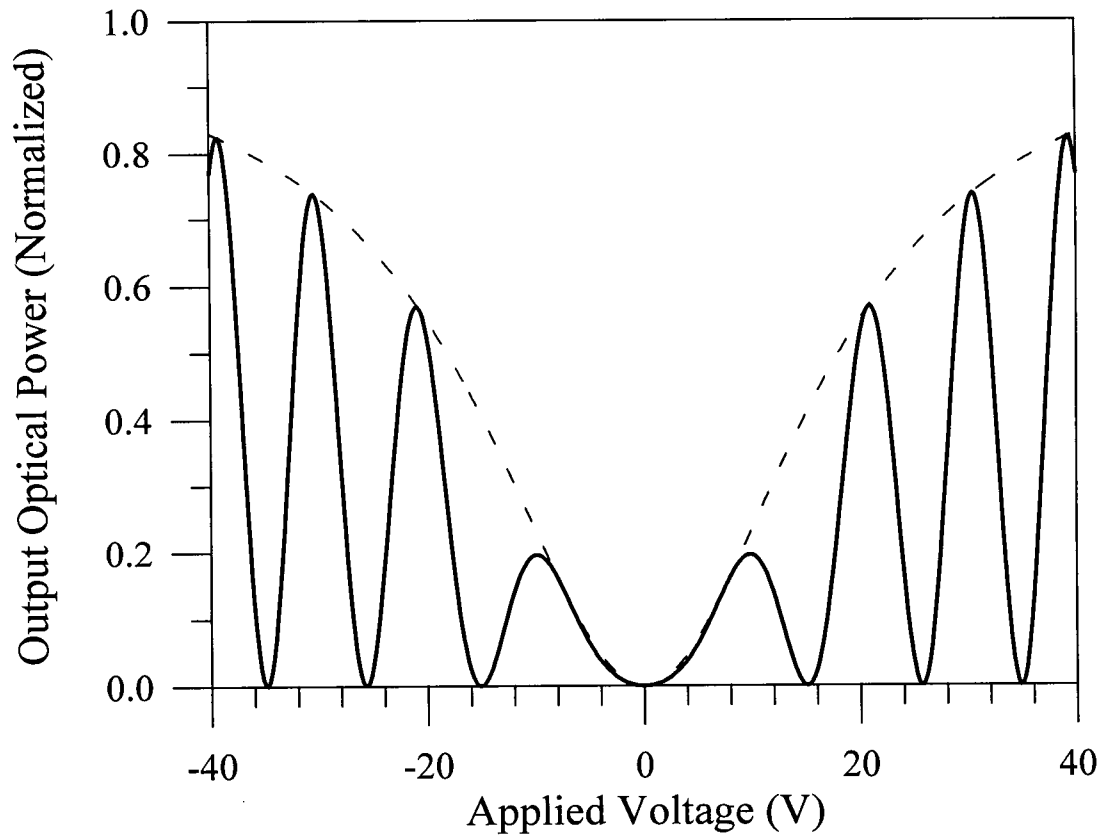
Figure 2.4.5. Normalized optical power converted from the TE-like polarization (parallel to the x axis) into the TM-like polarization (parallel to the z axis) as a function of the applied voltage for the device of Table 2.4.1. n_{TE} - n_{TM} = 0.00020. η is shown by the dashed line.

56
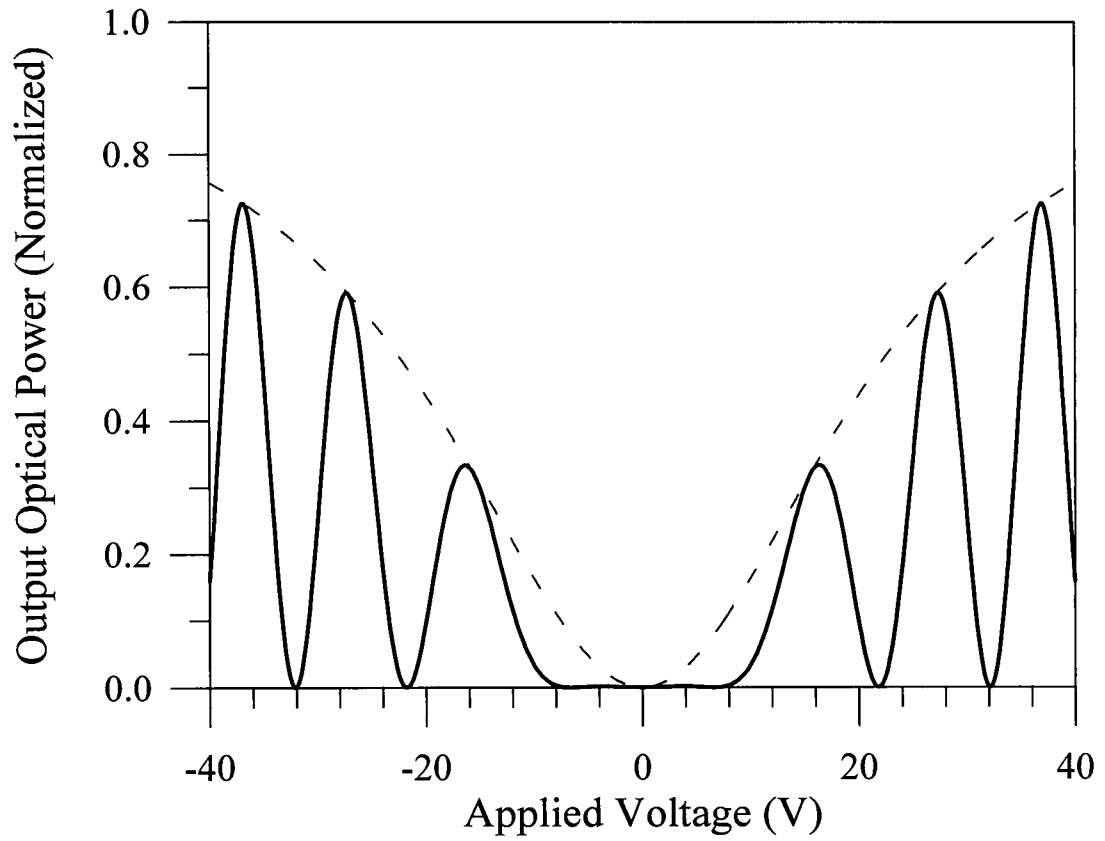
Figure 2.4.6. Normalized optical power converted from the TE-like polarization (parallel to the x axis) into the TM-like polarization (parallel to the z axis) as a function of the applied voltage for the device of Table 2.4.1. $n_{TE} - n_{TM} = 0.00025$. η is shown by the dashed line.
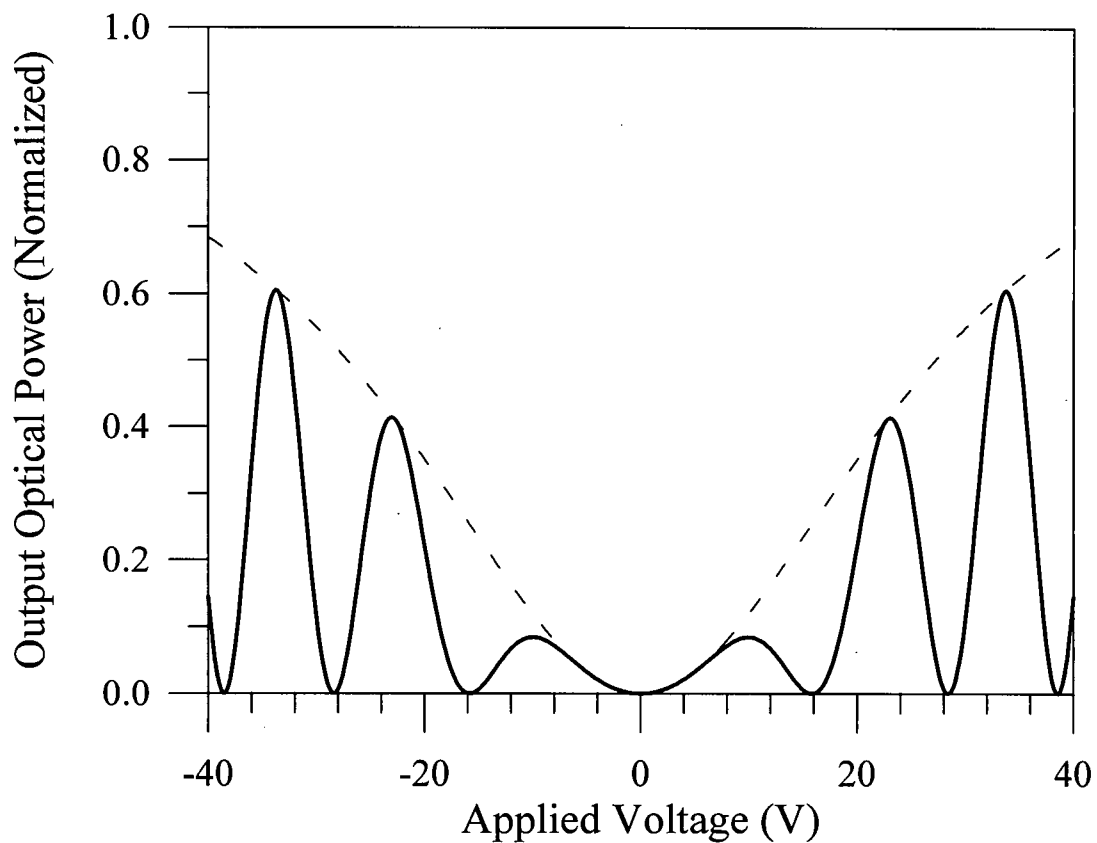
Figure 2.4.7. Normalized optical power converted from the TE-like polarization (parallel to the x axis) into the TM-like polarization (parallel to the z axis) as a function of the applied voltage for the device of Table 2.4.1. $n_{TE} - n_{TM} = 0.00030$. η is shown by the dashed line.
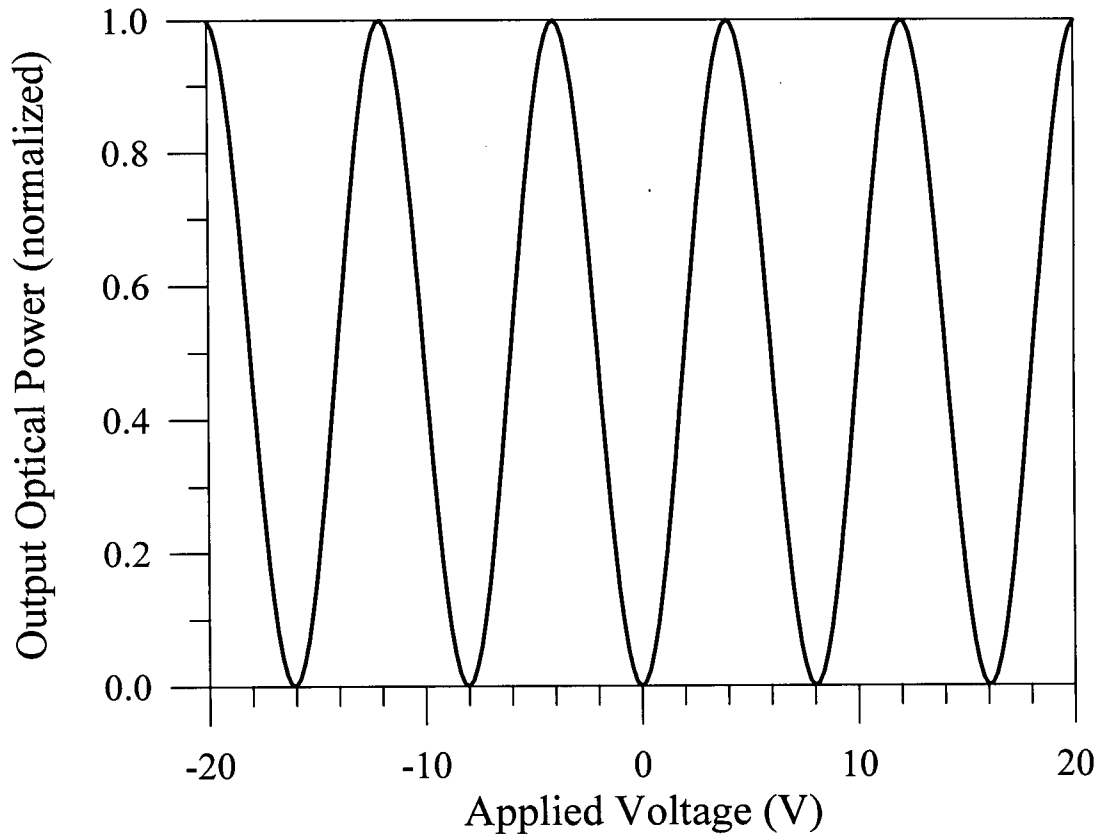
Figure 2.4.8. Normalized optical power converted from the TE-like polarization (parallel to the x axis) into the TM-like polarization (parallel to the z axis) as a function of the applied voltage for the device of Table 2.4.1. $n_{TE} = n_{TM} = 3.35800$, $n_{\mu} = 3.300$, $\alpha = 0$ Np/cm, $f = 40$ GHz.
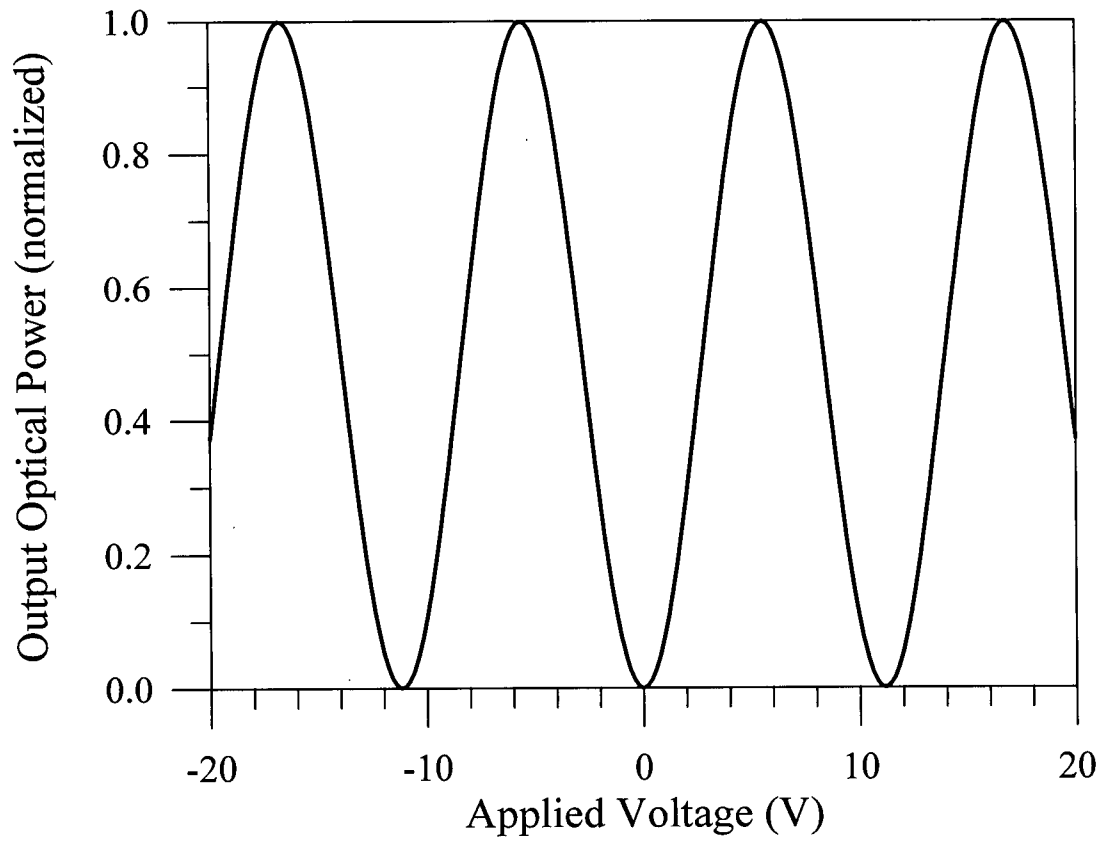
Figure 2.4.9. Normalized optical power converted from the TE-like polarization (parallel to the x axis) into the TM-like polarization (parallel to the z axis) as a function of the applied voltage for the device of Table 2.4.1. $n_{TE} = n_{TM} = 3.35800$, $n_\mu = 3.358$, $\alpha = 0.5$ Np/cm, $f = 40$ GHz.

60
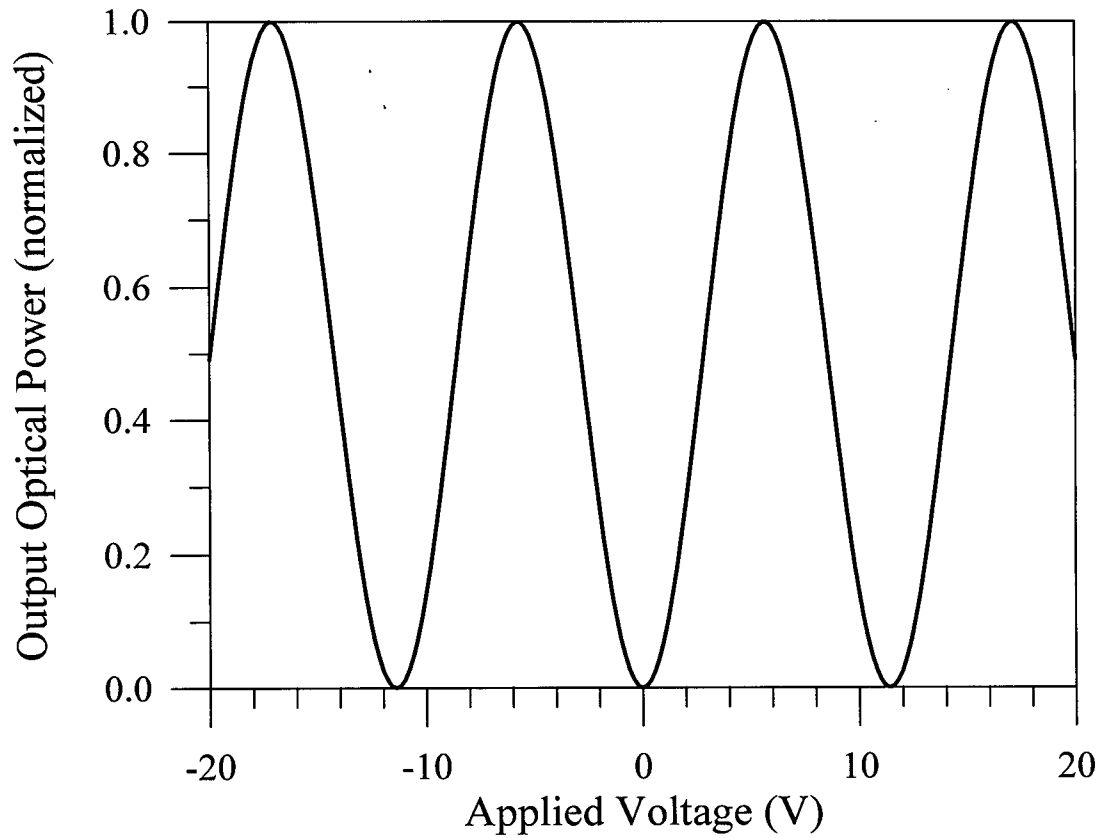
Figure 2.4.10. Normalized optical power converted from the TE-like polarization (parallel to the x axis) into the TM-like polarization (parallel to the z axis) as a function of the applied voltage for the device of Table 2.4.1. $n_{TE} = n_{TM} = 3.35800$, $n_\mu = 3.300$, $\alpha = 0.5$ Np/cm, $f = 40$ GHz.
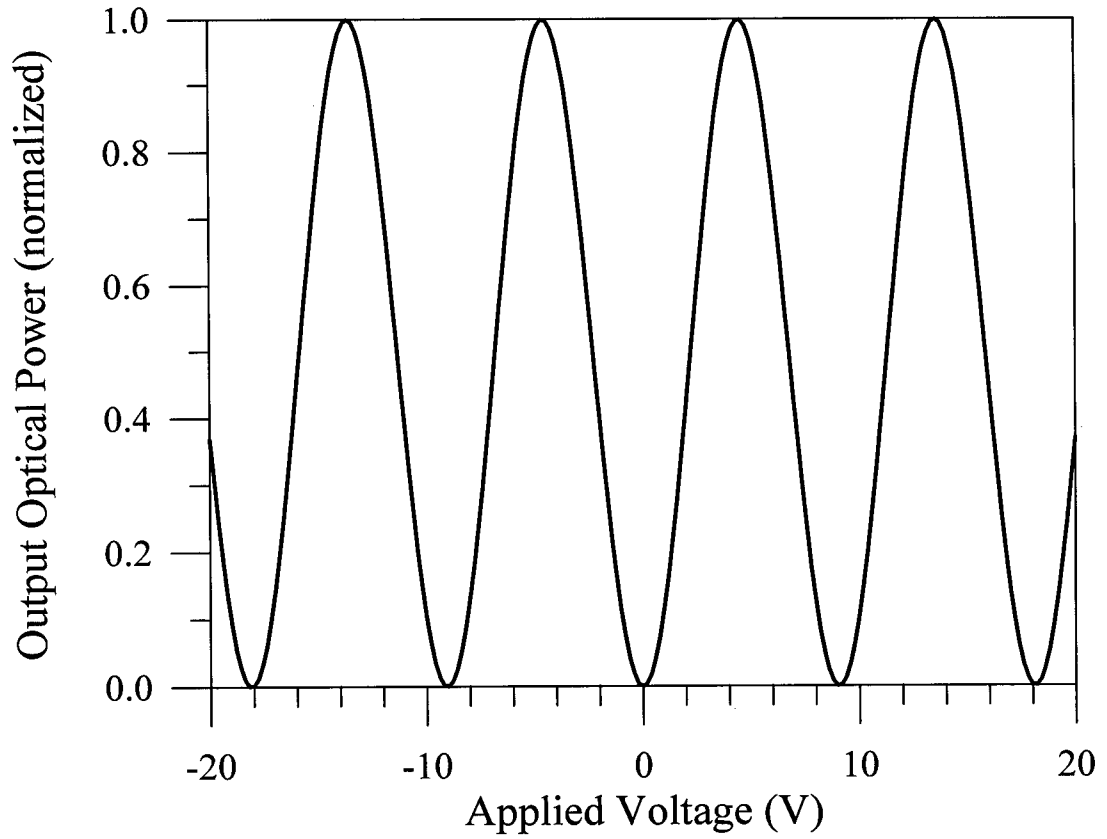
Figure 2.4.11. Normalized optical power converted from the TE-like polarization (parallel to the x axis) into the TM-like polarization (parallel to the z axis) as a function of the applied voltage for the device of Table 2.4.1. $n_{TE} = n_{TM} = 3.35800$, $n_\mu = 3.300$, $\alpha = 0$ Np/cm, $f = 100$ GHz.
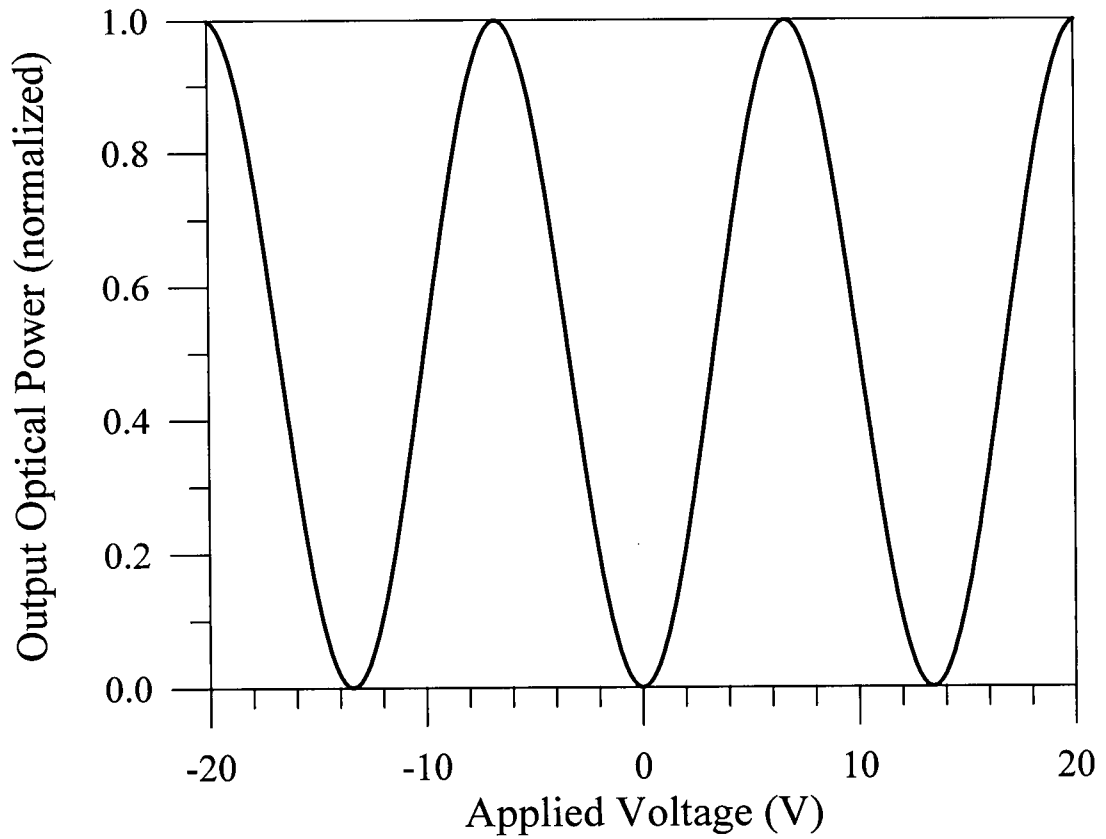
Figure 2.4.12. Normalized optical power converted from the TE-like polarization (parallel to the x axis) into the TM-like polarization (parallel to the z axis) as a function of the applied voltage for the device of Table 2.4.1. $n_{TE} = n_{TM} = 3.35800$, $n_\mu = 3.358$, $\alpha = 0.79$ Np/cm, $f = 100$ GHz.
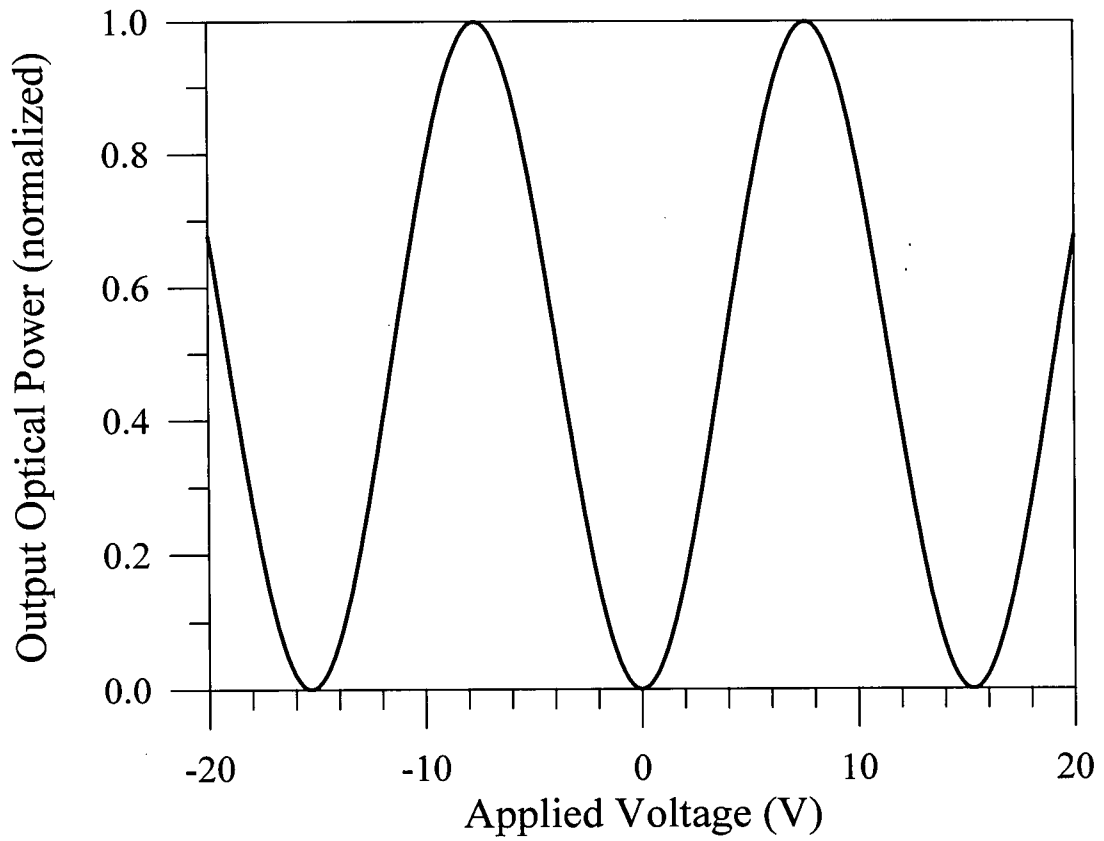
Figure 2.4.13. Normalized optical power converted from the TE-like polarization (parallel to the x axis) into the TM-like polarization (parallel to the z axis) as a function of the applied voltage for the device of Table 2.4.1. $n_{TE} = n_{TM} = 3.35800$, $n_\mu = 3.300$, $\alpha = 0.79$ Np/cm, $f = 100$ GHz.
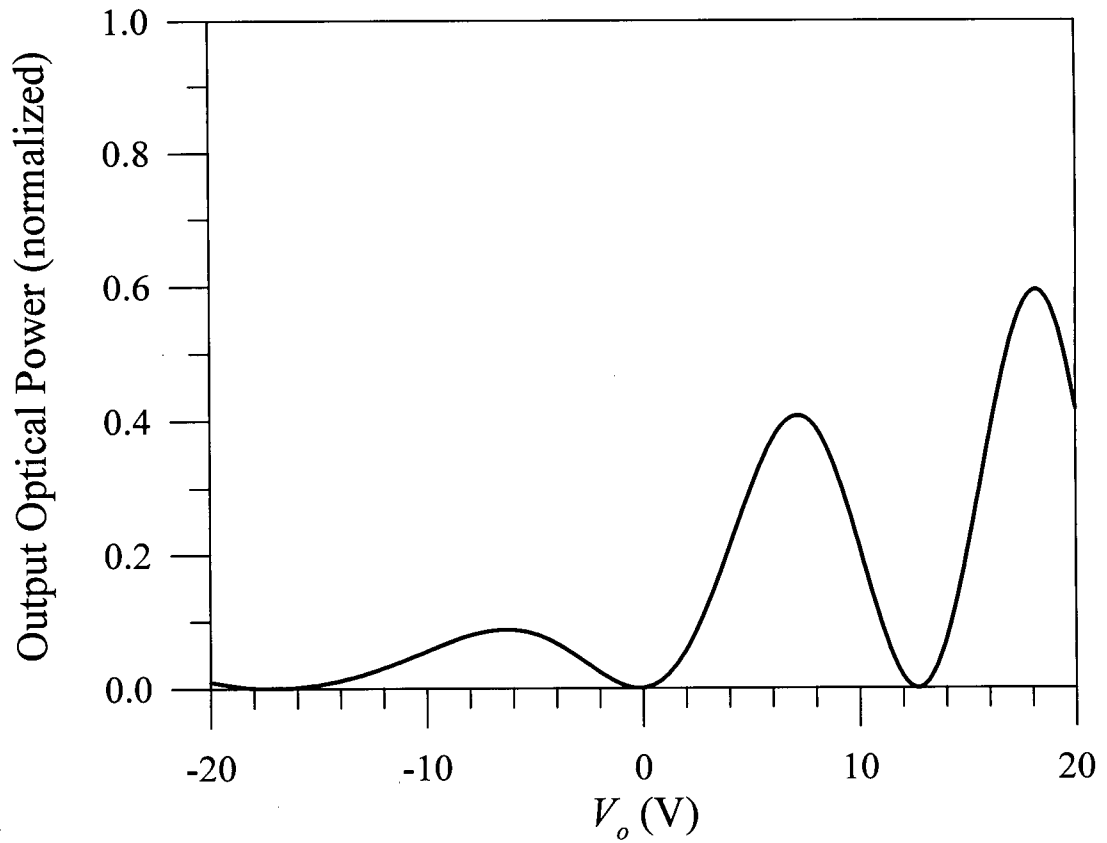
Figure 2.4.14. Normalized optical power converted from the TE-like polarization (parallel to the x axis) into the TM-like polarization (parallel to the z axis) as a function of the applied voltage for the device of Table 2.4.1. $n_{TE} - n_{TM} = 0.0003$, $n_{TM} = 3.358$, $n_{\mu} = 3.300$, $\alpha = 0$ Np/cm, $f = 40$ GHz, $V_b = 16$ V.
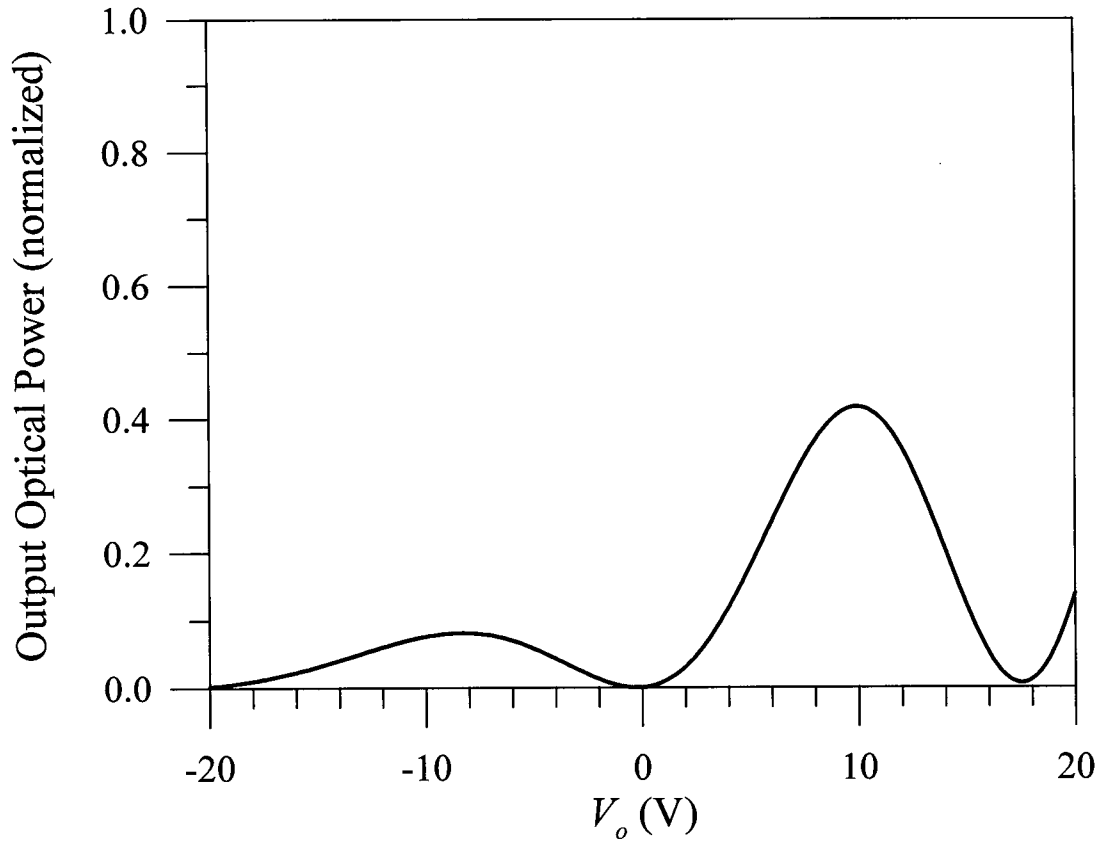
Figure 2.4.15. Normalized optical power converted from the TE-like polarization (parallel to the x axis) into the TM-like polarization (parallel to the z axis) as a function of the applied voltage for the device of Table 2.4.1. $n_{TE} - n_{TM} = 0.0003$, $n_{TM} = 3.358$, $n_{\mu} = 3.358$, $\alpha = 0.5$ Np/cm, $f = 40$ GHz, $V_b = 16$ V.
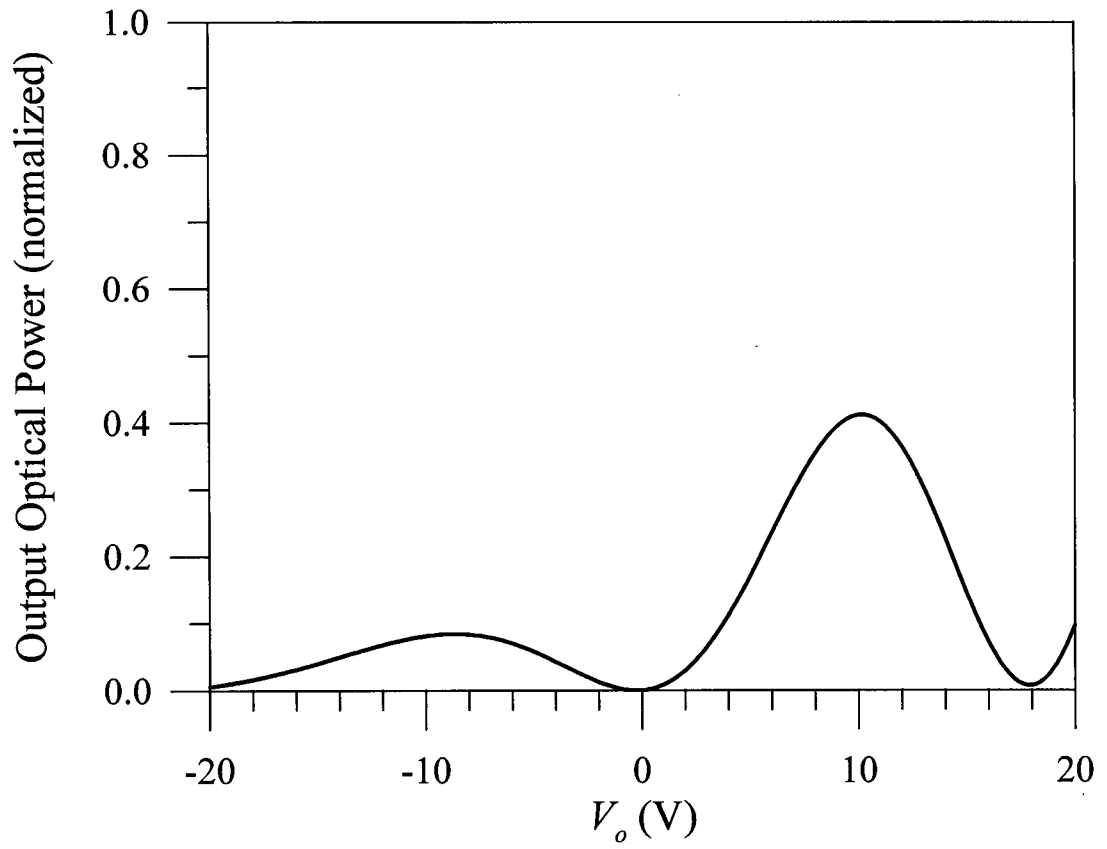
Figure 2.4.16. Normalized optical power converted from the TE-like polarization (parallel to the x axis) into the TM-like polarization (parallel to the z axis) as a function of the applied voltage for the device of Table 2.4.1. $n_{TE} - n_{TM} = 0.0003$, $n_{TM} = 3.358$, $n_{\mu} = 3.300$, $\alpha = 0.5$ Np/cm, $f = 40$ GHz, $V_b = 16$ V.
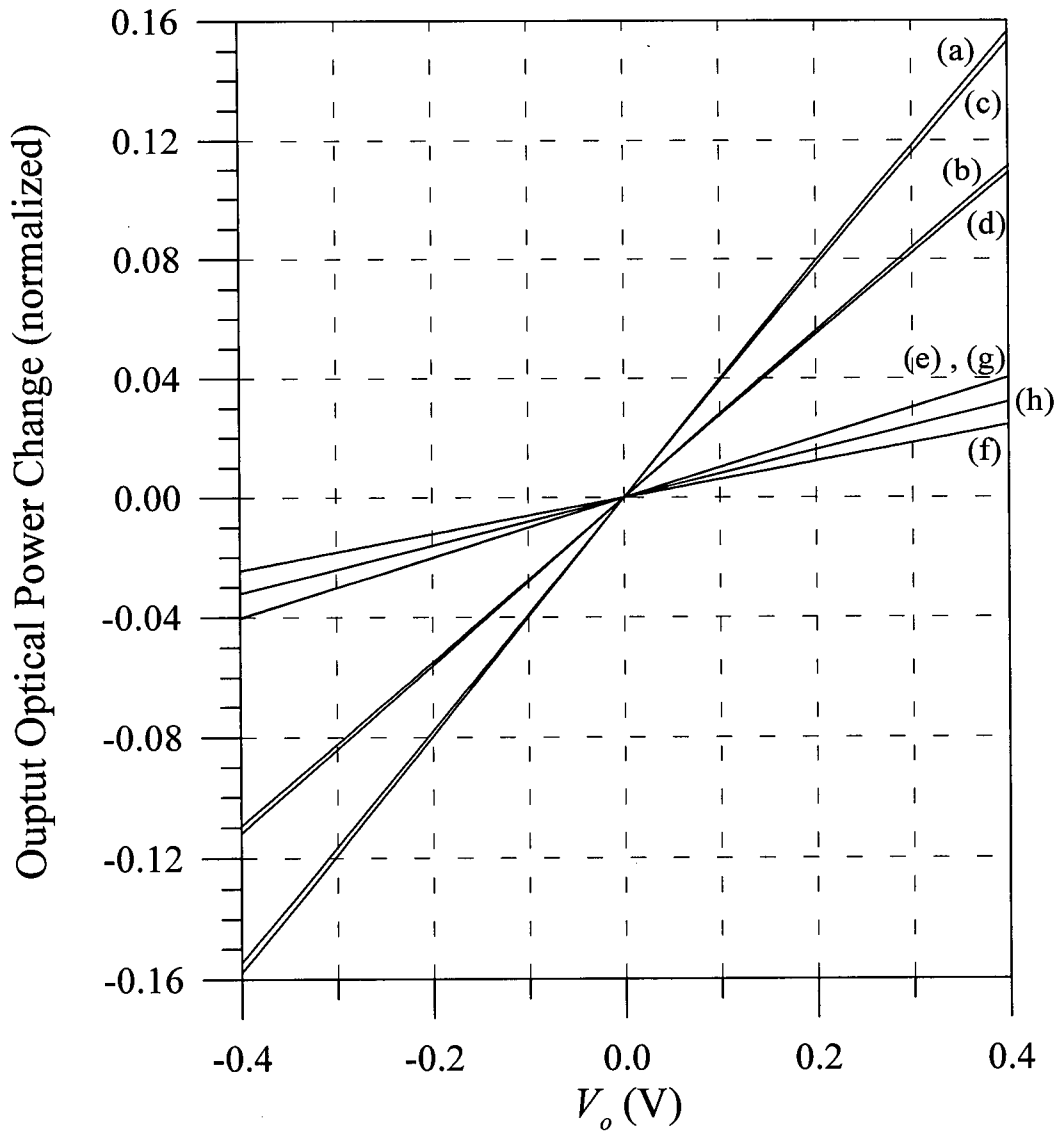
Figure 2.4.17. Change in the optical power converted from the TE-like polarization (parallel to the x axis) into the TM-like polarization (parallel to the z axis) as a function of the small-signal applied voltage for the device of Table 2.4.1. The optical power is, again, normalized with respect to the total optical power out of the waveguide. See Table 2.4.2 for details on each curve. $n_{TE} = n_{TM} = 3.35800$, $f = 40$ GHz.
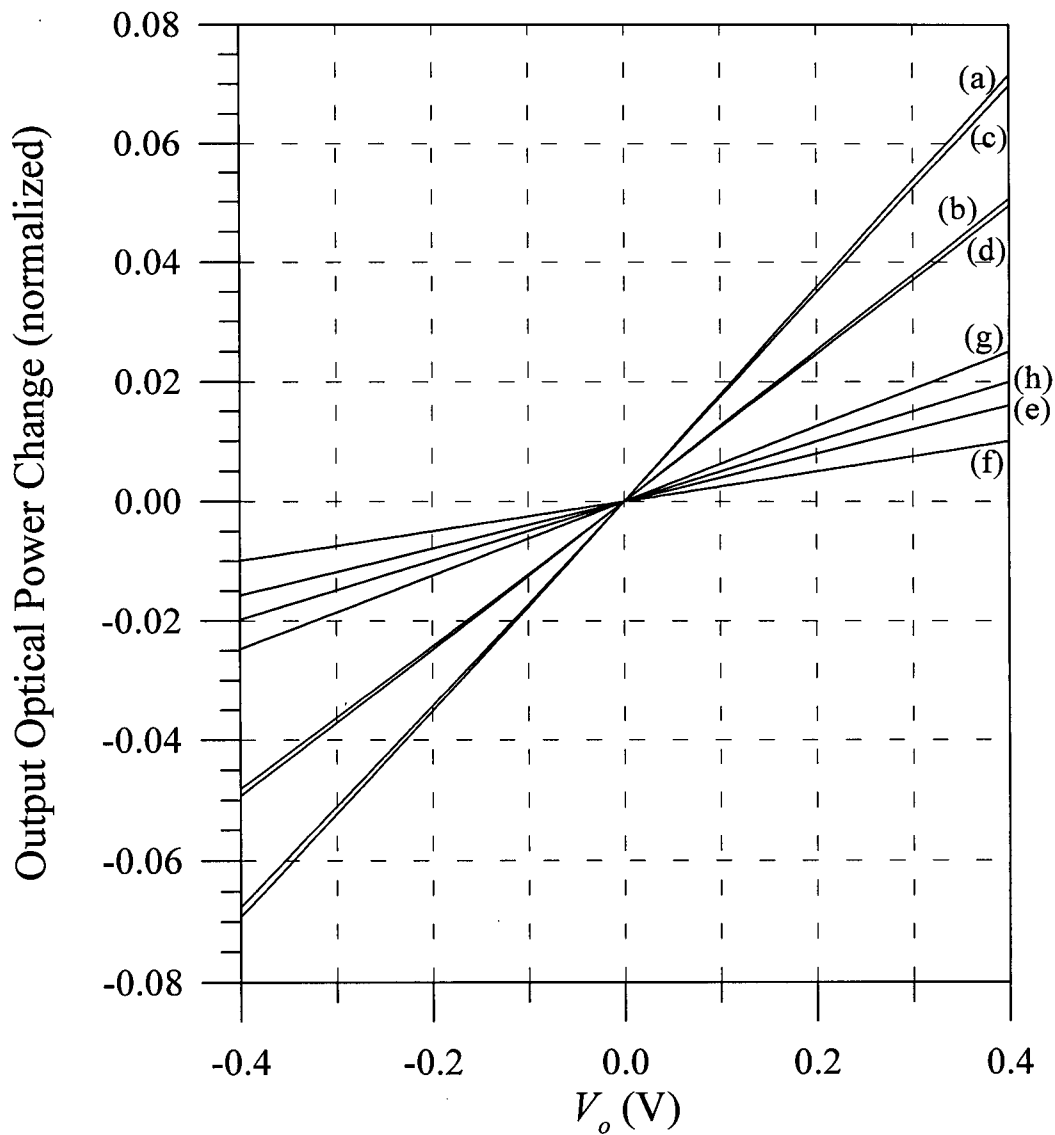
Figure 2.4.18. Change in the optical power converted from the TE-like polarization (parallel to the x axis) into the TM-like polarization (parallel to the z axis) as a function of the small-signal applied voltage for the device of Table 2.4.1. The optical power is, again, normalized with respect to the total optical power out of the waveguide. See Table 2.4.3 for details on each curve. $n_{TE} - n_{TM} = 0.0003$, $f = 40$ GHz.
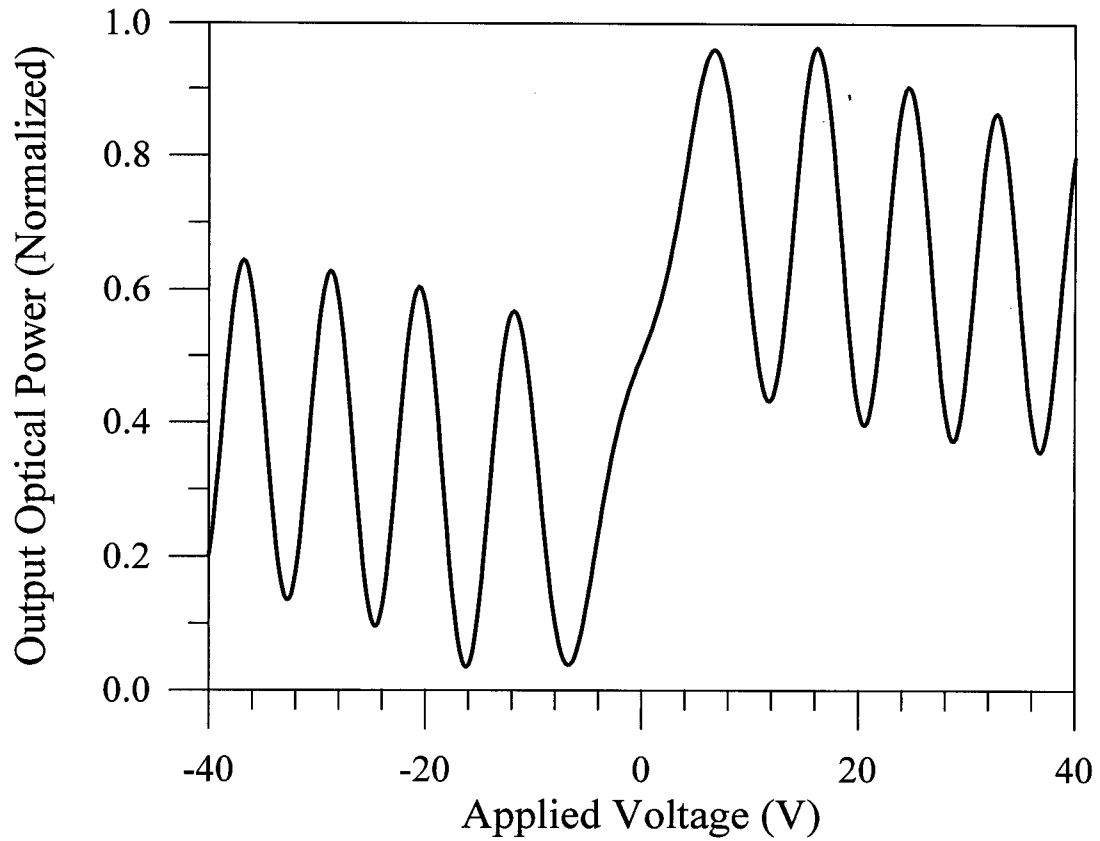
Figure 2.4.19. Normalized optical power out of the TM-like polarization (parallel to the z axis) as a function of the applied voltage for the device of Table 2.4.1. The input light is polarized at $45°$ to the x axis, and $n_{TE} - n_{TM} = 0.0001$.
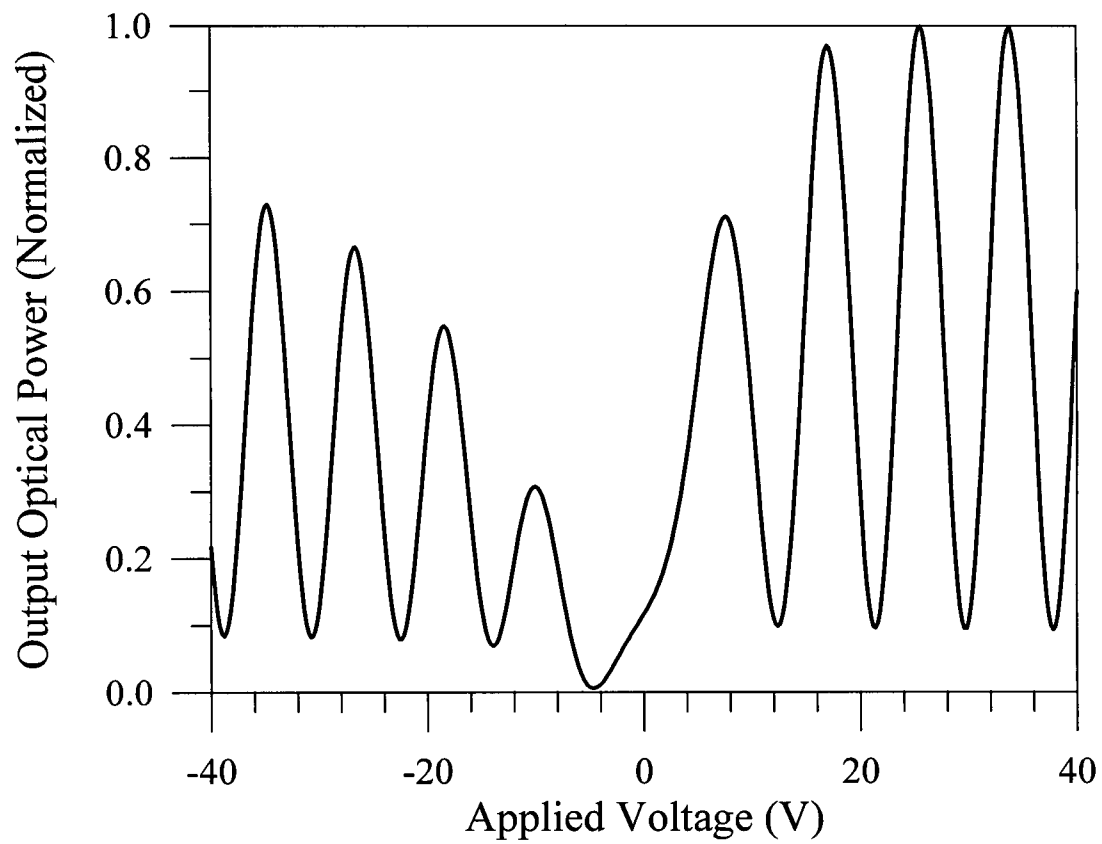
Figure 2.4.20. Normalized optical power out of the TM-like polarization (parallel to the z axis) as a function of the applied voltage for the device of Table 2.4.1. The input light is polarized at 20° to the x axis, and $n_{TE} - n_{TM} = 0.0001$.
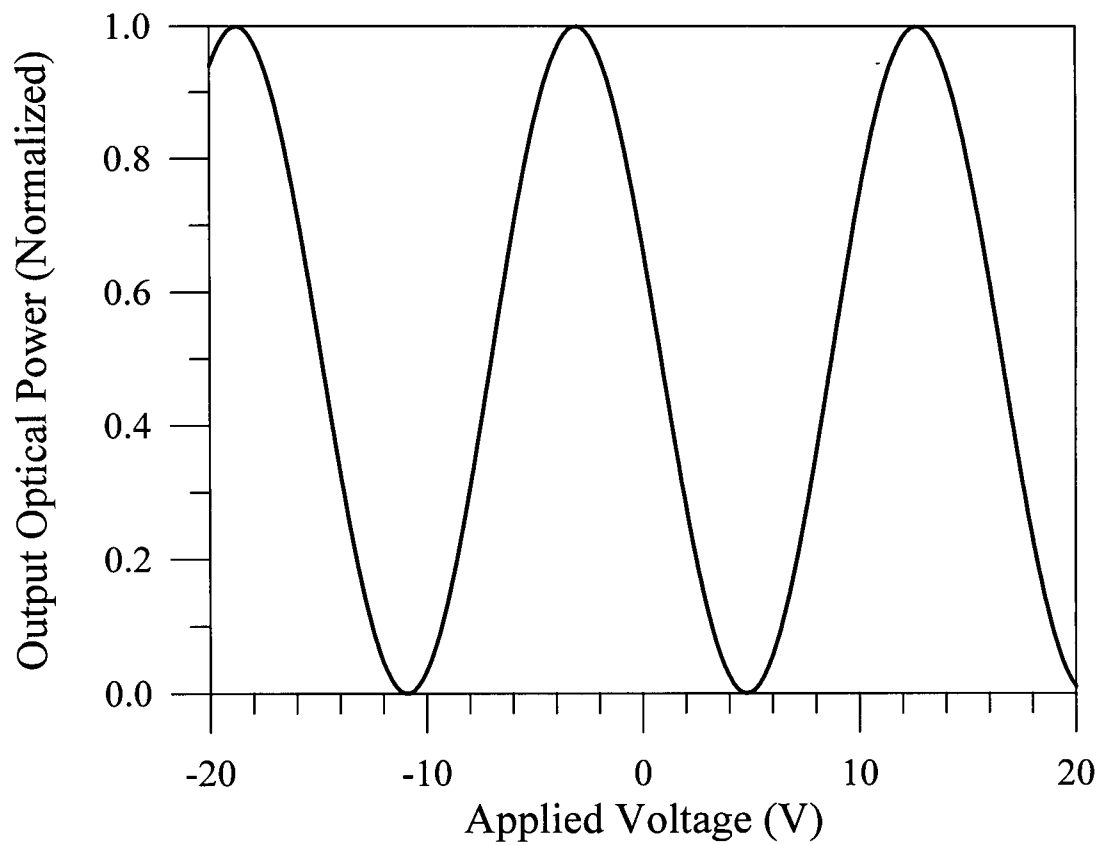
Figure 2.4.21. Normalized output optical power as a function of the applied voltage for the device of Table 2.4.1. The input light is polarized at 45° to the x axis, and the analyzer is oriented at -45° to the x axis. n_{TE} - n_{TM} = 0.0001.
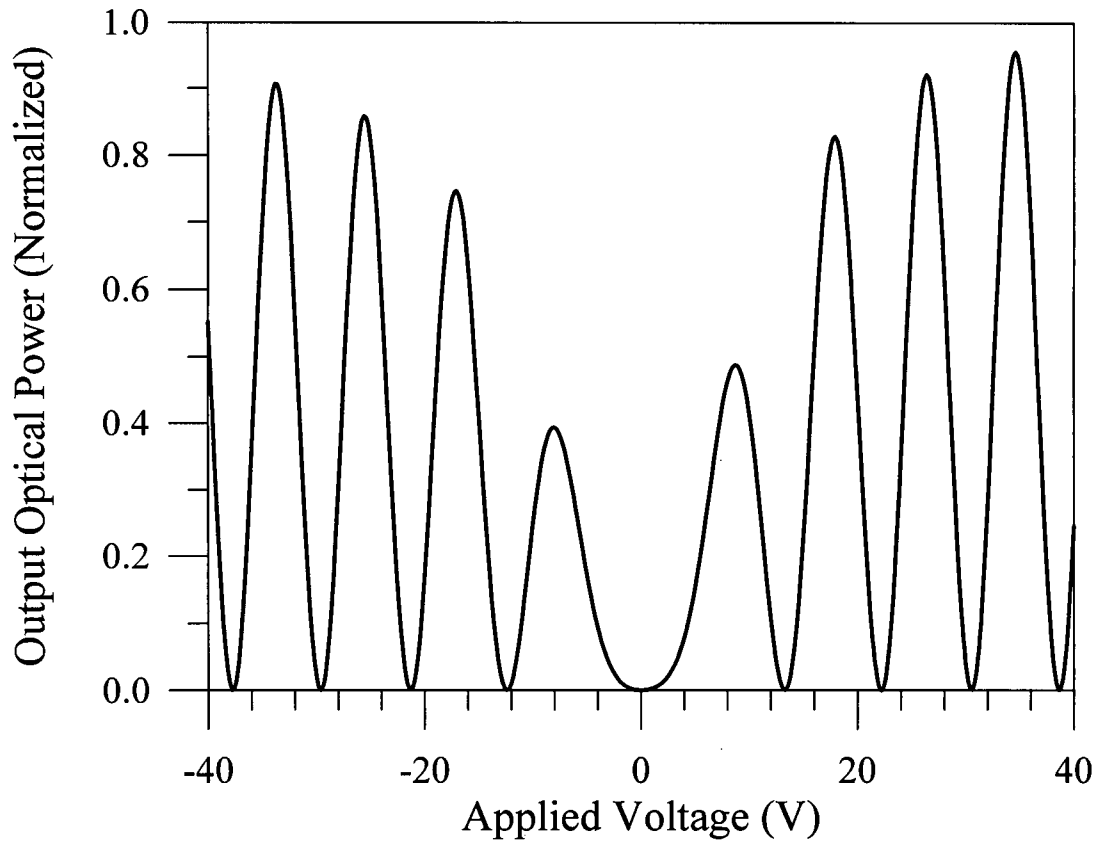
Figure 2.4.22. Normalized optical power converted from the TE-like
polarization (parallel to the x axis) into the TM-like polarization (parallel
to the z axis) as a function of the applied voltage for the device of Table 2.4.1.
$n_{TE} - n_{TM} = 0.00010.$ $E_3 = E_1 /10.$

Chapter 3. Design and Fabrication

3.1. Introduction

The fabrication of the modulators can be divided into two major processes: 1) design and fabrication of optical waveguides in AlGaAs/GaAs substrates, 2) design and fabrication of slow-wave electrodes. Most of our effort was spent on the design, fabrication, and testing of the slow-wave electrodes to achieve very low microwave losses and the required amount of slowing. The mask design and fabrication went through several iterations and the experience gained at each stage was used to design better electrodes. In this chapter, the structures of the substrate and optical waveguides used are given first. Then the process of the design and fabrication of various electrode structures is explained.

3.2. AlGaAs/GaAs Ridge Waveguides

There were two generations of optical waveguides fabricated. The first generation, generation 1, was based on the designs and modelling done in [67]. Since substrates of this kind were already available to us, we tried to use these substrates, mostly for economy. Also, our previous experience showed that the optical properties of the ridge waveguides fabricated in these substrates were quite satisfactory, see [67].

74

3.2.1. Generation 1

3.2.1.1. Substrate Structure

The AlGaAs/GaAs substrates were grown by Spire Corporation, Bedford, Massachusetts. The wafers were 2 inches in diameter. The epitaxial layers were grown using MOCVD, on (100) semi-insulating (SI) GaAs substrates that were 450 μm thick. Figure 3.2.1 gives the "target" structure of the substrate; the SI-GaAs was covered by 3.2 μm of $Al_{0.35}Ga_{0.65}As$, as a cladding layer, 1.3 μm of $Al_xGa_{1-x}As$ where x decreases linearly from 0.35 to 0.30, 1.3 μm of $Al_xGa_{1-x}As$ where x increases linearly from 0.30 to 0.35, and 0.7 μm of $Al_{0.35}Ga_{0.65}As$ as the cladding on the top. The modelling in [67], and our previous experimental results, indicated that for ridge waveguides 3 to 5 μm wide, with 1 μm etch depth, the waveguides are single mode at $\lambda_o = 1.3$ μm. Let's define Δn_{eff} as the difference between the effective refractive indices for the TE- and the TM-like modes, i.e., $\Delta n_{eff} = n_{TE} - n_{TM}$. Then for a 4 μm wide ridge, $n_{TE} \approx 3.245$, and $\Delta n_{eff} \approx 5.8 \times 10^{-5}$ at $\lambda_o = 1.3$ μm. These values are calculated using the effective index method [70], [71], and the dependence of the material refractive index on the mole fraction of aluminum and λ_o is obtained using the empirically determined Sellmeier equation [72], [67, p. 12]. Figure 3.2.2 shows the transfer function of a mode converter having a 4 μm wide ridge waveguide of the type given here and the electrode of Table 2.4.1 (compare with Figures 2.4.1-2.4.7). Again $\Gamma = 1$ is used here.

3.2.1.2. Mask Design

The mask for the optical waveguides included 20 rectangles, 30 mm long, located

parallel to one another at 1 mm intervals. All rectangles, except rectangles 9-12 (to be used with electrodes 3a-3d, see Table 3.3.4) were 3 μm wide. Rectangles 9-12 were 4 μm wide. The mask was laid out using a VLSI CAD package, Edge™, by Cadence Design System Inc., CA. Compressed forms of the mask files in GDSII format were sent to Precision Photo Mask (PPM) Inc., Montreal, Quebec, for mask fabrication. The masks were made on quartz substrates using electron-beam lithography. The precision was ±0.2 μm. The mask used for the fabrication of the waveguides was a copy of the original and was a light-field mask, i.e., the rectangles that formed the waveguide patterns were opaque and the rest of the mask was transparent. Note that these waveguides were all to be used for polarization/mode converters, i.e., no Mach-Zehnders were included here.

3.2.1.3. Optical Waveguide Fabrication

The fabrication of the ridge waveguides was done at UBC through the steps developed in [67]. These steps were later slightly modified. The fabrication involved the following steps:

1. The substrate was cleaned in a beaker of HF, 10% volume, for one minute.

2. 0.1 μm of titanium was sputtered on the substrate using the Perkin-Elmer Sputtering System model 3140, from Perkin-Elmer, Norwalk, CT. This Ti layer was to be used as the mask for etching the epitaxial layer.

3. Shipley's 1400-27 positive photoresist, from Shipley Company Inc., San Jose, CA, was spun on the samples at 4700 rpm for 35 seconds.

4. The photoresist was soft-baked at 95°C for 25 minutes. Water and solvents

are removed from the newly applied photoresist in the soft-baking process; as a result, the photo-resists hardens and adheres better to the substrate [73].

5.   After cooling down to room temperature, the photoresist was exposed through the waveguide mask, using the Karl-Suss MJB3 contact mask aligner, Karl Suss America Inc., Waterburgh, VT. The photoresist was exposed to UV light, $\lambda_o = 320$ nm, for 27 seconds.

6.   After cooling down to room temperature, the photoresist was developed in Shipley's MF-319 developer for 45 seconds.

7.   The photoresist was then hard-baked at 120°C for 20 minutes.

8.   The sample was then plasma etched, using CF_4 and Ar gases, in the active ion/plasma etching system model PK-12 from Plasma Therm Inc., Kresson, NJ, to remove the titanium not covered by the photoresist.

9.   The photoresist was then removed using a positive photoresist stripper.

10.   The (remaining) photo-resist residue was cleaned using oxygen plasma ashing in the PK-12 active ion/plasma etching system.

11.   The sample was cleaned in acetone and iso-propanol.

12.   The sample was then etched to remove 1 μm of material from the parts not covered by the titanium mask. The etchant consisted of a citric acid solution mixed with 30% hydrogen peroxide with a volume-ratio of 10:1. The citric acid solution itself was made by dissolving anhydrous citric acid crystals in de-ionized water at a ratio of 1 g per 1 ml. The etch took ~ 8 minutes.

13.   0.2 μm of SiO_2 was sputter-deposited onto the sample using the Perkin-Elmer

Sputtering System model 3140. The forward and reflected powers were set to 100 and 2.5 watts, respectively.

Later in the project, optical waveguides of this kind were also fabricated at the CRC, Communications Research Centre, Ottawa, Ontario, using the same masks and substrates, but using their fabrication process. Figure 3.2.3 shows SEM micrographs of the fabricated ridge waveguides of devices 5b and 5d, and the associated electrodes (also see Table 3.3.4).

3.2.2. Generation 2

The generation 1 optical waveguides fabricated had very good optical properties, i.e., the optical attenuation was acceptably low, ~ 1.5 dB/cm. However, later we found that the microwave loss of the electrodes fabricated on these substrates was extremely high. The problem appeared to be due to the amount of unintentional doping in the AlGaAs epitaxial layer, see [79]. Our collaborators at the CRC have studied this effect in more detail and found that for a doping $> 5 \times 10^{14}$ cm^{-3} the microwave loss of the substrate would be extremely high [75]. To have low microwave loss, close to that for electrodes fabricated on semi-insulating GaAs, the epitaxial layers should have a doping $< 1 \times 10^{14}$ cm^{-3}. Most AlGaAs material growers can limit the doping density in the AlGaAs layer to only ~ 10^{16} cm^{-3}. Since most of the customers are from the electronics industry where AlGaAs layers with dopings $< 10^{16}$ cm^{-3} are not absolutely essential, the growers are not willing to invest in a semi-insulating AlGaAs fabrication process. We actually found out that if AlGaAs layers are grown at low temperature, the mobility will, in fact, be very small. Finally, we found out that Nortel Technologies Inc. (previously known as Bell Northern Research), in Ottawa, Ontario,

could grow the material we needed. A new layer structure was chosen by our collaborators at the CRC and the material (the NortelTech sample) was grown at Nortel Technologies Inc. using molecular beam epitaxy (MBE).

3.2.2.1. Substrate Structure

The generation 2 substrate consists of the following layers: 500 μm of semi-insulating GaAs, 4 μm of $Al_{0.14}Ga_{0.86}As$ cladding layer, 1.8 μm of $Al_{0.08}Ga_{0.92}As$ core layer, 1.0 μm of $Al_{0.14}Ga_{0.86}As$ cladding layer, and 0.1 μm of GaAs passivation layer on top. More accurately, the aluminum mole fraction in the cladding layers is between 0.138 and 0.144, and that in the core layer is between 0.080 and 0.083. Figure 3.2.4 gives a schematic of the target structure. The doping in the AlGaAs layer is $\leq 1 \times 10^{14}$ cm^{-3}. Using the effective index method again, for this structure, for a 4 μm wide, 0.9 μm deep ridge waveguide, $n_{TE} \approx 3.357$, and $\Delta n_{eff} \approx 1.7 \times 10^{-4}$ at $\lambda_o = 1.3$ μm. Δn_{eff} increases with decreasing ridge width (and/or increasing wavelength); for example, for a 3 μm wide ridge, $\Delta n_{eff} \approx 2.2 \times 10^{-4}$ at $\lambda_o = 1.3$ μm. We were also interested in using these devices at $\lambda_o = 1.55$ μm. For the same 4 μm wide ridge waveguide, $n_{TE} \approx 3.322$, and $\Delta n_{eff} \approx 2.2 \times 10^{-4}$ at $\lambda_o = 1.55$ μm. The values calculated at the CRC using a 2-dimensional finite difference method (FDM) software, Seline, from BBV Software BV, Enschede, are $n_{TE} \approx 3.322$, and $\Delta n_{eff} \approx 2.4 \times 10^{-4}$ at $\lambda_o = 1.55$ μm. Figures 3.2.5 and 3.2.6 give the transfer functions (low frequency) for a modulator having a 4 μm wide ridge waveguide of the type described here and the slow-wave electrode of Table 2.4.1 at $\lambda_o = 1.3$ μm and $\lambda_o = 1.55$ μm, respectively. Generally, generation 2 substrates are easier to grow than generation 1 ones, since the former do not involve graded mole-fraction

epitaxial layers. However, the value of Δn_{eff} is about 3 times larger for generation 2 devices; hence, significantly larger bias voltages are required for mode converters fabricated in the new substrate, compare Figures 3.2.2, 3.2.5, and 3.2.6.

3.2.2.2. Mask Design

A new mask was designed for the optical waveguides. This was a joint effort between our group at UBC and our collaborators at the CRC. We had 37 modulators on the mask. We went through the design procedure together (also see the electrode mask design in section 3.3); however, the final decision on the dimensions for the first 24 electrodes was with the CRC group, and devices 25 to 37 were determined by us at UBC. Device type and waveguide dimensions for devices 25 to 37 are given in Table 3.2.1. The mask included both Mach-Zehnder and polarization converter type modulators. Details on the dimensions of the electrodes are provided in section 3.3.

3.2.2.3. Fabrication

The new mask, for generation 2 devices, was laid down at the CRC, and was fabricated at Nortel Technologies Inc. The modulators were fabricated at the CRC clean-room facility in Ottawa. The ridge waveguides were covered by 0.2 μm of SiO_2 optical buffer layer. Figure 3.2.7 shows SEM micrographs of a number of generation 2 ridge waveguides, and the associated electrodes.

Table 3.2.1. Device types and waveguide dimensions for generation 2 modulators.

Device #	Modulator Type	Ridge Width (μm)	Notes
25	PC-A-CPS	3	-
26	PC-A-CPS	3	-
27	PC-A-CPS	3	-
28	PC-A-CPS	3	-
29	PC-A-CPS	5	-
30	MZ-C-CPS	4	The separation between branch centres = 64 μm
31	MZ-C-CPS	4	The separation between branch centres = 52 μm
32	PC-C-CPS	4	With two straight channel waveguides at 42 μm
33	PC-A-CPS	4	-
34	PC-A-CPS	3	-
35	MZ-B-CPW	3	The separation between branch centres = 98 μm
36	MZ-B-CPW	3	The separation between branch centres = 89 μm
37	PC-A-CPW	3	With two straight channel waveguides at 91 μm

0.7 μm	Cladding Layer $\quad Al_{.35}Ga_{.65}As$
1.3 μm	Core Layer $\qquad \begin{array}{c} Al_{.35}Ga_{.65}As \\ \uparrow \\ Al_{.30}Ga_{.70}As \end{array}$
1.3 μm	Core Layer $\qquad \begin{array}{c} Al_{.30}Ga_{.70}As \\ \uparrow \\ Al_{.35}Ga_{.65}As \end{array}$
3.2 μm	$Al_{.35}Ga_{.65}As$ Cladding Layer
450 μm	Semi-Insulating GaAs
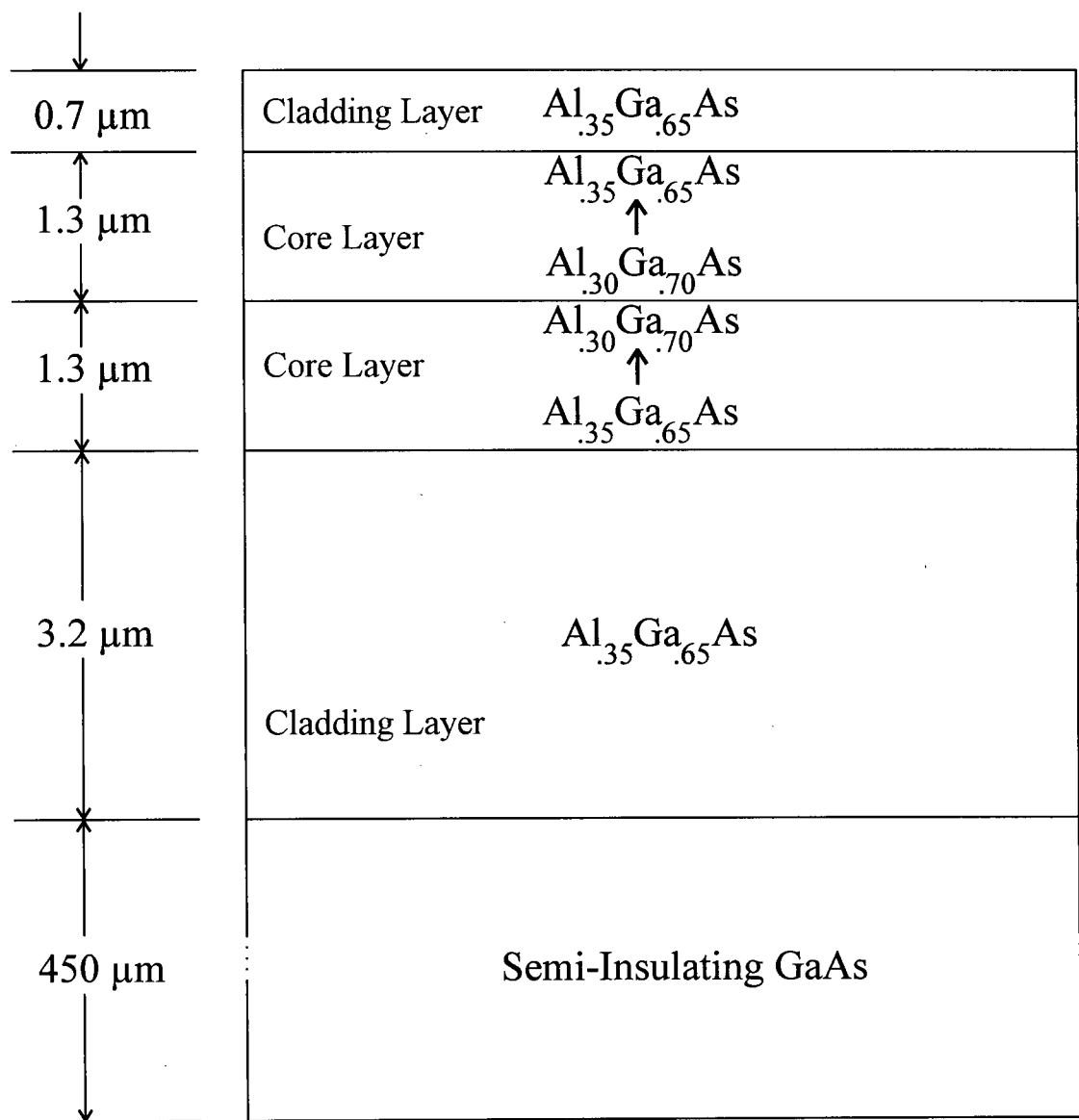
Figure 3.2.1. Target structure of the generation 1 AlGaAs/GaAs substrate grown by MOCVD.
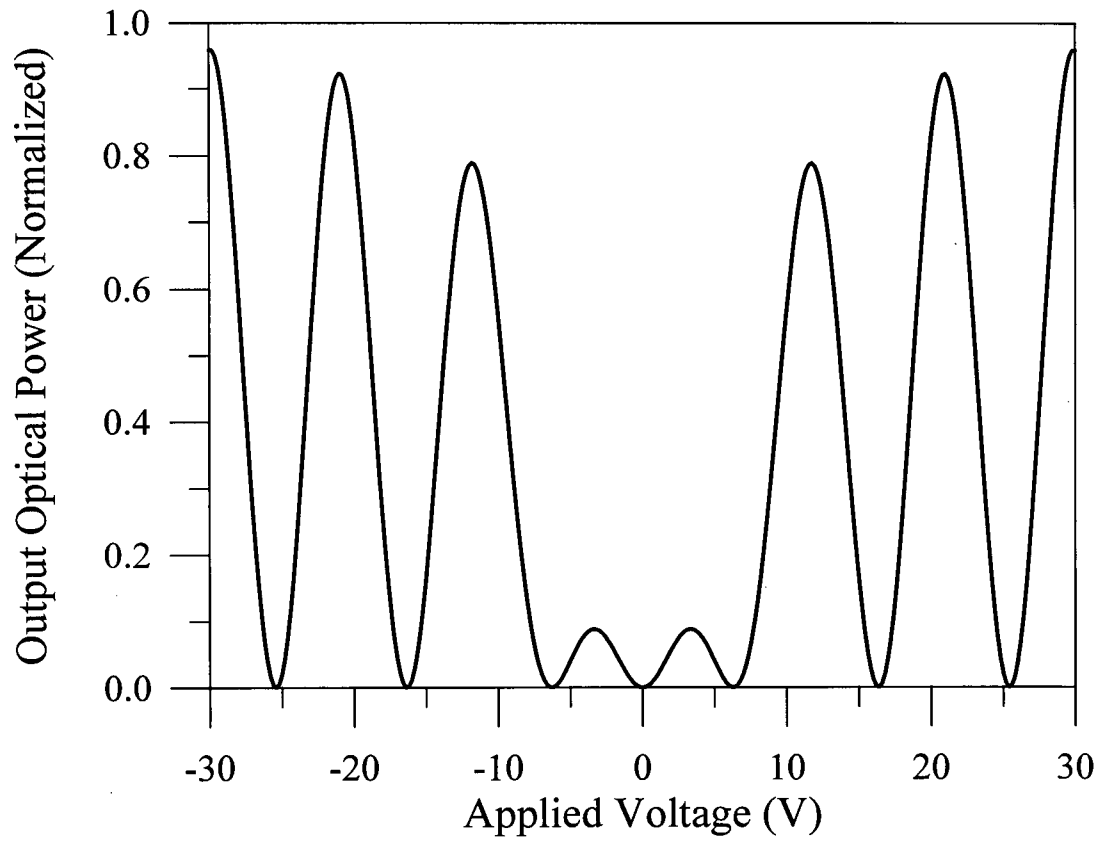
Figure 3.2.2. Normalized optical power converted from the TE-like polarization (parallel to the x axis) into the TM-like polarization (parallel to the z axis) as a function of the applied voltage for the device of Table 2.4.1. $n_{TE} = 3.245$, $\Delta n_{eff} = 0.00006$, and $\lambda_o = 1.3$ μm.
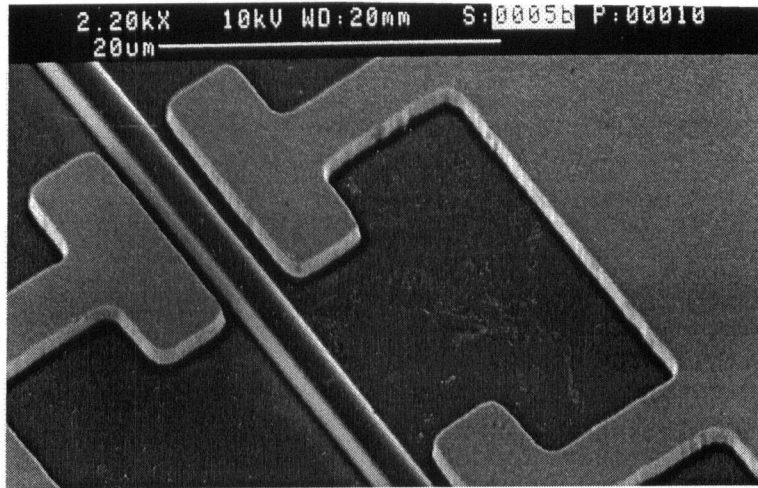
(a)
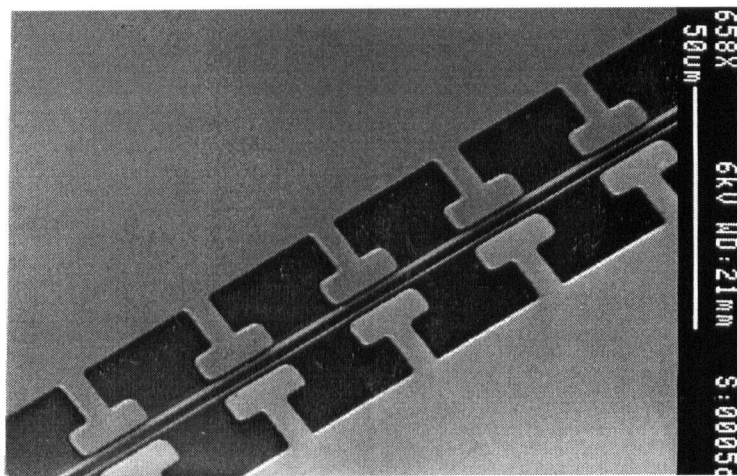
(b)

Figure 3.2.3. SEM pictures of the generation 1 devices (a) 5b and (b) 5d fabricated on the Spire AlGaAs/GaAs substrate.
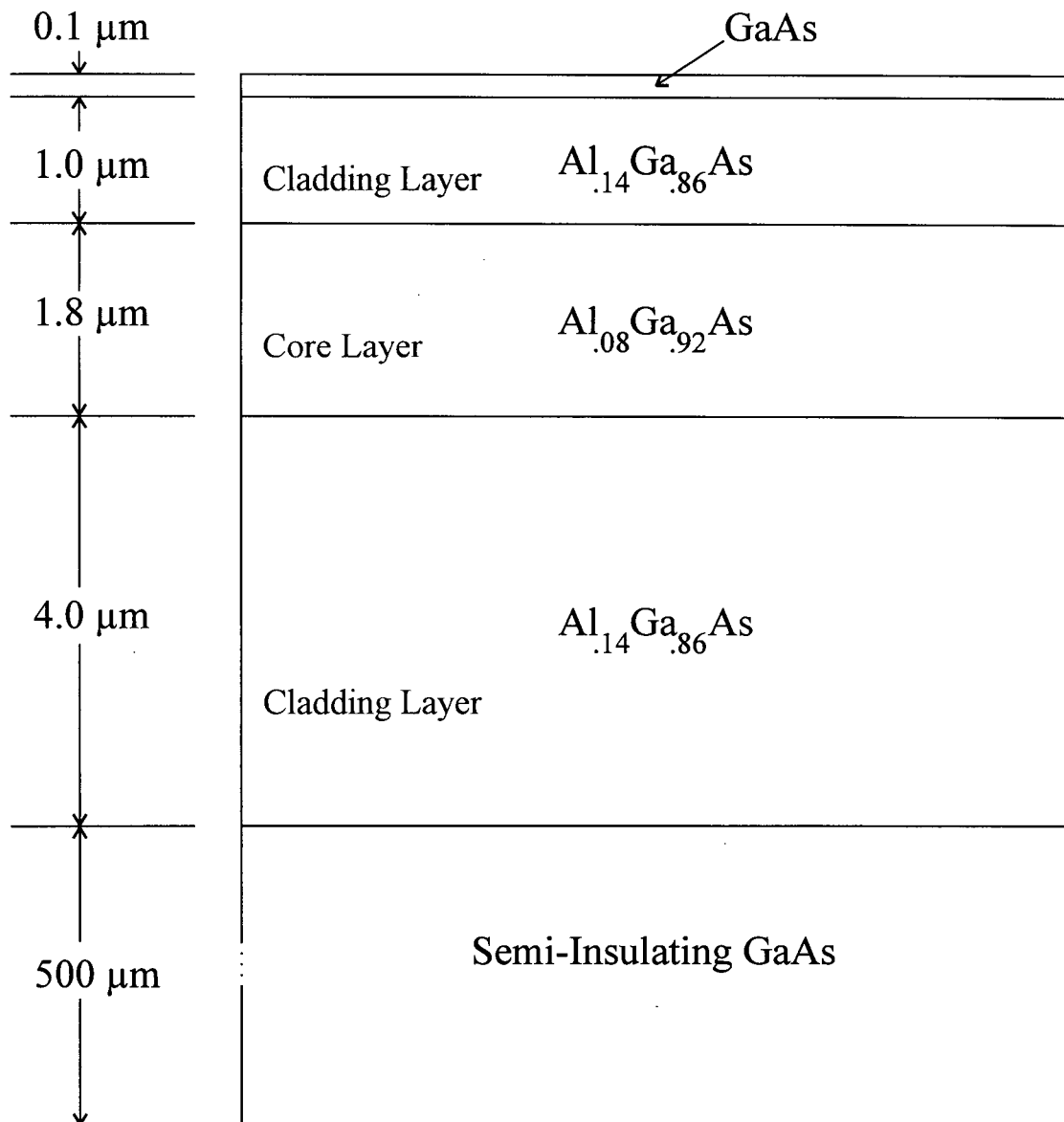
Figure 3.2.4. Target structure of the generation 2 AlGaAs/GaAs substrate grown by MBE.
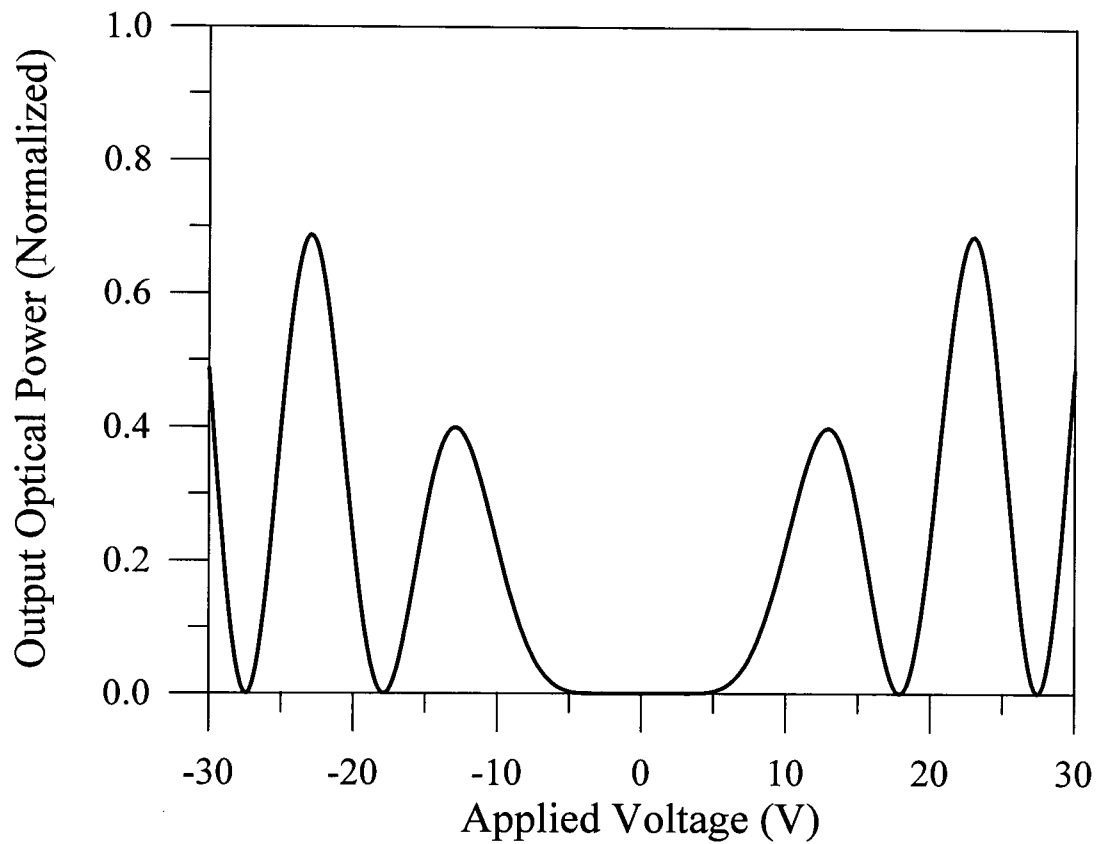
Figure 3.2.5. Normalized optical power converted from the TE-like polarization (parallel to the x axis) into the TM-like polarization (parallel to the z axis) as a function of the applied voltage for the device of Table 2.4.1. $n_{TE} = 3.357$, $\Delta n_{eff} = 0.00017$, and $\lambda_o = 1.3$ μm.
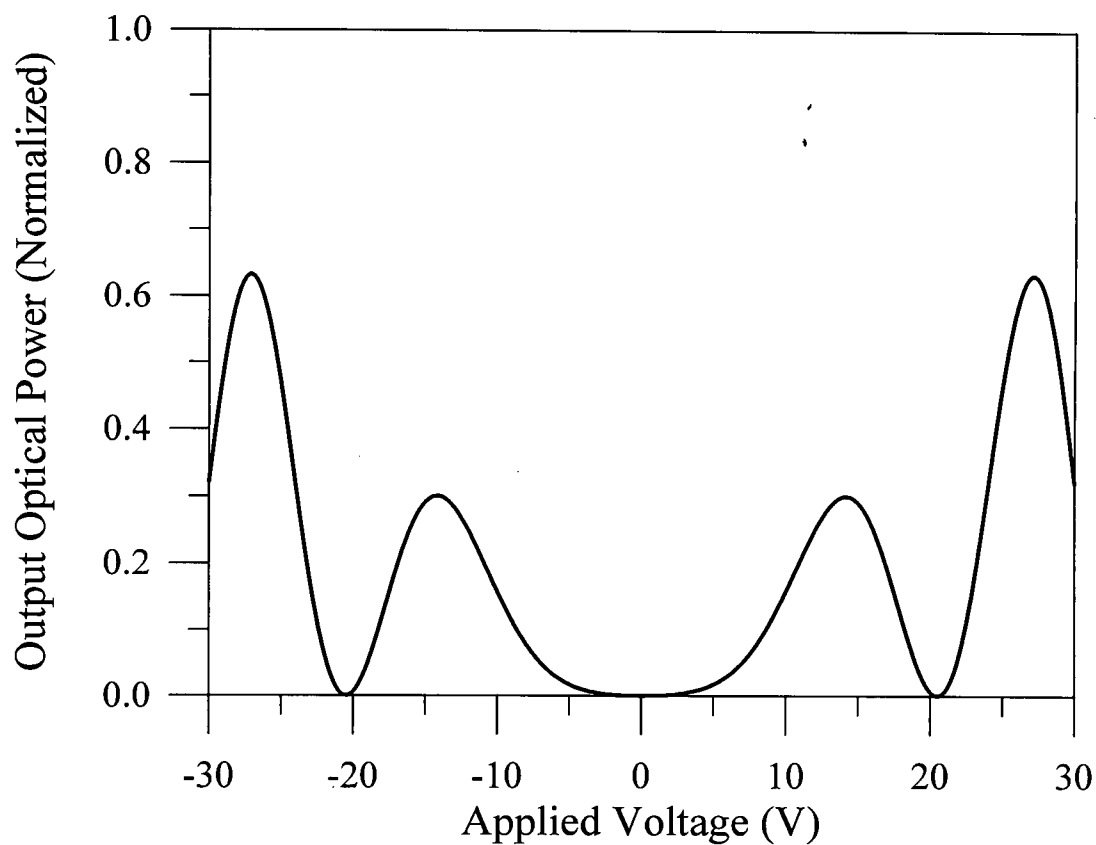
Figure 3.2.6. Normalized optical power converted from the TE-like polarization (parallel to the x axis) into the TM-like polarization (parallel to the z axis) as a function of the applied voltage for the device of Table 2.4.1. $n_{TE} = 3.322$, $\Delta n_{eff} = 0.00022$, and $\lambda_o = 1.55$ μm.
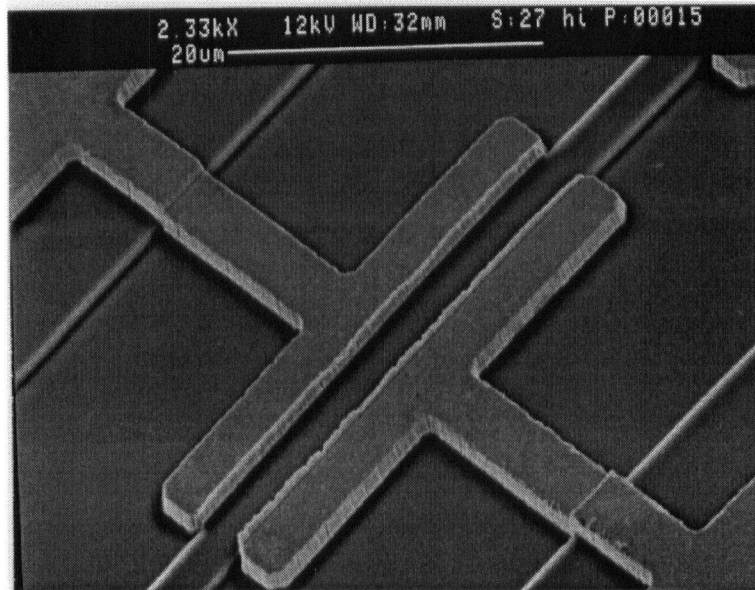
(a)
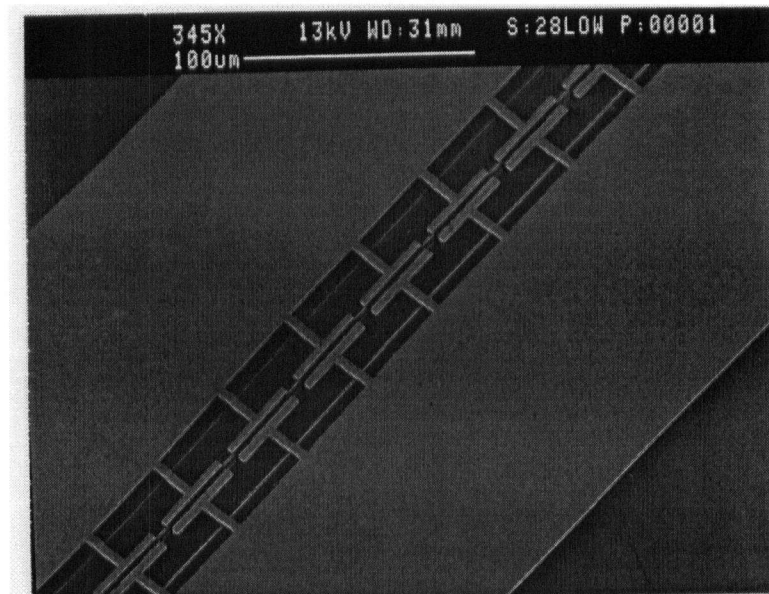
(b)

Figure 3.2.7. SEM pictures of the generation 2 devices (a) 27, (b)28, (c) 30, (d) 35, (e) 36, and (f) 37 fabricated on the NortelTech AlGaAs/GaAs substrate.

(e)

(f)

90

(e)

(f)

90
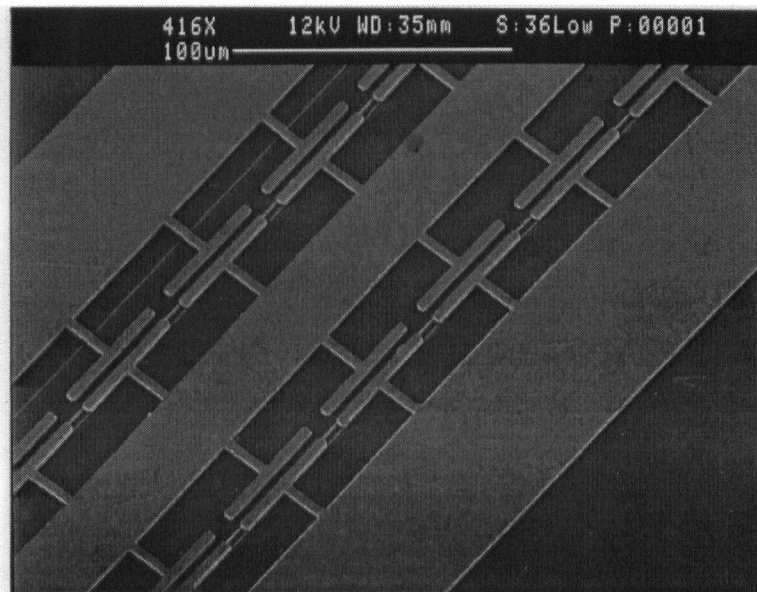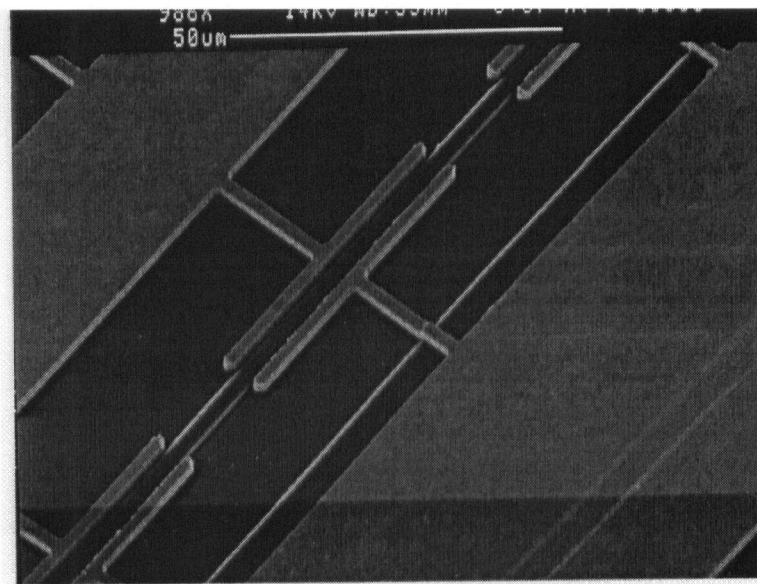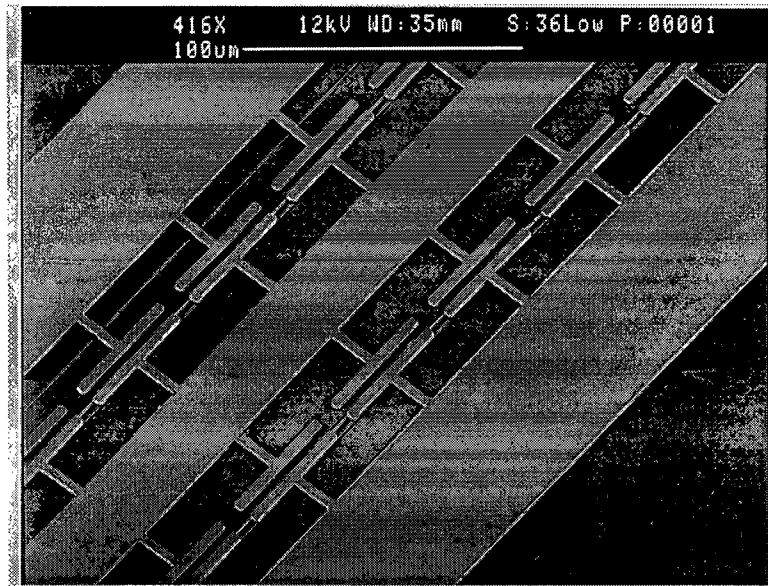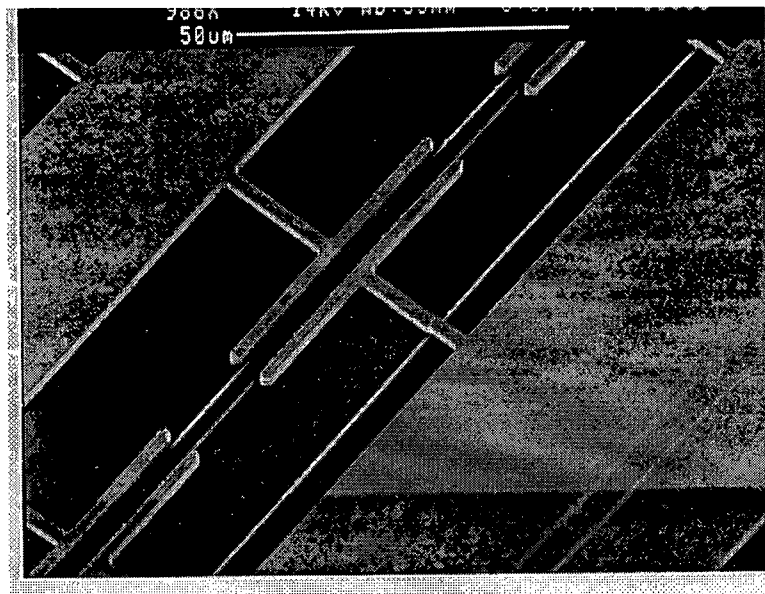
3.3. Slow-Wave Electrodes

The design and fabrication of slow-wave electrodes went through several iterations, and the experience gained at each stage was used to improve the design at the next stage. Similar to the optical waveguides, there were two generations of slow-wave electrodes fabricated. The first generation, generation 1, were based on the results of the measurements done on the electrodes previously designed and fabricated by Z. K. F. Lee and B. P. C. Tsou [23], [67]. These electrodes were to be used with generation 1 optical waveguides as explained in section 3.2.1. Generation 2 electrodes were designed using Sonnet™ release 2.4, a multilayered electromagnetic simulator for planar circuits, from Sonnet Software Inc., 135 Old Clover Rd, Liverpool, NY [66]. Generation 2 electrodes were designed to be used with generation 2 optical waveguides.

3.3.1. Generation 1

3.3.1.1. Electrode Design

The modulators were all of PC-A-CPS type. Since the effective index for the modes guided by generation 1 optical waveguides was ~ 3.245, at $\lambda_o = 1.3$ μm, see section 3.2.1.1, the target n_μ was chosen to be 3.25. Twenty slow-wave CPS electrodes of various lengths, 2.5 mm to 20 mm long, were designed. The design was mostly based on the measurements done on the previously fabricated electrodes. Table 3.3.1 gives the values of n_μ for a number of electrodes fabricated on semi-insulating GaAs. These electrodes were designed by Z. K. F. Lee using conformal mapping and the finite difference method [23]. A new batch of these

electrodes was fabricated and tested up to 40 GHz using an HP 8510C network analyzer together with an HP 8516A S-parameter test set and an HP8340 synthesized sweeper, all from Hewlett-Packard, Colorado Springs, CO. Table 3.3.1 provides both the values measured by Lee at 20 GHz [23] and the values we calculated from the measured S-parameters at 40 GHz. These electrodes were all shorted at one end and probed at the other end. The microwave index was calculated from the phase of the S_{11} parameter to be $n_\mu = c \, \phi \, / \, (4 \, \pi \, L f)$ where c is the speed of light in free space, ϕ is the phase of S_{11} in radians at 40 GHz (assuming $\phi = 0$ at d.c.), L is the length of the electrode, and $f = 40$ GHz. The maximum difference between the values obtained from the two sources is less than 3%. Electrode dimensions are also given in the table 3.3.1.

It should be noted that the values reported here are for electrodes fabricated on SI-GaAs, without any SiO_2 buffer layers. The inclusion of the optical buffer layer and the AlGaAs epitaxial layer reduces n_μ. Therefore, the structures that are likely to give n_μ close to 3.25 on SiO_2/AlGaAs/GaAs substrates have dimensions close to those of electrodes A4, A5, A7, and A8. Note that electrode A1 does not have pads, and is not suitable for PC-A type devices; however, it can be used for MZ-A type devices.

Another batch of devices designed by Lee and Tsou is given in Table 3.3.2. These electrodes were designed for Mach Zehnder modulators of type MZ-A-CPS [67] and were fabricated by lift-off photolithography, see section 3.3.1.3. They were surface deposited on SI-GaAs substrates. Two types of electrodes were tested: one set consisted of aluminum electrodes laid down directly on the surface of the SI-GaAs substrate (sample I), and the other had a 0.4 μm SiO_2, sputter-deposited, buffer layer between the aluminum electrodes and

the SI-GaAs substrate (sample II). These electrodes were tested up to 40 GHz, again using an HP 8510C network analyzer together with an HP 8516A S-parameter test set and an HP8340 synthesized sweeper. The values of n_μ, the characteristic impedance, Z_o, and the microwave loss, α, were calculated from the measured S-parameters (see [76], [57], and chapter 4). Table 3.3.3 provides the measured values of n_μ, α, and Z_o, at 40 GHz for both samples I and II. These electrodes were designed for various values of n_μ using a model in which half-buried, lossless, electrodes on lossless substrates of SI-GaAs were assumed, see [23] and [67]. Table 3.3.3 also includes these target design values for n_μ (target $Z_o = 50\ \Omega$).

Since the electrodes were surface deposited, as opposed to half buried, and t, the electrode thickness, was on the order of g_p, the gap between the pads, the capacitive effects of the fins and the pads were lower than the calculated values. Since $Z_o \propto 1/\sqrt{C}$ and $n_\mu \propto \sqrt{C}$, where C denotes the line capacitance per unit length, the measured Z_o was expected to be somewhat larger than 50 Ω and the measured n_μ was expected to be lower than the effective index for a corresponding half-buried slow-wave CPS, $n_{\mu\text{-}hb}$. Since the dielectric constant of SiO_2 is less than that of GaAs, the electrodes on sample II were expected to have even higher Z_o's and lower n_μ's than those of the corresponding electrodes on sample I.

For the electrodes having pads, i.e., B1-B5, on average, the change in the microwave effective index, $\Delta n_\mu \equiv n_\mu - 2.6$, was 81% of the target design value, $\Delta n_{\mu\text{-}hb} \equiv n_{\mu\text{-}hb} - 2.6$, for the electrodes on sample I (no SiO_2), i.e., $\Delta n_\mu \sim 0.81\Delta n_{\mu\text{-}hb}$. Also, Δn_μ for an electrode (B1-B5) fabricated on sample II (0.4 μm SiO_2) was about half of that for the corresponding electrode on sample I. Z_o was, on average, about 61 Ω for electrodes on sample I and 65 Ω for electrodes on sample II. In general, the closer the measured Δn_μ was to the design value, the

closer Z_o was to 50 Ω, and, as expected, all measured values of Δn_μ were less than their corresponding design values and all values of Z_o were greater than 50 Ω (we have already published this data in [29], portions are reproduced here with permission, © 1996 IEEE).

Based on these measurements, shown in Tables 3.3.1-3.3.3, new electrodes, generation 1, were designed for generation 1 optical waveguides. Since the electrode loss is a function of the gap between the electrodes, G_{SG}, and the main electrodes' widths, W_S and W_G (see Table 3.3.3 and Figure 3.3.1), we decided to use large electrodes, similar to electrode A5. Figure 3.3.1 gives the loss as a function of the electrode width, $W_S = W_G$, for the electrodes B1-B11 of sample I. It is clear that the larger the electrode width and the larger the gap between the main electrodes, the smaller the loss will be.

The effect of the SiO_2 layer is not expected to be as severe for our generation 1 electrodes as it was for sample II devices here. There are two reasons for this: 1) the SiO_2 layer on generation 1 optical waveguides is only 0.2 µm thick, as opposed to 0.4 µm for sample II here; 2) the ratio of the dimensions of the electrodes, most significantly g_p, to the electrode thickness, $t \sim 1$ µm, is larger for generation 1 electrodes (see Table 3.3.4), hence a higher percentage of the electric field will be confined in the substrate (as opposed to the superstrate, air) for generation 1 electrodes. This will, in turn, give a higher n_μ.

Another factor that is considered in the design of the generation 1 electrodes is the presence of ridges between the pads of the electrodes. This will increase the capacitive effect of the pads and can result in "over-slow" electrodes. On the other hand, the surface deposited electrodes seem to provide only ~80% of the designed slowing of the microwave (see above). So, we decided to use small variations in the electrode structures so that some of the

94

fabricated electrodes have n_μ close to 3.25.

Table 3.3.4 gives the dimensions chosen for the generation 1 electrodes. There are 20 slow-wave electrodes in five categories. Each category consists of four electrodes which differ only in their lengths. This was done to study the effect of the electrode's length on the modulator's performance. There are also 4 conventional, as opposed to slow-wave, coplanar strips on the mask. They were designed to be 50 Ω to be used for calibration when measuring microwave properties of the electrodes.

Later, after the fabrication of generation 1 devices, when the Sonnet™ EM [66] software became available, the electrodes were also modelled using Sonnet™. This was done mostly to investigate the agreement between the Sonnet™ results and the actual measurements since Sonnet™ was going to be used for designing generation 2 devices. In the model, the electrodes were assumed to be infinitely thin and lossless. The substrate was assumed to be lossless as well and to have $\epsilon_r = 13.1$. More details on this modelling and the characteristics of the software can be found in section 3.3.2.1. Table 3.3.5 gives the Sonnet™ results for the five electrode types of Table 3.3.4.

3.3.1.2. Electrode Mask

The mask for slow-wave electrodes contained the 24 structures of Table 3.3.4, located parallel to one another at 1 mm intervals. The electrodes also had 150 μm long connection pads with $W_S = W_G = 120$ μm, and $G_{SG} = 14$μm, at their ends. Similar to the optical waveguide mask, the mask for the electrodes was laid out using Edge™ from Cadence Design System Inc. Compressed forms of the mask files in GDSII format were sent to Precision

Photo Mask Inc., for mask fabrication. The masks were made on quartz substrates using electron-beam lithography. The precision was ±0.2 μm. The mask used for the actual fabrication was a copy of the original and was dark-field, i.e., the patterns defining the electrodes were transparent and the rest of the mask was opaque.

3.3.1.3. Electrode Fabrication

The fabrication of the electrodes was done at UBC using a simple single-step chlorobenzene lift-off process [23], [67], [77]. The fabrication involved the following steps:

1.   To improve adhesion to SiO_2, Shipley's Microposit Primer was spun on the wafers at 4000 rpm for ~15 seconds.

2.   A 5:1 mixture of Shipley's 1400-37 positive photoresist and thinner "A" was spun on the samples at 4000 rpm for 40 seconds.

3.   The photoresist was soft-baked at 70°C for 20 minutes.

4.   After cooling down to room temperature, the electrode patterns were aligned with the ridge waveguides and the photoresist was exposed through the electrode mask, using Karl-Suss MJB3 contact mask aligner. The photoresist was exposed to UV light, $\lambda_o = 320$ nm, for 48 seconds.

5.   The samples were soaked in chlorobenzene for ~ 8 minutes.

6.   The samples were removed from chlorobenzene and were blown dry using nitrogen gas. They were left for about 20 minutes to allow for complete evaporation of the remaining chlorobenzene.

7.   The photoresist was developed in Shipley's MF-319 developer. This process

took about 70 seconds.

8.   1 μm of aluminum (±2%) was evaporated onto the samples using a thermal evaporation system from Carl Herman & Associates Inc., Menlo Park, CA.

9.   The samples were allowed one hour to cool down before being removed from the evaporation chamber.

10.   The samples were immersed in acetone to remove the photoresist and the unwanted metal on it. The acetone was heated up to ~ 50°C to speed up the process. The metal on top of the photoresist peeled off in a few minutes as the photoresist was being dissolved in acetone.

11.   Finally, the samples were cleaned in iso-propanol and blown dry using nitrogen gas.

Again, later in the project, modulators of this kind were also fabricated at the CRC, using the same masks and substrates, but using their fabrication process. Figure 3.2.3 shows SEM micrographs of the fabricated electrodes 5b and 5d, and the associated ridge waveguides.

More electrodes of this type were fabricated on SI-GaAs in order to test the microwave properties of the electrodes up to 40 GHz. More details on the results are given in chapter 4. Also, a comparison of the measured data with those obtained using the Sonnet™ EM software, given in Table 3.3.5, was useful in the next generation of electrode design.

3.3.2. Generation 2

3.3.2.1. Electrode Design

The generation 2 electrodes were designed to be used with generation 2 optical waveguides. Since the effective index for the modes guided by generation 2 optical waveguides was ~ 3.32, at $\lambda_o = 1.55$ µm, see section 3.2.2.1, the target n_μ was chosen to be 3.32. The electrodes were designed using an electromagnetic simulation software, Sonnet™ EM, from Sonnet Software Inc., Liverpool, NY [66]. The software was capable of handling a structure with several dielectric layers having different values of permittivity. However, the presence of ridges could not be incorporated in the model. Also, electrode thickness was assumed to be zero by the software. The software would accept values for electrode resistivity and the loss tangent of the dielectric layers. Nevertheless, we did not use that feature because values for the loss tangent of the epitaxial layers were frequency-dependent and could not be estimated with any reasonable accuracy (mainly due to the limitations in the growth process). Another reason for ignoring losses in the modelling was that the computation time would increase by a factor of 4. The computation for one electrode could take as much as a full day; the inclusion of losses could have increased the total simulation time to several months. Also, from previous measurements, the losses were fairly reasonably known for the electrodes fabricated on SI-GaAs. For those fabricated on AlGaAs/GaAs substrates, we had to try to minimize the epitaxial layer doping to minimize the loss; the inclusion of losses in the model would not give us any significant new information.

The model used by the software consists of a metallic box filled with several dielectric

layers. The layers used in the model, from the bottom to the top, are as follows: 500 μm of

GaAs having $\epsilon_r = 13.1$, 5 μm of AlGaAs having $\epsilon_r = 12.1$, 0.2 μm of SiO_2 having $\epsilon_r = 3.9$,

and 1200 μm of air having $\epsilon_r = 1$. The electrodes, infinitely thin, were between the air and

the silicon dioxide layers. Due to software and hardware limitations, actual length electrodes

could not be simulated. Typically a length equivalent to 7 or 9 times the fin period, d, was

used. Then the calculated line capacitance and inductance per unit length were used to

estimated the microwave index and the characteristic impedance using

$$n_{\mu} = c \sqrt{L C} \qquad (3.3.1)$$

and

$$Z_o = \sqrt{\frac{L}{C}}, \qquad (3.3.2)$$

where L and C represent the line inductance per unit length and the line capacitance per unit

length, respectively, (these equations are more accurate at high frequencies, typically > 2

GHz, see [57]).

Over one hundred electrodes were modelled. Ideally, the electrodes should give an

$n_{\mu} = 3.32$ and $Z_o = 50$ Ω; these values correspond to $L = 553$ pH/mm and $C = 221$ fF/mm.

The electrodes were designed for various values of L and C close to these values. There were

several reasons for choosing to have this scatter in the design values (the values calculated

using Sonnet™ software and the above model); four of the more important reasons are as

follows:

a.   the material parameters and dielectric constants used in the model were not

necessarily the same as those of the fabricated substrate;

b.   The model ignored the effect of the electrodes' thickness and the presence of ridges;

c.   Inevitably, there would be variations and imperfections in the dimensions of the fabricated electrodes due to fabrication tolerances;

d.   Software limitations, e.g., the number of grid points used.

Problems a, c, and d were addressed by statistics: slightly different design values were chosen for various electrodes, so that some of them would be very close to the target values. Problem b was addressed in more detail. The presence of ridges between the pads would increase the capacitive effect of the pads, i.e., C would be higher than the value obtained from the model. Measurements on previously fabricated devices indicated that the actual C is typically $\sim 7 \%$ larger than the value estimated by Sonnet^{TM}. To compensate for this, for those modulators that have ridge waveguides between the pads, e.g., PC-A and PC-B types, typically, a lower value (< 221 fF/mm) was chosen as the target C. For the modulators that have ridges underneath the pads, the effect is not expected to be as strong as it is for the above case; nevertheless, the capacitance due to the pads is still expected to be larger than the value for the case where the ridges are not present. Therefore, again, target values lower than 221 fF/mm are required. Table 3.3.6 contains the dimensions for the 13 electrodes chosen (electrodes 25 to 37, see Table 3.2.1). Table 3.3.7 contains the values of L and C, calculated using Sonnet^{TM}, and the values of n_μ and Z_o, using equation (3.3.1) and (3.3.2), for the structures of Table 3.3.6. The simulations were done for a 5 GHz signal.

Another factor that affected the design of these electrodes was the ratio l_p/d, which we call the duty cycle, τ. To have a low half-wave voltage, i.e., to make efficient use of the available microwave power, a large duty cycle is preferred. On the other hand, a large τ can

result in a C that is too large; in other words, a large duty cycle can result in "over-slowing" of the microwave signal. This is a more significant problem with interdigitated and/or CPW type electrodes where more fins and pads are present per unit length of the electrode, as compared to regular slow-wave CPS electrodes, see section 2.3. Here, for our MZ modulators, devices 30, 31, 35, and 36, which use either CPW or interdigitated CPS electrodes, the design is admittedly expected to result in over-slow electrodes. Nevertheless, in order to get smaller half-wave voltages, we chose not to reduce the duty cycle. Also, there were several more MZ type devices fabricated amongst the first 24 devices chosen by the CRC group, and some of those devices had lower duty cycles. In practice, if the duty cycle is kept constant and l_p and d are increased, the capacitance per unit length decreases (partially because there are fewer fins per unit length). On the other hand, for our slow-wave model to work well, the pad dimensions have to be quite a bit smaller than the microwave wavelength. Consequently, even for large values of τ, there should be an optimum length for the pad where both the line capacitance is sufficiently low and the pad length is small compared to the wavelength. Obviously, this optimum length depends upon the maximum modulation frequency expected using that particular electrode. We have not attempted to find and incorporate that optimum length into our devices yet. However, for devices working below 100 GHz, we know that we can use pads that are at least twice the size of the ones used here with duty cycles close to 0.9.

3.3.2.2. Electrode Mask

Again, similar to the mask designed for generation 2 optical waveguides, we had 37

devices on the mask. Electrode dimensions for devices 25 to 37 are given in Tables 3.3.6. The new mask, for generation 2 electrodes, was laid down at the CRC, and was fabricated at Nortel Technologies Inc.

3.3.2.3. Electrode Fabrication

Several samples of the electrodes were fabricated on SI-GaAs at the CRC. They were tested for their microwave properties up to 40 GHz (see Chapter 4). Finally, the modulators, including both optical waveguides and slow-wave electrodes, were fabricated at the CRC clean-room facility in Ottawa. Figure 3.2.7 shows SEM micrographs of a number of generation 2 modulators. Figure 3.3.2 shows the plan view pictures of some of the modulators fabricated.

Table 3.3.1. The measured n_μ for some slow-wave electrodes. For these devices $G_{SG} = 60$ µm, $g_p = 4$ µm, $l_f = 4$ µm, $L = 1.5$ cm, and electrode thickness $t = 1.1$ µm.

Electrode #	$W_S = W_G$ (µm)	w_f (µm)	w_p (µm)	l_p (µm)	d (µm)	n_μ 20 GHz [23]	n_μ at 40 GHz
A1	72	28	0	0	18	3.33	3.27
A2	110	28	0	0	32	3.03	3.02
A3	110	21	7	8	32	3.17	3.16
A4	110	21	7	12	32	3.30	3.29
A5	110	21	7	16	32	3.38	3.40
A6	110	14	14	8	32	3.18	3.15
A7	110	14	14	12	32	3.32	3.24
A8	110	14	14	16	32	3.43	3.39

Table 3.3.2. Electrode dimensions for some slow-wave electrodes. For these devices $g_p =$ 2 µm, $l_f = 1.5$ µm, and electrode thickness $t = 1$ µm (aluminum electrodes). These electrodes were designed to be used in MZ-A-CPS type modulators (see section 2.3).

Electrode #	L (mm)	$W_S = W_G$ (µm)	G_{SG} (µm)	w_f (µm)	w_p (µm)	l_p (µm)	d (µm)
B1	22.0	65.5	17	4	3.5	6	25
B2	23.2	43.25	13	3	2.5	5	19
B3	22.0	29.5	17	4	3.5	6	12.5
B4	23.2	26	13	3	2.5	5	12
B5	23.2	18	13	3	2.5	5	9.5
B6	22.0	53	17	7.5	0	0	14
B7	23.2	33.5	13	5.5	0	0	11
B8	22.0	29.75	17	7.5	0	0	9
B9	22.0	19.5	17	7.5	0	0	7
B10	23.2	17.5	13	5.5	0	0	7
B11	23.2	10.75	13	5.5	0	0	5.75

Table 3.3.3. Microwave parameters measured for the devices of Table 3.3.2 at 40 GHz. Samlpe I electrodes are surface deposited on a SI-GaAs substrate. Sample II includes a 0.4 μm thick SiO$_2$ layer between the electrodes and the SI-GaAs substrate. The target (design) value of n_μ is for half-buried, lossless, electrodes on SI-GaAs.

Electrode #	Target n_μ	Sample I (without SiO$_2$)			Sample II (with 0.4 μm of SiO$_2$)		
		n_μ	α (Np/cm)	Z_o (Ω)	n_μ	α (Np/cm)	Z_o (Ω)
B1	3.00	2.96	0.47	57	2.81	0.45	58
B2	3.00	2.94	0.60	59	2.78	0.59	60
B3	3.43	3.25	0.69	62	3.00	0.69	65
B4	3.24	3.11	0.73	62	2.92	0.88	70
B5	3.43	3.25	0.94	65	2.96	0.89	70
B6	3.00	2.91	0.49	60	2.77	0.48	61
B7	3.00	2.90	0.65	67	2.74	0.64	65
B8	3.24	3.05	0.62	65	2.85	0.59	67
B9	3.43	3.16	0.76	69	2.91	0.79	74
B10	3.24	3.06	0.84	69	2.83	0.86	73
B11	3.43	3.16	1.12	77	2.87	1.06	81

Table 3.3.4. Electrode dimensions for generation 1 devices. For these devices $W_S = W_G$.

Elect. #	L (mm)	W_S (μm)	G_{SG} (μm)	g_p (μm)	w_f (μm)	w_p (μm)	l_f (μm)	l_p (μm)	d (μm)
1a	2.5	110	60	4	21	7	4	16	32
1b	5	110	60	4	21	7	4	16	32
1c	10	110	60	4	21	7	4	16	32
1d	20	110	60	4	21	7	4	16	32
2a	2.5	110	60	4	14	14	4	16	32
2b	5	110	60	4	14	14	4	16	32
2c	10	110	60	4	14	14	4	16	32
2d	20	110	60	4	14	14	4	16	32
3a	2.5	110	60	6	13	14	4	15	30
3b	5	110	60	6	13	14	4	15	30
3c	10	110	60	6	13	14	4	15	30
3d	20	110	60	6	13	14	4	15	30
4a	2.5	82	34	4	8	7	3	14	30
4b	5	82	34	4	8	7	3	14	30
4c	10	82	34	4	8	7	3	14	30
4d	20	82	34	4	8	7	3	14	30
5a	2.5	80	35	5	10	5	4	15	30
5b	5	80	35	5	10	5	4	15	30
5c	10	80	35	5	10	5	4	15	30
5d	20	80	35	5	10	5	4	15	30
6a	2.5	120	14	-	-	-	-	-	-
6b	5	120	14	-	-	-	-	-	-
6c	10	120	14	-	-	-	-	-	-
6d	20	120	14	-	-	-	-	-	-

Table 3.3.5. Estimated microwave index and characteristic impedance for the five slow-wave electrode types of Table 3.3.4. Electrode and dielectric losses are assumed to be zero.

Electrode #	Without SiO$_2$		With 0.2 μm of SiO$_2$, $\epsilon_r = 3.9$	
	n_μ	Z_o (Ω)	n_μ	Z_o (Ω)
1	3.39	53.4	3.27	55.6
2	3.68	52.1	3.58	53.7
3	3.60	51.6	3.51	53
4	3.31	54.3	Was not done	
5	3.28	55.9	Was not done	

Table 3.3.6. Electrode dimensions for generation 2 modulators.

Elect. #	L (mm)	W_S (µm)	W_G (µm)	G_{SG} (µm)	g_p (µm)	w_f (µm)	w_p (µm)	l_f (µm)	l_p (µm)	d (µm)
25	15	145	145	60	4	24	4	4	24	32
26	15	120	120	60	4	26	2	4	40	48
27	15	140	140	60	4	24	4	4	36	48
28	15	140	140	60	4	24	4	4	40	48
29	15	144	144	60	6	21	6	4	40	48
30	10	150	150	60	6	52	2	2	30	48
31	10	128	128	48	6	40	2	2	26	48
32	15	128	128	48	6	40	2	2	26	54
33	15	100	100	35	5	10	5	4	15	30
34	15	100	100	48	4	18	4	4	36	40
35	10	40	70	58	6	22	4	4	34	48
36	10	34	65	55	5	21	4	3	45	54
37	10	34	66	57	5	24	2	2	48	64

Table 3.3.7. Device types and microwave parameters calculated using Sonnet™ software for generation 2 electrodes of Table 3.3.6.

Device #	Modulator Type	L (pH/mm)	C (fF/mm)	n_μ	Z_o (Ω)
25	PC-A-CPS	567	241	3.50	48.6
26	PC-A-CPS	613	192	3.25	56.5
27	PC-A-CPS	574	208	3.28	52.6
28	PC-A-CPS	574	213	3.32	51.9
29	PC-A-CPS	567	214	3.30	51.5
30	MZ-C-CPS	557	244	3.50	47.8
31	MZ-C-CPS	569	219	3.35	51.0
32	PC-C-CPS	569	207	3.25	52.5
33	PC-A-CPS	576	208	3.29	52.6
34	PC-A-CPS	622	204	3.38	55.2
35	MZ-B-CPW	578	237	3.51	49.4
36	MZ-B-CPW	595	246	3.63	49.2
37	PC-A-CPW	602	212	3.39	53.3
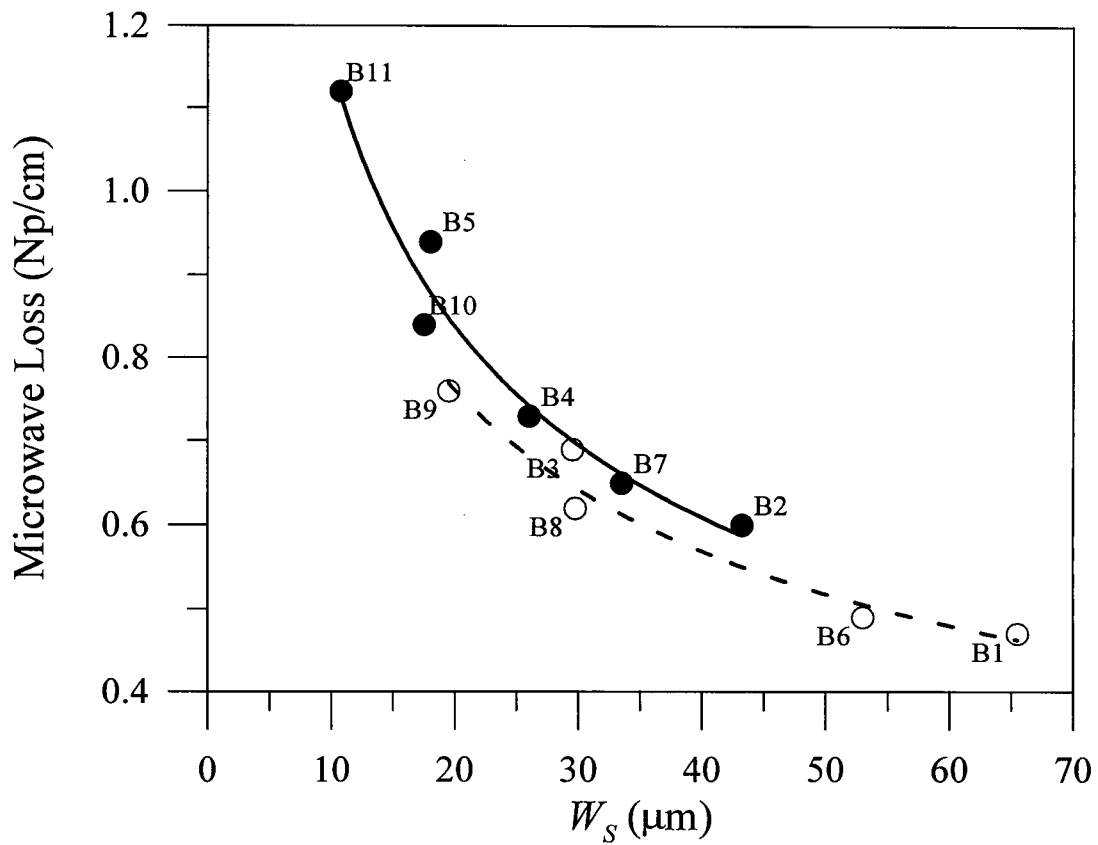
Figure 3.3.1. Measured microwave loss as a function of electrode width, $W_S = W_G$, for the electrodes of Table 3.3.2. The solid curve is a fit to the data shown by the solid dots having $G_{SG} = 13$ μm. The dashed curve is a fit to the data shown by the hollow dots having $G_{SG} = 17$ μm
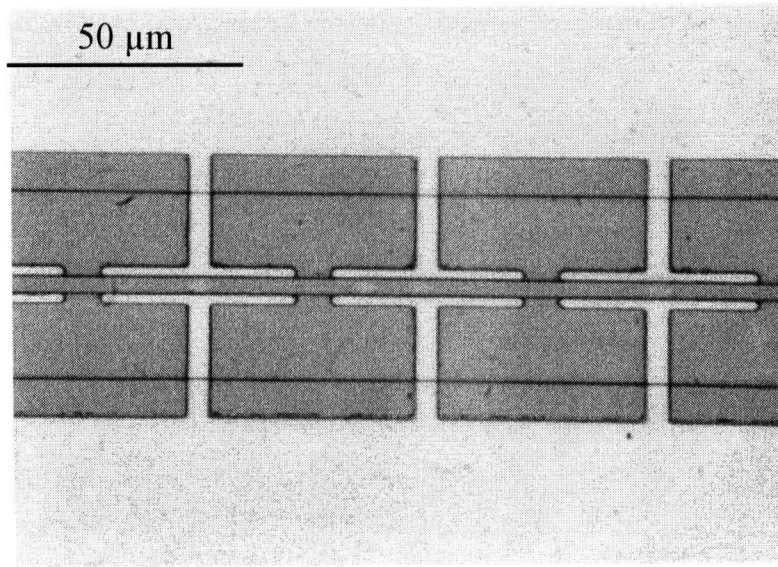
(a)
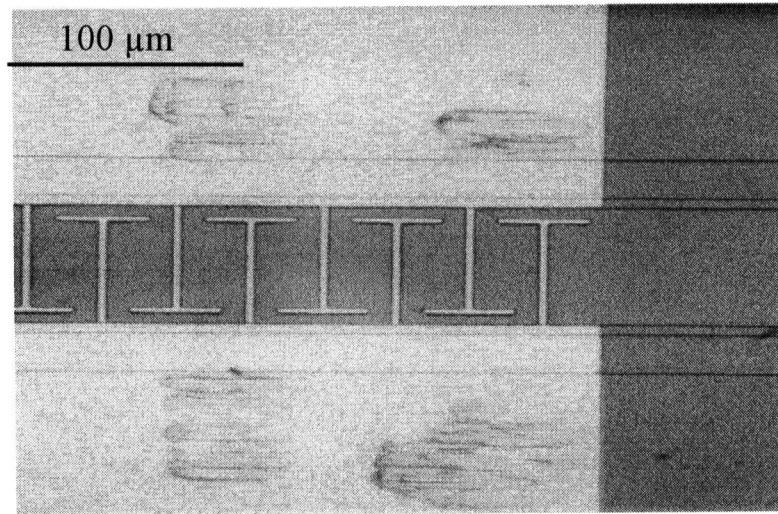
(b)

Figure 3.3.2. Plan view pictures of the generation 2 devices (a) 26, (b) 30, (c) 36, and (d) 37 fabricated on the NortelTech AlGaAs/GaAs substrate.

(c)

(d)

112
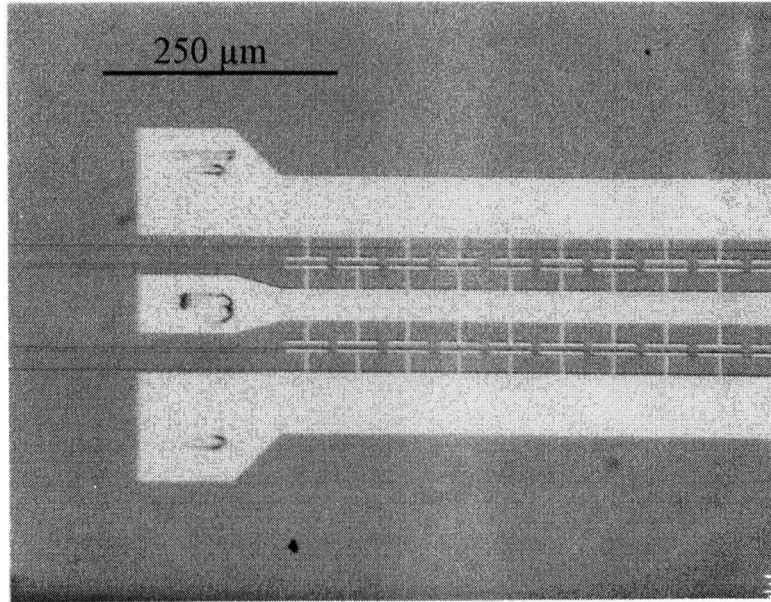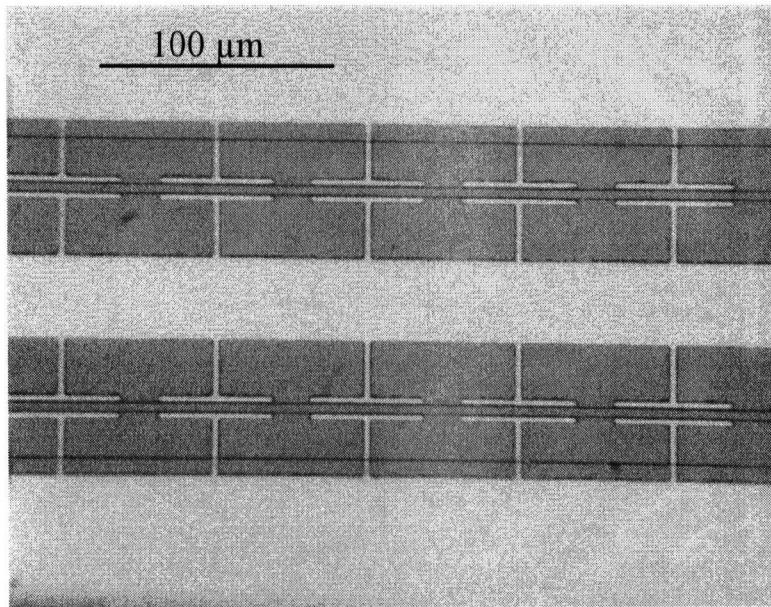
Chapter 4. Results

4.1. Introduction

The results of the experimental measurements on the fabricated devices are given in this chapter. These measurements are presented in two categories: 1) electrical (microwave) measurements on the electrodes, and 2) optical measurements on the modulators. The electrical measurements on the electrodes were performed first to investigate whether low-loss, velocity-matched electrodes could be achieved. These electrical measurements are presented for three electrode masks: 1) those designed by Lee and Tsou [67], 2) generation 1 electrodes, and 3) generation 2 electrodes. Various measurements and modelling results are compared. Optical measurements are divided into two groups: 1) low frequency and 2) high frequency measurements. Results for both Mach-Zehnders and mode converters are reported.

4.2. Microwave Characteristics of the Electrodes

4.2.1. Electrodes Designed by Lee and Tsou

As mentioned in chapter 3, several slow-wave CPS electrodes that were designed by Lee and Tsou [67] were fabricated and tested, and the results were used in designing new electrode structures, see section 3.3.1.1. Some of the measurements were reported in that section so that they could be used in the design of the next generation of devices. Here some additional information is presented.

In chapter 2, we claimed that the inclusion of fins and pads increases the line capacitance more than it affects the line inductance, and, therefore, microwave slowing is obtained. In order to illustrate this experimentally, we calculated the effects of the fins and pads from the measurements done on the electrodes of Table 3.3.2. Equations (3.3.1) and (3.3.2) result in the following relationships:

$$\frac{n_{sw}}{n_{con}} = \sqrt{\frac{L_{sw}}{L_{con}}} \times \sqrt{\frac{C_{sw}}{C_{con}}} \qquad (4.2.1)$$

and

$$\frac{Z_{sw}}{Z_{con}} = \sqrt{\frac{L_{sw}}{L_{con}}} \times \sqrt{\frac{C_{con}}{C_{sw}}}, \qquad (4.2.2)$$

where C_{con} and L_{con} are the calculated [78] line capacitance and inductance for surface deposited "conventional" CPS electrodes having the same dimensions as our electrodes but without the capacitive elements. n_{con} and Z_{con} are the calculated microwave index and the characteristic impedance for the conventional CPS electrodes on SI-GaAs (no SiO_2). sw-suffixes indicate the corresponding values for the "slow-wave" CPS electrodes. Using these equations, the changes in the line capacitance and the line inductance, effected by the capacitive elements, can be obtained from the measured values of n_{sw} (n_μ) and Z_{sw} (Z_o). Table 4.2.1 contains the calculated values of n_{sw}/n_{con}, Z_{sw}/Z_{con}, C_{sw}/C_{con} - 1, and L_{con}/L_{sw} - 1 for the electrodes of Table 3.3.2. As expected the increase in the line capacitance is substantially larger than the corresponding decrease in the line inductance for each of the electrodes. Table 4.2.1 illustrates the effectiveness of our approach toward obtaining slow-wave electrodes for use in compound semiconductor based electro-optic modulators.

More measurements on these devices are already reported in section 3.3.1.1. One point that is worth re-emphasis is the effect of the electrode dimensions on the microwave loss of the electrodes, as illustrated in Figure 3.3.1. The larger the interelectrode gap, G_{SG}, is and the wider the main electrodes, W_S and W_G, are, the lower the loss is.

4.2.2. Generation 1 Electrodes

Several samples were fabricated using the mask for generation 1 electrodes. Two samples one having gold and one having aluminum electrodes were fabricated on SI-GaAs in order to examine the effect of the electrode material on the microwave loss. Generation 1 electrodes were also fabricated on generation 1 AlGaAs/GaAs substrates. The following sections contain the results of the measurements.

4.2.2.1. Slow-Wave Electrodes on SI-GaAs

Two semi-insulating GaAs substrates were used for the fabrication of the electrodes. One sample had aluminum electrodes and the other one had gold (or more precisely, 0.125 μm Ti, 0.04 μm Pd, and 1 μm Au) electrodes. The electrodes on both samples were thermally evaporated, were nominally 1 μm thick, and were patterned using the generation 1 electrode mask. No SiO_2 layer was present underneath the electrodes. Table 4.2.2 provides the results of the microwave measurements on these electrodes. The measurements were done from 100 MHz to 40 GHz using an HP 8510C network analyzer together with an HP 8516A S-parameter test set and an HP8340 synthesized sweeper. The microwave probes used were WPH-101-152 ground-signal (GS) and WPH-102-152 signal-ground (SG) probes

115

from Cascade™ Microtech Inc., Beaverton, Oregon. The pitch between the probe tips was 150 μm. The probes were designed for operation up to 26 GHz, but we wanted to make the measurements at even higher frequencies, up to 40 GHz. Since there were no other GS or SG probes available, we used these electrodes in our measurements. The electrodes were calibrated on an Impedance Standard Substrate, SN20-47-005-016, from Cascade™ Microtech, Inc. The calibration was repeated several times until the measured reflection S-parameters, s_{11} and s_{22}, on a 50 Ω coplanar strip line were less than -15 dB over the entire frequency range, up to 40 GHz. This would imply that measurements done using these electrodes and this calibration would be reasonably accurate in this frequency range. Typically, the reflection S-parameters were low at low frequencies and were close to -15 dB at frequencies above 25 GHz.

The microwave line parameters, Z_o, α, and n_μ were calculated from the measured S-parameters using the following equations, see [76] and [57]:

$$Z_o = Z_{oR} \frac{(1+s_{11})(1+s_{22}) - s_{12}s_{21}}{s_{22} - s_{11} \pm \sqrt{(1 + s_{12}s_{21} - s_{11}s_{22})^2 - 4s_{21}}} , \qquad (4.2.3)$$

$$\alpha + j\beta = \frac{1}{L} \ln \left(\frac{1 + s_{12}s_{21} - s_{11}s_{22}}{2\,s_{21}} \pm \sqrt{\left(\frac{1 + s_{12}s_{21} - s_{11}s_{22}}{2\,s_{21}} \right)^2 - 1} \right) , \qquad (4.2.4)$$

and
$$n_\mu = \frac{c\,\beta}{2\,\pi f} , \qquad (4.2.5)$$

116

where Z_{oR} is the impedance reference (= 50 Ω here), L is the length of the electrode, α is the attenuation coefficient (in Np/cm if L is in cm), β is the microwave propagation constant, c is the speed of light in vacuum, and f is the frequency of the microwave signal. For equation (4.2.3) the solution for which Re$\{Z_o\}$ is positive is chosen and, similarly, for (4.2.4), the solution giving a positive α is chosen. Figures 4.2.1 to 4.2.9 show n_μ, α, and Z_o as functions of frequency, up to 40 GHz, for several of the electrodes in Table 4.2.2.

The first fact to point out in Table 4.2.2 is that the electrodes having fins and pads are in fact slow-wave electrodes. Also, on average, there is no significant difference between the aluminum electrodes and the gold ones; the microwave losses of the gold electrodes are very slightly lower than those of the aluminum ones. Considering the possible variations in the device fabrication and the measurements, all three parameters, n_μ, α, and Z_o, are practically the same for both aluminum and gold electrodes. Average n_μ, α at 40 GHz, and Z_o, are 3.30, 0.40 Np/cm, and 58 Ω, respectively, for the slow-wave electrodes.

n_μ and Z_o are, again on average, 0.2 less and 4 Ω larger than the values estimated using Sonnet^{TM}. These differences are even higher for the longer electrodes, the ones that are of interest to us. The differences between the Sonnet^{TM} values and the measured ones are mostly due to the fabrication limitations and variations. Apparently, Sonnet^{TM} over-estimates the capacitive effect of the fins and pads, or perhaps more accurately said, the fins and pads fabricated do not contribute to the line capacitance as much as estimated by the software. This difference between the theoretical and measured results is larger for those electrodes which have wide pads, i.e., those having larger w_p / l_p ratios, such as electrodes 2a-3d (also see section 4.2.3).

117

These measurements also show that longer electrodes have lower n_μ. In our theory and design, we have implicitly assumed that electrode length does not affect the amount of microwave slowing (infinitely long electrodes were assumed). This is expected to be a fair assumption as long as the electrode length is much longer than the coplanar structure's width, $W = W_G + W_S + G_{SG}$. The data in Table 4.2.2 support this statement. For short, 2.5 mm long, electrodes where $W \sim 0.1\ L$, n_μ is distinctly larger than that for the longer ones. In fact, n_μ changes appreciably as a function of length for short electrodes. For long, 1 and 2 cm long, electrodes, on the other hand, n_μ does not change significantly with length. Since the electrodes of interest to us are the longer ones, it is fair to assume that microwave slowing would be relatively independent of the electrodes' length. Note that the above statement about the relationship between n_μ and L is also correct for the conventional CPS electrodes 6a-6d.

Another fact to take a note of for these electrodes is that the electrode loss is quite small, and, therefore, the bandwidth of a modulator using these electrodes could be very large. For example, assuming that loss is dependent on the square root of frequency (see equation 2.2.12), a modulator having 2 cm long, velocity-matched electrodes with a loss of 0.4 Np/cm measured at 40 GHz, would have an optical 3-dB bandwidth of about 160 GHz. The average α for the long, 1 and 2 cm long, slow-wave electrodes of Table 4.2.2 is 0.36 Np/cm at 40 GHz which allows for even wider bandwidths, $\sim$ 200 GHz for a 2-cm long velocity-matched device.

118

4.2.2.2. Slow-Wave Electrodes on Generation 1 AlGaAs/GaAs Substrates

Generation 1 modulators, having gold electrodes, were fabricated on Spire AlGaAs/GaAs substrates as mentioned in chapter 3. On these devices, both ridges and 0.2 μm of SiO$_2$ were present. Table 4.2.3 gives the results of the microwave measurements on these devices. The same set-up as the one described in section 4.2.2.1 was used for the measurements. As mentioned in chapter 3, the microwave losses were extremely high. The high loss is due to the high level of unintentional doping of the AlGaAs layer. Such high losses render these particular samples essentially useless for modulation at high frequencies (hence, these devices were not used for high-speed optical modulation). It should also be noted that since the measured transmission S-parameters, s_{12} and s_{21}, are quite small here, the errors in the calculation of n_μ's and Z_o's in Table 4.2.3 using equations (4.2.3)-(4.2.5) may be quite large. Figure 4.2.10 shows n_μ, α, and Z_o as functions of frequency for device 2c of Table 4.2.3. These measurements, nonetheless, constituted an important step in our eventual success in fabricating high-speed modulators in that they clearly illustrated the importance of controlling the amount of unintentional doping in the AlGaAs layers. Our collaborators at the CRC have studied this effect in more detail [75] leading to the fabrication of the low-loss, epitaxial substrate needed for such high-speed electro-optic modulators, see section 3.2.2.

4.2.3. Generation 2 Electrodes

Again, several samples were fabricated using the mask for generation 2 electrodes. Four samples were fabricated with and without an SiO$_2$ layer and with and without ridges on SI-GaAs substrates to investigate the effects of the SiO$_2$ layer and the ridges on the slowing

of the microwave signal. These electrodes were also fabricated on generation 2 AlGaAs/GaAs substrates containing optical ridge waveguides. The resulting modulators were tested for both the microwave properties of the electrodes, presented here, and the optical modulation of light, presented in section 4.3.

4.2.3.1. Slow-Wave Electrodes on SI-GaAs

A number of samples were fabricated on SI-GaAs. The electrodes were all Ti/Pt/Au (0.2 μm/0.3 μm/1 μm) electrodes and were patterned using the generation 2 mask. Four samples in particular were prepared in order to investigate the effects of the SiO_2 buffer layer and the ridges near the pads. The following names were used for these four sample:

a. NrNs: for the sample with **n**o **r**idges and **n**o **S**iO_2 layer;

b. NrWs: for the sample with **n**o **r**idges but **w**ith a **S**iO_2 layer;

c. WrNs: for the sample **w**ith **r**idges but with **n**o **S**iO_2 layer;

d. WrWs: for the sample **w**ith **r**idges and **w**ith a **S**iO_2 layer.

The measured microwave parameters for the electrodes fabricated on samples NrNs, NrWs, and WrNs are given in Table 4.2.4. That portion of the sample WrWs that contained devices 25 to 37, those designed by us at UBC, was broken during fabrication at the CRC (for additional information on devices with both ridges and an SiO_2 layer, one may refer to the measurements done on the devices fabricated on the AlGaAs/GaAs substrate, see the following section, 4.2.3.2). The electrode dimensions, device types, and the Sonnet^{TM} simulation results for these devices are given in Tables 3.3.6 and 3.3.7.

Let us first compare the samples NrNs and NrWs. Devices 26 and 33 are excluded in this comparison because they were damaged when being fabricated on NrWs. Excluding these two devices, the average values of n_μ, α, and Z_o for the electrodes on NrNs are 3.65, 0.24 Np/cm, and 48.3 Ω, respectively. The corresponding values for the electrodes on NrWs are 3.53, 0.28 Np/cm, and 49.7 Ω, respectively. In other words, for the electrodes on NrNs, n_μ is 0.12 larger and Z_o is ~1.5 Ω less than those for electrodes on NrWs. This means that the inclusion of the 0.2 μm thick SiO_2 layer has increased, as expected, the speed of microwave signal by decreasing the effective capacitance of the electrodes. However, this reduction in the microwave slowing is significantly smaller than it was for the electrodes on the sample II of Table 3.3.3 reported in chapter 3. There are two major reasons for this difference: 1) here the ratio of the electrodes' planar dimensions to their thickness, 1.5 μm, is larger, and 2) here the thickness of the SiO_2 layer is half of that for Sample II of Table 3.3.3.

The effects of ridges can also be explained here. Note that we could not include ridges in the Sonnet™ model and we, therefore, needed to investigate these experimentally. Electrodes are divided into two groups for the purpose of the comparison between the "ridged" (the ones having ridges on the substrate) and "non-ridged" (the ones having no ridges on the substrate) electrodes: 1) the electrodes that have ridges "between" the pads, i.e., electrodes 25-29, 32-34, and 37, which are all intended to be used for polarization converters, and 2) the electrodes that have ridges "underneath" the electrodes or pads, i.e., electrodes 30, 31, 35, and 36, which are to be used for MZ modulators. For the first category the inclusion of a ridge is expected to increase the capacitance of the pads, and, therefore, to increase n_μ and to decrease Z_o. The experimental results confirm this hypothesis: for the electrodes on

121

WrNs n_μ and Z_o are, on average, 0.11 larger and 1.5 Ω less, respectively, as compared to the values measured for the electrodes on NrNs. Also, again as expected, the larger the duty cycle, l_p / d, is and the smaller the gap between the pads, g_p, is the larger this extra capacitance will be. For the electrodes that have ridges underneath them, group 2 (MZ type ones), the effect of the ridges is not expected to be significant and our measurements in Table 4.2.4 confirm this statement.

Unfortunately, sample WrWs broke and we cannot provide a good comparison between NrNs devices and WrWs ones. It is, however, desired to know the collective effect of the presence of ridges and SiO_2. Let us divide these electrodes into two groups again; for group 2 (MZ type) electrodes, as mentioned above, the ridges can effectively be ignored; therefore, only the effect of the SiO_2 buffer layer is present. For group 1 electrodes, where the ridges are located between the pads, on the other hand, the issue is more complicated. The effects of the inclusion of the ridges and the presence of the SiO_2 layer seem to be equal in magnitude and opposite in sign, as explained above. Therefore, at first glance, it may be expected that devices on WrWs have about the same n_μ's and Z_o's as the ones on NrNs do. However, if we look into the structure for WrWs devices, we realize that the effect of the ridges is not as strong here as it is for WrNs devices. Let us remember that the ridge height is 0.9 μm, the electrode thickness is 1.5 μm, and the SiO_2 layer thickness is 0.2 μm. The ridge between the pads of the electrodes on WrNs is effectively a 0.9 μm thick layer of SI-GaAs whereas for WrWs structures, the ridge consists of a 0.7 μm thick layer of SI-GaAs followed by a 0.2 μm thick layer of SiO_2, which has a significantly lower dielectric constant as compared to SI-GaAs. Therefore, the capacitive effect of the pads is less for WrWs

devices. To summarize, group 1 electrodes fabricated on WrWs would have microwave properties only slightly different from those fabricated on NrNs, and they (WrWs electrodes) would be closer in performance to the NrWs devices than to the WrNs devices.

Figures 4.2.11 to 4.2.20 show n_μ, α, and Z_o as functions of frequency for a number of electrodes of Table 4.2.4. It can be seen from the plots of the microwave loss that the measured loss fluctuates up to 0.1 Np/cm for some CPS electrodes, especially at higher frequencies, mainly due to the quality of the probes used. Therefore, the values of α at 40 GHz given in the above tables are not accurate indications of the relative loss of a particular electrode as compared to another one. It should also be noted that the set-up used for the microwave measurements presented in this section was similar to that described in section 4.2.2.1. The only difference was that for CPW electrodes, electrodes 35-37, ground-signal-ground Pico-probes model 40A-GSG-150-C from GGB Industries Inc., Naples, FL, were used. These probes were specified for operation up to 40 GHz and were in a much better condition (almost new) than the GS and SG Cascade probes used on CPS electrodes were. That is, in part, why the plots for CPW electrodes are smoother than those for CPS electrodes.

Another point to notice here is that electrode 33 on NrNs is very similar in its dimensions, to electrodes 5 (5c and 5d) of Tables 3.3.4 and 4.2.2. They only differ in their lengths, the electrodes' thicknesses, and most significantly in the main electrodes' widths, W_S and W_G; wider electrodes are used here (device NrNs-33) to reduce the characteristic impedance of the electrodes.

4.2.3.2. Slow-Wave Electrodes on Generation 2 AlGaAs/GaAs Substrates

Generation 2 modulators, having gold electrodes, were fabricated on NortelTech AlGaAs/GaAs substrates as mentioned in chapter 3. On these devices, both ridges and 0.2 μm of SiO_2 were present. Table 4.2.5 provides the results of the microwave measurements on the electrodes. The same set-up as the one described in sections 4.2.2.1 and 4.2.3.1 was used for the measurements. Electrodes 25 and 28 were broken and were not included in the comparison between the measured and the Sonnet^{TM} data. The measurements were done twice, and the data presented in Table 4.2.5 are the average of the two measurements.

Figures 2.4.21 to 2.4.26 show n_μ, α, and Z_o as functions of frequency for a number of electrodes of Table 4.2.5. As mentioned in chapter 3, the substrate had a low unintentional doping in its epitaxial layers; therefore, the electrode losses were reasonably low, and the modulators could be used for both electrical and optical measurements. Microwave losses were on average 0.17 Np/cm larger than those for the electrodes fabricated on SI-GaAs substrates (Table 4.2.4). This additional loss is due to the AlGaAs layer. The average loss for these electrodes at 40 GHz is still quite low, about 0.41 Np/cm, which allows for an optical 3-dB bandwidth well in excess of 150 GHz (assuming perfect microwave-to-lightwave velocity match), see equation (2.2.14).

The microwave index, n_μ, and the characteristic impedance, Z_o, for polarization converter type devices on this AlGaAs/GaAs substrate are very close to the values of n_μ and Z_o for the electrodes fabricated on the SI-GaAs substrates. As anticipated in the previous section, the values of n_μ and Z_o are very close to those for NrNs electrodes. Here n_μ is, on average, only 0.04 smaller than that for the electrodes fabricated on SI-GaAs without any

ridges or SiO$_2$ layers (NrNs). For MZ type devices, on the other hand, the measured n_μ and Z_o are very close to those for the electrodes fabricated on the SI-GaAs having the SiO$_2$ buffer layer (NrWs). This is, again, in agreement with the predictions in the previous section.

These measurements show that the values estimated for n_μ using Sonnet^{TM} are, on average, 0.15 lower than those measured. If we exclude device 33, this number would be even larger, 0.19. It appears that for narrow pads with large duty cycles, Sonnet^{TM} underestimates the slowing effect of the capacitive elements, and for wider pads with smaller duty cycles, Sonnet^{TM} overestimates this effect (also see Table 4.2.2).

Over all, the electrodes fabricated are generally "over-slow"; i.e., the microwave signal is slowed more than was needed to obtain the desired n_μ. The effective optical refractive index, n_{eff}, for a guided mode in the ridge waveguides is 3.32 and the average n_μ is 3.53. Excluding device 33, the average n_μ for the PC-A-CPS type devices is 3.42 which is quite close to n_{eff}. This would allow for these 1.5 cm long devices to have bandwidths in excess of 120 GHz if we ignore the loss, and a bandwidth of 85 GHz if we use $\alpha_o = 0.063$ Np/cm/GHz$^{1/2}$, see section 2.2 (this value of α_o is obtained from an $\alpha = 0.4$ Np/cm at 40 GHz). Other devices, which have higher n_μ's, may have smaller bandwidths. Nevertheless, all the data presented in this chapter collectively indicate that ultra wide-band modulators having bandwidths well in excess of 100 GHz can be achieved using low-loss, slow-wave electrodes of the types presented here.

Table 4.2.1. Comparison between the line capacitance and the line inductance per unit length for conventional, surface deposited, CPS electrodes and those of the slow-wave electrodes of Table 3.3.2. Reprinted from [30] with permission, © 1995 IEEE.

Electrode #	n_{sw} / n_{con}	Z_{sw} / Z_{con}	$C_{sw} / C_{con} - 1$	$L_{con} / L_{sw} - 1$
B1	1.14	0.84	0.36	0.04
B2	1.14	0.82	0.39	0.07
B3	1.26	0.72	0.76	0.11
B4	1.21	0.74	0.64	0.12
B5	1.27	0.69	0.83	0.15
B6	1.12	0.83	0.35	0.07
B7	1.12	0.86	0.30	0.03
B8	1.18	0.76	0.55	0.11
B9	1.23	0.71	0.73	0.15
B10	1.19	0.73	0.64	0.16
B11	1.23	0.69	0.80	0.18

Table 4.2.2. Microwave parameters measured for generation 1 gold and generation 1 aluminum electrodes on SI-GaAs, up to 40 GHz. The values of n_μ and Z_o are the average values over the frequency range 5 to 40 GHz. α is the value measured at 40 GHz.

Elect. #	L (mm)	Aluminum			Gold			Sonnet™	
		Z_o (Ω)	n_μ	α (Np/cm)	Z_o (Ω)	n_μ	α (Np/cm)	n_μ	Z_o (Ω)
1a	2.5	57	3.46	0.39	56	3.51	0.39	3.39	53.4
1b	5	58	3.38	0.39	57	3.39	0.40	3.39	53.4
1c	10	59	3.34	0.40	58	3.34	0.40	3.39	53.4
1d	20	Broken			58	3.31	0.24	3.39	53.4
2a	2.5	56	3.51	0.42	56	3.51	0.48	3.68	52.1
2b	5	56	3.43	0.40	56	3.41	0.40	3.68	52.1
2c	10	58	3.38	0.44	58	3.36	0.44	3.68	52.1
2d	20	58	3.33	0.34	57	3.36	0.28	3.68	52.1
3a	2.5	58	3.42	0.43	58	3.40	0.45	3.60	51.6
3b	5	58	3.27	0.31	58	3.32	0.36	3.60	51.6
3c	10	Broken			58	3.29	0.36	3.60	51.6
3d	20	60	3.27	0.32	58	3.28	0.26	3.60	51.6
4a	2.5	57	3.28	0.43	58	3.24	0.50	3.31	54.3
4b	5	56	3.17	0.44	57	3.16	0.38	3.31	54.3
4c	10	57	3.15	0.40	57	3.12	0.40	3.31	54.3
4d	20	59	3.11	0.38	56	3.12	0.36	3.31	54.3
5a	2.5	58	3.28	0.47	59	3.23	0.50	3.28	55.9
5b	5	58	3.16	0.41	58	3.13	0.40	3.28	55.9
5c	10	58	3.13	0.39	Broken			3.28	55.9
5d	20	Broken			58	3.09	0.35	3.28	55.9
6a	2.5	51	2.81	0.59	51	2.77	0.53	-	-
6b	5	50	2.73	0.45	49	2.70	0.41	-	-
6c	10	50	2.70	0.46	50	2.68	0.37	-	-
6d	20	50	2.67	0.37	49	2.67	0.38	-	-

Table 4.2.3. Microwave parameters measured for generation 1 electrodes on Spire AlGaAs/GaAs substrates. The average values of n_μ and Z_o are over the frequency range 5 to 40 GHz.

Device #	Z_o (Ω) at 40 GHz	n_μ at 40 GHz	α (Np/cm) at 40 GHz	Average Z_o (Ω)	Average n_μ
1a	40	3.43	3.4	34	3.90
1b	40	3.15	6.0	33	3.23
1c	41	3.00	7.0	33	3.38
1d	40	3.18	7.8	33	3.59
2a	45	3.12	3.7	37	3.87
2b	47	7.66	6.7	38	7.93
2c	46	3.35	8.9	37	3.85
2d	46	3.62	9.4	38	4.14
3a	45	3.12	3.7	37	3.87
3b	45	3.20	7.2	37	4.35
3c	44	3.37	9.2	36	3.85
3d	45	3.66	9.4	37	4.17
4a	47	3.90	3.5	39	3.99
4b	50	3.28	6.5	46	3.17
4c	47	3.64	10.6	38	4.05
4d	47	3.81	9.4	38	4.29
5a	46	3.52	4.2	38	3.98
5b	45	4.02	5.9	38	4.52
5c	46	3.71	9.6	38	4.14
5d	47	3.88	9.2	38	4.34
6a	47	3.89	4.0	40	3.93
6b	61	3.25	5.7	61	3.26
6c	49	3.58	8.9	41	3.99
6d	48	3.81	8.4	39	4.24

Table 4.2.4. Microwave parameters measured for generation 2 electrodes on SI-GaAs, up to 40 GHz. The values of n_μ and Z_o are the average values over the frequency range 5 to 40 GHz. α is the value measured at 40 GHz. The values given in the "average" row are the averages for all of the devices in each column. The values given in the "avg. PC" row are the averages for the polarization converter type devices in each column. The values given in the "avg. MZ" row are the averages for the Mach-Zehnder type devices in each column (devices 30, 31, 35, and 36). The electrode dimensions are given in Table 3.3.6.

Device #	NrNs			NrWs			WrNs		
	n_μ	α (Np/cm)	Z_o (Ω)	n_μ	α (Np/cm)	Z_o (Ω)	n_μ	α (Np/cm)	Z_o (Ω)
25	3.47	0.24	50.8	3.35	0.17	52.5	3.59	0.20	48.7
26	3.41	0.20	53.8	Broken			3.59	0.17	51.1
27	3.43	0.19	51.8	3.37	0.30	52.8	3.56	0.19	49.4
28	3.49	0.23	50.9	3.37	0.26	51.9	3.65	0.17	48.6
29	3.40	0.22	51.7	3.31	0.28	52.5	3.49	0.24	52.3
30	3.96	0.10	44.3	3.83	0.27	45.9	3.97	0.29	44.6
31	3.72	0.24	46.0	3.61	0.18	47.5	3.70	0.16	46.0
32	3.60	0.15	47.5	3.48	0.27	49.2	3.55	0.32	48.7
33	3.10	0.22	53.3	Broken			3.17	0.20	52.1
34	3.51	0.24	51.7	3.38	0.25	53.2	3.65	0.17	49.3
35	3.78	0.31	45.0	3.66	0.34	46.7	3.77	0.31	45.1
36	4.00	0.36	43.9	3.86	0.37	45.9	3.99	0.36	43.6
37	3.77	0.32	47.5	3.64	0.36	49.2	3.91	0.34	45.6
average	3.59	0.23	49.1	3.53	0.28	49.7	3.66	0.24	48.1
avg. PC	3.46	0.22	51.0	3.42	0.27	51.6	3.57	0.22	49.5
avg. MZ	3.87	0.25	44.8	3.74	0.29	46.5	3.86	0.28	44.8

Table 4.2.5. Microwave parameters measured for generation 2 electrodes on NortelTech AlGaAs/GaAs substrate. The values of n_μ and Z_o are the average values over the frequency range 5 to 40 GHz. α is the value measured at 40 GHz. The values given in the "average" row are the averages for all of the devices in each column. The values given in the "avg. PC" row are the averages for the polarization converter type devices in each column. The values given in the "avg. MZ" row are the averages for the Mach-Zehnder type devices in each column (devices 30, 31, 35, and 36). The electrode dimensions are given in Table 3.3.6. The Sonnet™ results from Table 3.3.7 are reproduced here for comparison.

Device #	Measurements			Sonnet™	
	n_μ	α (Np/cm)	Z_o (Ω)	n_μ	Z_o (Ω)
25	Broken			-	-
26	3.41	0.39	53.3	3.25	56.5
27	3.40	0.37	51.2	3.28	52.6
28	Broken			-	-
29	3.37	0.37	51.5	3.30	51.5
30	3.82	0.40	45.1	3.50	47.8
31	3.55	0.37	47.1	3.35	51.0
32	3.53	0.41	48.2	3.25	52.5
33	3.05	0.38	53.2	3.29	52.6
34	3.48	0.43	51.2	3.38	55.2
35	3.63	0.50	46.5	3.51	49.4
36	3.82	0.54	46.0	3.63	49.2
37	3.72	0.51	47.7	3.39	53.3
average	3.53	0.42	49.2	3.38	52.0
avg. PC	3.42	0.41	50.9	3.31	53.5
avg. MZ	3.70	0.45	46.2	3.50	49.3
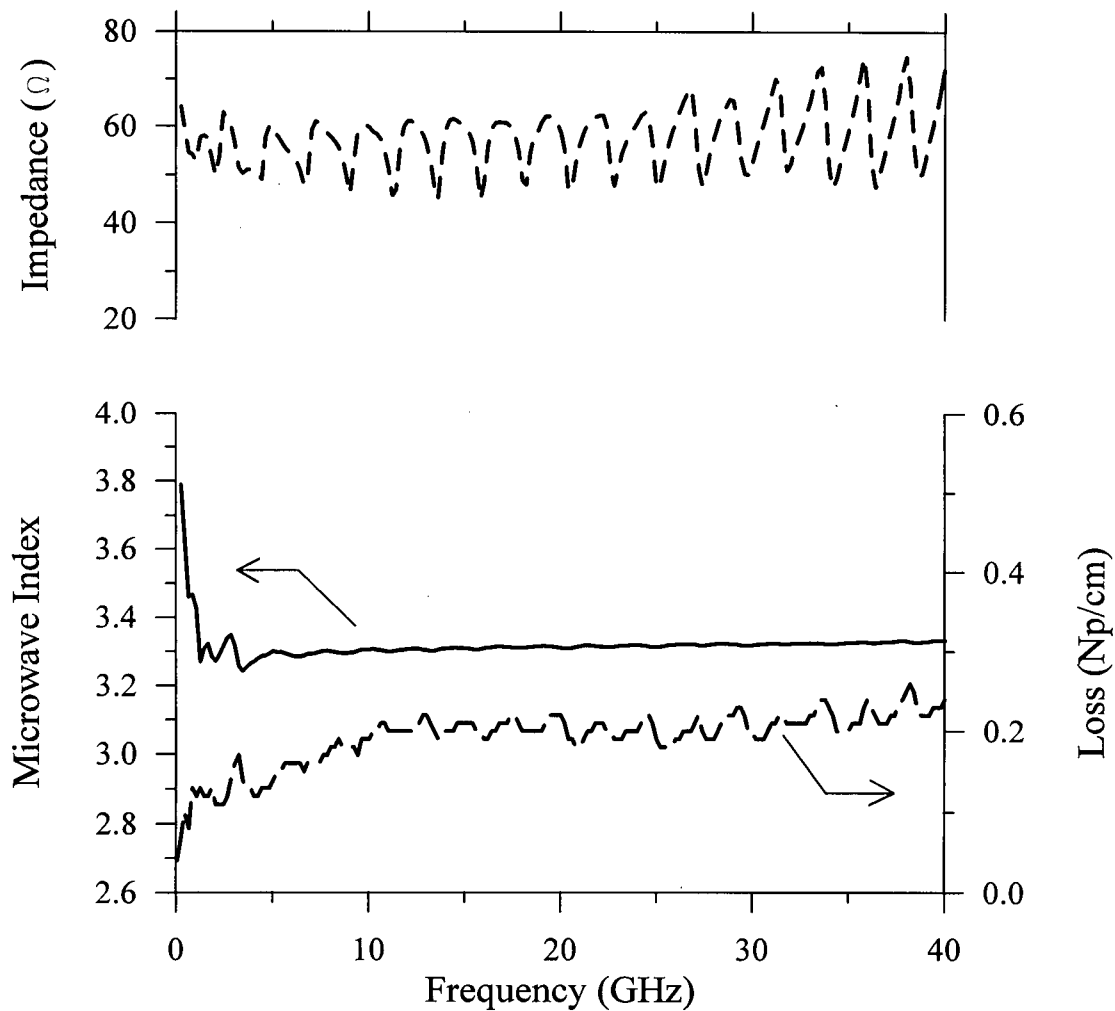
Figure 4.2.1. The microwave index (solid line), microwave loss coefficient (long-dashed line), and characteristic impedance (short-dashed line), measured for the gold electrode 1d of Table 4.2.2.

131
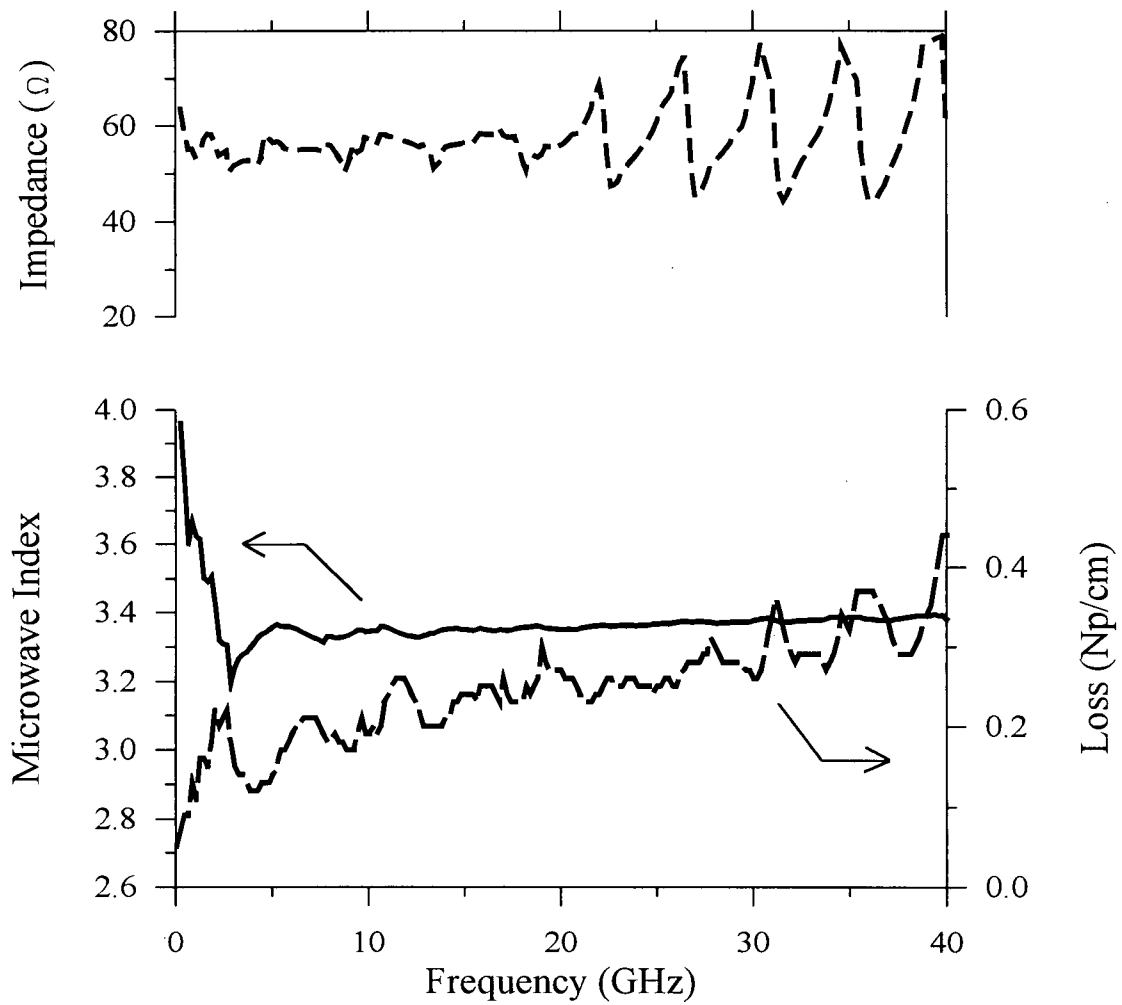
Figure 4.2.2. The microwave index (solid line), microwave loss coefficient
(long-dashed line), and characteristic impedance (short-dashed line), measured
for the gold electrode 2c of Table 4.2.2.
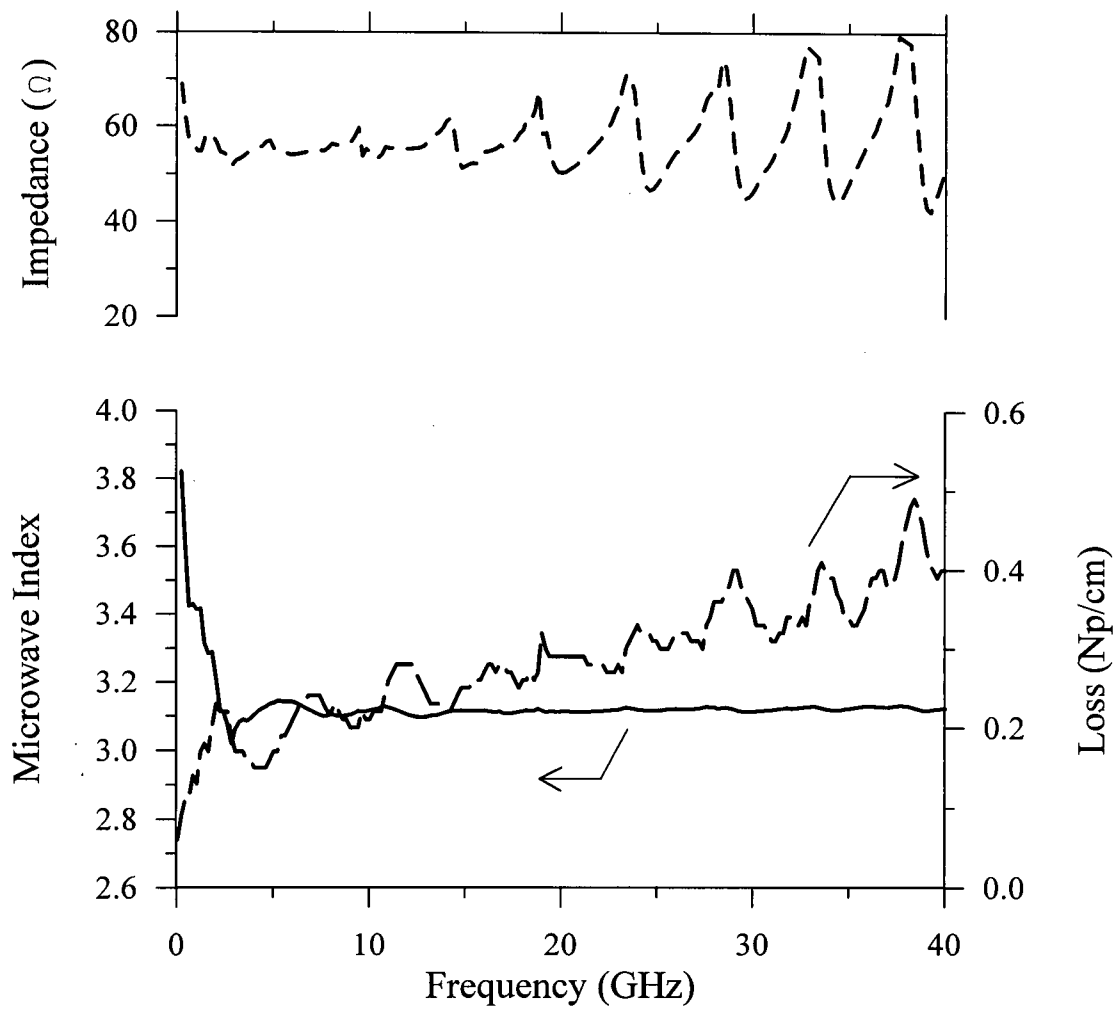
Figure 4.2.3. The microwave index (solid line), microwave loss coefficient (long-dashed line), and characteristic impedance (short-dashed line), measured for the gold electrode 4c of Table 4.2.2.
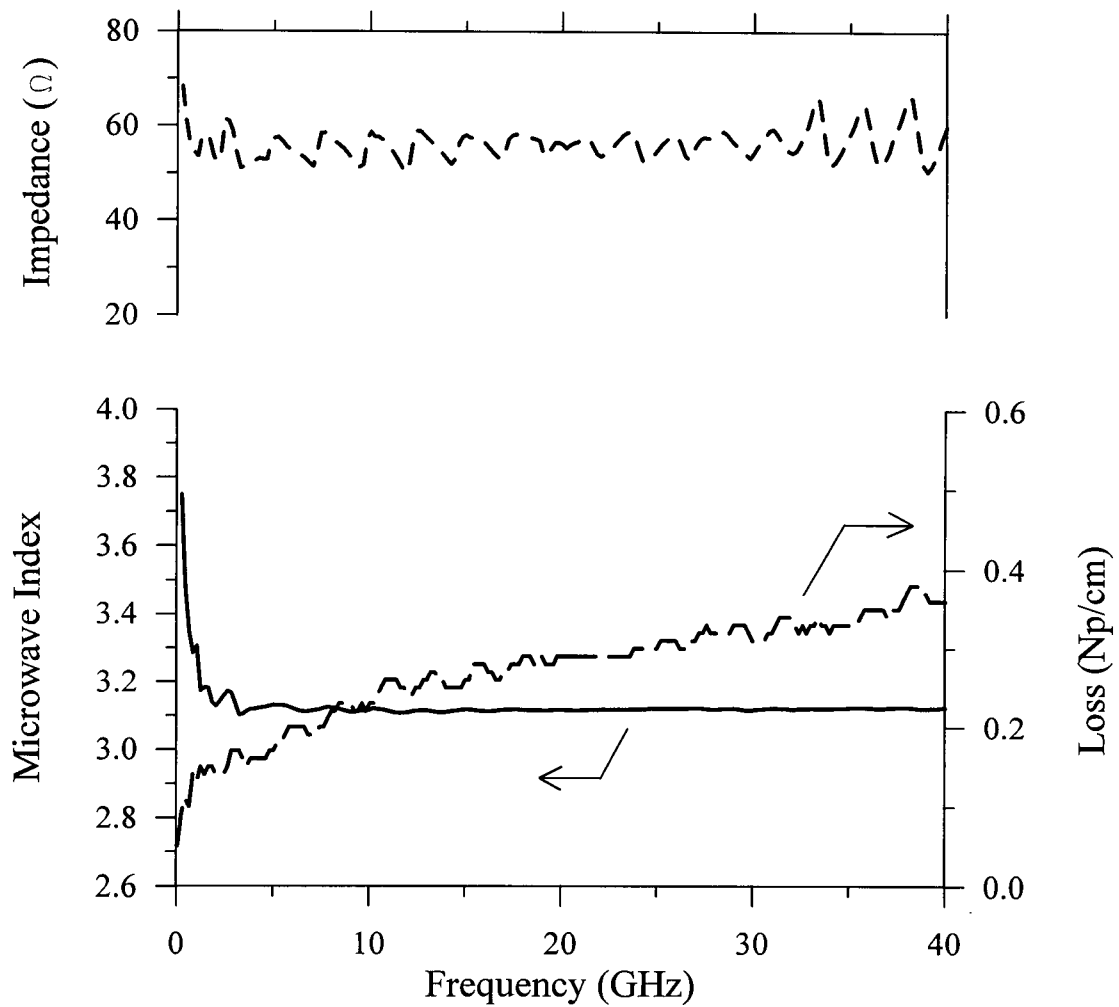
Figure 4.2.4. The microwave index (solid line), microwave loss coefficient (long-dashed line), and characteristic impedance (short-dashed line), measured for the gold electrode 4d of Table 4.2.2.

134
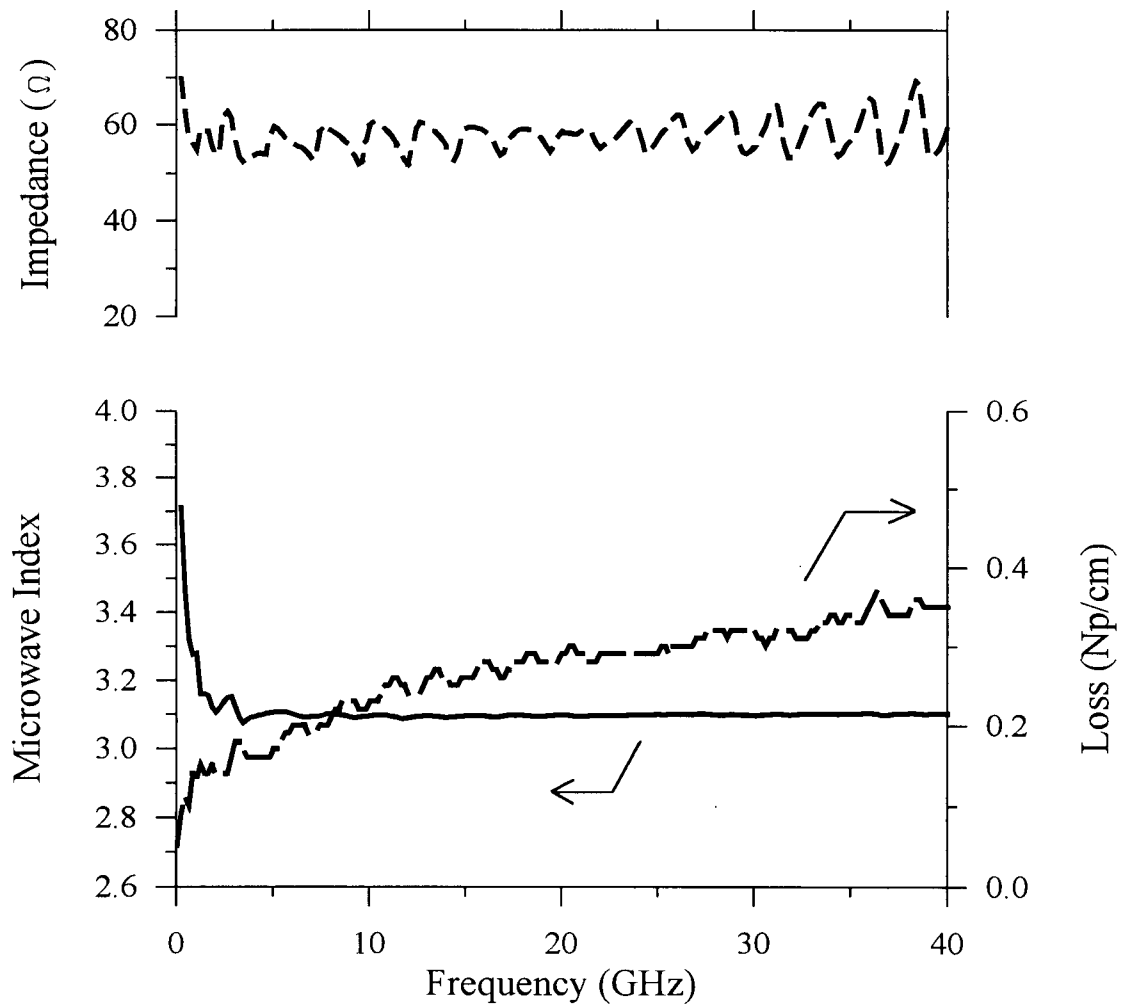
Figure 4.2.5. The microwave index (solid line), microwave loss coefficient (long-dashed line), and characteristic impedance (short-dashed line), measured for the gold electrode 5d of Table 4.2.2.

135
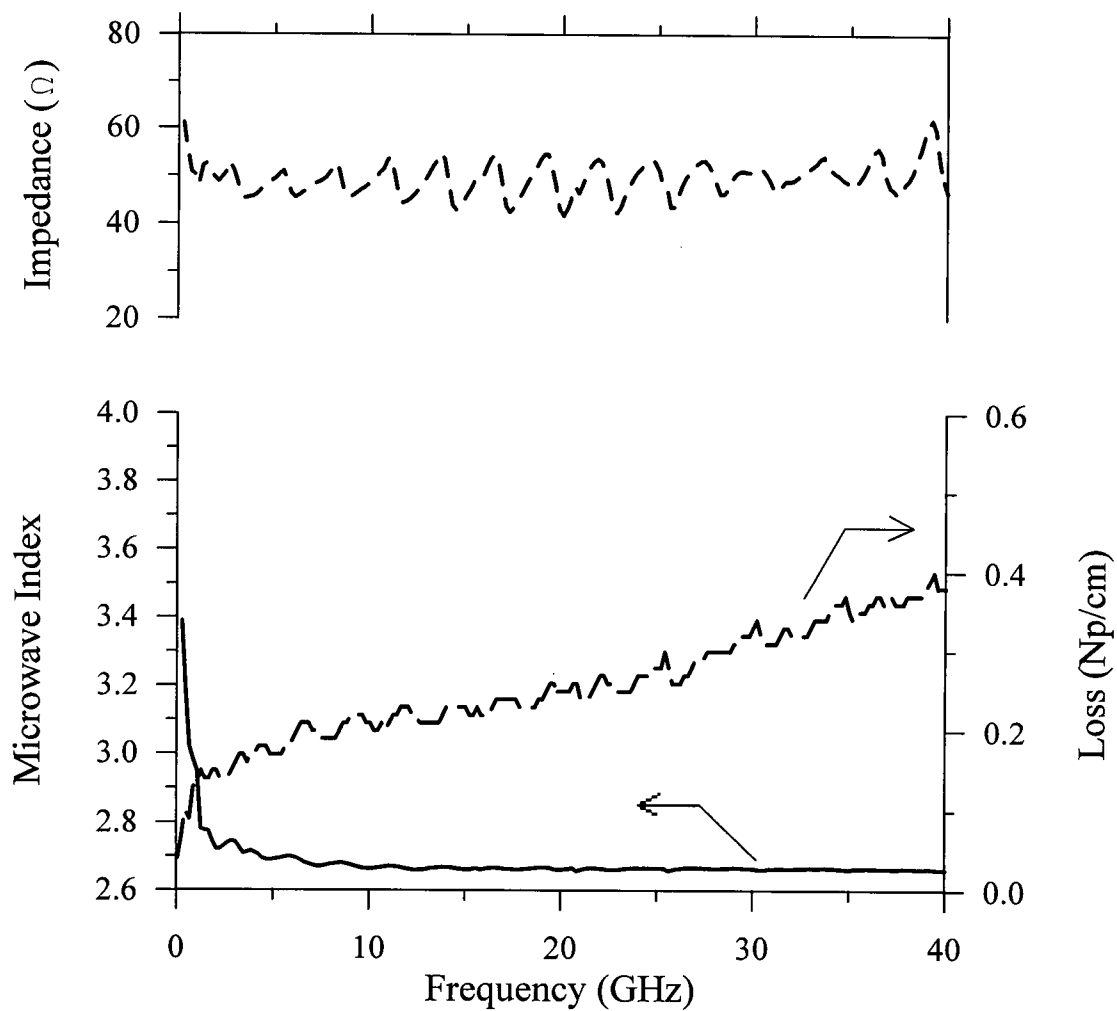
Figure 4.2.6. The microwave index (solid line), microwave loss coefficient (long-dashed line), and characteristic impedance (short-dashed line), measured for the gold electrode 6d of Table 4.2.2. This is not a slow-wave electrode.
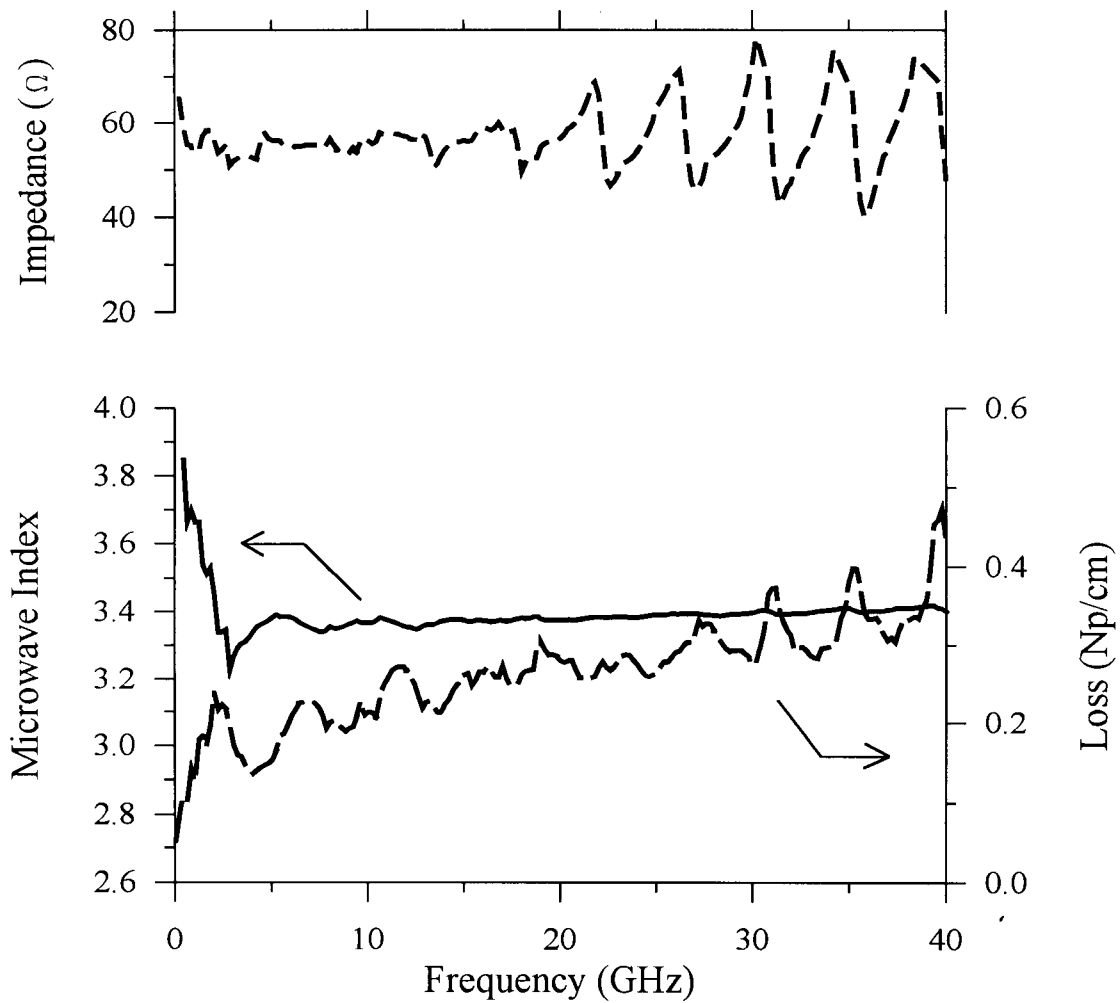
Figure 4.2.7. The microwave index (solid line), microwave loss coefficient
(long-dashed line), and characteristic impedance (short-dashed line), measured
for the aluminum electrode 2c of Table 4.2.2.

137
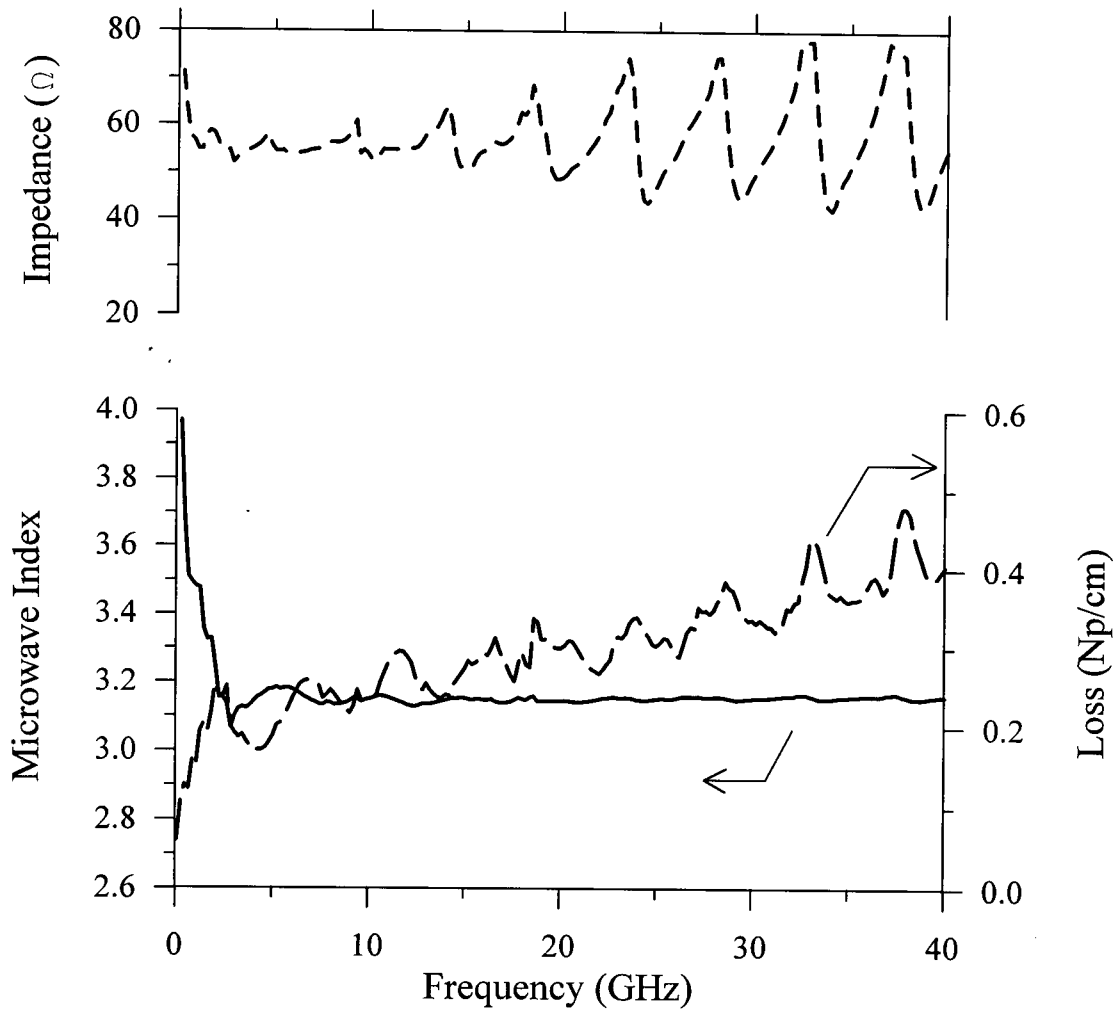
Figure 4.2.8. The microwave index (solid line), microwave loss coefficient (long-dashed line), and characteristic impedance (short-dashed line), measured for the aluminum electrode 4c of Table 4.2.2.

138
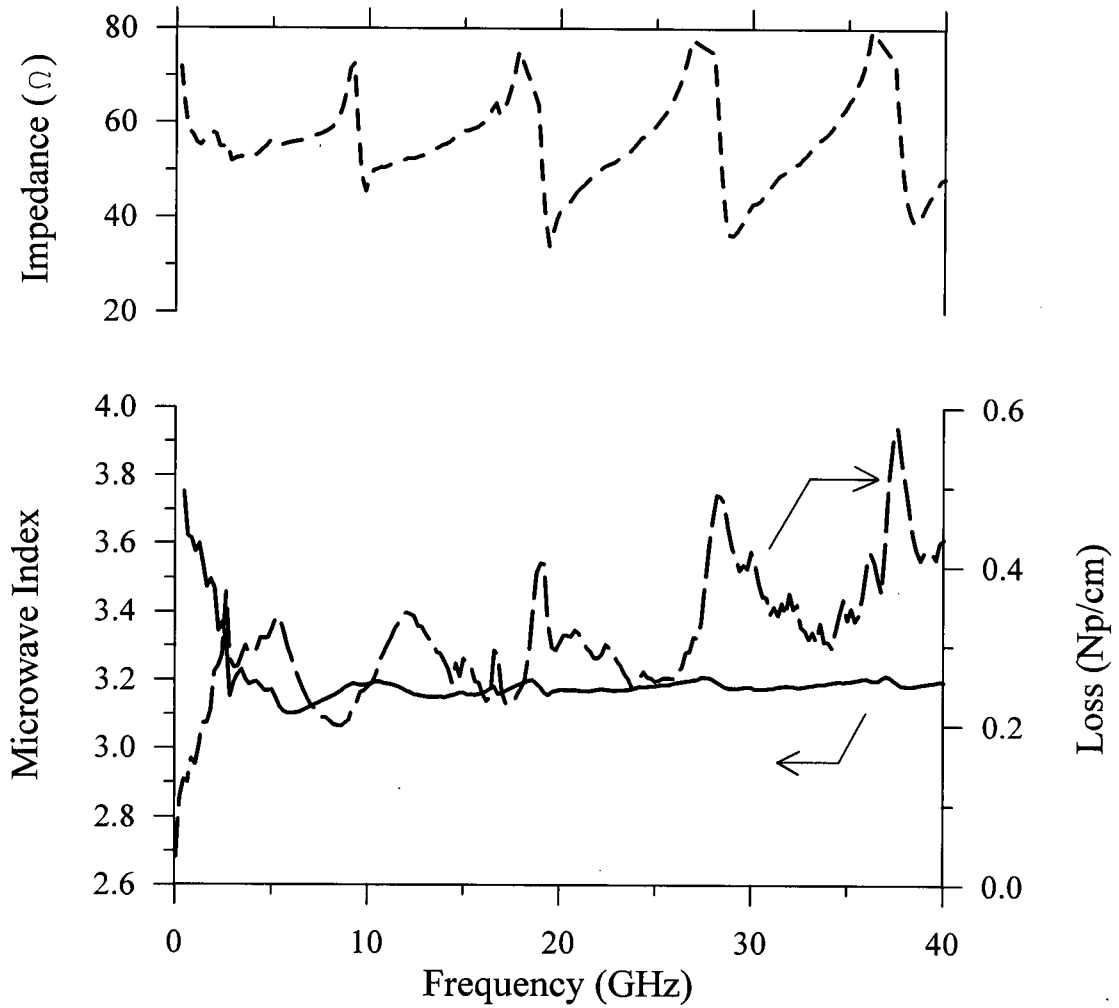
Figure 4.2.9. The microwave index (solid line), microwave loss coefficient (long-dashed line), and characteristic impedance (short-dashed line), measured for the aluminum electrode 4b of Table 4.2.2.
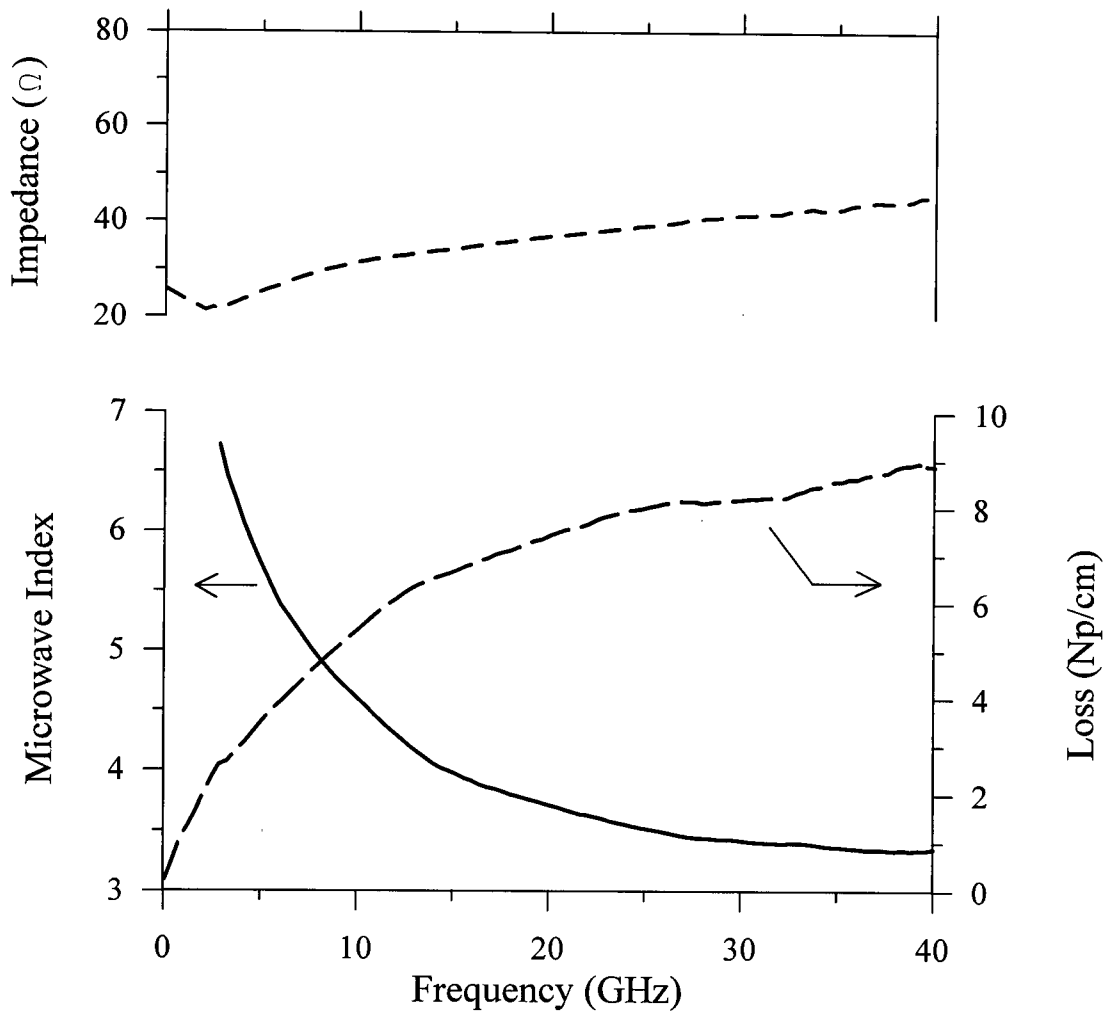
Figure 4.2.10. The microwave index (solid line), microwave loss coefficient (long-dashed line), and characteristic impedance (short-dashed line), measured for electrode 2c of Table 4.2.3.
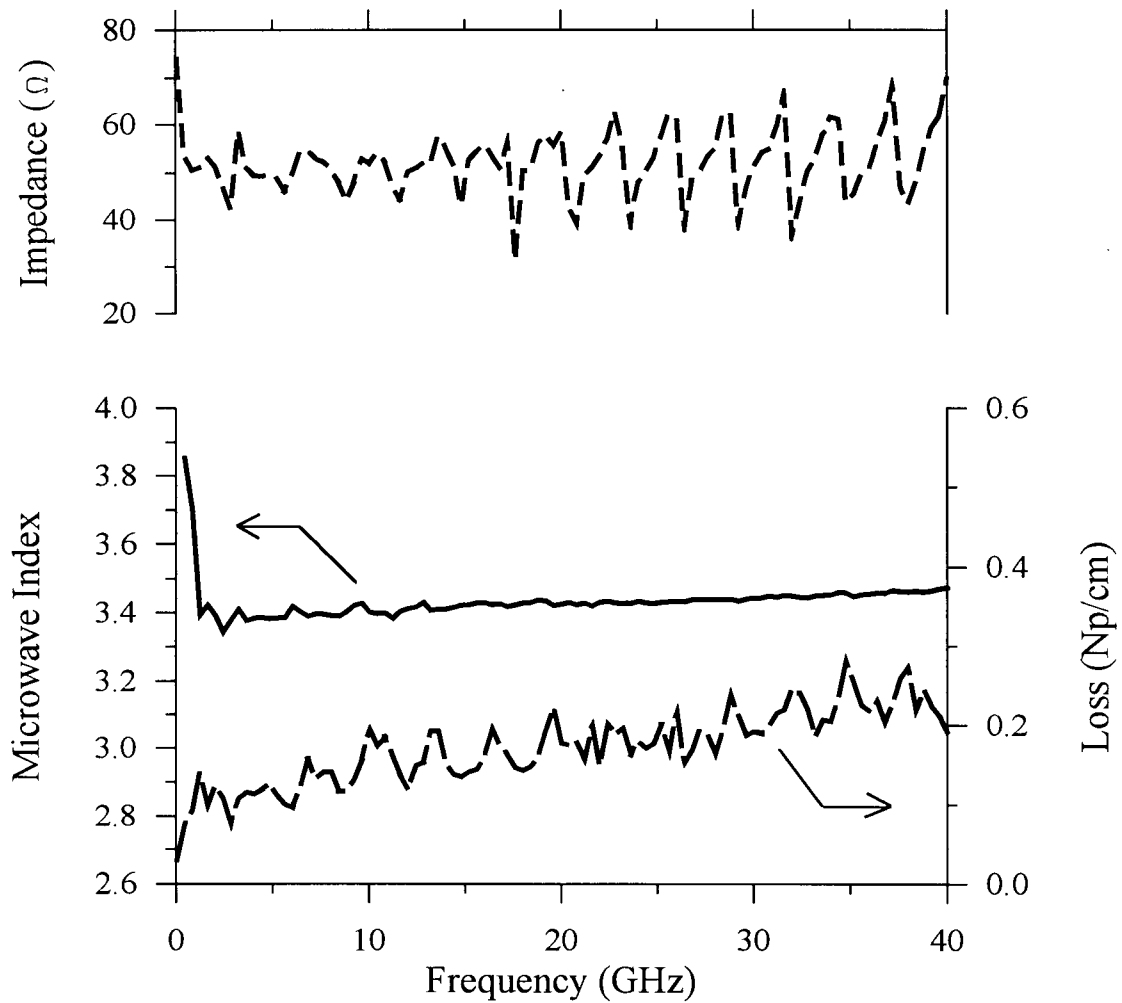
Figure 4.2.11. The microwave index (solid line), microwave loss coefficient
(long-dashed line), and characteristic impedance (short-dashed line), measured
for device NrNs-27 of Table 4.2.4.

141
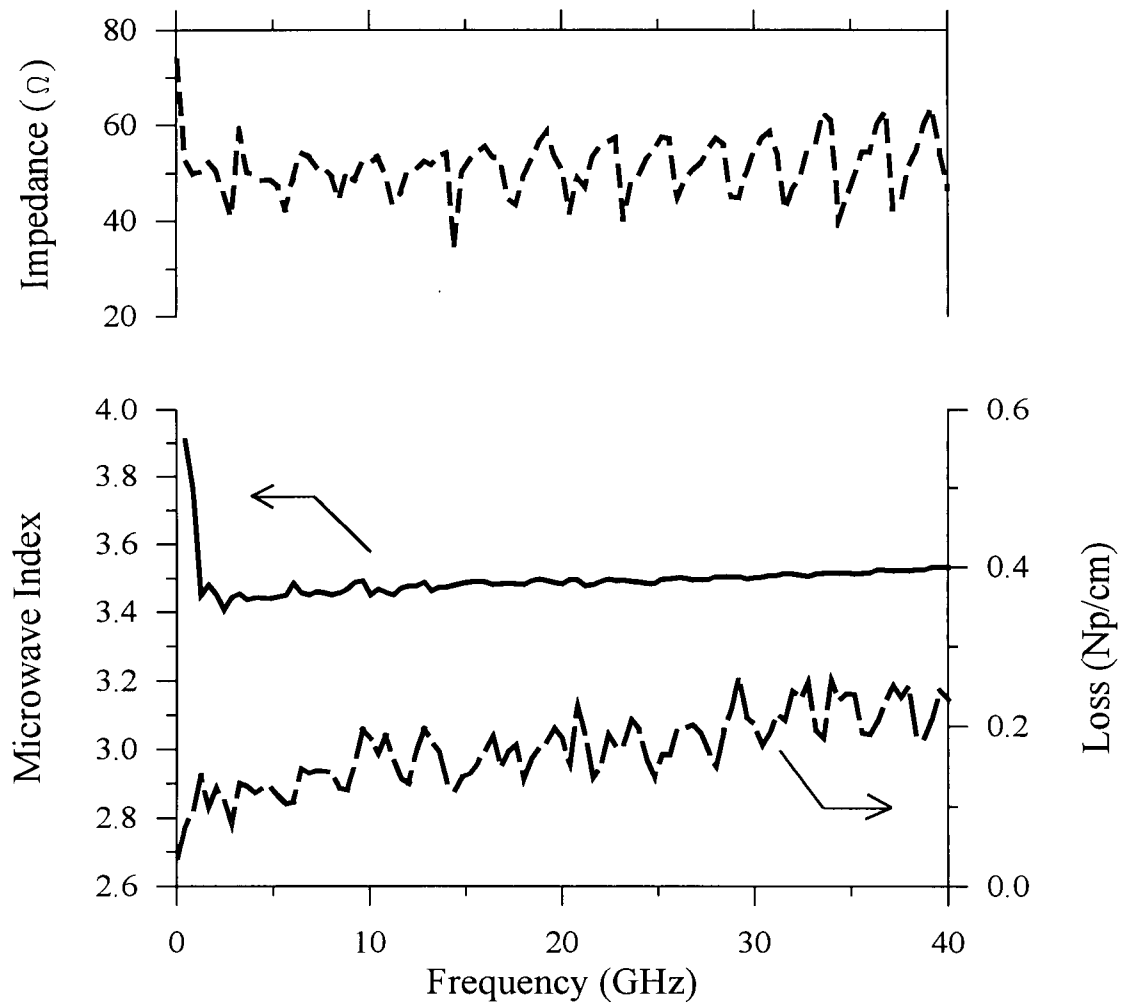
Figure 4.2.12. The microwave index (solid line), microwave loss coefficient (long-dashed line), and characteristic impedance (short-dashed line), measured for device NrNs-28 of Table 4.2.4.

142
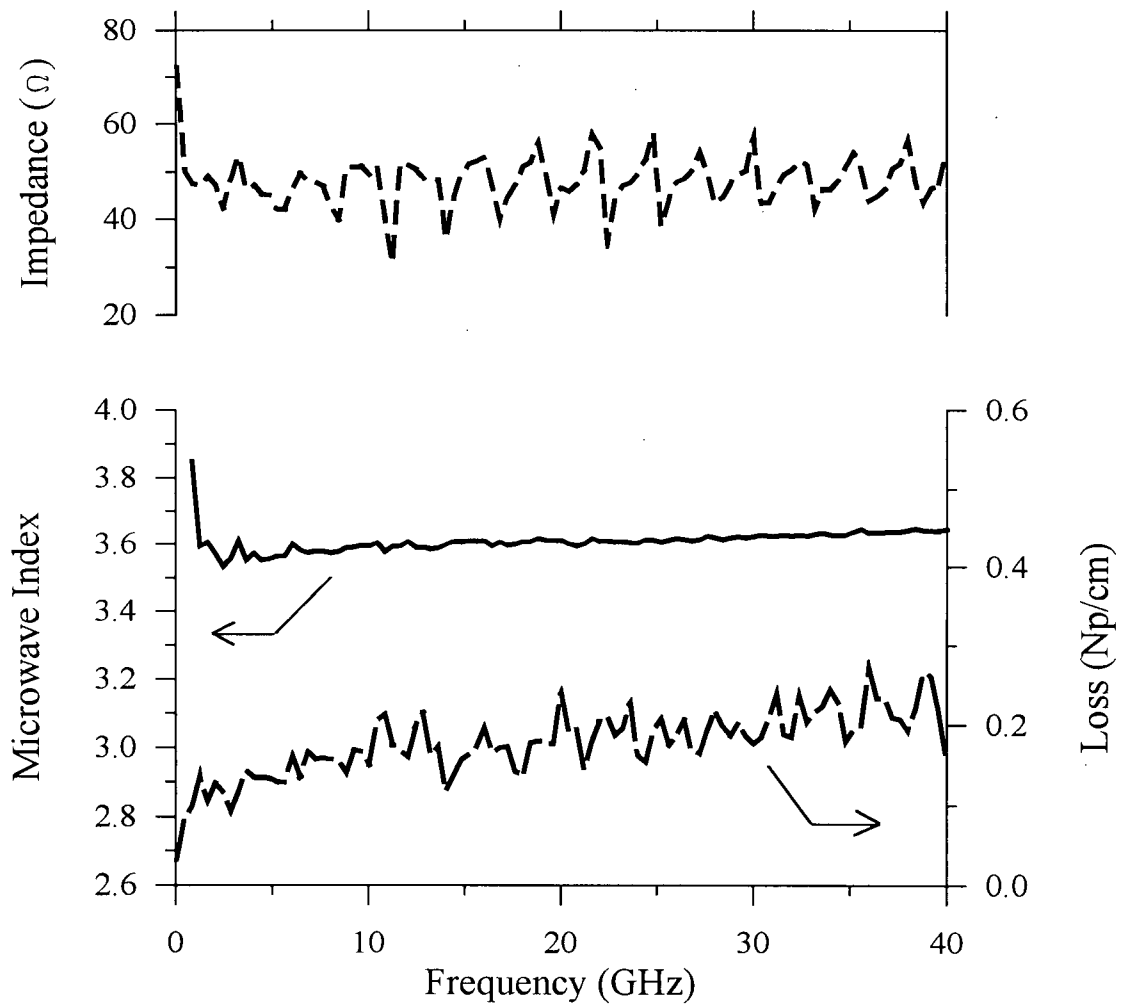
Figure 4.2.13. The microwave index (solid line), microwave loss coefficient (long-dashed line), and characteristic impedance (short-dashed line), measured for device NrNs-32 of Table 4.2.4.
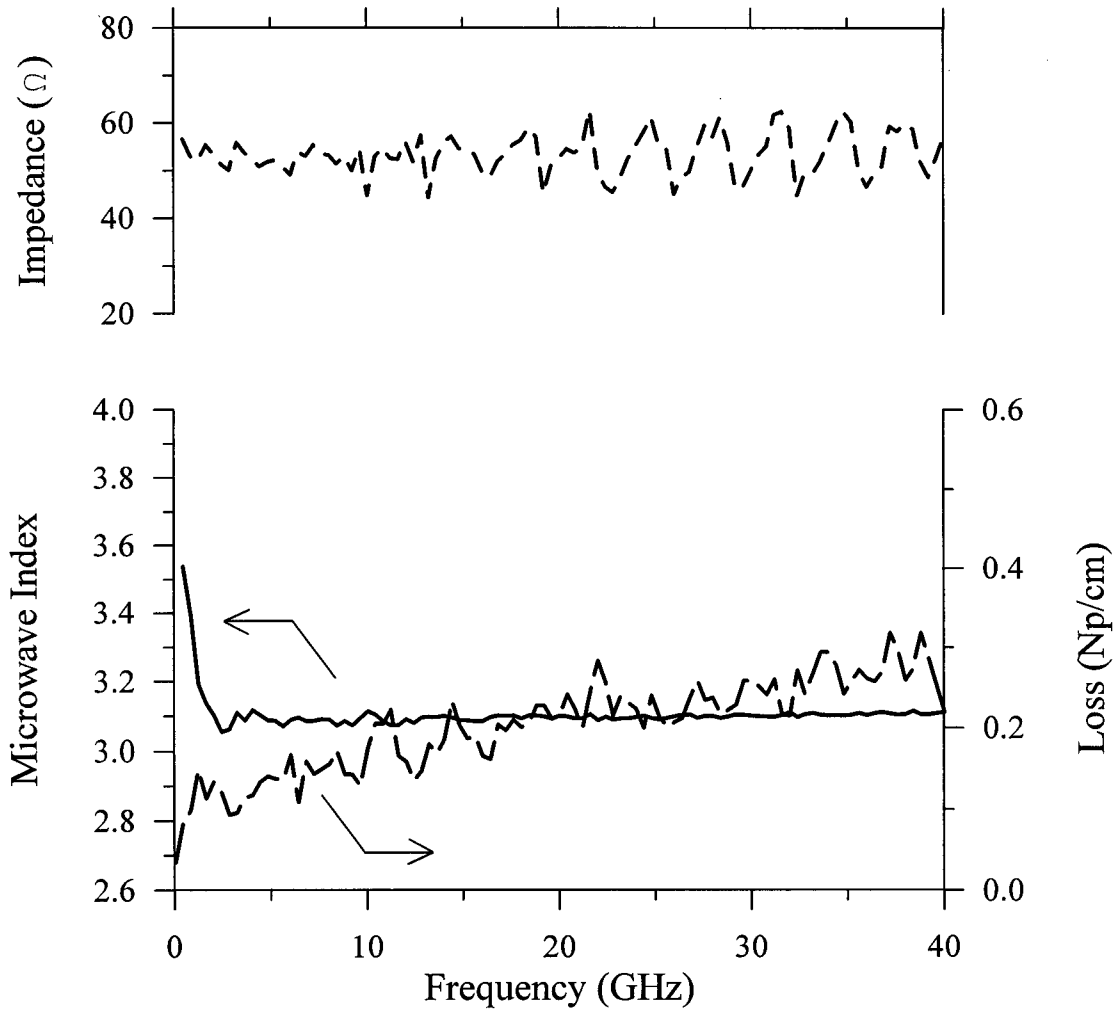
Figure 4.2.14. The microwave index (solid line), microwave loss coefficient (long-dashed line), and characteristic impedance (short-dashed line), measured for device NrNs-33 of Table 4.2.4.
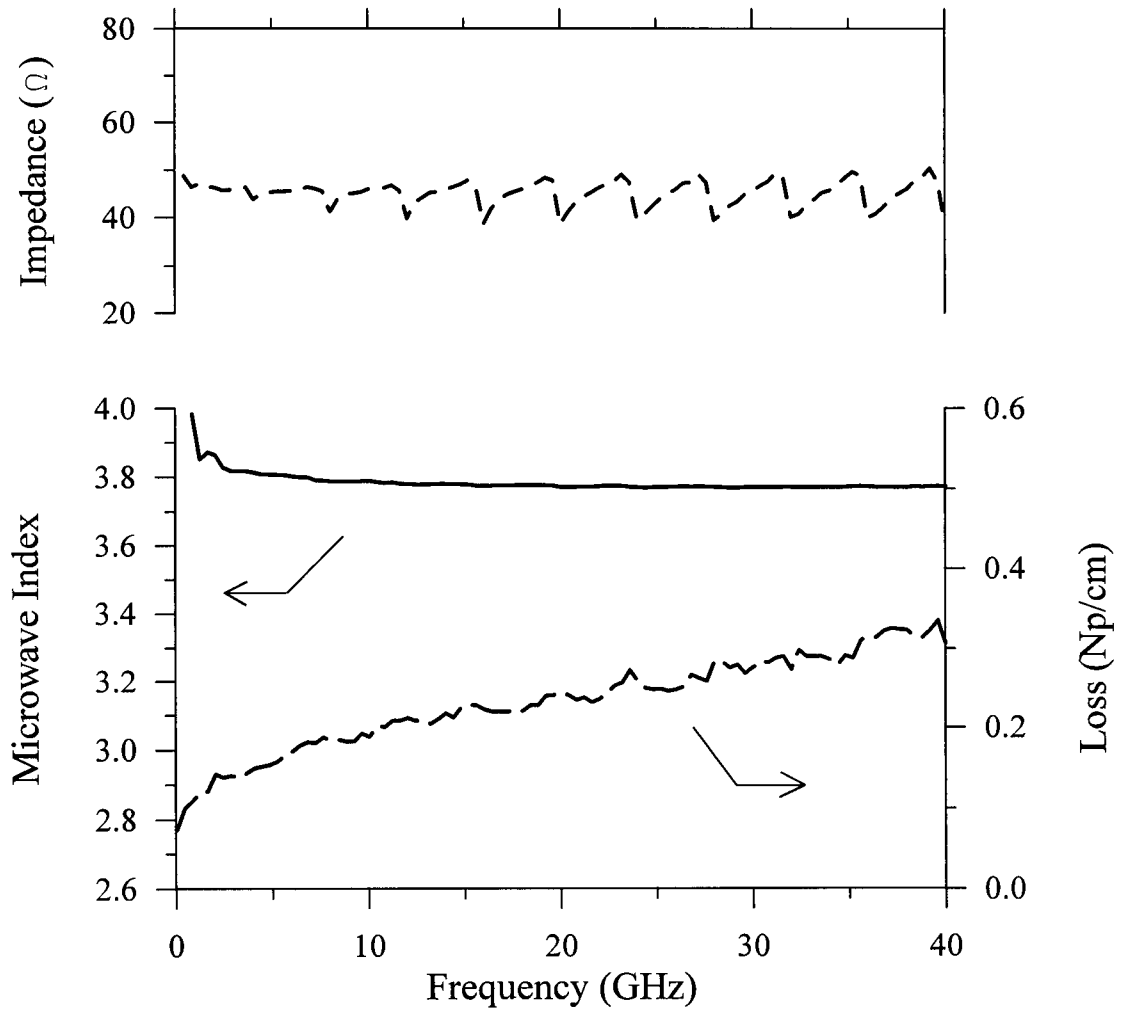
Figure 4.2.15. The microwave index (solid line), microwave loss coefficient (long-dashed line), and characteristic impedance (short-dashed line), measured for device NrNs-35 of Table 4.2.4.

145
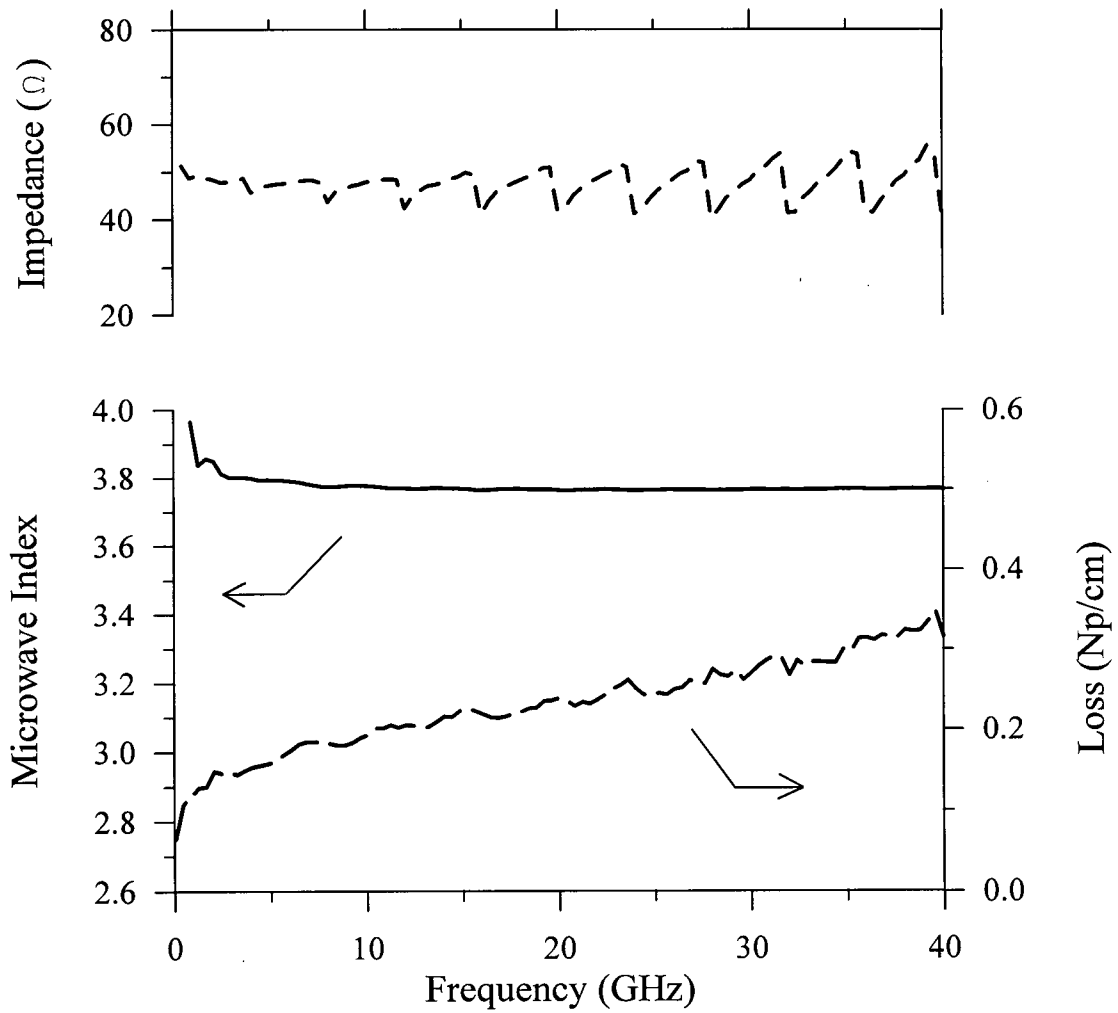
Figure 4.2.16. The microwave index (solid line), microwave loss coefficient (long-dashed line), and characteristic impedance (short-dashed line), measured for device NrNs-37 of Table 4.2.4.
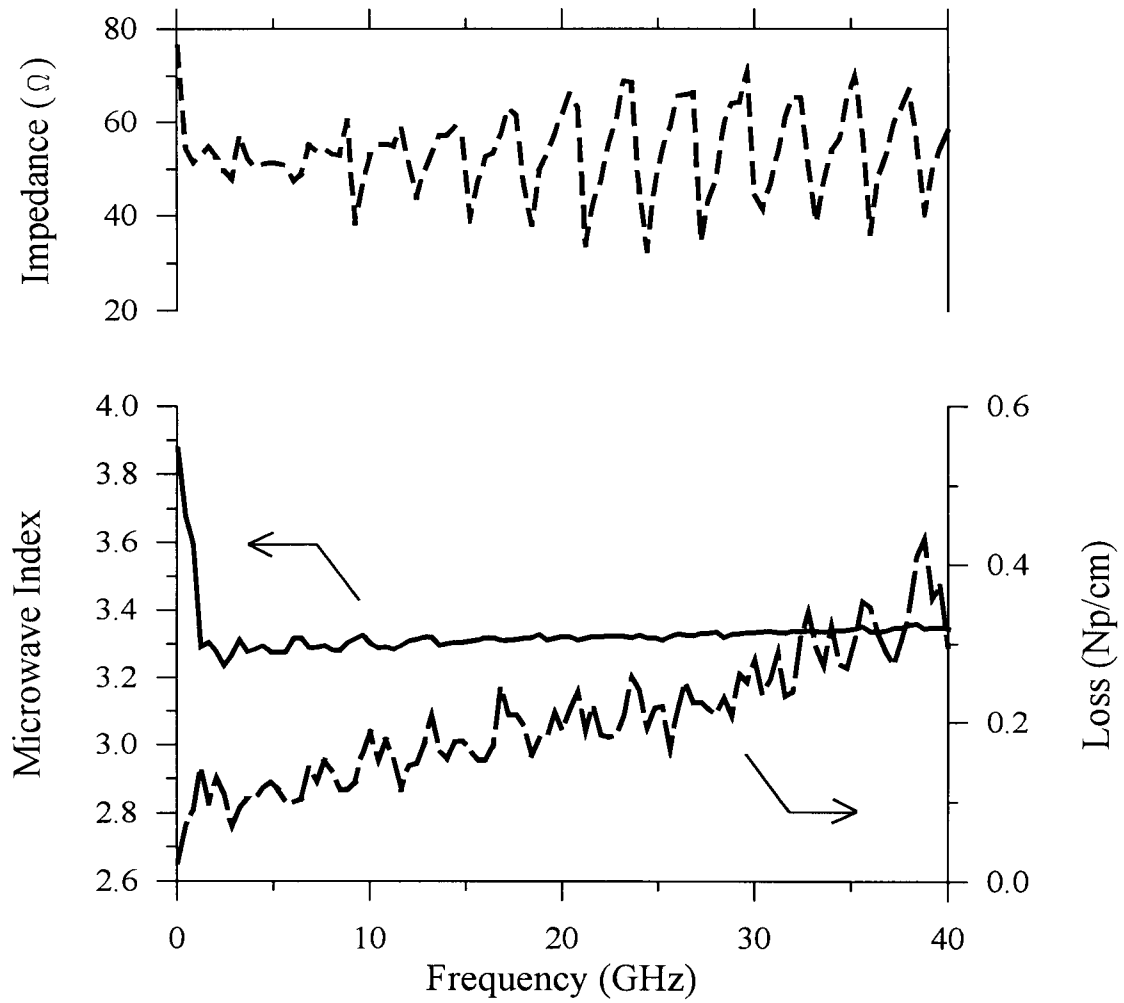
Figure 4.2.17. The microwave index (solid line), microwave loss coefficient (long-dashed line), and characteristic impedance (short-dashed line), measured for device NrWs-27 of Table 4.2.4.
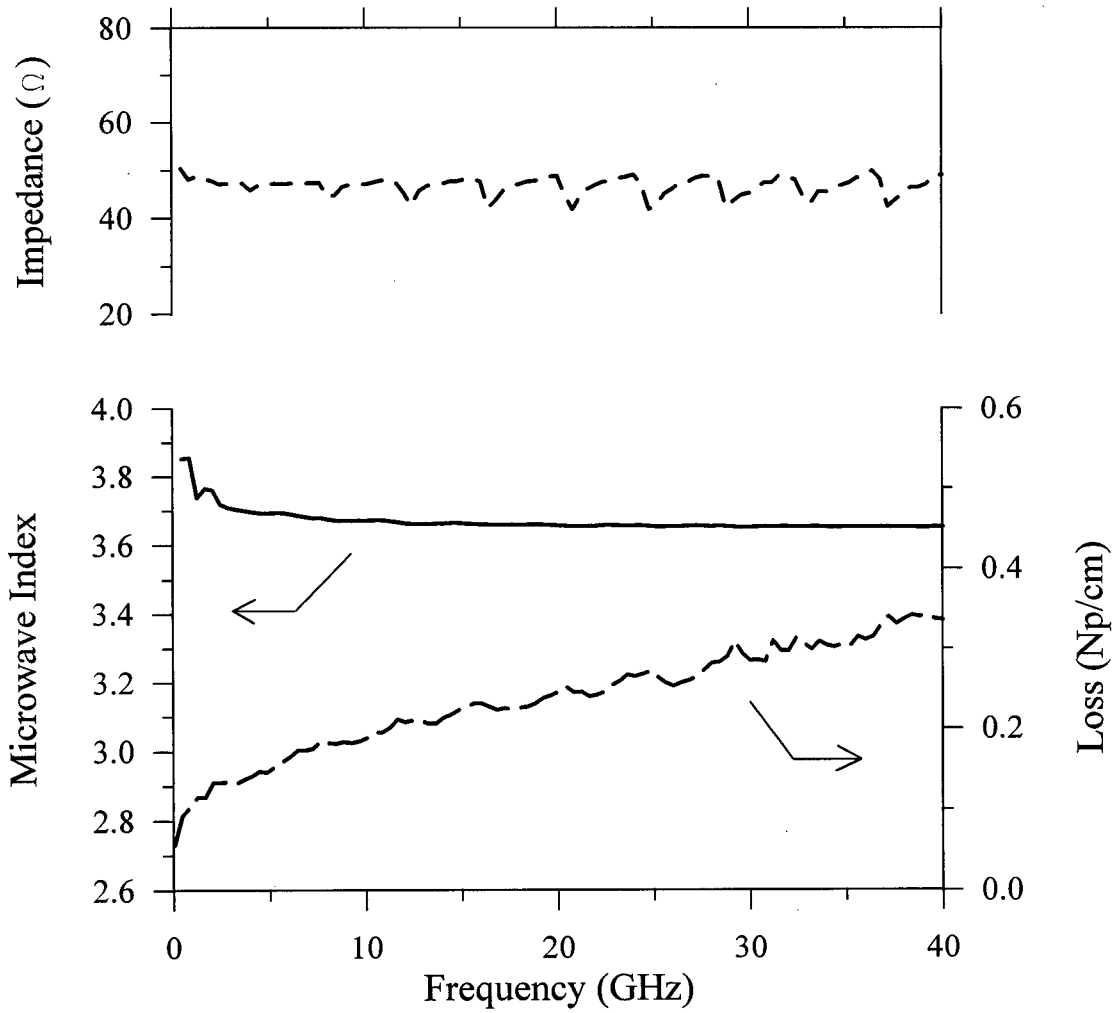
Figure 4.2.18. The microwave index (solid line), microwave loss coefficient (long-dashed line), and characteristic impedance (short-dashed line), measured for device NrWs-35 of Table 4.2.4.

148
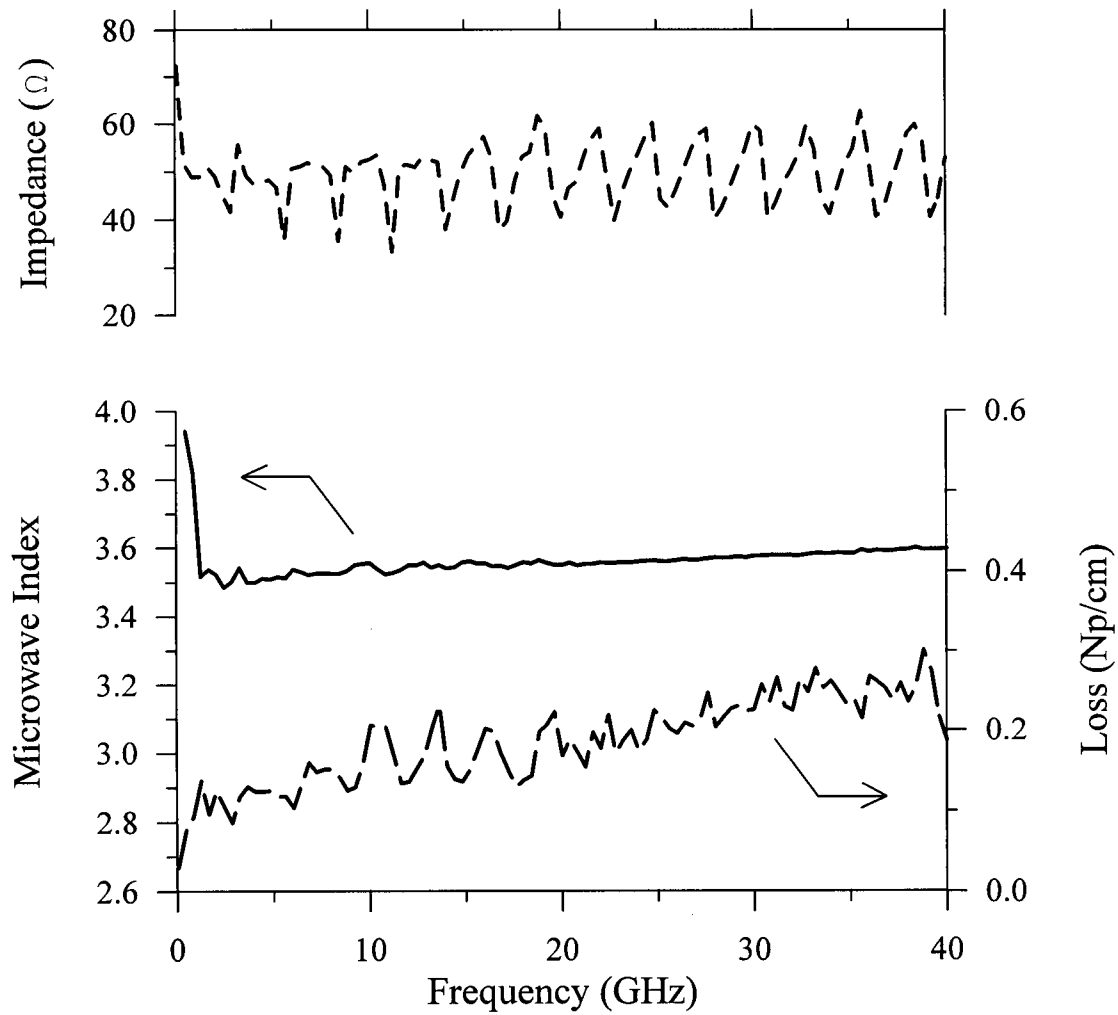
Figure 4.2.19. The microwave index (solid line), microwave loss coefficient
(long-dashed line), and characteristic impedance (short-dashed line), measured
for device WrNs-27 of Table 4.2.4.
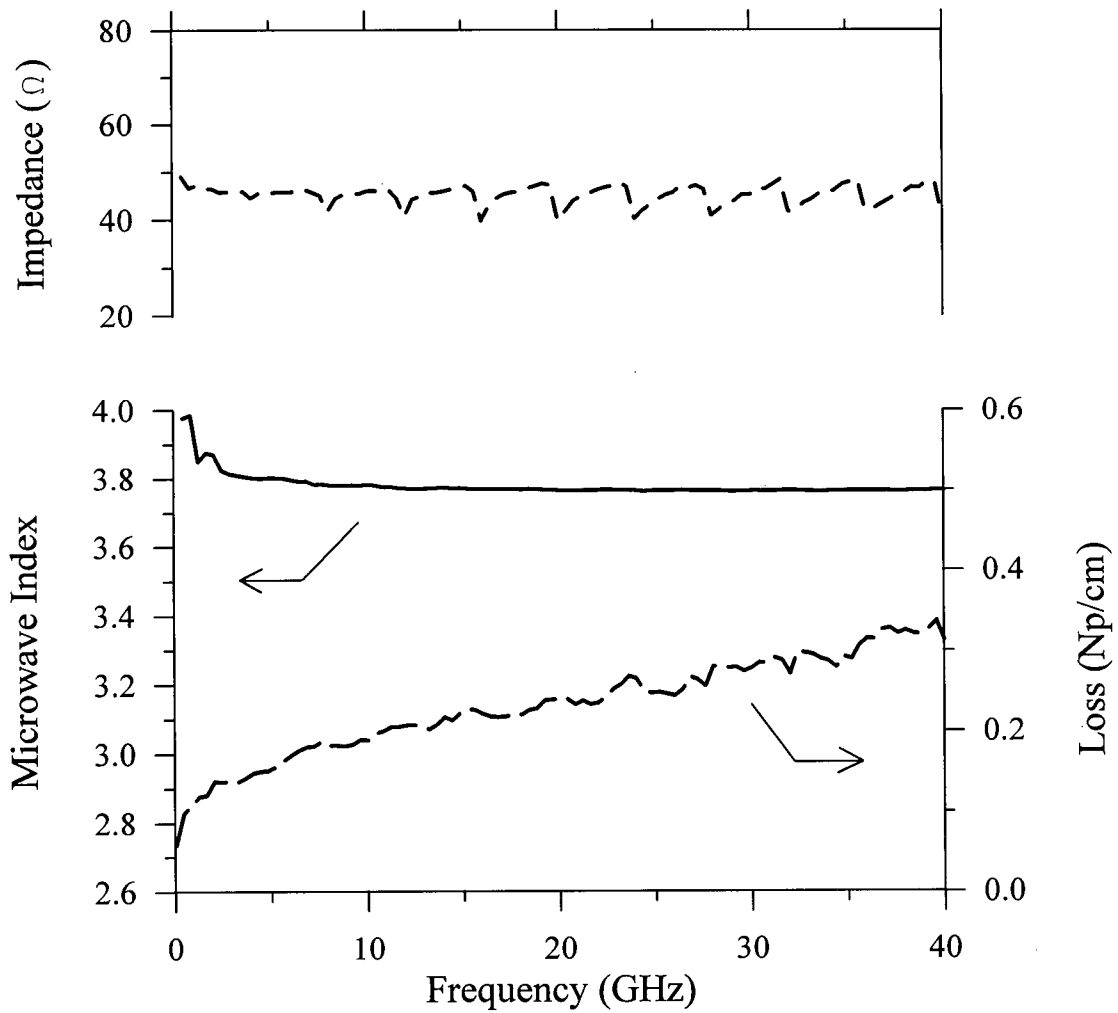
Figure 4.2.20. The microwave index (solid line), microwave loss coefficient (long-dashed line), and characteristic impedance (short-dashed line), measured for device WrNs-35 of Table 4.2.4.
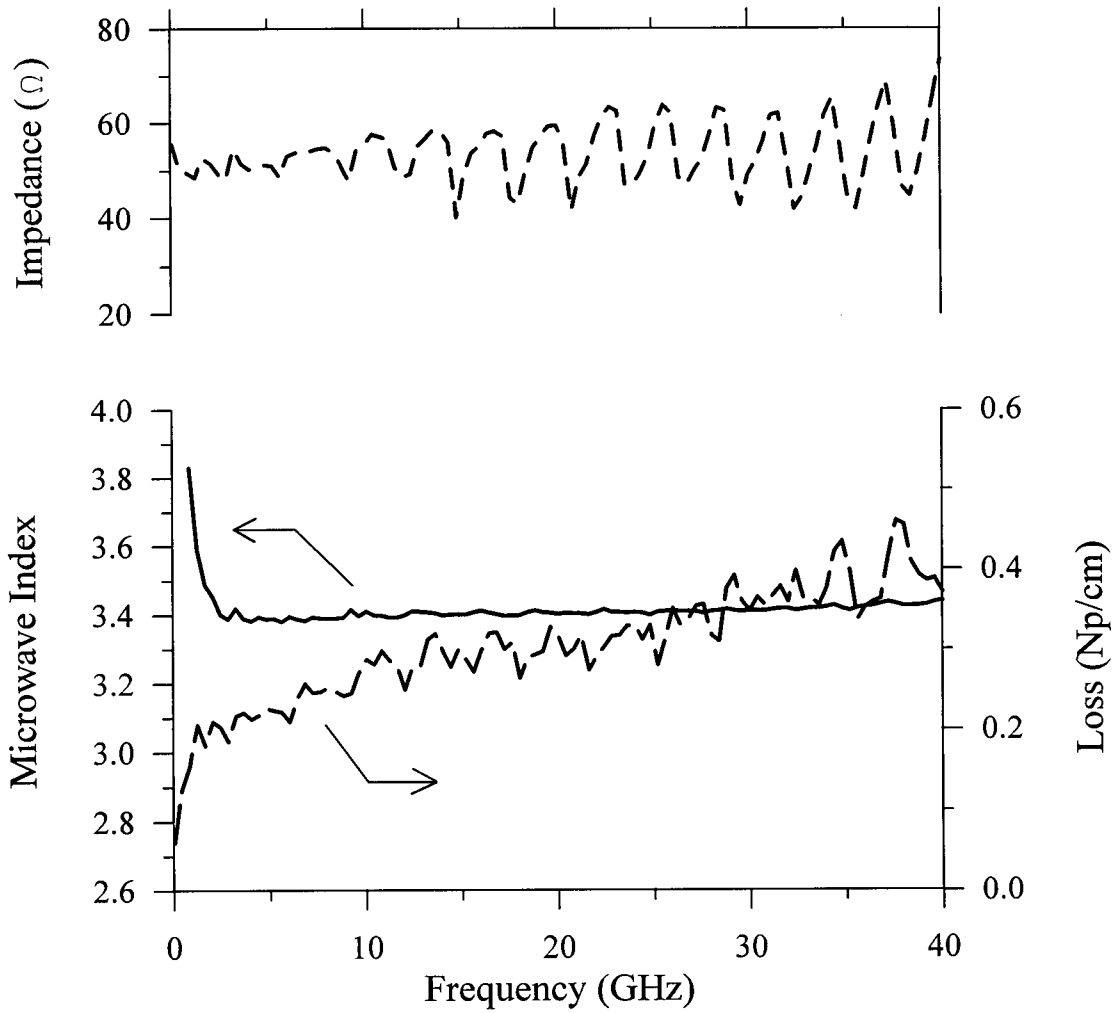
Figure 4.2.21. The microwave index (solid line), microwave loss coefficient (long-dashed line), and characteristic impedance (short-dashed line), measured for device 26 of Table 4.2.5 (generation 2 AlGaAs/GaAs substrate).

151
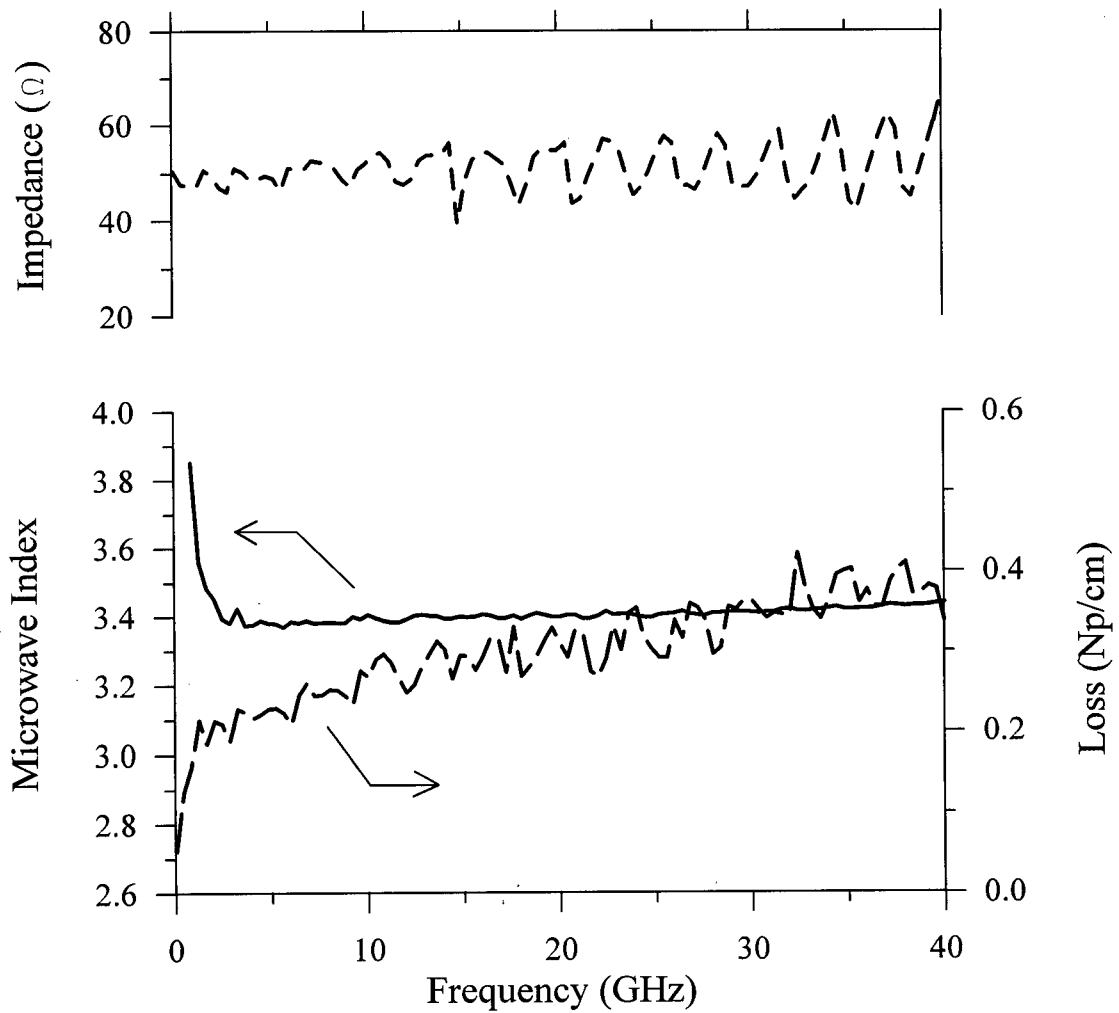
Figure 4.2.22. The microwave index (solid line), microwave loss coefficient
(long-dashed line), and characteristic impedance (short-dashed line), measured
for device 27 of Table 4.2.5 (generation 2 AlGaAs/GaAs substrate).
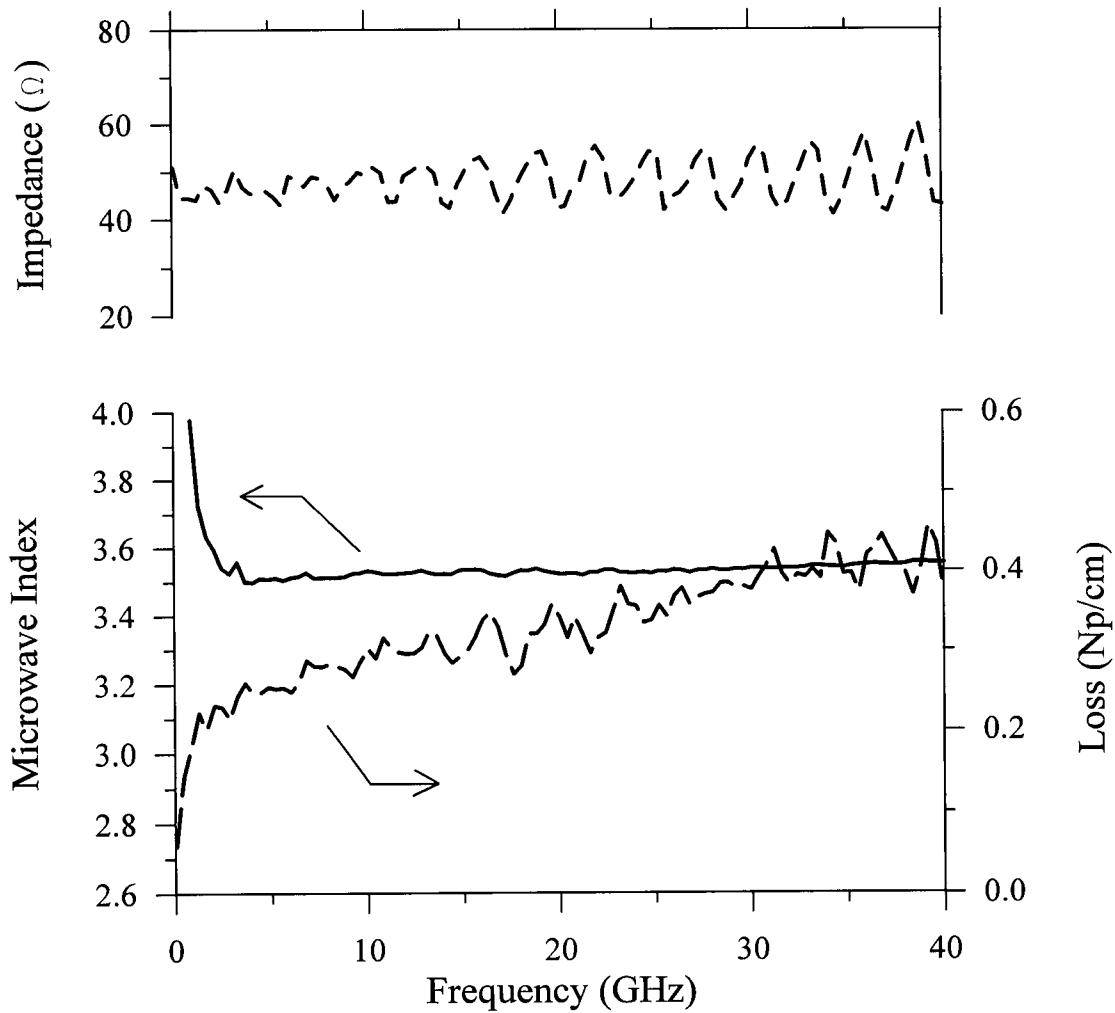
Figure 4.2.23. The microwave index (solid line), microwave loss coefficient (long-dashed line), and characteristic impedance (short-dashed line), measured for device 32 of Table 4.2.5 (generation 2 AlGaAs/GaAs substrate).

153
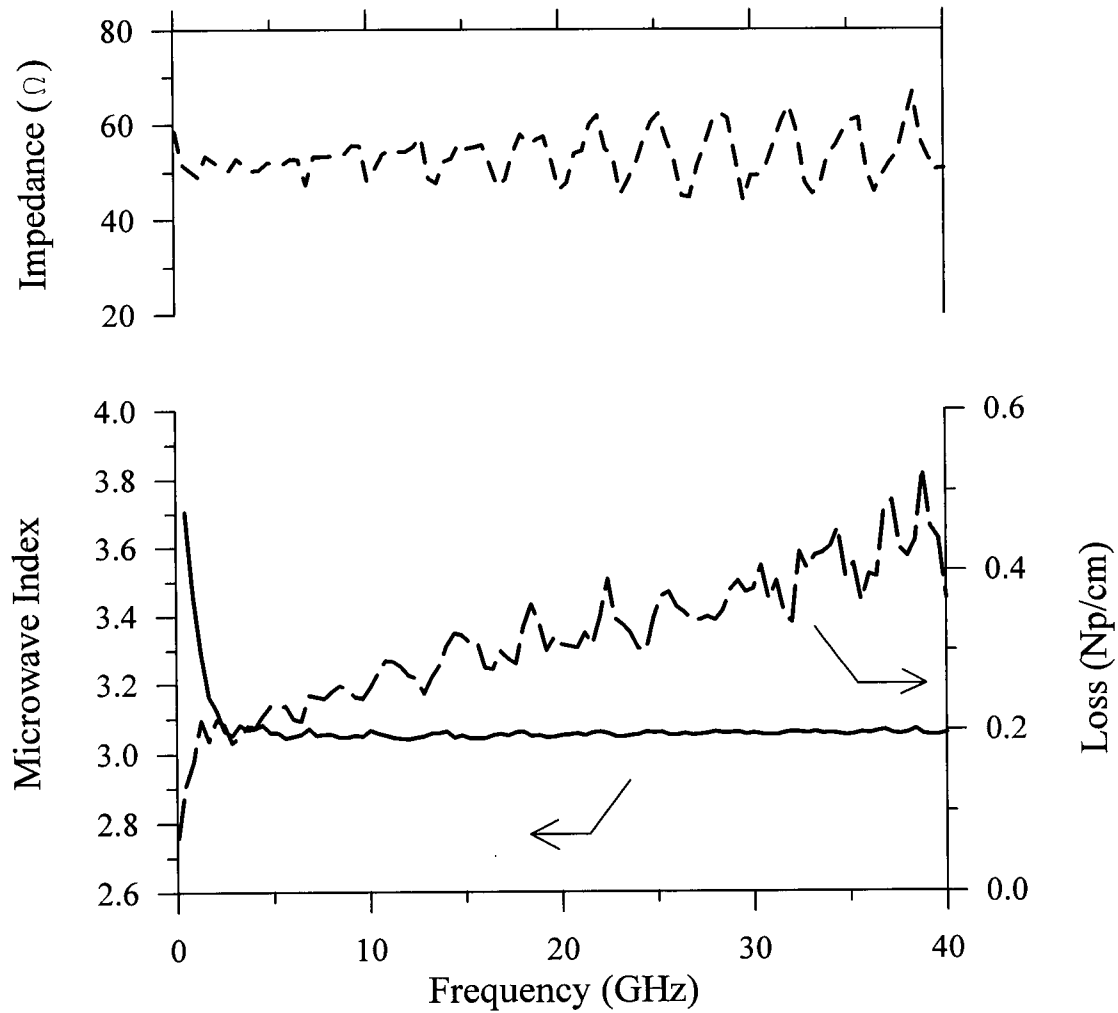
Figure 4.2.24. The microwave index (solid line), microwave loss coefficient (long-dashed line), and characteristic impedance (short-dashed line), measured for device 33 of Table 4.2.5 (generation 2 AlGaAs/GaAs substrate).
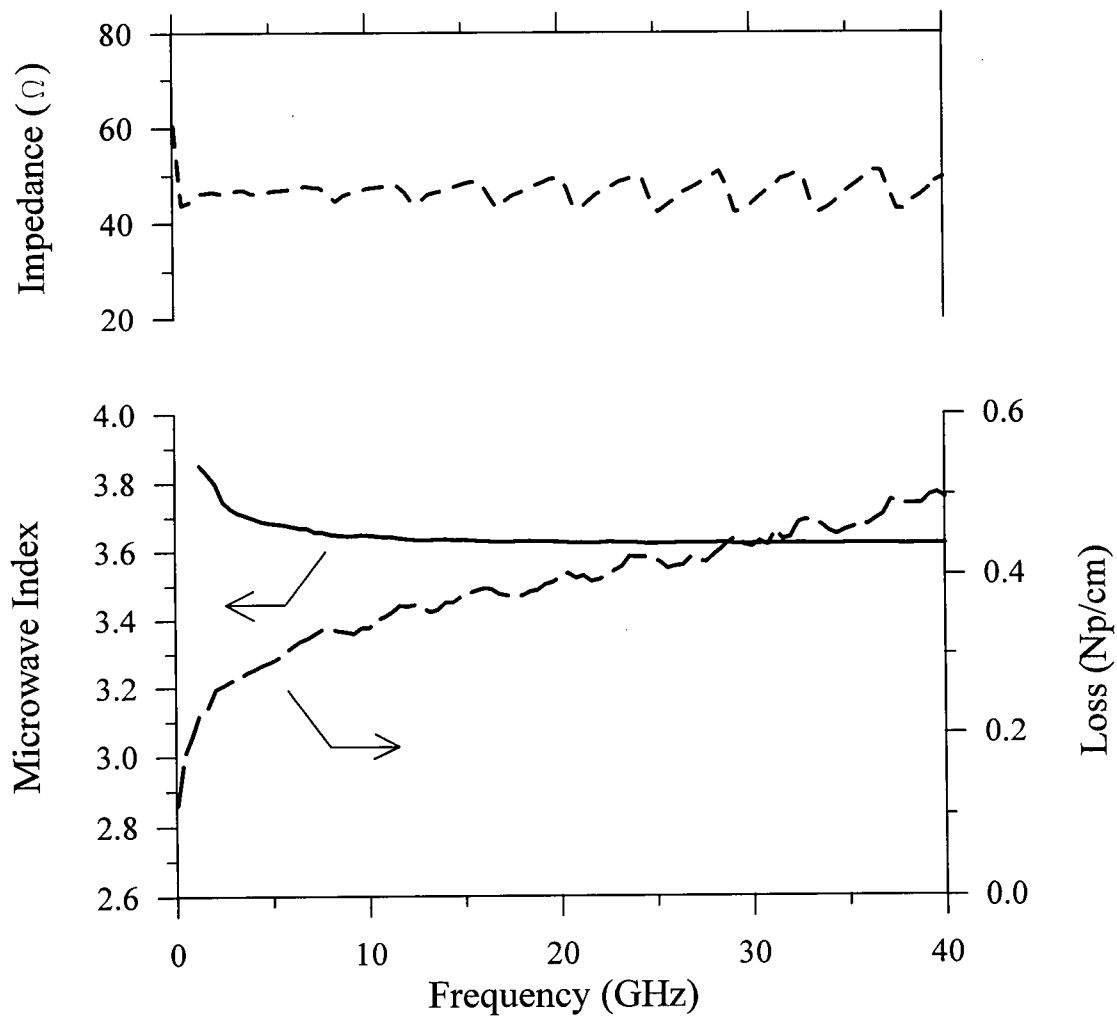
Figure 4.2.25. The microwave index (solid line), microwave loss coefficient
(long-dashed line), and characteristic impedance (short-dashed line), measured
for device 35 of Table 4.2.5 (generation 2 AlGaAs/GaAs substrate).
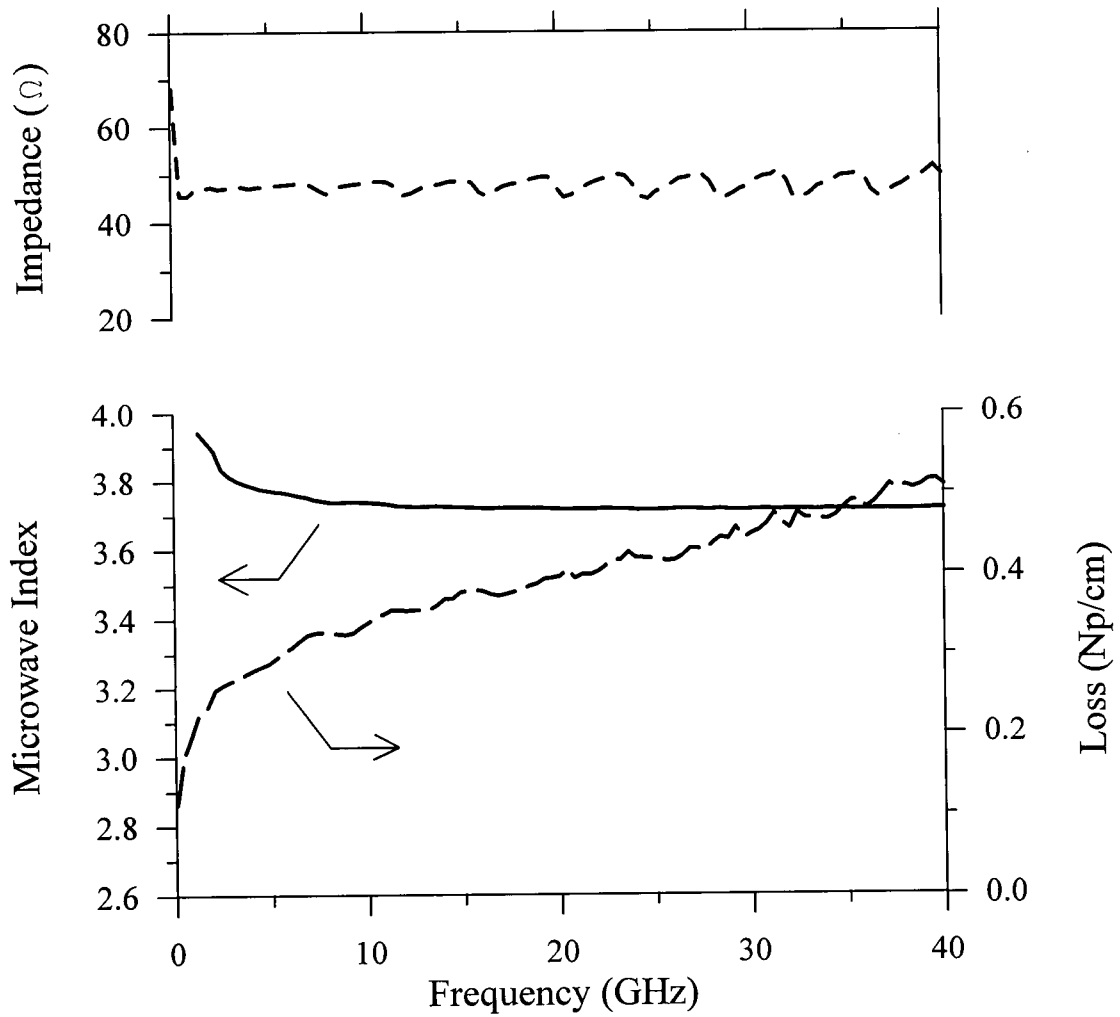
Figure 4.2.26. The microwave index (solid line), microwave loss coefficient (long-dashed line), and characteristic impedance (short-dashed line), measured for device 37 of Table 4.2.5 (generation 2 AlGaAs/GaAs substrate).

4.3. Optical Measurements

The fabricated generation 2 devices were tested for both low and high frequency modulation of light. Low frequency measurements were done at UBC at frequencies below 1 MHz. The laser diode used for these measurements had a λ_o of 1.3 μm. The results of these measurements on both the Mach-Zehnder (MZ) and the polarization converter (PC) type modulators are presented in section 4.3.1. High frequency measurements, up to 20 GHz, were performed at the CRC using a 1.55 μm laser. Again both MZ and PC type devices were tested; the results are presented in section 4.3.2.

4.3.1. Low-Frequency Results

Figure 4.3.1 shows a block diagram of the set-up used for the low-frequency optical measurements at UBC. The infrared laser was an LAS 300-1300-6 diode laser from LaserMax Inc., Rochester, NJ. The wavelength was 1.3 μm and the polarization ratio was quoted to be greater than 200:1. The laser light was coupled into a piece of polarization-maintaining (PM) fibre. The optical power at the output of the fibre was ~ 1 mW; the polarization ratio was close to 100:1. The output end of the fibre was held in a micropositioner such that the light coming out of the fibre was horizontally polarized (parallel to the x axis, see section 2.3). The fibre end was positioned flush with the input end of the optical ridge waveguides in order to couple light into the TE-like mode of the waveguides. The photo-detector was a model 1811 IR from New Focus Inc, Santa Clara, CA. The conversion gain of this detector was about 3.28×10^4 V/W and the dark level was -0.03 V. The detector bandwidth was quoted as 125 MHz. The digital oscilloscope was an HP54600A

dual channel digital storage scope from Hewlett-Packard. A microcomputer was attached to the oscilloscope using an RS-232 link. Both the applied electrical signal and the modulated optical signal were measured on the oscilloscope. A data acquisition program, Scopelink™ from Hewlett-Packard, was used to transfer both image and text data from the oscilloscope to the computer. The signal generator was a model LS51 function generator from Servomex Inc., capable of applying ±75 volts at up to 500 Hz. In the later stages of the experiment, the above signal generator was replaced by a lower-voltage higher-frequency function generator, model PM5132 from Philips, Germany, together with a high-voltage amplifier, model 3211 from New Focus, Inc. The amplifier could be used at up to 1 MHz, had a gain of 40, and had cut-off voltages of ±200 V. The electrical signal was applied to the coplanar electrodes using two (or three, as the need may be) micromanipulator probes, model PRO195RE from Wentworth Laboratories, Brookfield, CT. Other probes were also used during various stages of the measurements.

4.3.1.1. Mach-Zehnder Type Modulators

Figure 4.3.2 shows the results of the measurements on device 36 (see Table 3.3.6 for the electrodes' dimensions). A ±55 volts, 500 Hz sinusoidal signal was applied to the electrodes. The ideal transfer function of a MZ modulators can be written as

$$I_{out} = \frac{I_{in}}{2}\left[1 + \cos\left(\frac{\pi V}{V_\pi} + \phi_i\right)\right] \tag{4.3.1}$$

where I_{out} and I_{in} are the optical power at the output and the input of the modulator,

158

respectively, V is the applied voltage, V_π is the half-wave voltage, and ϕ_i is the intrinsic bias of the modulator. For a non-ideal MZ modulator, the transfer function can be rewritten as

$$I_{out} = I_{dc} + \gamma \cos\left(\frac{\pi V}{V_\pi} + \phi_i \right) \qquad (4.3.2)$$

where I_{dc} is a constant offset and γ is the amplitude of the sinusoidal portion. The extinction ratio can then be defined as $(I_{dc} + \gamma)/(I_{dc} - \gamma)$. The half-wave voltage is defined as the voltage required to obtain a phase difference of π radians between the fundamental modes propagating in the two branches of the MZ interferometer and may be estimated using equation (2.4.17).

The extinction ratio for this device is $\sim 100{:}1$ (limited by the input light polarization), the half-wave voltage is ~ 25 V, and the intrinsic bias is $\sim \pi/5$. The estimated half-wave voltage for this device, using equation (2.4.17), is $7.35/\Gamma$ volts at $\lambda_o = 1.3$. The comparison between the measured value of V_π and its theoretical value results in a $\Gamma \sim 0.3$. Γ in the range of 0.5 to 0.7 (these values are not optimized) has been reported for devices having conventional coplanar electrodes on ridge waveguides of this type (without an SiO_2 layer) [15], [67]. The field reduction due to the SiO_2 layer, most importantly, accounts for the lower value of Γ here. The value of V_π here is rather large; however, the modulator design was not optimized for a low value of V_π; it was intended to show that this kind of modulator can be achieved using slow-wave electrodes (V_π may, in fact, be smaller or, equivalently, Γ may be larger than reported here; see the discussion in the next section about electric field screening in the epitaxial layer).

4.3.1.2. Polarization Converter Type Modulators

Figures 4.3.3 to 4.3.5 show the results of the measurements on devices 27, 29, and 37, respectively (see Table 3.3.6 for the electrodes' dimensions). The same set-up given in section 4.3.1.1 (see Figure 4.3.1) was used. The only difference was that the analyzer was oriented with its transmission axis parallel to the z axis (see section 2.4) so that the vertically polarized light (from the TM-like mode of the waveguides) could pass through it. As mentioned in the previous section, the input light was coupled into the TE-like mode of the waveguide; i.e., the devices were tested as TE-to-TM mode converters. Figures 4.3.3 to 4.3.5 confirm that the transfer function of these mode converters are of the type predicted by our model, developed in chapter 2. Also it can be seen that the half-wave voltage, as expected (see equation 2.4.17), depends on the electrode length, L, the duty cycle, τ, and the gap-width, g_p.

The mode converters' performances, as shown in the Figures 4.3.3 to 4.3.5 do not appear to be perfectly symmetric with respect to the polarity of the applied voltage. The imperfections in the device fabrication, and most importantly, the electrode-to-ridge relative alignment, can partially explain this lack of symmetry, see Figures 2.4.20 and 2.4.22. We also speculate that mobile charged particles in the epitaxial layer and/or AlGaAs/SiO$_2$ interface, probably, contribute to this effect as well. These charged particles may also work to screen the applied electric field and, therefore, to reduce the effectiveness of the modulating power. I would like to emphasize that this theory (mobile charged particles) is only a speculation at this point in time, and a more thorough investigation of this effect is in progress in collaboration with the CRC.

160

To investigate whether these charged particles contribute to the screening of the applied field, the measurements were performed at various frequencies. It is expected that slowly moving particles, having long relaxation times, would not move significantly in response to higher frequency signals and, therefore, would not screen the applied field. Figure 4.3.6 shows the response of device 26 to 120 V (peak-to-peak) applied signals from 20 Hz to 20 kHz. We were limited by the bandwidth of the measuring system. As can be seen in Figure 4.3.6, the modulation improves significantly as the frequency increases from 20 Hz to 1 kHz. This result implies that our explanation in terms of "slowly moving charged particles screening the applied electric field" appears to have merit. Also, the improvement in the response becomes smaller and smaller as the frequency increases above a few kHz; therefore, the relaxation time constant for most of these charged particles should be larger than 1 ms. It should also be noted that the measurements reported in Figures 4.3.2-4.3.4 were done at ~ 500 Hz; the performances will probably be better (smaller V_π) at higher frequencies.

The above observation regarding the relationship between the frequency of the applied signal and the amount of optical modulation also implies that a d.c. voltage cannot be used to bias these particular devices. For the purpose of testing at microwave frequencies, perhaps a relatively low-frequency (~ kHz) square signal can be used to periodically bias these devices, see section 4.3.2.2. Also, applying a large d.c. bias can result in device break down. For example, a sinusoidal voltage of amplitude 80 volts (0 d.c. bias) was applied to device 26 for several hours without damaging the device. The same device was, a few days later, tested using a sinusoidal voltage of amplitude 20 volts, and a d.c. bias of -60 volts. The device

broke down after ~ 10 minutes. Figure 4.3.7 shows a photograph of the damaged pads and ridge waveguide.

Also, a comparison of the values of V_π measured at frequencies above 1 kHz (at larger voltages) with those estimated using equation (2.4.17) gives a $\Gamma \sim 0.5$ for these devices. For example, for device 27, $V_\pi \approx 8$ V (at ~ -40 V), see Figure 4.3.3 and V_π as calculated from equation (2.4.17) is $4.2/\Gamma$ volts. Considering the effect of the SiO_2 layer in reducing the field in the AlGaAs substrate, this value of Γ is in good agreement with those reported elsewhere for similar devices that use conventional coplanar electrodes, see [15] for example.

4.3.2. High-Frequency Results

Figure 4.3.8 shows a block diagram of the set-up that I made for the high-frequency optical measurements at the CRC (I used the equipment available there to set up for my experiments). The infrared laser was a 1.52 μm diode laser model PT-450A-1550 from Sea Star Optics, Victoria, BC. The fibre end was positioned flush with the input end of the optical ridge waveguides in order to couple light mostly into the TE-like mode of the waveguides. The optical power at the end of the input PM fibre was ~ 1 mW; the polarization ratio was close to 100:1. The photo-detector was a model HP 70810B photo-detector from Hewlett-Packard. The conversion gain of this detector was about 2432 V/W, and the low-frequency cut-off of the photo-detector was 10 kHz. The detector was usable up to 22 GHz. The gain of the detector was a function of frequency, and the data obtained had to be corrected using the correction table provided by the manufacturer; Figure 4.3.9 shows a plot of the correction factors to be used as a function of frequency. The microwave sweeper was

162

an HP 8350B sweep oscillator together with an HP 83594A RF plug-in for operation from 2 GHz to 26.5 GHz and an HP 83522A RF plug-in for operation from 0.1 GHz to 2.4 GHz, all from Hewlett-Packard. The bias-Tee was an HP 11590A for operation from 1 GHz to 18 GHz. The microwave spectrum analyzer was a model HP 8565E, again from Hewlett-Packard, usable from 30 Hz to 50 GHz. The microwave probes used were the same as those described in section 4.2. The fibre polarization-splitting unit (FPS) was a model FOBS-12-333-PSS-1550-PBS from OZ Optics, Kanata, Ontario, with a loss of ~ 6 dB (depending on how well the fibres were connected to it). The FPS was not needed for the measurements on the MZ type devices. The interrogating PM fibre was aligned to the output end of the optical ridge waveguide so that the power from the TE-like mode of the waveguide would couple into one of its two major axes and the power from the TM-like mode of the waveguide would couple into its other major axis. The two polarizations were separated using the FPS and the chosen polarization was transmitted to the photo-detector using a single-mode (SM) fibre.

4.3.2.1. Mach-Zehnder Type Modulators

Device 35 was tested for small-signal optical modulation up to 20 GHz; we were limited by the photo-detector band-width and the sweep oscillator power. Figure 4.3.10 shows the results of the optical measurement from 2 to 19.5 GHz. The measured data are corrected for the variations in the detector gain (see Figure 4.3.9) and the input power trend as functions of frequency. Figure 4.3.11 shows the measured RF power out of the input cable which was connected to the HP 83594A RF plug-in via the bias-Tee in the calibration test where the output power of the HP 83594A RF plug-in was set to 0 dBm.

Because of the wide range of the sweep (2 to 20 GHz) for both the spectrum-analyzer and the sweep oscillator, the measurement had to be taken over a long period of time (~ 1 hour) to get a large number of data points. Still, many of the samples were taken when the centre frequency of the spectrum analyzer did not necessarily coincide with the centre frequency of the sweep oscillator. This in part explains the scatter in the measured data shown in Figure 4.3.10 — no statistics have been applied to these data points. The fluctuation in the applied microwave power (see Figure 4.3.11) also, partially, contributes to the spread of the measured data points. A good indication of the device performance can be obtained by connecting the dots corresponding to the maximum values of the output in each frequency interval. The microwave power applied was nominally 12 dBm and no bias voltage was applied. Also, similar to the low-frequency set-up, in this set-up the output end of the input fibre was held in a micropositioner such that the light coming out of the fibre was essentially horizontally polarized (parallel to the x axis), and the fibre end was positioned flush with the input end of the optical ridge waveguides in order to couple the light into the TE-like mode of the waveguides only.

Over all, there is no significant decay in the modulation up to 20 GHz. The difference between the values measured at ~ 2 GHz and those measured at ~19 GHz is less than 1 dB. Table 4.3.1 provides the expected performance of the device at several frequencies up to 40 GHz, calculated (see section 2.2) from the measured microwave index and loss for this device as given in Figure 4.2.25. The expected optical modulation drop from 2 to 20 GHz is only 0.5 dB, which is on the order of the accuracy of the optical measurements. As can be seen from Table 4.3.1, the 3-dB optical bandwidth of this device is expected to be larger than 40

164

GHz. In fact using $n_\mu = 3.62$ and $\alpha = \alpha_o \times \sqrt{f}$ with $\alpha_o = 0.082$ Np/(cm.GHz$^{1/2}$) (calculated

from the measured value of the loss at 40 GHz), the 3-dB optical bandwidth of this particular

device is estimated to be 49 GHz ($n_{eff} = 3.32$ was used), see section 2.2. However, for better

microwave-to-lightwave velocity match, e.g., $|n_\mu - n_{eff}| = 0.1$, the bandwidth for an

otherwise identical device could be in excess of 120 GHz.

4.3.2.2. Polarization Converter Type Modulators

For high-frequency, small-signal modulation using polarization converter type devices,

the TE-to-TM mode converter configuration was used in a slightly different configuration.

The main reason was that we were not able to bias the mode converters using a d.c. voltage

(this was explained in section 4.3.1.2). The mode converters, as explained in section 2.4, are

not very useful for small-signal operation if they are biased at zero voltage and if the modal

birefringence in the optical waveguide is significant. For example, consider device 27.

Figure 4.3.12 shows the transfer function of this device (at two scales) at low-frequency

obtained using the model developed in chapter 2 (section 2.4) . The input light is assumed

to be 100% coupled into the TE-like mode (x-polarized), and the power out of the TM-like

mode of the waveguide (z-polarized) is plotted as a function of the voltage applied to the

electrodes. The following values, which are very close to those expected for device 27 and

the set-up, were used in obtaining this transfer function: $\lambda_o = 1.52$ μm, $n_{TE} = 3.322$, $n_{TE} - n_{TM}$

$= 0.00024$, and $\Gamma = 0.5$. As can be seen from Figure 4.3.12, this device would be a very

inefficient modulator for small-signal modulation (e.g., $|V| < 2$ volts) if it were biased at $V_b =$

0. In fact, it would be a (rather inefficient) second harmonic generator or frequency doubler

(possibly another application for PC type devices!). We even tried to bias device 33, applying a 400 Hz, ±15 V signal through the bias-Tee and the Cascade™ GS probes to which we had access. As mentioned before, the GS and SG microwave probes, as opposed to GSG ones from GGB indutries, were old and in a poor shape. The GS probe actually broke down under the above-mentioned applied bias, damaging device 33 in the process; neighbouring devices, 32 and 34, were also partially damaged. Therefore, we decided to discontinue applying a bias when using GS or SG probes, i.e., when testing CPS type electrodes.

Because of this biasing problem, we tested the polarization converter type devices in a slightly different mode of operation. The same modulator configuration that was used for Figure 4.3.12 was used with one difference: the input fibre was rotated by about 20°, i.e., the input light was aligned with its plane of polarization at 20° to the x axis (horizontal) and 70° to the z axis. In this way, about 88% of the optical power coupled from the fibre into the waveguide would be in the TE-like mode and about 12% would be in the TM-like mode at the input of the waveguide. Figure 4.3.13 shows the transfer function of device 27, for the same parameters used for Figure 4.3.12, with the input light polarized at 20° to the x axis. Again, the output optical power out of the TM-like mode (z-polarized) is plotted. The input section of the ridge waveguide, the region from the substrate edge to the start of the electrodes, is taken as 1 mm (close to that for device 27). As can be seen from Figure 4.3.13, this configuration does not provide a mode converter with a very good extinction ratio; however, it has a relatively linear transfer function near the zero-bias point, and can be used for small-signal modulation; for an applied sinusoidal voltage having an amplitude of 2 volts, the optical power could change by ~ 4 % of the total optical power out of the waveguide, see

figure 4.3.13.b. Of course, this device is not as efficient as one that is properly biased or one that has $n_{TE} - n_{TM} = 0$; nevertheless, it is sufficient for our small-signal modulation testing at high frequencies.

The above suggested configuration was used to test device 27. The light out of the input fibre was linearly polarized at ~ 20° to the x axis. The optical power coupled into the output PM fibre was about 80 µW. Since this amount of optical power was sufficient for our measurements (the detector was sufficiently sensitive), the coupling of the light between the ridge waveguides and the optical fibres was not optimized any further. The polarizing-beam splitter separated the two orthogonally polarized (parallel to the x and z axes) light components into two single mode (SM) fibres. The optical power from one SM fibre was ~ 35 µw and the power from the other one was ~ 6 µW. This implies that ~ 85% of the power coupled into the ridge waveguide was coupled into one mode, the TE-like mode, and ~ 15% was coupled into the other polarization, the TM-like mode (note that since the amount of optical loss in the fibre optic beam-splitter is not identical for both polarizations, these numbers are not highly accurate). Figure 4.3.14 shows a plot of the modulated optical signal as a function of the applied microwave power at 7 GHz for device 27. The y axis on Figure 4.3.14.a shows the value of the photo-detector microwave power, P_{det}, in dBm, that we measured after correction for the detector's gain at 7 GHz (see Figure 4.3.9). The x axis shows the applied microwave power, $P_{applied}$, in dBm after correction for the loss in the input cable and the bias-Tee. Figure 4.3.14.b shows the same plot where the y axis indicates the optical power, I_{mod}, in µW (converted from dBm output power of the photo-detector) and the x axis indicates the amplitude of the applied voltage, V_o, in volts (converted from dBm input

power). These values are obtained using

$$I_{mod} = 260.1 \times 10^{\frac{P_{det}}{20}}$$
(4.3.3)

$$V_o = 10^{\frac{P_{applied} - 10}{20}}$$
(4.3.4)

For the above equations all lines and loads are assumed to be equal to 50 Ω, and the detector

gain of 2432 V/W (provided by the manufacturer) is used. The curves fitted to the data in

Figure 4.3.14 are parabolic functions (polynomial of order 2). Figure 4.3.14 shows that this

device has a relatively linear response in this range as suggested by the model.

Figure 4.3.15 shows the results of the optical measurements from 2 to 19.5 GHz for

device 27. Again, the measured data are corrected for the variations in the detector gain (see

Figure 4.3.9) and the input power trend as functions of frequency. As pointed out in section

4.3.2.1, many of the samples were taken when the centre frequency of the spectrum analyzer

did not necessarily coincide with the centre frequency of the sweep oscillator. This, in part,

explains the scatter in the measured data shown in Figure 4.3.15. These data were taken over

~10 minutes, as opposed to ~ 1 hour for the data plotted in Figure 4.3.10; that's partially why

the spread of the dots plotted in Figure 4.3.15 is greater than that of those plotted in Figure

4.3.10. The fluctuation in the applied microwave power (see Figure 4.3.11) also contributes

to the spread of the measured data points. The microwave power applied was nominally 15

dBm and no bias voltage was applied. The data are normalized with respect to the maximum

output power detected (at ~ 5 GHz), and, again, a good indication of the device performance

can be obtained by connecting the dots corresponding to the maximum values of the output in each frequency interval.

Figure 4.3.15 does not show an appreciable drop in the modulation up to 20 GHz. Table 4.3.2 provides the expected performance of the device at several frequencies up to 40 GHz using the same model parameters that were used for Figure 4.3.13. The data were calculated using the model developed in section 2.4 and using the measured microwave index and loss for device 27 given in Figure 4.2.22. The expected optical modulation drop from 2 to 20 GHz is only 0.45 dB, which is, again, on the order of the accuracy of the optical measurements. As can be seen from Table 4.3.2, the 3-dB optical bandwidth of this device is expected to be larger than 40 GHz. Using $n_\mu = 3.41$ and $\alpha = \alpha_o \times \sqrt{f}$ with $\alpha_o = 0.060$ Np/cm/GHz$^{1/2}$ (calculated from the measured value of the loss at 40 GHz), the 3-dB optical bandwidth is estimated to be 55 GHz. Note that for a well biased device with no modal birefringence (i.e., $n_{TE} - n_{TM} = 0$), and otherwise exactly identical to device 27, the 3-dB optical bandwidth of this mode converter would be 93 GHz, see section 2.2, equation (2.2.16).

Figure 4.3.16 shows the results of the optical measurement from 2 to 19.5 GHz for device 37, another polarization converter type device. The electrode for device 37 "over-slows" the microwave signal significantly, see figure 4.2.26, and, therefore, this device is expected to have a narrower bandwidth as compared to device 27. The set-up used here was identical to that used for device 27, described above. The theoretical transfer function for this device calculated using our model is given in Figure 4.3.17. Again, $\lambda_o = 1.52$ μm, $n_{TE} = 3.322$, $n_{TE} - n_{TM} = 0.00024$, and $\Gamma = 0.5$ were used. The electrode for this device was shorter

than that of device 27, it was only 1 cm long. The input optical waveguide section was 3.5 mm long. Again, one can see some scatter on the measured data in Figure 4.3.16; the performance of the device can be found using the upper edge of the data band. This device shows a 2 dB drop in the optical signal from 2 to 18 GHz. Table 4.3.3 provides the expected performance of the device at several frequencies up to 40 GHz. Again, these data were calculated using the model developed in section 2.4 and using the measured microwave index and loss for device 37 as given in Figure 4.2.26. The expected optical modulation drop from 2 to 20 GHz is ~1.3 dB, which is close to but less than what was measured. The 3-dB optical bandwidth of this device is calculated to be 29 GHz. Again, note that for a well biased device with no modal birefringence (i.e., $n_{TE} - n_{TM} = 0$), and otherwise exactly identical to device 37, the 3-dB optical bandwidth of the mode converter would be 38 GHz.

Table 4.3.1. High-frequency performance of device 35 (MZ-B-CPW type), calculated using the measured values for microwave index and loss (see Figure 4.2.25). M represents the amount of optical modulation at a particular frequency (for a well-biased modulator) relative to the amount of optical modulation at low frequency (d.c.).

Frequency (GHz)	α (Np/cm)	n_μ	M (dB) optical
2	0.26	3.79	-0.56
5	0.30	3.68	-0.66
10	0.34	3.65	-0.80
20	0.40	3.62	-1.13
30	0.45	3.62	-1.60
40	0.52	3.62	-2.27

Table 4.3.2. High-frequency performance of device 27 (PC-A-CPS type), calculated using the measured values for microwave index and loss (see Figure 4.2.22). M represents the amount of optical modulation at a particular frequency relative to the amount of optical modulation at low frequency (d.c.). See Figure 4.3.13 for the low-frequency response of the model.

Frequency (GHz)	α (Np/cm)	n_μ	M (dB) optical
2	0.21	3.45	-0.78
10	0.27	3.41	-0.99
20	0.31	3.40	-1.23
40	0.38	3.41	-2.08

Table 4.3.3. High-frequency performance of device 37 (PC-A-CPW type), calculated using the measured values for microwave index and loss (see Figure 4.2.26). M represents the amount of optical modulation at a particular frequency relative to the amount of optical modulation at low frequency (d.c.). See Figure 4.3.17 for the low-frequency response of the model.

Frequency (GHz)	α (Np/cm)	n_μ	M (dB) optical
2	0.26	3.89	-0.39
10	0.34	3.74	-0.77
20	0.40	3.72	-1.66
30	0.45	3.72	-3.28
40	0.51	3.72	-4.60
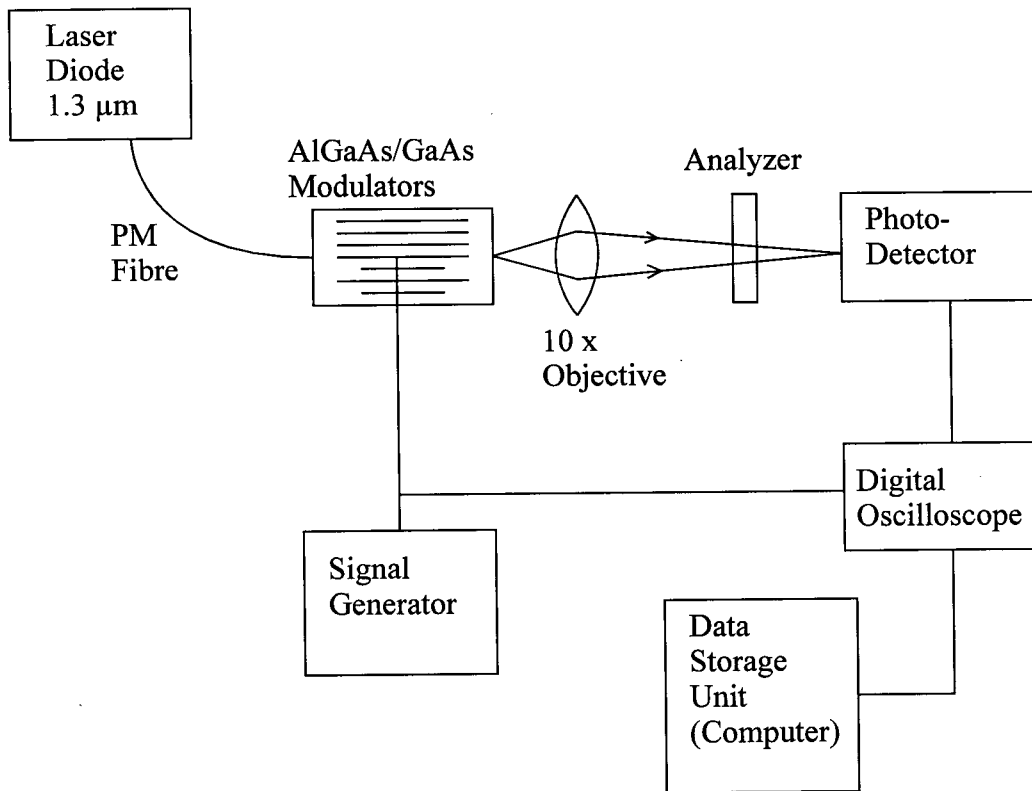
Figure 4.3.1. Block diagram of the set-up used for the low-frequency optical measurements.
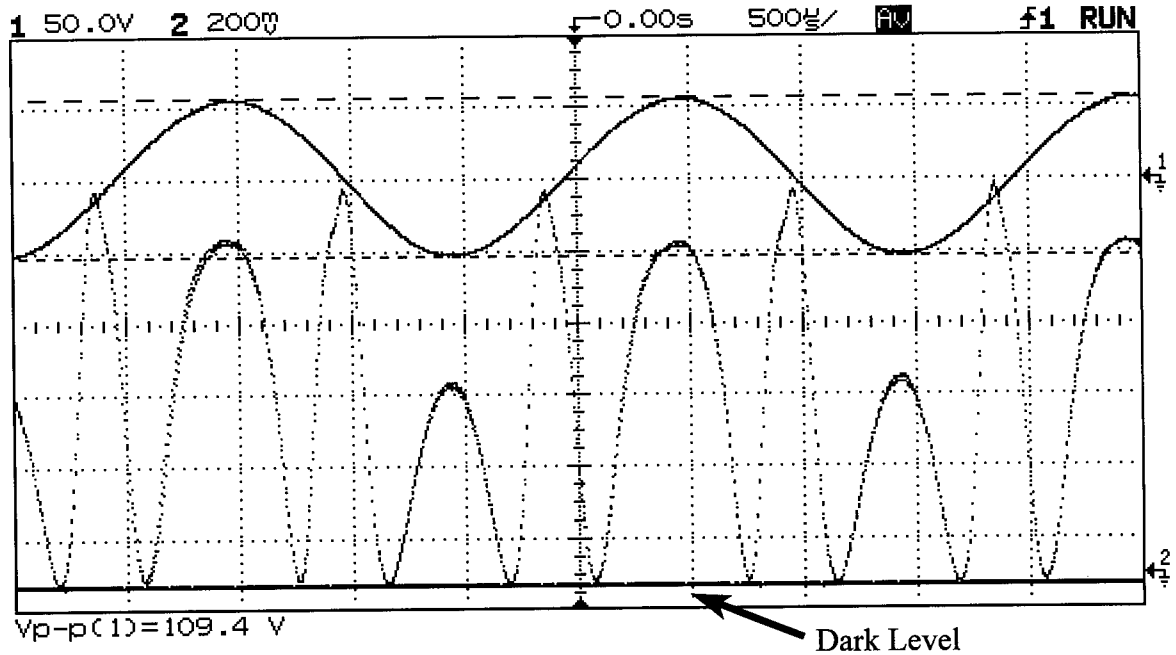
Figure 4.3.2. Oscilloscope image showing the modulation characteristics of device 36 (MZ-B-CPW type). The upper trace shows the applied voltage and the lower trace is the output of the modulator measured using the IR photo-detector.
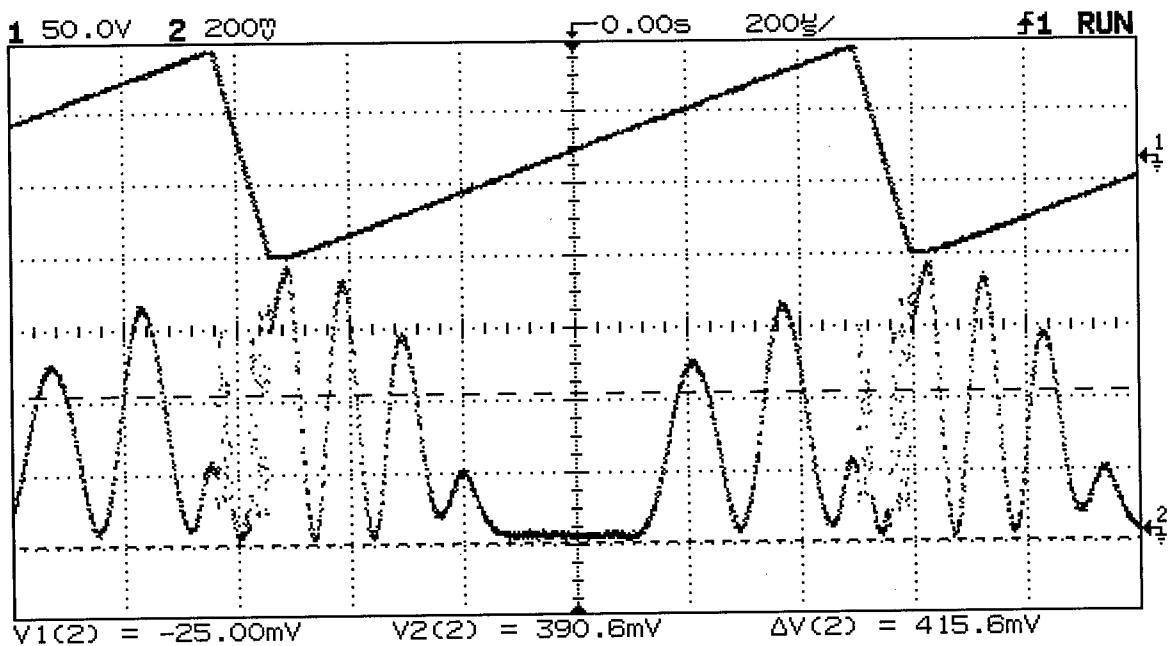
Figure 4.3.3. Oscilloscope image showing the modulation characteristics of device 27 (PC-A-CPS type). The upper trace shows the applied voltage and the lower trace is the output of the modulator (the TM-like polarization) measured using the IR photo-detector.

174
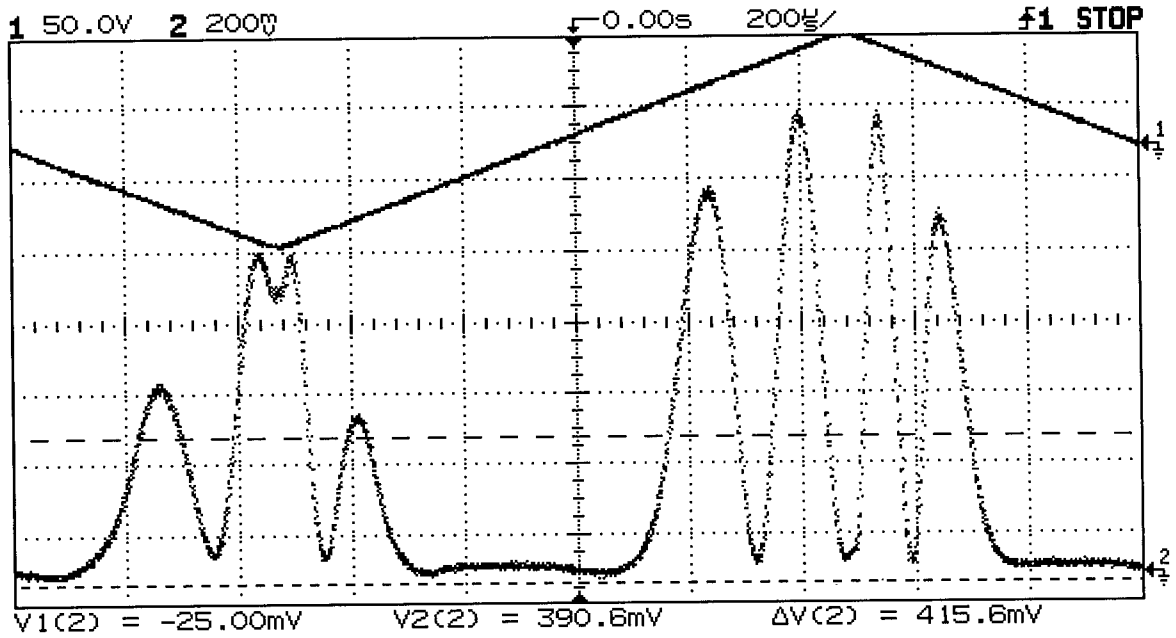
Figure 4.3.4. Oscilloscope image showing the modulation characteristics of device 29 (PC-A-CPS type). The upper trace shows the applied voltage and the lower trace is the output of the modulator (the TM-like polarization) measured using the IR photo-detector.
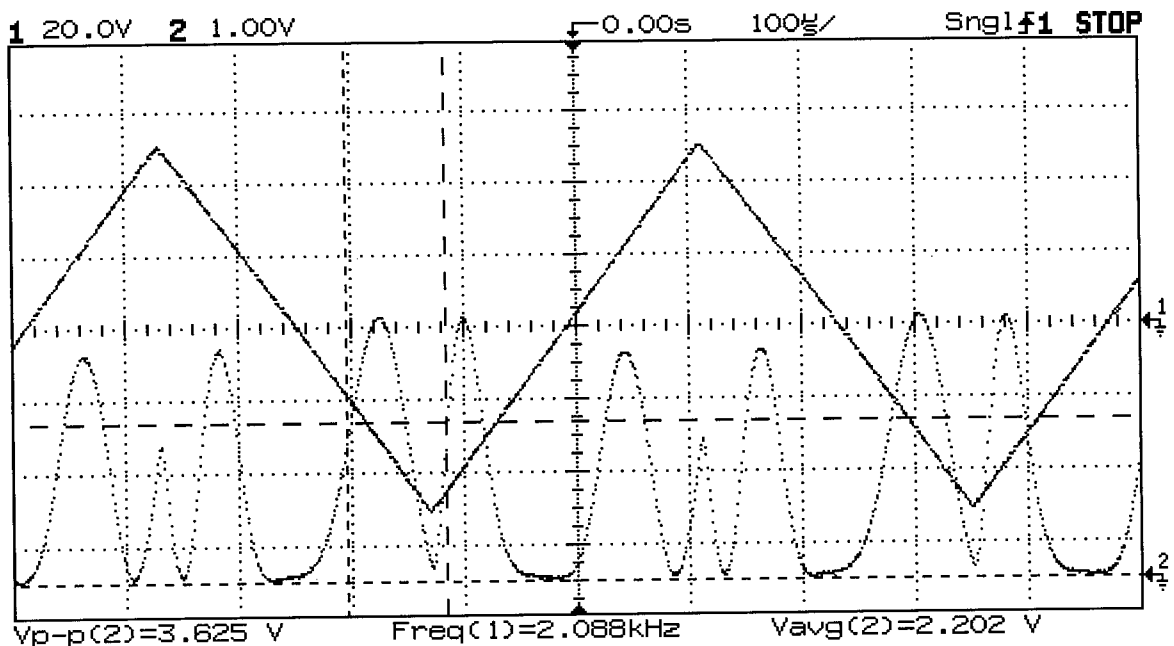
Figure 4.3.5. Oscilloscope image showing the modulation characteristics of device 37 (PC-A-CPW type). The upper trace shows the applied voltage and the lower trace is the output of the modulator (the TM-like polarization) measured using the IR photo-detector.
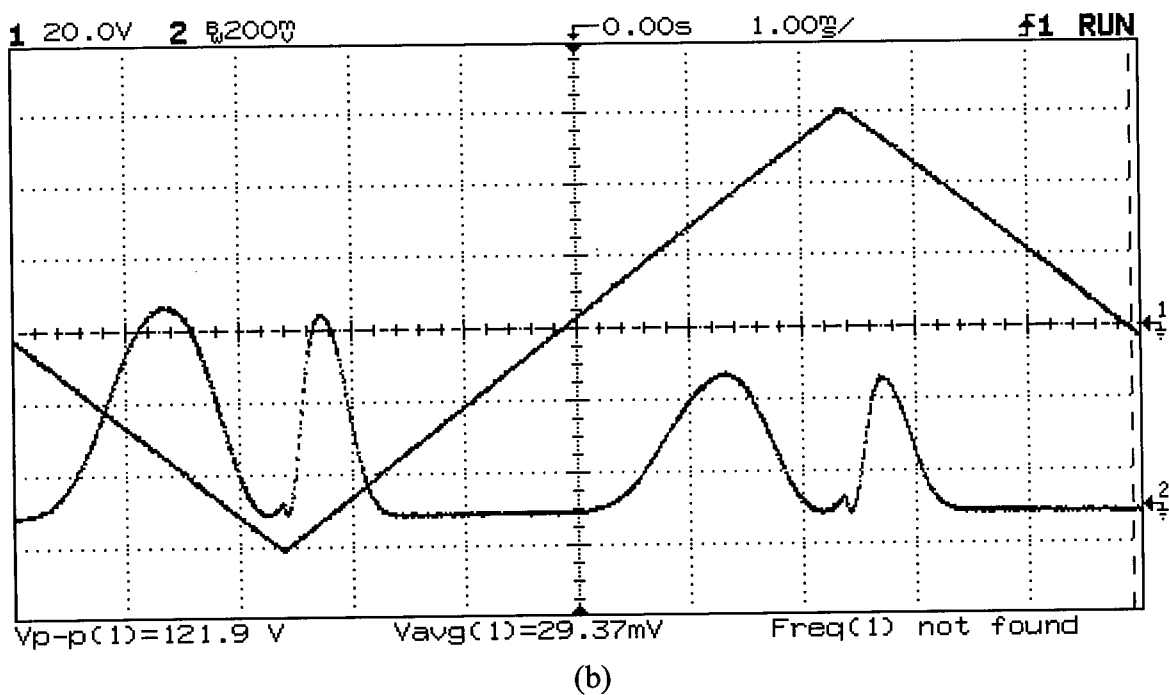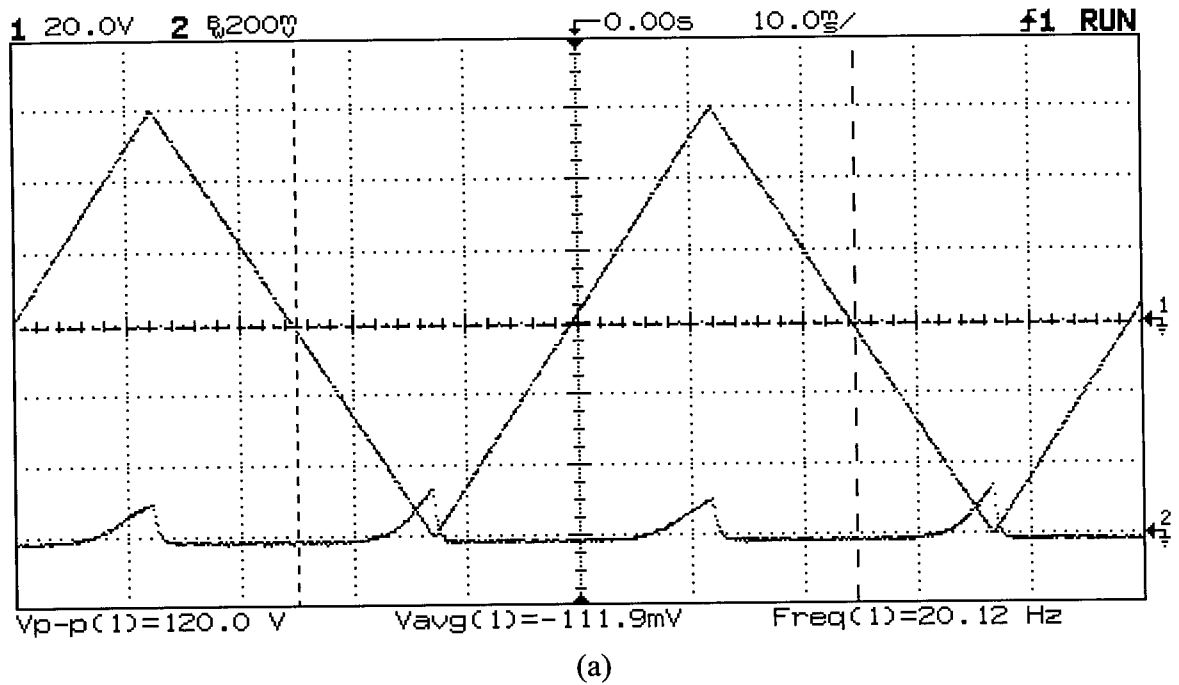
Figure 4.3.6. Oscilloscope images showing the modulation characteristics of device 26. The upper traces show the applied voltage and the lower traces show the output of the modulator (the TM-like polarization) measured using the IR photo-detector. The frequency of the applied signal was (a) 20 Hz, (b) 100 Hz, (c) 500 Hz, (d) 1 kHz, (e) 5 kHz, and (f) 20 kHz.

176

Vp-p(1)=120.0 V   Vavg(1)=11.56mV   Freq(1) not found

(c)

Vp-p(1)=125.6 V   Vavg(1)=27.50mV   Freq(1) not found

(d)

177

Vp-p(1)=123.1 V   Vavg(1)=63.29mV   Freq(1) not found

(e)

Vp-p(1)=121.9 V   Vavg(1)=-71.41mV   Freq(1) not found

(f)

178
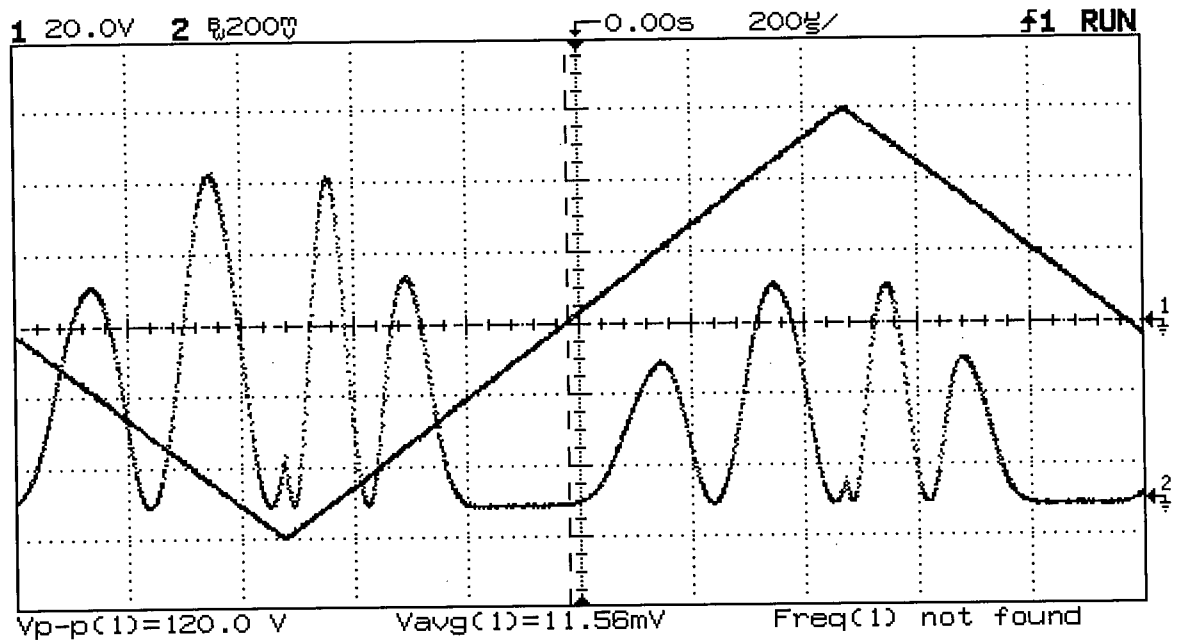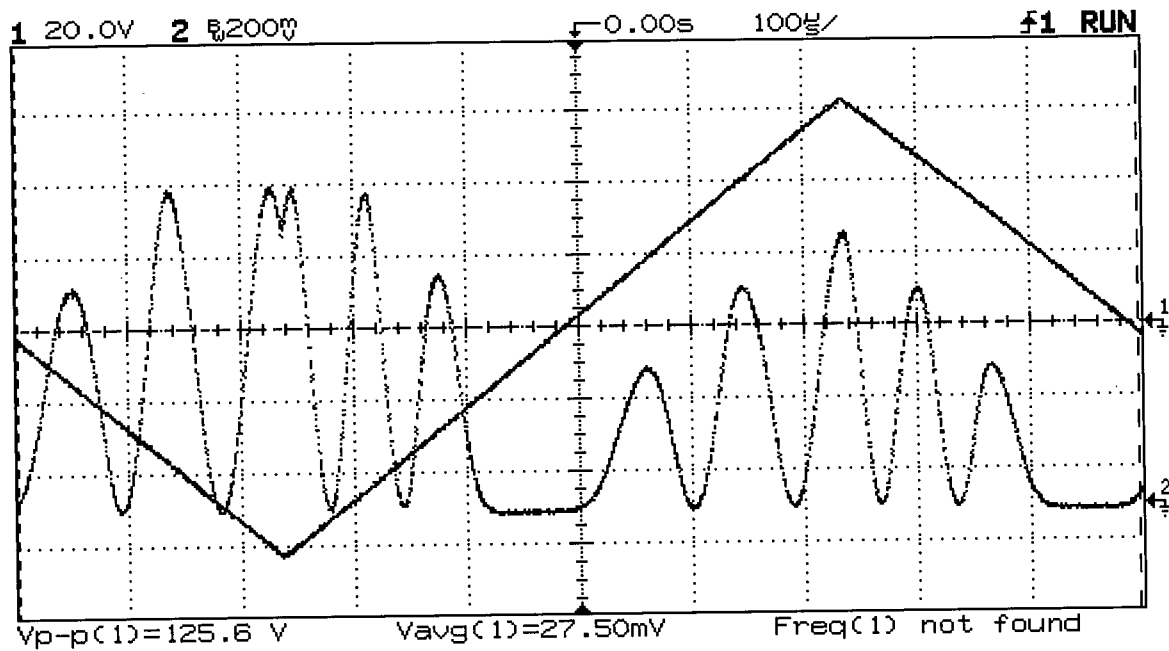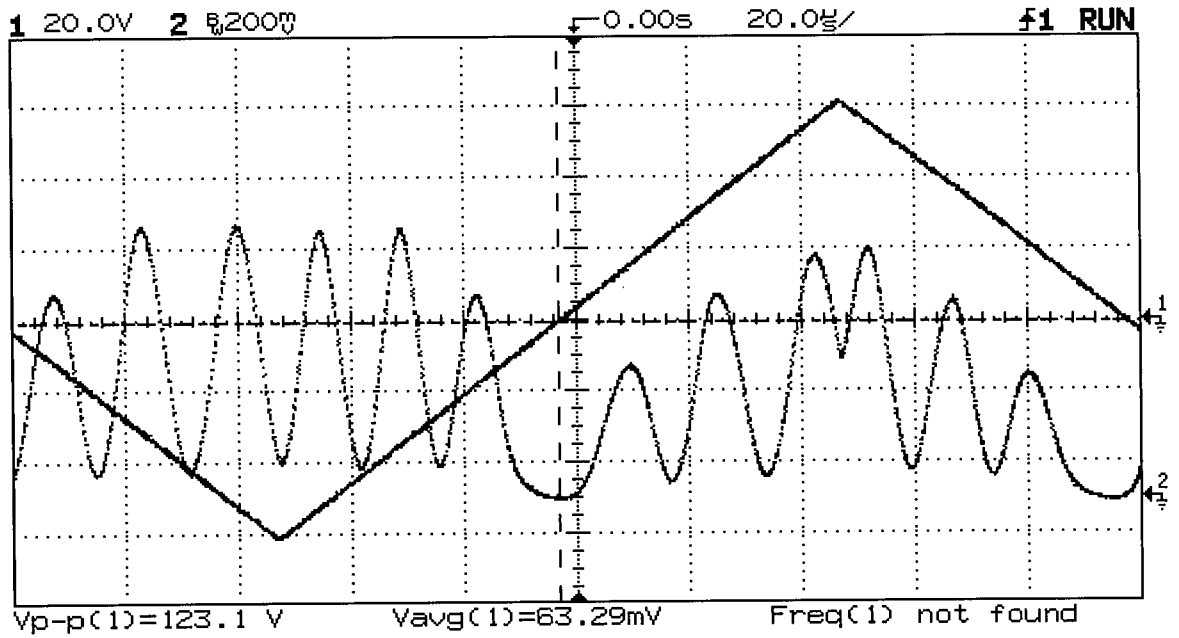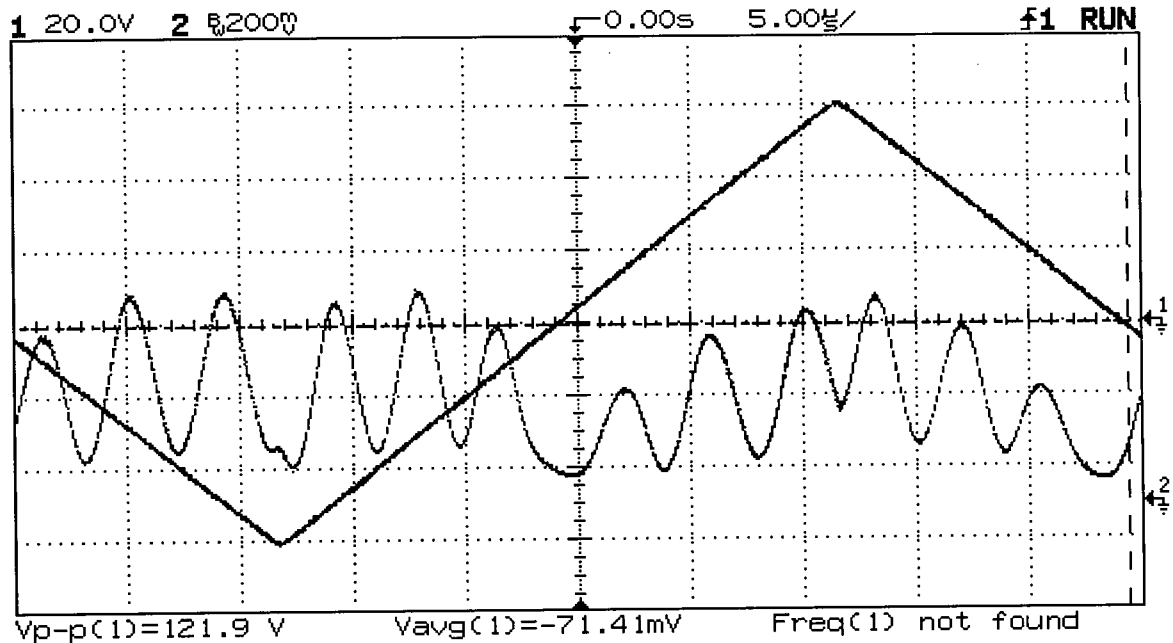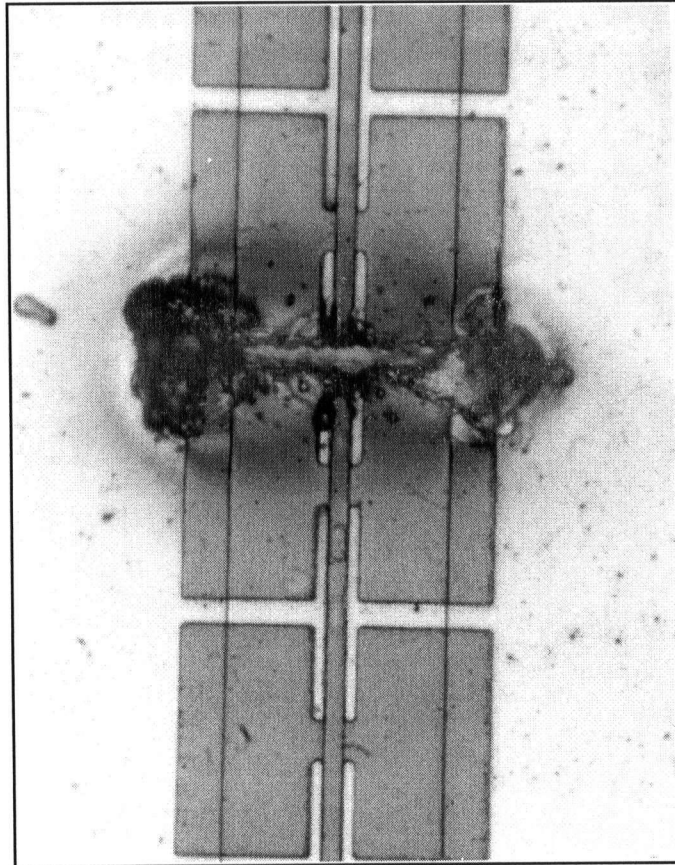
Figure 4.3.7. Picture of the damaged fins and pads of device 26 on the generation 2 AlGaAs/GaAs substrate. A d.c. bias of -60 V, and a sinusoidal voltage of amplitude 20 V, was applied for ~ 10 minutes.
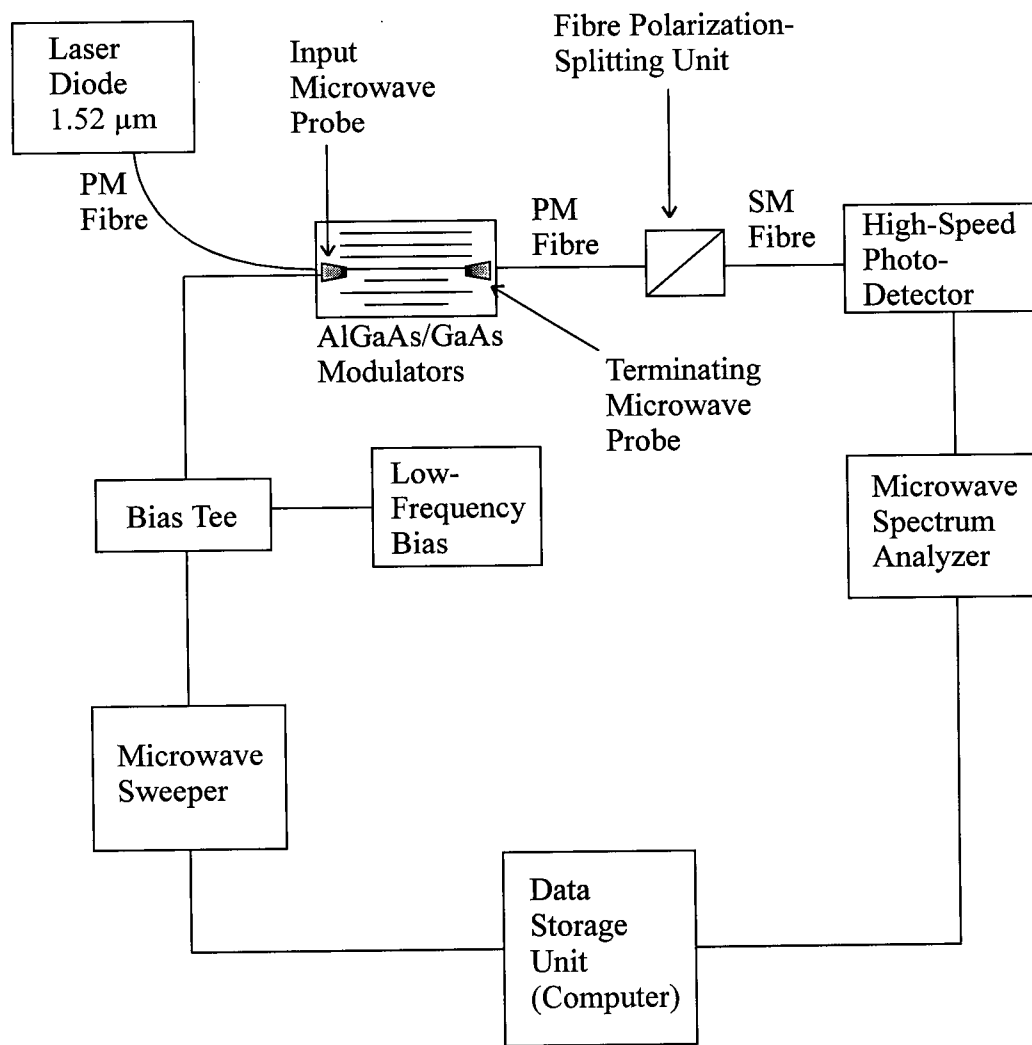
Figure 4.3.8. Block diagram of the set-up used for the high-frequency optical measurements.
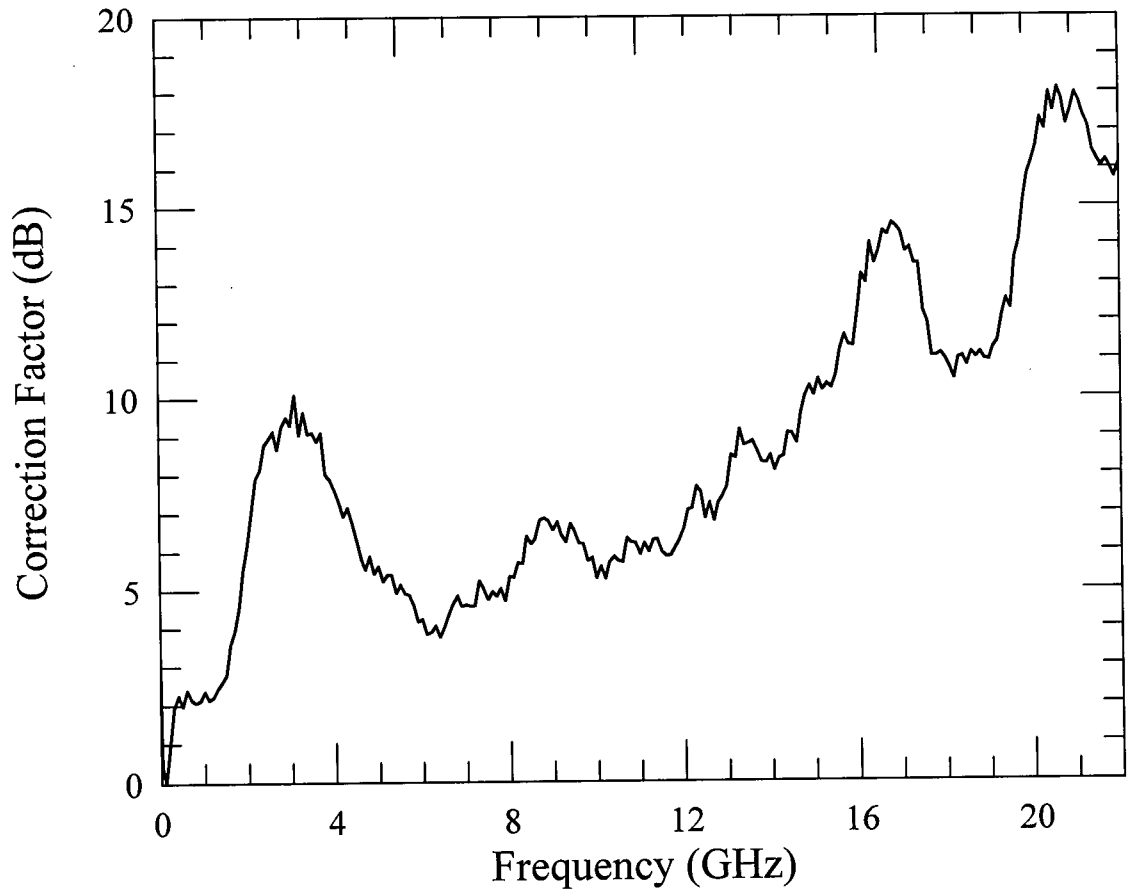
Figure 4.3.9. The correction factor to be used with the HP 70810B photo-detector as a function of frequency.
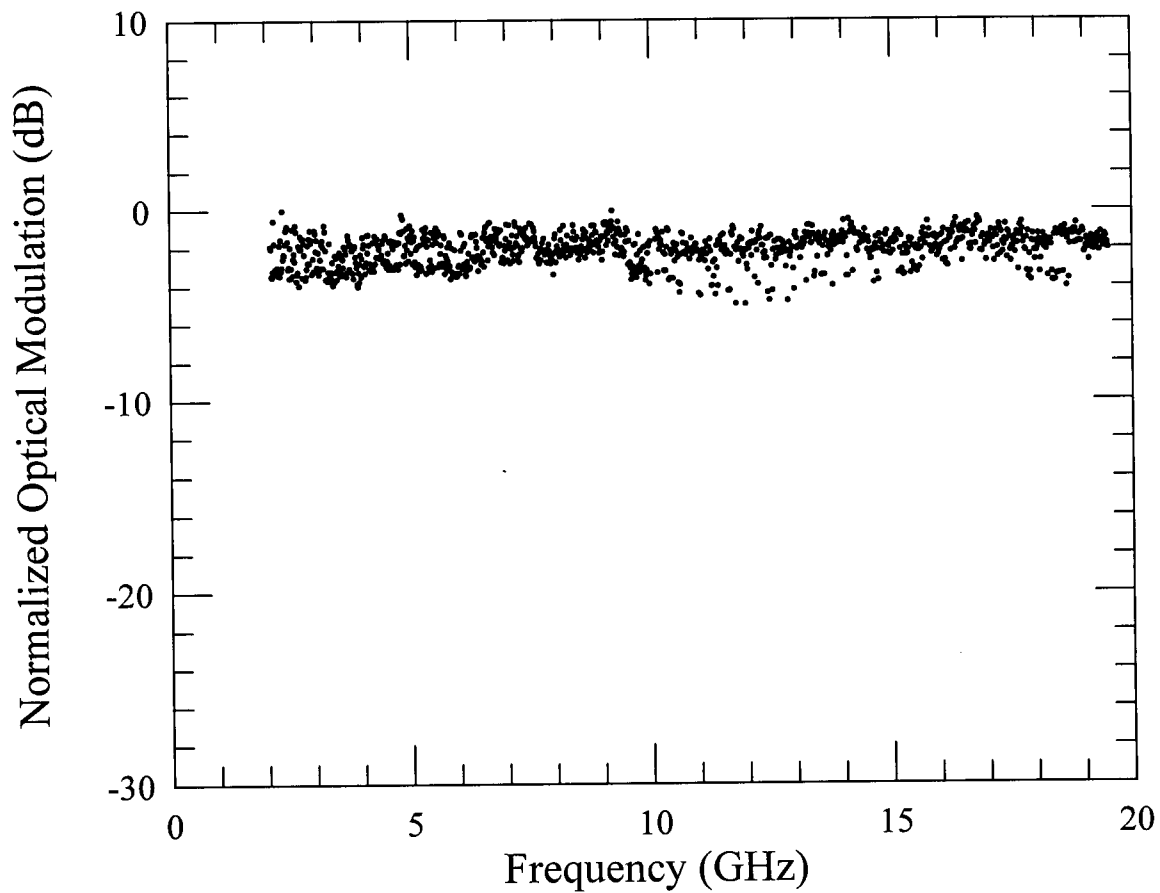
Figure 4.3.10. Normalized (to the highest value) small-signal optical output of device 35 (MZ-B-CPW type) as a function of frequency.
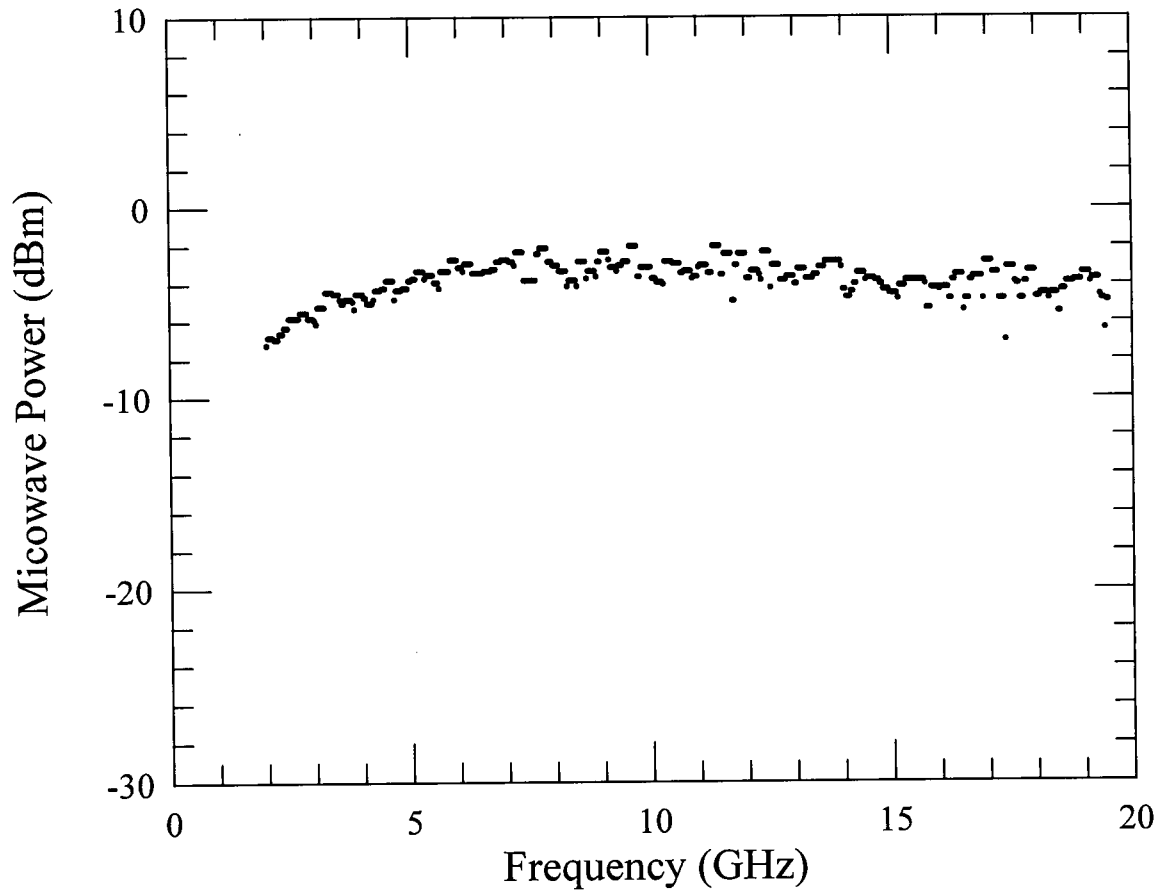
Figure 4.3.11. The microwave power at the output of the microwave cable connected to the HP 83594A plug-in, via the bias-Tee, for a nominal output power of 0 dBm.
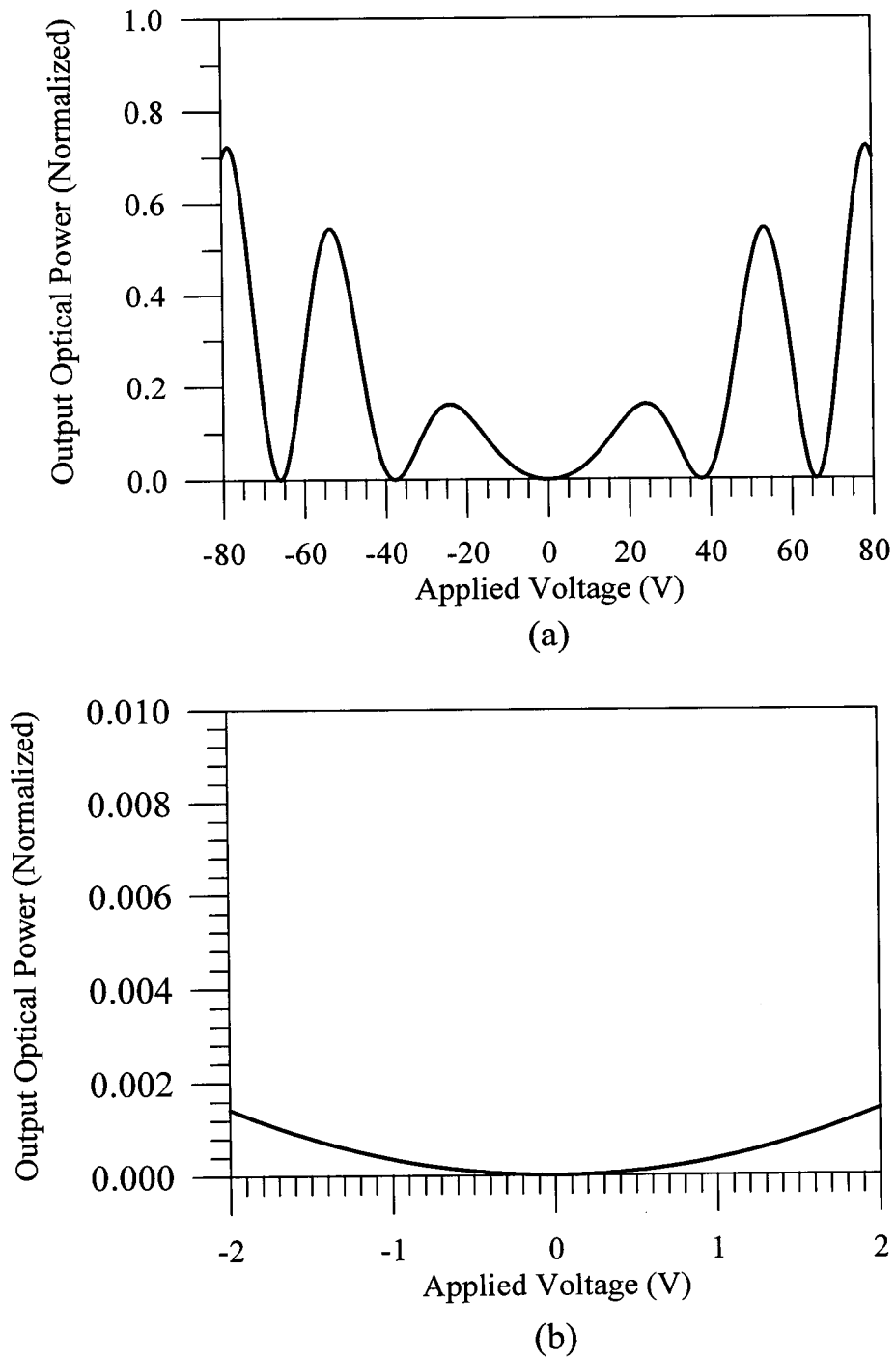
Figure 4.3.12. a) Normalized optical power converted from the TE-like polarization (parallel to the x axis) into the TM-like polarization (parallel to the z axis) as a function of the applied voltage for device 27 assuming n_{TE} = 3.322, n_{TE} - n_{TM} = 0.00024, λ_o= 1.52 µm, and Γ = 0.5. b) plot (a) expanded in the region where the applied voltage is between -2 V and 2 V.
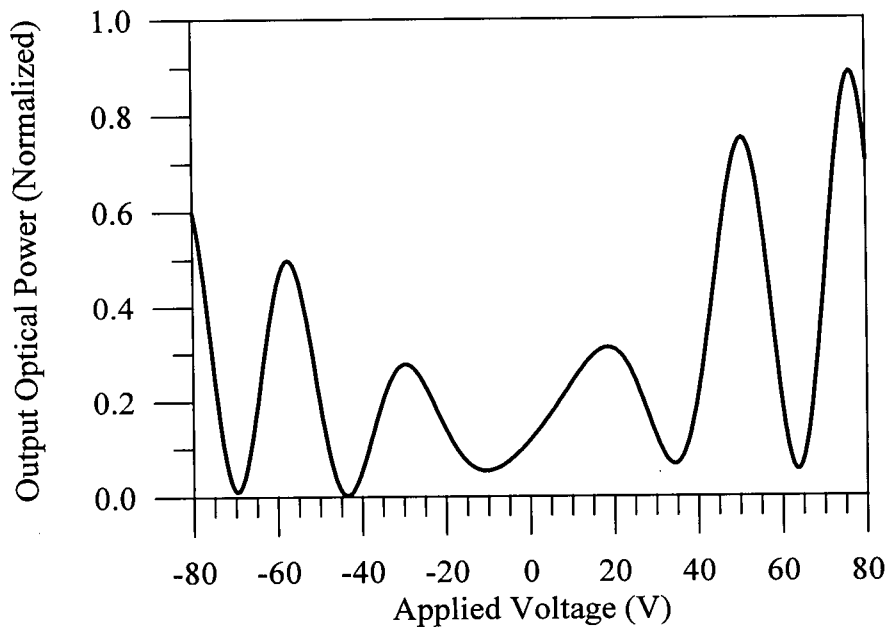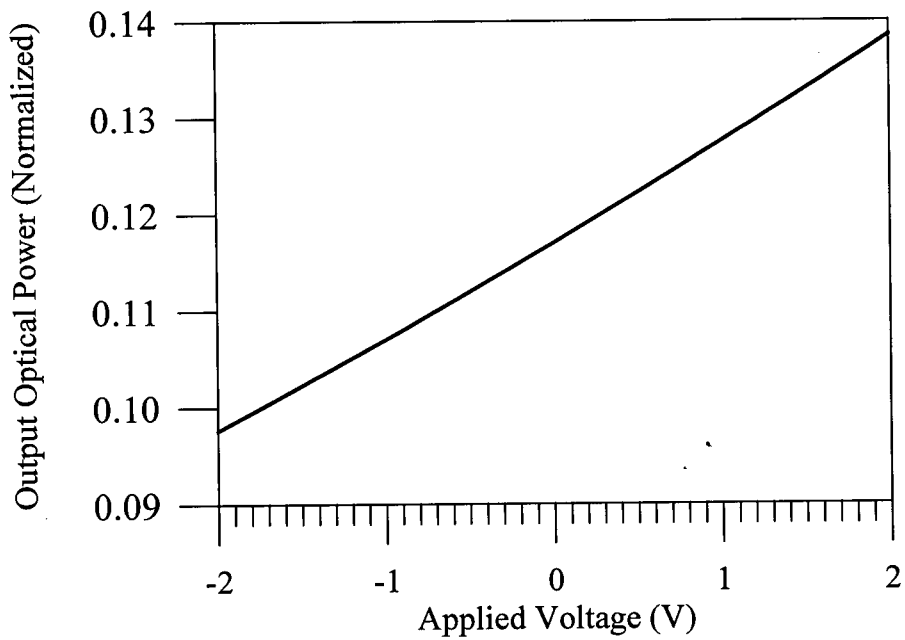
Figure 4.3.13. a) Normalized optical power in the TM-like mode at the output of the waveguide for an input light polarized at 20° to the x axis (or at 70° to the z axis) as a function of the applied voltage for device 27 assuming $n_{TE} = 3.322$, n_{TE} - $n_{TM} = 0.00024$, $\lambda_o = 1.52$ μm, and $\Gamma = 0.5$. b) plot (a) expanded in the region where the applied voltage is between -2 V and 2 V.

185
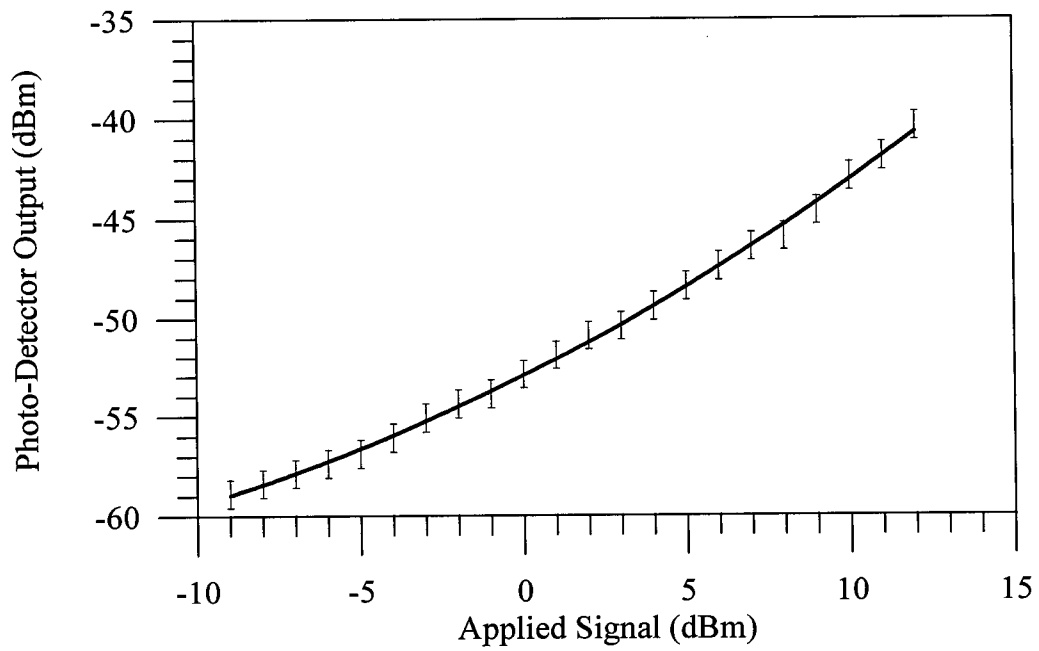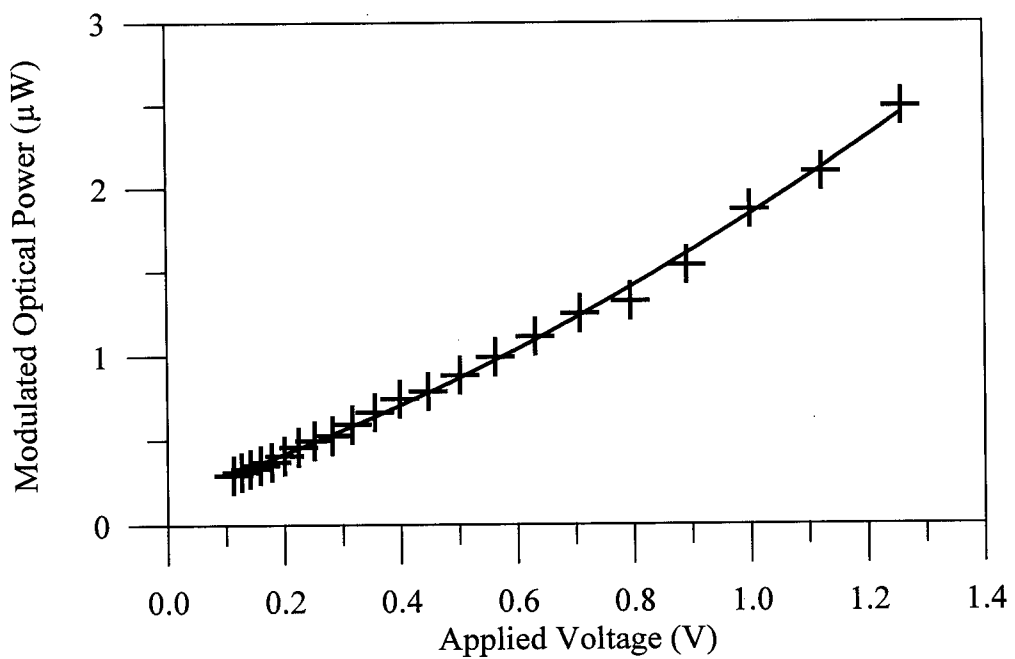
Figure 4.3.14. a) Photo-detector output as a function of the applied microwave power for device 27 at 7 GHz. b) Same as (a) but using different units, i.e., small-signal modulated optical power in μW as a function of the amplitude of the applied voltage in volts.

186
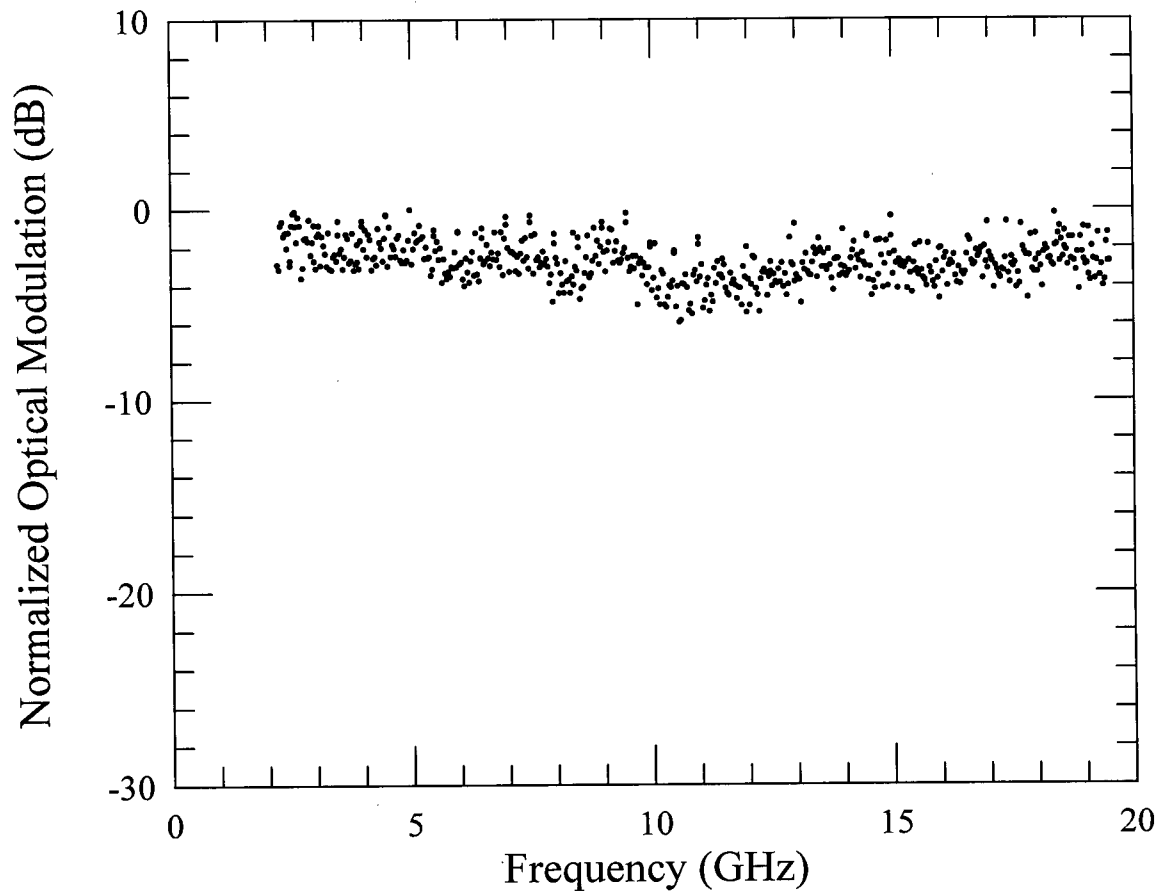
Figure 4.3.15. Normalized (to the highest value) small-signal optical output of device 27 (PC-A-CPS type) as a function of frequency.
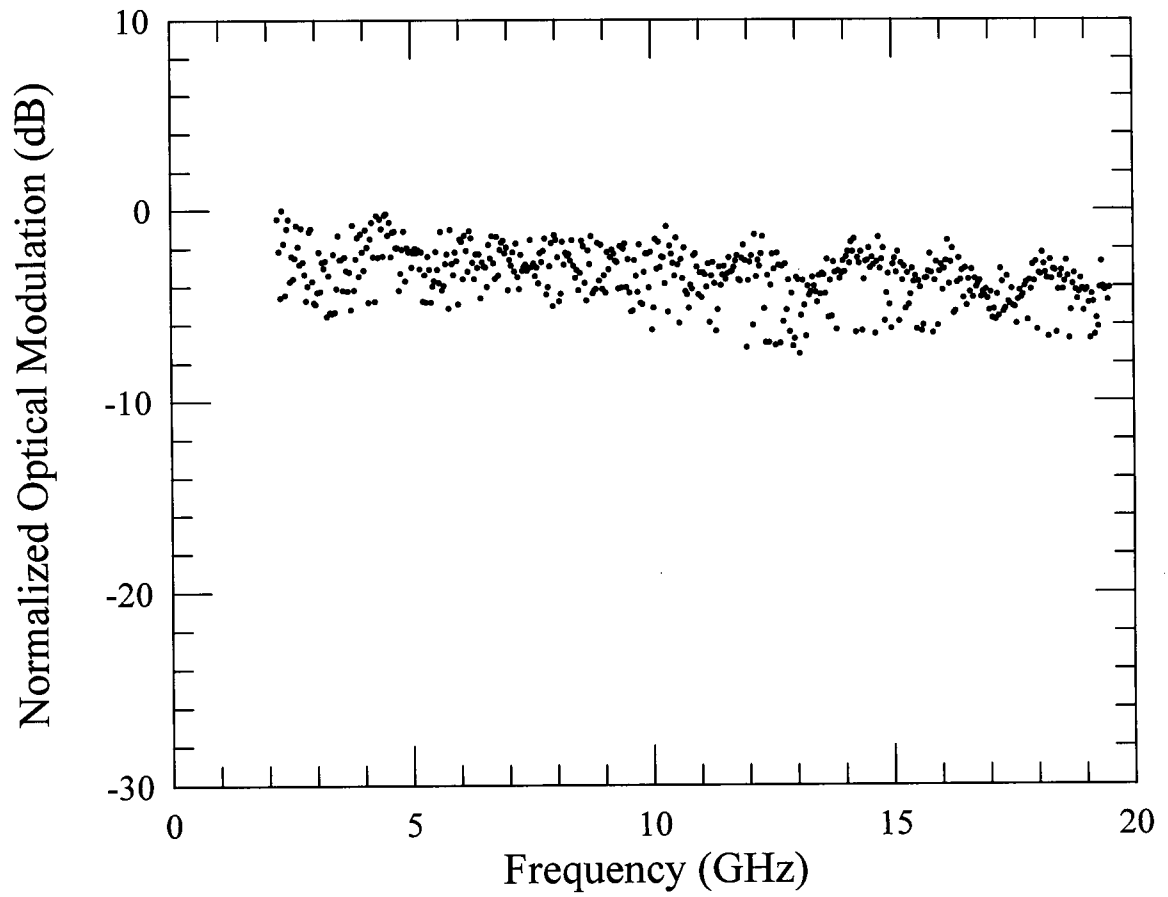
Figure 4.3.16. Normalized (to the highest value near 2 GHz) small-signal optical output of device 37 (PC-A-CPW type) as a function of frequency.
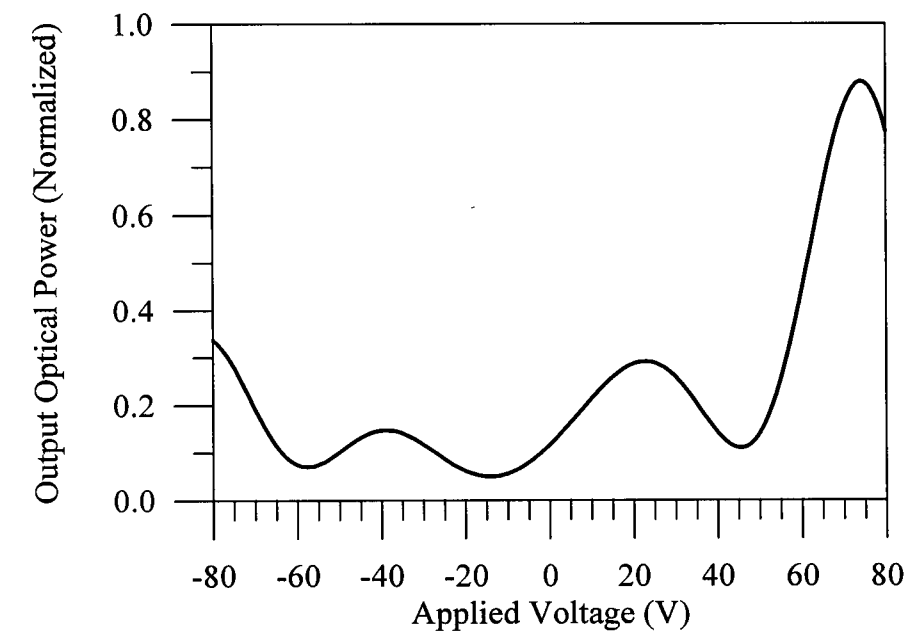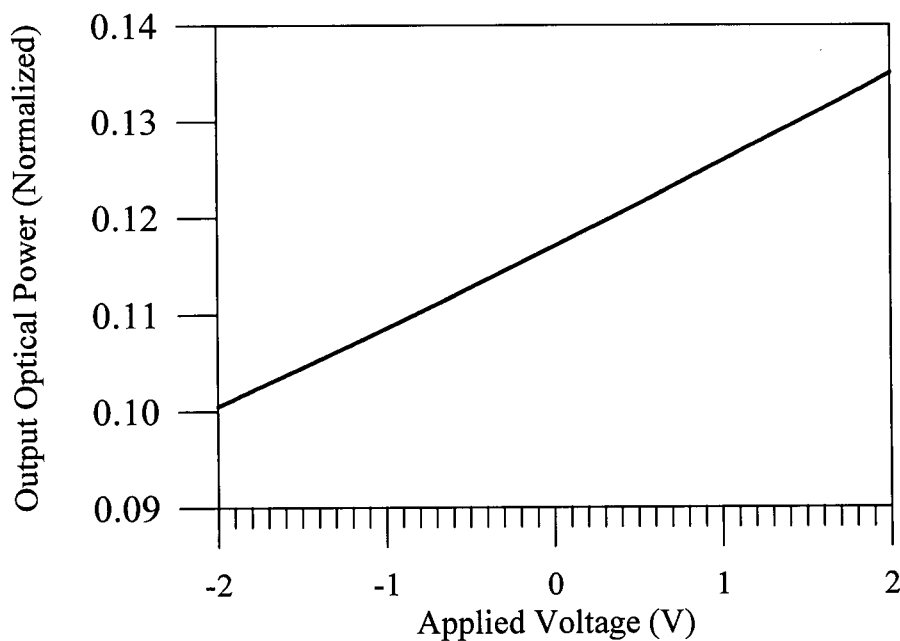
Figure 4.3.17. a) Normalized optical power in the TM-like mode at the output of the waveguide for an input light polarized at $20°$ to the x axis (or at $70°$ to the z axis) as a function of the applied voltage for device 37 assuming $n_{TE} = 3.322$, $n_{TE} - n_{TM} = 0.00024$, $\lambda_o = 1.52$ μm, and $\Gamma = 0.5$. b) plot (a) expanded in the region where the applied voltage is between -2 V and 2 V.

Chapter 5. Summary, Discussion and Conclusions, and Suggestions for Future Work

5.1. Summary

Guided-wave electro-optic external modulators in AlGaAs/GaAs were studied. The problem of microwave-to-lightwave velocity matching was addressed. Slow-wave, travelling-wave, coplanar electrodes having capacitively loading fins and pads in their inter-electrode gaps were designed, fabricated, and tested at up to 40 GHz. The measurements showed that excellent microwave-to-lightwave velocity matching could be achieved; microwave indices within 1 % of the target values, the effective index of the optical waveguides, were measured.

Polarization converters (PC) using slow-wave electrodes were studied in detail. A "wave-plate" model was developed to study this particular group of devices. The polarization converter was divided into a number of small sections, wave-plates, each having its fast and slow axes in directions dependent on the applied electric field in that particular section. The collective effect of these wave-plates determines the transfer function of the polarization converter. The effect of the modal birefringence of the waveguide was also considered in the model. Low-frequency measurements, made on the fabricated devices, showed very good qualitative agreement between the measured performances of the mode-converters and those predicted using the model. For high frequencies, the effects of the microwave-lightwave velocity mismatch and the microwave loss were also taken into account in the model developed.

The slow-wave electrodes fabricated were low-loss; typical microwave losses for the electrodes fabricated on semi-insulating GaAs substrates were 0.22 Np/cm and 0.34 Np/cm

for slow-wave CPS and CPW electrodes, respectively, at 40 GHz. For the electrodes fabricated on AlGaAs/GaAs substrates, grown by molecular beam epitaxy (MBE), the corresponding losses were 0.17 Np/cm larger.

Both the Mach-Zehnder (MZ) type modulators and the polarization converters were fabricated in AlGaAs/GaAs substrates grown by MBE. The transfer functions obtained for both types were in good qualitative agreement with the expected performances of these devices at low frequencies. At very low frequencies, ≤ 1 kHz, the material showed some "field-screening" effect; we observed that the amount of modulation was significantly reduced at frequencies below 100 Hz. The source of this effect is yet under investigation in collaboration with the CRC. A possible explanation is provided: slowly moving charged particles partially block/cancel the applied electric field.

High-frequency, small-signal modulation of light using both types of modulators, i.e., the MZ type and the PC type, was done at up to 20 GHz. Ultra-wide-band devices with 3-dB optical bandwidths in excess of 20 GHz were measured. The decrease in the amount of the optical modulation for some of the devices reported was less than 1 dB in the range 2 GHz to 19.5 GHz. Due to equipment limitations, we were not able to make optical measurements at frequencies larger than 20 GHz at this point in time.

5.2. Discussion and Conclusions

The modulators studied in this thesis are intended for ultra-high-speed modulation of light. From the point of view of the user of such modulators, different technologies and devices are compared based on the following criteria: the useable bandwidth of the modulator,

191

the drive power needed for modulation at high frequencies, and the optical quality (the optical insertion loss) of the modulator. Generally, it is desired to have the widest bandwidth for the lowest drive power and the lowest optical insertion loss. For electro-optic modulators, the half-wave voltage of a modulator is usually used as an indication of the power needed for the modulation; of course, the actual drive power is proportional to the square of the voltage applied. The advantages of the external modulation and the restrictions of the direct modulation of laser light imply that at frequencies above ~ 30 GHz, external modulation is the preferred technology [4]. The competing technologies for external modulators are the electro-optic and the electro-absorptive modulators. The former one is, arguably, the more mature technology, offers very small optical insertion losses, and devices having ultra-wide bandwidths (~70 GHz) have be shown in that technology [20], [21]. The half-wave voltage for these devices is, however, rather large. For wide-band Mach-Zehnder type devices fabricated in AlGaAs/GaAs substrates, the smallest V_π's reported are in the range 10 to 16 volts [21], [31]. Recently, electro-absorptive modulators with small-signal bandwidths up to 50 GHz have been reported [17], [18]. The attractive feature of these devices is the low drive power; drive voltages as low as 2.5 V to achieve ~20 dB extinction ratios are reported in [17] for devices with bandwidths ~ 40 GHz. The optical insertion losses for these modulators are, however, significantly higher than those achievable for the electro-optic modulators [17]. Also, increasing the bandwidth of these electro-absorptive modulators any further is a very difficult task since they use lumped electrodes and, therefore, are restricted by the RC time constant of the structure; further reduction in the dimensions of the structures used will have a severe penalty in terms of the extinction ratio (also, the fabrication will be extremely

difficult). In summary, the electro-optic modulators using travelling-wave electrodes still seem to be the most promising technology for bandwidths in excess of 40 GHz; however, the drive power has to be reduced. On this note, let us summarize the advantages of the modulators that use velocity-matched electrodes first and then compare the Mach-Zehnder (MZ) and the polarization converter (PC) type devices studied here.

Over all, the results show that ultra-high-speed modulators having bandwidths of several 10's of GHz are possible using slow-wave coplanar electrodes with guided-wave electro-optic modulators fabricated in III-V compound semiconductors. In fact, a reasonable extrapolation of the microwave measurements made at 40 GHz suggests that bandwidths in excess of 100 GHz are achievable using some of the proposed modulator configurations.

The use of slow-wave electrodes eliminates the microwave-to-lightwave velocity matching problem and, hence, allows for longer modulators. The particular slow-wave electrodes used also result in lower microwave losses, as compared to conventional electrodes, and, at the same time, allow for significantly higher effective electric fields in the optical waveguides, see section 2.2. The combined effect of the these factors is that ultra-wide-band devices that require significantly smaller drive powers can be achieved. One of the major restrictions for modulation at high frequencies is the availability (or more precisely, the unavailability) of high-power drive sources at those frequencies. The reduction in the need for drive power at high frequencies is a very significant factor in making these modulators useful. Modulators of the types described in this thesis, using slow-wave electrodes, may need orders of magnitude less drive power at very high frequencies as compared to those that can be obtained using conventional electrodes, see equation (2.2.16)-(2.2.18) and Table 2.4.2.

Again, as reported in this thesis, when the microwave-to-lightwave velocity matching is achieved, both the MZ and the PC type modulators can have bandwidths in excess of 100 GHz, and for an efficient use of the microwave power (to achieve small V_π's) the optical waveguides should be running close to the pads of the electrodes, see section 2.2 and 2.3. As regards the electrode types employed, for an efficient MZ modulator, either slow-wave CPW (SW-CPW) or interdigitated CPS electrodes (ID-CPS) have to be used, i.e., types MZ-B-CPW or MZ-C-CPS, respectively (see Figure 2.3.2 and 2.3.3). The problem with both of these electrode types is that for small distances between the pads, g_p, the electrodes are "over-slow," see the results on electrodes 30, 31, 35, 36, and 37 of generation 2 electrodes. For both the SW-CPW electrodes (Figure 2.3.2) and the ID-CPS electrodes (Figure 2.3.3) the effective capacitances (per unit length of the electrodes) due to the capacitive elements are twice that for the simple slow-wave CPS (SW-CPS) electrodes (Figure 2.3.4) having the same capacitive element dimensions. Polarization converters, as opposed to MZ modulators, can use SW-CPS electrodes, as well as SW-CPW and ID-CPS electrodes, see Figures 2.3.4-2.3.6. SW-CPS electrodes have less capacitive loading per unit length, and do not result in significant over-slowing of the microwave signal.

Let us compare the MZ type modulators using SW-CPW electrodes (MZ-B-CPW type) with polarization converters using SW-CPS electrodes (PC-A-CPS type) in more detail. The amount of the capacitance of the fins and pads depends, amongst many other factors, strongly on their dimensions and the size of the gap between the pads. The smaller the gap, g_p, the larger the duty cycle τ (i.e., l_p / d), and the wider the fins and pads (i.e., the larger l_f and w_p) are, the larger the capacitance and, consequently, the slower the microwave signal

will be. SW-CPW electrodes measured, devices 35-37, are significantly over-slow; n_μ is, on average, 0.4 larger than the effective optical refractive index, $n_{eff} \simeq 3.32$. This large difference can limit the bandwidth of these modulators at high frequencies, see equations (2.2.16)-(2.2.18). The real problem here is that it is not easy to reduce the capacitive effect of these fins and pads without increasing the half-wave voltage of the modulator. Consider device 36 as an example: g_p, τ, and w_p are 5 µm, 0.83, and 4 µm, respectively. L = 10 mm, and the measured $V_\pi \simeq 25$ V (see section 4.3.1.1). The measured n_μ at 40 GHz for this device was 3.82, i.e., n_μ - $n_{eff} \simeq 0.5$. This amount of microwave-lightwave velocity mismatch restricts the bandwidth of this particular modulator to 36 GHz if we ignore the microwave loss, and to 31 GHz if we consider the losses measured. Therefore, it is important to improve the velocity matching to increase the bandwidth. Device 35 shows a structure for which, as compared to 36, g_p has been increased to 6 µm and τ has been reduced to 0.71 to speed up the microwave. The measured n_μ at 40 GHz for this device was 3.63, i.e., n_μ - $n_{eff} \simeq 0.3$ and the electrode is still significantly over-slow. Of course, increasing g_p and reducing τ has the undesirable side-effect of increasing V_π (by ~ 40% here). Device 37 shows another SW-CPW structure that could be used; as compared to 36, w_p has been reduced to 2 µm, d has been increased to 64 µm, and τ has been reduced to 0.75 to speed up the microwave. The measured n_μ at 40 GHz for this device was 3.72, i.e., n_μ - $n_{eff} \simeq 0.4$ and this electrode is also still significantly over-slow. And again, reducing τ would have the undesirable side-effect of increasing V_π by 11% in this case. In short, getting a good microwave-to-lightwave velocity match (and, hence, a wide bandwidth) and a low value of drive power at the same time is very difficult. We have, recently, come across a similar modulator of this kind, developed

independently, reported in the literature [31]. For this device, $w_p = 2$ μm, $d = 100$ μm, $g_p = 6$ μm, and $\tau = 0.9$. In our opinion, these values are close the values for a modulator having very good microwave-to-lightwave velocity matching (within 1%) which is optimized for the lowest value of V_π. The reported V_π, at $\lambda_o = 1.3$ μm, for this device is 14 V (the device is 1 cm long and has a bandwidth in excess of 40 GHz). In our opinion, again, using longer electrodes, and considering the effect of loss, V_π may be reduced to ~7 V for MZ modulators of this type while still having bandwidths in excess of 50 GHz.

The mode converters that use SW-CPS electrodes, on the other hand, show a much better V_π to bandwidth ratio. For these electrodes, g_p can be smaller, and τ and w_p can be larger without resulting in significant over-slowing of the microwave. For example, compare device 26 of generation 2 devices with device 36 given above; for electrode 26, g_p, τ, and w_p are 4 μm, 0.83, and 4 μm, respectively. $L = 15$ mm, and the measured $V_\pi \approx 9$ V at a bias voltage of ~ -20 V(see Figure 4.3.6.e). The measured n_μ at 40 GHz for this device was 3.40, i.e., $n_\mu - n_{eff} \approx 0.08$. This amount of microwave-lightwave velocity mismatch allows for a bandwidth of 150 GHz for this particular modulator if we ignore the microwave loss, and 100 GHz if we take the effects of the microwave loss into account. This is a significant improvement as compared to device 36, both in terms of the bandwidth and the drive power needed. Furthermore, the half-wave voltage of the PC-A-CPS type devices such as device 26 can be further reduced while keeping the bandwidth extremely high. For example, for device 26, if g_p and w_p are both reduced from 4 μm to 3 μm, V_π can be reduced by ~ 25% without any significant increase in n_μ (and decrease in the bandwidth). Using $n_\mu = 3.41$, $\alpha_o = 0.058$ Np/cm/GHz$^{1/2}$ (the values measured for device 26) a modulator with $g_p = w_p = 3$ μm,

and $L = 30$ mm, and otherwise identical to device 26, would have a $V_\pi \simeq 3$V and a bandwidth of 55 GHz at $\lambda_o = 1.3$ μm ($n_{eff} = 3.36$), if we ignore the modal birefringence. If narrower pads, e.g., $w_p = 2$ μm, are used perfect velocity matching can be achieved, resulting in a bandwidth in excess of 85 GHz for the above 3-cm-long device while having the same value for V_π (i.e., 3V).

The substrate layers that we used were designed to give optical mode profiles that are closer to those of single-mode optical fibres so that the optical insertion loss is small. At the cost of the optical insertion loss, the epitaxial layers can be designed to give much smaller optical mode profiles and, consequently, give larger optical-filed-electric-field overlap factors. For example, comparing the theoretical value of V_π for the MZ modulator of [31] and the measured value, 14 V, gives a $\Gamma = 0.6$. The Γ we measured for our MZ device 36 was about 0.3. The most important factors that account for this difference are the difference in the optical mode sizes and the presence of the SiO_2 layer in our structures. For our PC type devices, $\Gamma \simeq 0.5$ is measured. Reducing the thickness of, or eliminating, the SiO_2 layer and using more different epitaxial layers can easily increase Γ by 50 % resulting in a $V_\pi \simeq 2$V for the 3-cm-long PC type device described in the previous paragraph.

Another factor to consider is that CPS electrodes are less lossy as compared to CPW electrodes having sizes appropriate for these modulators. The measured loss at 40 GHz for our SW-CPW electrodes fabricated on SI-GaAs were more than 50% higher than those measured for SW-CPS electrodes. This implies that the modulators that use SW-CPS electrodes (e.g., PC type devices) can be ~ 50% longer than those that use SW-CPW electrodes (e.g., MZ type devices) while having the same bandwidths. The immediate

advantage of having longer electrodes is that V_π is reduced, e.g., in this case, V_π reduces by 33% and, consequently, the microwave power needed for the same amount of modulation is reduced to less than half.

Another advantage of the PC type devices over the MZ type devices is that PC type devices have significantly lower optical insertion losses. The optical waveguide for a PC type device is a single, straight channel waveguide which does not need to be significantly longer than the electrode length. For a MZ modulator, the presence of the Y-branches significantly increases the optical loss of the modulator. Also, the total optical waveguide length has to be substantially larger than the electrode length (in order to accommodate the Y-branches), further increasing the optical power loss.

The only issue that is a disadvantage for PC type modulators is that the modal birefringence has to be kept small for these devices to be efficient at low bias voltages. Nevertheless, the amount of modal birefringence can be kept to sufficiently small values by a proper choice of the epitaxial layer's structure and geometry, see [79]-[82]. The use of simple tensile strain layers in the epitaxial layers [80]-[82], or compensated tensile strain layers [79], can result in extremely small, possibly zero, modal birefringence. For example, Bissessur et al. have reported on a 2 μm wide InP/InGaAsP/InP ridge waveguide that effectively has zero modal birefringence at $\lambda_o = 1.53$ μm [80]. Suppression of modal birefringence in our PC type devices should be investigated and constitutes one of our suggestions for future work.

To summarize, the PC type modulators can have better optical insertion losses and need smaller drive powers as compared to MZ type modulators using slow-wave electrodes.

For PC type modulators using SW-CPS electrodes, the half-wave voltage can be reduced to ~ 1 V by optimizing the electrode and substrate structure and dimensions while having perfect microwave-to-lightwave velocity match and, consequently, bandwidths in excess of 100 GHz. For MZ type modulators that have perfect microwave to lightwave velocity match, the value of V_π would be significantly larger. Reducing V_π to below 5 V and at the same time keeping the bandwidth wider than 50 GHz is extremely difficult for these MZ type devices. The drive power needed for a PC type modulator (that uses slow-wave CPS electrodes) can easily be more than one order of magnitude smaller than that needed for a MZ (MZ-B-CPW) type modulator having the same bandwidth. Considering the above discussion, we would also like to conclude that the PC-A-CPS type devices can offer wider bandwidths, lower drive powers, and lower insertion losses as compared to electro-absorptive modulators (see the values reported in [17] and [18]), and, therefore, electro-optic modulators are still the preferred technology for ultra wide-band external modulators.

Finally, it should be pointed out that even though our work has been done in AlGaAs/GaAs, the concepts developed and presented in this thesis can be used with devices made in other materials. For example, devices fabricated in InP-based substrates (e.g., InGaAsP/InP) have similar problems as regards microwave-to-lightwave velocity matching and modal birefringence, and the same modulator configurations used and suggested here can be fabricated in those materials.

5.3. Suggestions for Future Work

This thesis provides a study of high-speed optical modulators fabricated in AlGaAs/GaAs. The devices fabricated and tested were designed to show that the desired microwave-to-lightwave velocity match and low microwave loss could be achieved, and, therefore, ultra-wide bandwidths and low drive powers are possible. However, there was no effort made to optimize these devices. For these devices to be useable in commercial systems, the modulator structures have to be optimized to take advantage of the particular characteristics of these types of modulators. Even though the optimization and the design of a particular modulator is dependent on the particular application that it is going to be used for, here, we provide a few general guidelines to improve the performance of these devices.

Our modelling and measurements showed that the modal birefringence of the optical waveguide reduces the efficiency of the polarization converter type devices presented here. To achieve efficient polarization converters it is desired to minimize the modal birefringence as much as possible. This could involve a thorough study of the optical waveguide structures in semiconductor (and other) materials. As a starting point, we suggest the use of strained layers in the epitaxial layers that form the core of the waveguide. It is reported in the literature that strained layers in various III-V compound semiconductors can significantly reduce the modal birefringence of the waveguides [79]-[82]. Even if the modal birefringence cannot be totally eliminated, it may be reduced to levels that allow for the fabrication of efficient devices.

The modal birefringence may also be dynamically controlled by applying a d.c. field that affects one mode but not the other one. For example, when using PC-A-CPS type

200

devices, see Figure 2.3.4, an additional narrow electrode can be placed on the top of the optical waveguide. Application of a voltage to that electrode will result in an electric field in the [001] direction which only affects the propagation constant of the TE-like mode of the waveguide. Of course, the design of a practical scheme may be more complicated than this, and the eventual solution may prove to be a combination of the above suggestions.

One of the important issues that requires further study is the quality of the substrate material as regards its electrical and optical properties. Our collaborators at the CRC have concentrated their efforts on improving the substrate quality. One of the results, which has been used and reported here, is that we have been able to obtain epitaxial layers with a low doping density; hence, low microwave loss is achieved. However, at 40 GHz, the losses for the electrodes fabricated on the AlGaAs/GaAs substrates were about 0.17 Np/cm higher than those for the electrodes fabricated on SI-GaAs, i.e., more improvement is possible. This extra loss may be more noticeable at even higher frequencies, and its minimization is desired.

Also, as mentioned in section 4.3, at very low frequencies, < 100 Hz, the optical modulation seems to be inefficient. We appear to observe a "field screening effect" which we, ad hoc, explained as being due to slowly moving charged particles (this theory was only a speculation). This issue has to be addressed in detail especially if one needs to use a d.c. bias for these devices. Devices having small d.c. drifts are possible. There are reports on devices of this kind being effectively biased using a d.c. voltage, see for example [15]. Again, as a starting point for this investigation, we suggest looking into the quality of the epitaxial material and the possibility of the presence of an inversion layer or trapped charged particles at the SiO_2/AlGaAs interface. We are now fabricating similar devices at the CRC that do not

have the SiO$_2$ buffer layer. We intend to experimentally investigate the effect of the presence of the SiO$_2$ layer on this phenomenon. We are also interested in the effects of the SiO$_2$ layer in reducing the optical loss of the waveguide.

In increasing the efficiency of these modulators one can improve their designs. For example, reducing the thickness of the SiO$_2$ layer would increase the value of the electric-field-optical-field overlap factor, Γ, and, consequently reduce the half-wave voltage V_π. Also, the waveguide width and the gap between the pads, g_p, can be reduced to further decrease V_π. For the electrodes that were slightly "over-slow" the capacitive effects of the fins and pads can be reduced by using narrower fins and/or pads, i.e., reducing l_f and w_p, see Figure 2.2.1. It is important to keep the duty cycle, τ, large in order to minimize V_π and to maximize the efficiency, η, see equation (2.4.18). The capacitive effect of the fins and pads can also be reduced by keeping τ constant and increasing l_p and d at the same time ($\tau = l_p / d$). However, one should remember that the fins and pads should be kept considerably smaller than the wavelength of the microwave signal.

References

[1] C. Lin, "Optical Fibre TransmissionTechnology," in *Handbook of Microwave and Optical Components, Vol. 4, Fibre and Electrooptical Components.* Kai Chang, Ed. New York: Wiley, 1991.

[2] T. Tamir (Ed.), *Guided-Wave Optoelectronics,* 2nd edition, Springer Series in Electronics and Photonics 26, Springer-Verlag, Berlin, 1990.

[3] "BNR pushes the art in III-V devices for gigabit data superhighway", *Electronic Products & Technology,* pp. 62-64, Oct. 1993.

[4] S. Weisser, J. D. Ralston, E. C. Larkins, I. Esquivita, and J. Rosensweig, "Efficient high-speed direct modulation in p-doped $In_{0.35}Ga_{0.65}As$/GaAs multiquantum well lasers," *Electron. Lett.,* vol. 28, pp. 2141-2143, 1992.

[5] R. Jungerman, C. Johnsen, D.J. McQuate, K. Salomaa, M.P. Zurakowski, R.C. Bray, G. Conrad, D. Cropper, and P. Hernday, "High-Speed Optical Modulator for Application in Instrumentation," *IEEE J. Lightwave Technol.,* vol. 8, no. 9, pp. 1363-1370, 1990.

[6] R. Olashansky, W. Powazinik, P. Hill, V. Lanzisera, and R.B. Lauer, "InGaAsP Buried Heterostructure Laser with 22 GHz Bandwidth and High Modulation Efficiency," *Electron. Lett.,* vol. 23, pp. 839-841, 1987.

[7] J.E. Bowers, B.R. Hemenway, A.H. Gnauck, and D.P. Wilt, "High-Speed InGaAsP Constricted-Mesa Lasers," *IEEE J. of Q.E.,* vol. QE-22, no. 6, pp. 833-843, 1986.

[8] R.S. Vodhanel, A.F. Elrefaie, M.Z. Iqbal, R.E. Wagner, J.L. Gimlett, and S. Tsuji, "Performance of Directly Modulated DFB Lasers in 10-Gb/s ASK, FSK, and DPSK Lightwave Systems," *IEEE J. Lightwave Technol.,* vol. 8, no. 9, pp. 1379-1386, 1990.

[9] C.M. Olsen, H. Izadpanah, and C. Lin, "Wavelength Chirp in a High-*k*L Quarter-Wave-Shifted DFB Laser: Characterization and Influence on System Performance," *IEEE J. Lightwave Technol.,* vol. 8, no. 12, pp. 1810-1815, 1990.

[10] K. Kamite, H. Sudo, M. Yano, H. Ishikawa, H. Imai, "Ultra-High Speed InGaAsP/InP DFB Lasers Emitting at 1.3 µm Wavelength," *IEEE J. of Q.E.,* vol. QE-23, no. 6, pp. 1054-1058, 1987.

[11] M. Yamada, and Y. Haraguchi, "Linewidth Broadening os SCH Quantum-Well Lasers Enhanced by Carrier Fluctuation in Optical Guiding Layer," *IEEE J. of Q.E.,*

vol. QE-27, no. 6, pp. 1676-1681, 1991.

[12]   M. Okai, T. Tsuchiya, K. Uomi, N. Chinone, and T. Harada, "Corrugation-Pitch Modulated MQW-DFB laser with narrow spectral line-width (170 kHz)," *IEEE Photonics Tech. Lett.*, vol. 2, pp. 529-530, 1990.

[13]   C. Zah, R. Bhat, F.J. Favire, S.G. Menocal, N.C. Andreadakis, K. Cheung, D.D. Hwang, M.A. Koza, and T. Lee, "Low-Threshold 1.5 μm Compressive-Strained Multiple- and Single-Quantum-Well Lasers," *IEEE J. of Q.E.*, vol. QE-27, no. 6, pp. 1440-1450, 1991.

[14]   S. Morin, B. Deveaud, F. Clerot, K. Fujiwara, and K. Mitsunaga, "Capture of Photoexcited Carriers in a Single Quantum Well with Different Confinement Structures," *IEEE J. of Q.E.*, vol. QE-27, no. 6, pp. 1669-1675, 1991.

[15]   S. Y. Wang and S. H. Lin, "High speed III-V electrooptic waveguide Modulators at $\lambda = 1.3$ μm," *IEEE J. Lightwave Technol.*, vol. 6, no. 6, pp. 758-771, 1988.

[16]   T.H. Wood, "Multiple Quantum Well (MQW) Waveguide Modulators," *IEEE J. Lightwave Technol.*, vol. 6, no. 6, pp. 743-757, 1988.

[17]   R. Weinmann, D. Baums, U. Cebulla, H. Haisch, D. Kaiser, E. Kühn, E. Lach, K. Satzke, J. Weber, P. Wiedemann, and E. Zielinski, "Polarization-Independent and Ultra-High Bandwidth Electroabsorption Modulators in Multiquantum-Well Deep-Ridge Waveguide Technology," *IEEE Photonics Technol. Lett.*, vol. 8, no. 7, pp. 891-893, July, 1996.

[18]   T. Ido, S. Tanaka, M. Suzuki, and H. Inoue, "An ultra-high-speed (50 GHz) MQW electro-absorption modulator for 40 Gbits/s optical modulation," in *Proc. IOOC'95*, 1995, pp. 1-2, paper PD1-1.

[19]   J. Nees, S. Williamson, and G. Mourou, "100 GHz Travelling Wave Electrooptic Phase Modulator," *Appl. Phys. Lett.*, vol. 54, no. 20, pp. 1962-1964, 1989.

[20]   K. Noguchi, O. Mitomi, H. Miyazawa, and S. Seki, " A Broadband Ti:LiNbO$_3$ Optical Modulator with a Ridge Structure", *IEEE J. Lightwave Technol.*, vol. 13, no. 6, pp. 1164-1168, 1995

[21]   R. G. Walker, "High Speed Semiconductor Guided-Wave Optical Modulators," *IEE Colloq., No. 022, Microwave Opto-Electronics*, pp. 1/1-1/6, 1994.

[22]   R. G. Walker, "GaAs/AlGaAs Travelling-Wave Modulators for MM-Wave Frequencies," *IEE Colloq., No. 110, Towards Terabit transmission*, pp. 4/1-4/6,

1995.

[23]   Z.K.F. Lee, *Slow-Wave Electrode Structures for III-V Semiconductor Based Electro-Optic Travelling-Wave Modulators*, M.A.Sc. Thesis, University of British Columbia, April 1992.

[24]   Z.K.F. Lee and N.A.F. Jaeger, "Electrode structure for microwave to optical wave velocity match in III-V semiconductor electro-optic modulators", *CLEO 92*, paper CThS5, pp. 554-555, 1992.

[25]   N.A.F. Jaeger and Z.K.F. Lee, "Slow-wave electrode for use in compound semiconductor electrooptic modulators", *IEEE J. Q. E.*, vol. 28, no. 8, pp. 1778-1784, 1992.

[26]   N.A.F. Jaeger and Z.K.F. Lee, "Velocity-matched slow-wave electrodes for integrated electro-optic modulators" *Proc. of 20th International Congress on High-Speed Photography and Photonics*, Victoria, BC, SPIE vol. 1801, 965-973, 1992.

[27]   F. Rahmatian, H. Kato, N.A.F. Jaeger, R. James, E. Berolo, "Slow-Wave Electrodes on GaAs for Integrated Electro-Optic Modulators," *Canadian Journal of Physics*, vol.74 (Suppl.), pp. S35-S38, 1996.

[28]   N.A.F. Jaeger and F. Rahmatian, "Electro-Optic Modulator," US Patent Number 5,566,257, Oct. 15, 1996.

[29]   N. A. F. Jaeger, F. Rahmatian, H. Kato, R. James, E. Berolo, and Z. K. F. Lee, "Velocity- Matched Electrodes for Compound Semiconductor Travelling-Wave Electrooptic Modulators: Experimental Results," *IEEE Microwave and Guided Wave Letters*, vol. 6., no. 2, pp. 82-84, Feb. 1996.

[30]   N. A. F. Jaeger, F. Rahmatian, H. Kato, R. James, and E. Berolo, "Capacitively-Loaded Travelling-Wave Electrodes for Electro-Optic Modulators," *Proceedings 1995 Canadian Conference in Electrical and Computer Engineering*, Montreal, Quebec, Canada, pp. 1166-1169, Sept. 5-8, 1995.

[31]   R. Spickermann, S. R. Sakamoto, M. G. Peters, and N. Dagli, "GaAs/AlGaAs travelling wave electro-optic modulator with an electrical bandwidth > 40 GHz," *Electronics Lett.*, vol. 32, no. 12, pp. 1095-1096, June 1996.

[32]   R.V. Schmidt, I.P. Kaminow, "Metal-diffused optical waveguides in LiNbO$_3$", *Appl. Phys. Lett.*, vol. 25, pp. 458-460, 1974.

[33]   A. Neyer, "Integrated-Optic Devices in Lithium Niobate: Technology and

Applications," *Electro-Optic and Magneto-Optic Materials II*, SPIE, vol. 1274, pp. 2-17, 1990.

[34]   "High Frequency Intensity Modulators," Preliminary Data Sheet, United Technologies Photonics, East Hartford, CT, 1992.

[35]   T. Findakly, P. Suchoski, and F. Leonberger, "High-quality $LiTaO_3$ integrated-optical waveguides and devices fabricated by annealed-proton-exchange technique," *Opt. Lett.*, vol. 1, pp. 797-799, 1988.

[36]   I. Savatinova, S. Tonchev, R. todorov, M. N. Armenise, V. M. N. Passaro, and C. C. Ziling, "Electro-Optic Effect in Proton Exchanged $LiNbO_3$ and $LiTaO_3$ Waveguides," *J. Lightwave Technol.*, vol. 14, no. 3, pp. 403-409, 1996.

[37]   R.G. Walker, "High-speed III-V semiconductor intensity modulators", *IEEE J. Q. E.*, vol. QE-27, no. 3, pp. 654-667, 1991.

[38]   R. Keil, and F. Auracher, "Coupling of Single-Mode Ti-Diffused $LiNbO_3$ Waveguides to Single-Mode Fibres," *Optics Communications*, vol. 30, no. 1, pp. 23-28, 1979.

[39]   R.C. Alferness, L.L. Buhl, M.D. Divino, S.K. Korotky, L.W. Stulz, "Low-loss Broadband $Ti:LiNbO_3$ waveguide phase modulator for coherent systems", *Electron. Lett.*, vol. 22, pp.309-310, 1986.

[40]   K. Komatsu, S. Yamasaki, M. Kondo, Y. Ohta, "Low loss broad-band $LiNbO_3$ guide-wave phase modulators using titanium/magnesium double diffusion method", *J. Lightwave Technol.*, vol. LT-5, pp. 1239-1245, 1987.

[41]   H. Haga, M. Isutzu, and T. Suets, "$LiNbO_3$ traveling-wave light modulator/switch with an etched groove", *IEEE J. Q. E.*, vol. QE-22, no. 6, pp. 902-906, 1986.

[42]   M. Rangaraj, T. Hosoi, and M. Kondo, "A wide-band $Ti:LiNbO_3$ optical modulator with conventional coplanar waveguide type electrode", *IEEE Photonics Tech. Lett.*, vol. 4, no. 9, pp. 1020-1022, Sept. 1992.

[43]   G.K. Gopalakrishnan, C.H. Bulmer, W.K. Burns, R.W. McElhanon, and A.S. Greenblatt, "40 GHz, low half-wave voltage $Ti:LiNbO_3$ intensity modulator", *Electronics Lett.*, vol. 28, no. 9, pp. 826-827, April 1992.

[44]   F.J. Leonberger, "High-speed operation of $LiNbO_3$ electro-optic interferometric waveguide modulators", *Optics Lett.*, vol. 5, no. 7, pp. 312-314, July 1980.

[45]   R.A. Becker, "Broad-band guided-wave electrooptic modulators", *IEEE J. Q. E.*, vol.

QE-20, no. 7, pp. 723-727, 1984.

[46]   R.G. Walker, "High-speed electrooptic modulation in GaAs/GaAlAs waveguide devices", *IEEE J. Lightwave Technol.*, vol. LT-5, no. 10,pp. 1444-1453, 1987.

[47]   K. Kawano, T. Kitoh, H. Jumonji, T. Nozawa, and M. Yanajibashi, "New travelling-wave electrode Mach-Zehnder optical modulator with 20 GHz bandwidth and 4.7 V driving voltage at 1.52 µm wavelength", *Electronics Lett.*, vol. 25, no. 20, pp. 1382-1383, Sept. 1989.

[48]   K. Noguchi, O. Mitomi, K. Kawano, and M. Yanajibashi, "Highly efficient 40 GHz bandwidth Ti:LiNbO$_3$ optical modulator employing ridge structure", *IEEE Photonics Tech. Lett.*, vol. 5, no. 1, pp. 52-54, Jan. 1993.

[49]   K. Noguchi and K. Kawano, "Proposal for Ti:LiNbO$_3$ optical modulator with modulation bandwidth of more than 150 GHz", *Electronics Lett.*, vol. 28, no. 18, pp. 1759-1761, Aug. 1992.

[50]   S. H. Lin, S. Y. Wang and Y. M. Houng, "GaAs traveling-wave polarization electro-optic waveguide modulator with band-width in excess of 20 GHz at 1.3 µm, "*Appl. Phys. Lett.*, vol. 51, pp. 83-85, 1987.

[51]   D.W. Dolfi, M. Nazarathy, and R.L. Jungerman, "40 GHz electro-optic modulator with 7.5 V drive voltage", *Electronics Lett.*, vol. 24, no. 9, pp. 528-529, April 1988.

[52]   D.W. Dolfi and T.R. Ranganath, "50 GHz velocity-matched broad wavelength LiNbO$_3$ modulator with multimode active section", *Electronics Lett.*, vol. 28, no. 13, pp. 1197-1198, Junel 1992.

[53]   H. R. Khazaei, R. James, E. Berolo, F. Rahmatian, N.A.F. Jaeger, and F. Ghannouchi, "Novel Coplanar Strip Slow Wave Structure for Ultra Wide Bandwidth Electro-Optic Modulators," *Microwave and Optical Technology Letters*, accepted for publication in the Aug. 5, 1997 issue.

[54]   I. Kim, M.R.T. Tan, and S.Y. Wang, "Analysis of a new microwave low-loss and velocity-matched III-V transmission line for traveling-wave electrooptic modulators", *IEEE J. Lightwave Technol.*, vol. 8, no. 5, pp. 728-738, 1990.

[55]   K. Kawano, "Effects of ridge depth on characteristics of shielded velocity-matched (SVM) Ti:LiNbO$_3$ optical modulators with ridge structures", *IEEE Photonics Tech. Lett.*, vol. 5, no. 9, pp. 993-995, Sept. 1993.

[56]   F. Rahmatian, A. Kulpa, N.A.F. Jaeger, R. James, M. Begin, H. Khazaei, E. Berolo,

and F. Ghannouchi, "Low-Loss Slow-Wave Coplanar Strips and Coplanar Waveguides for Electro-Optic Modulators," *Proc. CLEO/Europe '96*, Hamburg, Germany, September 8-13, 1996, p. 255.

[57]   R. Spickermann and N. Dagli, "Experimental analysis of millimeter wave coplanar waveguide slow wave structures on GaAs," *IEEE Trans. on Microwave Theory and Tech.*, vol. 42, no. 10, pp. 1918-1924, Oct. 1994.

[58]   R. Spickermann and N. Dagli, "Millimeter wave coplanar slow wave structure on GaAs Suitable for use in electro-optic modulators," *Electronics Lett.*, vol. 29, no. 9, pp. 774-775, April 1993.

[59]   S.R. Sakamoto, R. Spickermann, and N. Dagli, "Narrow gap coplanar slow wave electrode for travelling wave electro-optic modulators," *Electronics Lett.*, vol. 31, no. 14, pp. 1183-1185, July 1995.

[60]   N. Dagli, r. Spickermann, S. R. Sakamoto, and M. Peters, "Ultra wide electrical bandwidth GaAs/AlGaAs electrooptic modulators," *1995 IEEE MTT-S Digest*, pp. 251-254, 1995.

[61]   R. Spickermann, M. G. Peters, and N. Dagli, "A Polarization Independent GaAs-AlGaAs Electrooptic Modulator," *IEEE J. Q. E.*, vol. 32, no. 5, pp. 764-769, 1996.

[62]   R. K. Hoffman, *Handbook of Microwave Integrated Circuits*, Norwood, MA: Artech House, 1987.

[63]   R. V. Schmidt, in *Integrated Optics: Physics and Applications*. Edited by S. Martellucci and A. N. Chester. Plenum Press, New York, 1983, pp. 181-210.

[64]   W. H. Haydl, "Experimentally observed frequency variation of the attenuation of millimeter-wave coplanar transmission lines with thin metallization", *IEEE Microwave and Guided Wave Lett.*, vol. 2., no. 8, pp. 322-324, Aug. 1992.

[65]   W. H. Haydl, J. Braunstein, T. Kitazawa, M. Schlechtweg, P. Tasker, and L. F. Eastman, "Attentuation of millimeterwave coplanar lines on gallium arsenide and indium phosphide over the range 1-60 GHz," *1992 IEEE MTT-S Digest*, pp. 349-352, 1992.

[66]   *Sonnet*™ *Em User's manual*, release 2.4, Sonnet Software, Inc., 135 Old Clover Rd, Liverpool, NY 13090-3773.

[67]   B.P.C. Tsou, *Electrooptic Mach-Zehnder Modulators in Gallium Arsenide*, M.A.Sc. thesis, University of British Columbia, Sept. 1993.

[68]   A. Yariv, and P. Yeh, *Optical Waves in Crystals*, John Wiley and Sons, New York, 1984.

[69]   J.F. Nye, *Physical Properties of Crystals*, Oxford University Press, Oxford, 1985.

[70]   R.M. Knox, and P.P. Toulios, "Integrated Circuits for the Millimeter Through Optical Frequency Range," *Proc. Symposium on Submillimeter Waves*, Brooklyn, N.Y., Mar. 31-Apr. 2, 1970.

[71]   G.B. Hocker, and W.K. Burns, "Mode Dispersion in Diffused Channel Waveguides by the Effective Index Method," *Appl. Opt.*, vol. 16, no. 1, pp. 113-118, 1977.

[72]   J. T. Boyd, "Theory of Parametric Oscillation Phase Matched in GaAs Thin-Film Waveguides," *IEEE J. Quantum Electron.*, vol. 8, no. 10, pp. 788-796, 1972.

[73]   R. Williams, *Modern GaAs Processing Methods*, Norwood, MA: Artech House, 1990, p. 129.

[74]   W. K. Burns and G.B. Hocker, "End fire coupling between optical fibers and diffused channel waveguides," *Applied Optics*, vol. 16, no. 8, pp. 2048-2050, 1977.

[75]   H. R. Khazaei, O. Berolo, R. James, W. J. Wang. P. Maigné, M. Young, K. Ozard, M. Reeves, and F. M. Ghannouchi, "Charge Carrier Effect on the Microwave Losses Observed on Travelling Wave Electro-Optic Modulators," submitted to *IEEE J. of Q. E.*

[76]   R. E. Collin, *Foundation for Microwave Engineering*, 2nd edition, New York: McGraw-Hill, 1992, pp. 551-557.

[77]   M. Hatzakis, B. J. Canavello, and J. M. Shaw, "Single-Step Optical Lift-Off Process," *IBM J. Res. Develop.*, vol. 24, no. 4, pp. 452-460, 1980.

[78]   K. C. Gupta, R. Garg, and I. J. Bahl, *Microstrip Lines and Slotlines*, Norwood, MA: Artech House, 1979, pp. 260-280.

[79]   J. B. D. Soole, C. Caneau, H. P. LeBlanc, N. C. Andreadakis, A. Rajhel, C. Youtsey, and I. Adesida, "Suppression of Modal Birefringence in InP-InGaAsP Waveguides through Use of Compensated Tensile strain," *IEEE Photonics Tech. Lett.*, vol. 9, no. 1, pp. 61-63, 1997.

[80]   H. Bissessur, P. Pagnod-Rossiaux, R. Mestric, and B. Martin, "Extremely Small Polarization Independent Phased-Array Demultiplexers on InP," *IEEE Photonics*

Tech. Lett., vol. 8, no. 4, pp. 554-556, 1996.

[81]   Y. C. Chan and K. Tada, "Realization of Tensile Strain on GaAs Substrates for Polarization Independent Optical Modulation," *IEEE Photonics Tech. Lett.*, vol. 5, no. 12, pp. 1380-1383, 1993.

[82]   T. Aizawa, K. G. Ravikumar, and R. Yamauchi, "Polarization Independent Refractive Change in InGaAs/InGaAsP Tensile Strained Quantum Well," *Electron. Lett.*, vol. 29, no. 1, pp. 21-22, 1993.